

Optical Properties of Metamaterials Based on Porous Semiconductors and Nanocomposites – Theoretical Considerations and Experiments

Dissertation

Zur Erlangung des akademischen Grades
Doktor der Ingenieurwissenschaften
(Dr.-Ing.)
der Technischen Fakultät
der Christian-Albrechts-Universität zu Kiel

Vladimir Yevgenyevich Kochergin

Kiel
2006

1. Gutachter

.....

2. Gutachter

.....

Datum der mündlichen Prüfung

.....

Contents

1	Introduction	1
2	Novel Optical Elements Made From Porous Si	3
2.1	Introduction	3
2.2	Pore Primer and Pore etching	4
2.3	Different Modes of Light Propagation Through Porous Si	7
2.4	Optical Components from Mesoporous Si	7
2.4.1	Background and Theoretical Considerations	8
2.4.2	Environmental Instability Problem	10
2.4.3	Substrate Absorption Problem	13
2.5	Macroporous Si Long Wave Pass Filters	15
2.6	Optical Components Based on Normal Waveguide Mode Propagation Through Macroporous Silicon	18
2.6.1	Fabrication	31
2.6.2	Omnidirectional Filters for Visible Wavelengths	34
2.7	Optical Components Utilizing Leaky Waveguide Mode of Propagation of Light Through Macroporous Silicon	35
2.7.1	Light Transmission Through The Macroporous Si in the UV- Near IR Spectral Region	35
2.7.2	Coated MPSi Array	43
2.7.3	Wide Field-of-View Design	51
2.7.4	Fabrication and Results	52
2.7.5	Optical Testing	55
2.8	Polarization Components for the UV Spectral Range	57
2.8.1	Theoretical Considerations and Fabrication	58
2.8.2	Optical testing	61
2.9	Retroreflection Suppression Plate	62
2.9.1	Theoretical Considerations	64
2.9.2	Optical Testing	66
2.10	Discussion and Conclusions	67
3	Effective Medium Approach for Calculations of Linear and Nonlinear Optical Properties of Porous Semiconductor Materials	69
3.1	Introduction	69
3.2	Effective optical properties of porous semiconductor materials	70
3.3	Effective permittivity tensor calculations	70
3.4	(110)-Oriented Si Containing Mesopores	74
3.5	(100)-Oriented III-V Compound Semiconductors Containing Crystallographic Pores	79
3.6	Surface Plasmon Enhancement of an Optical Anisotropy in Porous Si/Metal Composites: Introduction	83
3.7	Effective Permittivity Tensor Calculations	83
3.8	Effective Medium Approach for Estimation of Second Harmonic Generation in Certain Porous Semiconductor Materials	91
3.9	Effective Nonlinear Susceptibility Tensor Calculations	92
3.10	SHG From Silver-Filled Pores Etched into a (110) Si Substrate	97

3.11	Discussion of SHG in Certain Porous Semiconductor Composites	99
3.12	Chapter III Conclusions	100
4.	Theoretical Analysis of Optical and Magneto-Optical Phenomena in metal Nanocomposites	101
4.1	Introduction	101
4.2	Linear Optical Properties of Metal Nanocomposites: Background	102
4.3	Experimental Results	103
4.3.1	Two-Dimensional Gold - Polymer Nanocomposite	104
4.3.2	Three-Dimensional Au-Polystyrene Nanocomposite Films	105
4.4	Modified Effective Medium Approximation	107
4.5	Polarizability of the Metal Nanoparticle Dimer	109
4.6	Expansion of EMA by Accounting Dimer Polarizabilities	113
4.7	Application of Modified EMA to Polymer/Au Nanocomposite	115
4.8	Magneto-Optical Properties of Metal Nanocomposites: Background	117
4.9	Faraday Effect in Metal/Dielectric Composites at Low Metal Concentrations	119
4.10	Gold Nanoparticles Embedded into the Magneto-Optically Active Dielectric	120
4.11	Magneto-Optically Active Dielectric Nanoparticles Embedded in Gold	123
4.12	Magneto-optically Active Metal Nanoparticle Embedded in a Dielectric Matrix	124
4.13	Mixture of Magneto-Optically Active Metal Nanoparticles and Gold Nanoparticles Embedded in a Dielectric Matrix	125
4.14	Faraday Effect in Metal/Dielectric Composites at Intermediate Metal Concentrations	127
4.15	Faraday Effect in Metal/Dielectric Composites Near the Percolation Threshold	128
4.16	Cubic Array of Au Nanodiscs Embedded in YIG	129
4.17	Square Array of Au Spherical Nanoparticles Embedded in YIG	132
4.18	Magneto-Optical Kerr Effect in Ordered Nanoparticle Arrays	134
4.19	Application of Scaling Theory to the Estimation of Magneto-Optical Effects in Metal/Dielectric Nanocomposites	137
4.20	Discussion of the Magneto-Optical Effects in Metal/Dielectric Nanocomposites	140
4.21	MO Core-Shell Nanoparticle Composites	141
4.21.1.	Magneto-Optical Properties of the Composite Material Consisting of YIG Core/Au Shell Nanoparticles Embedded into Isotropic Dielectric Material	142
4.21.2.	Magneto-Optical Properties of a Composite Material Consisting of YIG Shell/Au Core Nanoparticles Embedded into an Isotropic Dielectric Material	144
4.21.3.	Magneto-Optical Properties of the Composite Material Consisting of Ni Shell/Au Core Nanoparticles Embedded into Isotropic Dielectric Material	145
4.21.4.	Magneto-Optical Properties of a Composite Material Consisting of Au Shell/Ni Core Nanoparticles Embedded into an Isotropic Dielectric Material	148

4.22	Discussion of the Magneto-Optical Effects in Nanocomposite Materials Containing Core-Shell Nanoparticles	149
5.	Summary and Conclusions	151
5.1	Summary	150
5.2	Outlook and Future Research	153
A.	Publications of V. Kochergin with Relevance to the Thesis	157
A.1	Scientific Journals and Proceedings	157
A.2	Books	160
A.3	Patents	160
A.3.1	Issued Patents	160
A.3.2	Patents Pending	160
A.4	Conference Oral Contributions	161
A.5	Conference Posters	162
	Bibliography	164
	Curriculum Vitae	174
	List of Abbreviations	176
	Acknowledgements	178
	Eidesstattliche Erklärung	178

Chapter I

Introduction

Engineering the optical properties at will by designing and manufacturing an artificial composite material is a very attractive area of science and technology. Already in the Middle Age optical properties of composite materials (metal nanoparticles in glass) were used in stained glass windows [1], despite of the fact that the understanding of the origin of colors in such materials was not understood before Michael Faraday [2] explained the optical properties of small metal particles in the 19th century. The next big step in engineering optical properties by using (one-dimensional) composite materials was made during the first half of the 20th century, when thin-film based optical filters were introduced [3-5]. In the middle of 1980th a new frontier in optics/material science emerged, endeavoring to control optical properties by creating two- and three-dimensional composite materials. Such materials were called photonic crystals (PC) or Photonic Bandgap Materials (PBG) (see, for example [6-7]). At the same time, advancements in the fabrication of nano- and micro-composite materials employing metal nanoparticles [8-10] also offered engineers to produce unique optical properties. The development of porous semiconductor materials (see, for example, [11] and references therein), which could be seen as a special case of composite materials, also led to the discovery of a number of unique optical properties [12-13].

This dissertation is devoted to the exploration of optical properties of certain composite materials, to the design of the artificial composite materials to exhibit desirable optical properties, and to the design and fabrication of some optical components exploiting these artificially designed composite materials.

Chapter II describes a number of optical components made from porous semiconductors with specifically designed morphologies. Designs of different types of spectral filters (designed for UV, visible, IR and far IR ranges), UV polarization components and IR retroreflection suppression plate are presented. A theoretical analysis of these passive optical components is given in each case, followed by some details on their fabrication, and in some cases on optical tests. It will be shown that the optical components introduced in Chapter II exhibit quite unique performance characteristics, often not realizable otherwise. Some of these components meanwhile have been successfully commercialized and are used by the international scientific and research community.

Chapter III is devoted to the more fundamental question of methods of calculations of the effective linear and nonlinear optical properties of porous semiconductors in the case of pore sizes being much smaller than the wavelength of light. In particular, the optical anisotropy of different porous semiconductors is studied. A significant biaxial anisotropy (a property with a sizeable value only for a few natural materials) is predicted for certain porous semiconductors. The linear and nonlinear properties of composite materials consisted of metal-filled porous semiconductors are considered as well.

The first part of Chapter IV addresses the basic problem of accurate calculations of the effective optical properties of metal-dielectric composites at intermediate metal

concentrations (already significant, but still below the percolation threshold). Despite of the fact that this area of optics is relatively old, there is still no widely accepted accurate and simple model that permits calculating linear optical properties of metal nanocomposites in the intermediate metal filling fractions (5 % to 15 %). A modified Effective Medium Theory (EMT) is presented to address this issue.

The last part of the Chapter IV is devoted to theoretical investigations of magneto-optical properties of metal nanocomposites. The magneto-optical effects in composite materials containing metal nanoparticles were investigated in the past only for the case of low metal concentrations and for certain magneto-optical metals. Here the cases of low, medium, near-percolation and high concentrations of metals are theoretically analyzed for both metal and dielectric materials exhibiting magneto-optical activity. Moreover, the magneto-optical effects in metal-dielectric composites consisting of core-shell nanoparticles are analyzed in the low concentration limit. A number of practical materials with significantly enhanced magneto-optical effects (an important feature for a number of applications) are suggested.

Chapter V gives the conclusions of this thesis and describes the possible future research.

Chapter II

Novel Optical Elements Made From Porous Si

2.1. Introduction

Microporous Si became famous almost over night because of its unexpected optical property of showing strong luminescence from yellow to blue, depending on its precise structure [12-13]. However, exploiting this property for devices proved difficult if not impossible up to now. While meso and macroporous Si does not show luminescence, the large set of different porous Si structures does contain many elements with peculiar if not unique optical properties, and this chapter describes a subset with the common denominator that wave propagation in pore direction will be considered.

Porosity quite generally changes the effective index of refraction from its volume value n_V to an effective value n_P , which can be very roughly approximated as $n_P = n_V - pn_V + p$ with p = porosity = relative pore volume. A porosity of 1 thus would be only pores; in practice p is confined to about $0.2 < p < 0.8$. This relation between the porosity and refractive index only applies if the size scale of the pores (average diameter, distances, etc; in what follows surmised under “pore geometry”) is sufficiently smaller than the wavelength considered, so that the metamaterial “porous semiconductor” can be treated with an effective medium theory, e.g. from Bruggeman [14]. A more accurate relation between the porosity (and pore morphology) and the effective refractive index of porous semiconductors will be presented in Chapter III. Since porosities and pore geometries can be adjusted in a wide range (for a review see, e.g. [15], many applications based on adjustable n_P 's have been suggested and are investigated. Most prominent are variants of so-called Bragg mirrors; structures with alternating layers of different porosity; allowing to design transmission and reflection properties as a function of wavelength almost arbitrarily, cf., e.g., [16].

For a given geometry and porosity, pores may still have completely different morphologies. At the extremes one may have a completely random sponge-like structure, or ordered straight cylinder-shaped pores all extending in a well-defined (crystallographic) direction. With the latter type, n_P cannot only be adjusted to a particular value, but two possible kinds of symmetry breaking can be used to induce anisotropies in n_P that cannot only be adjusted, but may be of a kind not found in “natural” materials. Consider, e.g. the case of pore growth in $\langle 100 \rangle$ for Si, or $\langle 111B \rangle$ for III-V semiconductors (the “B” refers to the subset of all $\{111\}$ directions pointing from the group V atom to the group III atoms in III-V semiconductor compounds; cf. [17]. On suitable substrates ($\{110\}$ for Si or $\{100\}$ for the III-V's), two sets of crystallographically identical pores at equal densities grow into the substrate at angles of 45° or 55° , respectively. The cubic symmetry of the single crystal substrate is broken, and the resulting optically homogeneous metamaterial is optically anisotropic, showing effects like birefringence [18-21]. A second kind of symmetry breaking would occur if the density of the two kinds of pores is made to be different; a feat that is generally possible. Rather peculiar optical anisotropies may result, as will be shown in Chapter III.

If the porous semiconductor can no longer be considered being optically homogeneous, the interaction of light and the porous structure can take many forms. If some periodicity in the pore

structure is produced, either by “seeding” pores with appropriate structuring techniques (e.g. optical or e-beam lithography or nanoimprinting) or by exploiting self-organization features, photonic crystals result, commonly in two dimensions, but on occasion also in three dimension [22-25]. Photonic crystals based on porous semiconductors have been extensively covered in [26], suffice it to say that in two-dimensional photonic pore crystals usually only the propagation of light perpendicular to the pores is of interest. Besides the phenomena related to the presence of an optical bandgap, some peculiar properties of the dispersion curves at wavelengths outside the gap region, like very small effective propagation velocities (strongly reduced “speed of light”) or an effective negative index of refraction, are finding increasing interest [7].

The non-linear properties of porous semiconductors may also be completely different from those of the bulk; again we must consider porous semiconductors to be metamaterials with novel features. The most outstanding example is porous GaP, where a more than hundredfold enhancement of the second harmonic generation (SHG) has been observed [27-29]. However, neither is this effect fully understood, nor has the field be exhaustively explored at present.

Comparatively little work has been done concerning the propagation of light in pore direction, in particular for geometrically well-defined arrays of straight pores with large aspect ratios. Most noteworthy is the work of Lehmann et al. [30], where it was shown that uniform and ordered arrays of straight macropores with diameters in the 1 μm region and lengths of several 100 μm act as efficient short pass filters in the blue to UV region, i.e. membranes of these pore array are transparent to blue or UV light, but not to longer wavelengths.

This Chapter presents and summarizes new results concerning wave propagation along pores in a variety of structures. Some necessary background issues are briefly reviewed, and theoretical and experimental results are given relative to possible applications. More complicated structures than just plain porous membranes (e.g. coated and filled pores) are introduced and discussed. It will be shown that porous semiconductors employed in this way show great promise for a multitude of novel optical components; in fact, first products are already on the market.

2.2. Pore Primer and Pore Etching

Here I will only consider pores obtained by electrochemical (anodic) etching, omitting the emerging technology of (electroless) metal assisted chemical etching (cf., e.g. [31] for a recent paper on this subject). There is an amazing variety of pores both with respect to their geometry and their morphology for the most important semiconductors Si, III-V's, Ge and SiC. Here I will just define some necessary terms, more details about the zoology of pores in semiconductors is presented in [11].

The most cursory distinction between different pore types is by geometry, i.e. average diameters: According to IUPAC standards the following terms will be used: micropores denote pores with diameter < 10 nm, mesopores range from 10 nm – 50 nm, everything > 50 nm is called a macropore. Note that “officially” there is no such thing as a nanopore; and that in many publications the definition given above is not strictly adhered to. The next important parameter concerns the (macro)pore nucleation procedure. Nucleation is either random, i.e. pores nucleate and grow more or less at random (possibly with a large degree of self-organization, cf., e.g., the self-organized formation of pore single crystal in InP [32]), or it is

seeded by e.g. openings in a mask layer, resulting in defined pore geometries and morphologies, provided the growth after nucleation can be controlled. The morphology of pores spans the range from perfectly straight with a defined cross-section, to wildly branched or even fractal. Here I will mostly consider straight cylindrical macropores in Si, possibly with controlled diameter variations (although some mesoporous optical components with branched pores will be discussed as well).

Another important pore parameter is the preferred growth direction. It is either in current flow direction (“curro pores”), prominent in III-V semiconductors, or in a crystallographic direction (“crysto pores”). As far as Si is concerned, the two crystallographic directions expressed in pore growth are normally $\langle 100 \rangle$, and under special circumstances $\langle 113 \rangle$ [25]. In III-V compounds only $\langle 111B \rangle$ directions are found [11], whereas Ge expresses $\langle 100 \rangle$ and $\langle 111 \rangle$ [33].

It remains to discuss how to produce macropores (mostly perpendicular to the surface) with tightly controlled geometry. Two basic possibilities exist: Using n-type $\{100\}$ Si employing backside illumination in an HF based electrolyte diluted by essentially water or water with some ethanol (aqueous electrolyte), or p-type Si in an HF based electrolyte diluted by organic solvents like acetonitrile (MeCN), Dimethylformamide (DMF) or Dimethylsulfoxide (DMSO). It should be noted that p-doped $\{100\}$ silicon wafers with HF-based aqueous electrolyte diluted with ethanol also produces macropores over some range of doping densities of silicon. The basic pore geometry in these cases is controlled by many parameters like current density, voltage, temperature, electrolyte flow conditions, backside illumination intensity together with the minority carrier life time of the Si in the case of n-type Si, and, most important, the doping level.

In order to denote certain pore types, I will use the self-explaining short-hand description introduced in [15], random macropores in n-type Si with a specific resistivity of $5 \Omega\text{cm}$ are denoted, e.g. as n-macro(aqu, bsi, random, $5 \Omega\text{cm}$). More specifics about the etching procedure will be provided below.

Pore etching

Pore etching on standard size wafers up to 200 mm diameter is done with a commercial ET&TE large area system which has been adopted to some specific needs, or in custom built systems for smaller samples. Essentially, macropore etching processes in a variety of (proprietary) modes including the standard n-macro(aqu, bsi) case and mesopore etching (including multilayer techniques) are of interest in the context of this Chapter. In the case of macropores seeded, i.e. lithographically defined structures, or random, i.e. self-nucleated structures have been used; usually on $\{100\}$, but also on $\{111\}$ oriented wafers.

A special requirement with respect to all porous structures is the precise control of the geometry over large areas (the whole wafer). In the case of macropores this includes the pore diameter, the roughness of the pore walls, and the pore depth. For mesopores, crucial parameters are the porosity, the thickness of the layers and the flatness of the many interfaces. Precise control of the geometry over large areas is not an easy task and translates into the following basic requirements for the etching apparatus and the etching process.

- i) The basic electrochemical reactions as controlled by the etching cell must be the same everywhere. This requires adequate control of the electrolyte flow, temperature and con-

- centration of the ingredients (the HF concentration, e.g. might decrease with time because it is used up in the reaction, if no controlled replenishment is introduced) as well as a constant electrical field between the counter electrode and the wafer (External voltages might be very large for some etching modes). The equipment used has been optimized for these requirements; some details can be found in [34].
- ii) The backside illumination in connection with the ohmic backside contact for n-macro(aqu, bsi) must be optimized for large areas; in particular rather large illumination intensities are needed to allow sizeable absolute currents for large wafers. A densely packed LED matrix with more than 2.000 matched LEDs was used, driven by special hardware included in the software controlling of the complete etching process.
 - iii) All components in contact with the electrolyte must withstand electrolyte on occasion even more aggressive than HF. An all-Teflon design optimized for safety is necessary for this.

Some problems remain, however: Unavoidable doping fluctuations in commercial wafers (usually present in a circular pattern) are always expressed in fluctuations of the pore geometry if no special measures are taken. Suffice it to say that proper control of the etching temperature (in particular below room temperature) can solve or at least alleviate that problem. This puts additional requirements on the etching apparatus, of course.

Another set of problems results from the unavoidable changes of the etching process with increasing depth of the pores due to, e.g., changing transport properties of reactants and actants inside growing pores, decreasing potential at the pore tips due to ohmic losses in the pore, increasing leakage currents flowing through the pore walls, or increasing hole currents flowing to the pore tips in the case of n-macro(aqu, bsi) pores because the distance between the hole source (= illuminate backside) and the pore tip decreases. These problems can be addressed by changing the external parameters as a function of time in a suitable way (i.e. increase the potential and decrease the illumination intensity), but for precise control of, e.g., the thickness and porosity of mesoporous layers, or the pore diameter as a function of depth, an active feedback control loop is required. There are several ways to generate a control signal that contains the necessary information about the conditions at the pore tips, and several ways to use that signal for adjusting crucial etching parameters like external voltage, current, temperature, or e.g. HF concentration. Suffice it to say that in-situ FFT impedance spectroscopy, or assessments of resistive elements in the circuit, proved useful for obtaining good results. Of course, for any active feedback process, at best some average of the conditions at the tips of some billion of pores can be obtained, and the resulting signal is completely meaningless if the etching process is not very homogeneous.

It is equally of course, but nevertheless worthwhile mentioning, that obvious problems in n-type Si associated with diffusion lengths considerably smaller than the wafer thickness, or, far worse, inhomogeneous diffusion lengths across a wafer, cannot be compensated at all. Pore geometries in this case will reflect the diffusion length distribution, and nothing can be done to circumvent the problem except using p-macropores whenever possible.

Utilizing all of the above, it is still not easy (but possible) to grow suitable macropores with depths exceeding 300 μm in both n and p-type wafers.

2.3. Different Modes of Light Propagation Through Porous Silicon

The wide variety of possible geometries and dimensions of structures that could be fabricated from porous silicon gives the opportunity to control the optical properties in several different ways depending on the relation between the wavelength of the light, the pore geometry, the pore morphology, etc. In general, light propagation through a porous silicon structure in the direction of the pores is described in three different modes:

i) Propagation in porous Si at wavelengths considerably larger than the pore geometry and above the absorption edge of the silicon (or “subwavelength mode”). The electromagnetic wave in this case “sees” a homogeneous isotropic or anisotropic medium. Such a mode is found for microporous and mesoporous silicon and wavelengths typically above 500 nm, or for macroporous silicon in the more far IR spectral range.

ii) Propagation in porous silicon at wavelengths comparable to the pore geometry but still above the absorption edge of silicon. For macroporous silicon this corresponds to the mid IR wavelength range. In this case the type of light propagation is defined mostly by the geometry of the pore array. Two different types of light propagation are possible in this case. The first one is the Bloch mode-type of propagation, typical for Photonic Crystals [22, 35, 36]. This type of light propagation was quite well reviewed recently [7]. In this Chapter the second type of light propagation through such structures will be introduced in relation to certain optical components utilizing such a mode of light propagation. It is based on a waveguide type of propagation for electromagnetic waves traveling through a medium with a high index (= Si) bounded partially by a low index medium (pores filled with air or something else). Light transmission channels in this “normal waveguide mode” are possible in the pore growth direction.

iii) Propagation in porous silicon at wavelengths smaller than the pore sizes and below the absorption edge of Si. For macroporous silicon this corresponds typically to the UV and the visible spectral ranges. In this case the electromagnetic waves propagate through the medium with the low index ($n = 1$ for air filled pores), which is surrounded by a medium with fairly large index (Si) in the so-called “leaky waveguide mode”, and this is possible only along the pore growth direction. This mode of light propagation will also be discussed in more detail in this Chapter.

All of these modes of light propagation through porous silicon may be used in different optical components, as will be shown in this chapter.

2.4. Optical Components from Mesoporous Silicon

Porous silicon with pore sizes below the wavelength of the light in the micro, meso, or lower macro region (in what follows always addressed as “mesoporous”) offers the opportunity to “engineer” the refractive index at the visible and the IR spectral range by variations of the porosity of the layer. This property can be utilized in a number of optical components that will be reviewed later. Note that the luminescence properties of microporous silicon [12] will not be considered here. In contrast to the other sections of this Chapter, a lot of work has been dedicated previously to this particular optical use of porous Si as outlined below. My contribution here is limited to the development of one possible way for solving the environmental instability problem in IR optical filters based on mesoporous silicon, and in providing a solu-

tion for the substrate absorption problem. Two improvements permitted to address not only near IR and visible ranges for optical filters based on mesoporous silicon, but mid and far IR spectral ranges as well.

The optical applications of mesoporous silicon considered here are based on optical effects occurring in the subwavelength mode of light propagation ($\lambda \gg d$, where λ is the wavelength of light and d is the characteristic dimension of porous silicon, e.g., average pore-to-pore distance). In such a mode of light propagation, the light “sees” the porous silicon as a (possibly anisotropic) effective medium. The properties of this effective medium can be controlled to a wide extent by adjusting the pore structure, i.e. porosity, sizes of the pores, orientations of the pores, etc, as will be discussed in detail in Chapter III.

A number of methods for calculations of effective dielectric constants and refractive indices of porous silicon layers can be used such as the Bruggeman method [14], the Looyenga formulation [37], or the Maxwell-Garnett approach [38]. For micro- and meso-porous silicon etched on (100)-oriented wafers these approaches provide good agreement between the theoretical predictions and the experiments performed so far with mesoporous silicon etched on (110) oriented substrates (which exhibit optical anisotropy), as was shown in [18-21, 39]. Other methods are suggested in Chapter III.

2.4.1. Background and Theoretical Considerations

Reflective types of optical filters or mirrors based on mesoporous silicon superlattices were proposed first by G. Vincent over a decade ago [40]. In this paper porous silicon superlattices (roughly two microns thick) were etched on p-doped (100) oriented 8-15 Ωcm wafers; the porous layer was microporous silicon. The porosity, and concomitantly the refractive index modulations, were formed by modulating the applied current density during the electrochemical etching. Independently, in the same year another group [41-42] demonstrated a similar approach. In [41] it was shown that in addition to modulating the current density, porous silicon superlattices could also be formed by anodization of substrates with layers of different doping concentrations or different compositions at constant current density. Since then a large number of papers was published with respect to (meso)porous silicon filters and mirrors. Porous silicon filters were envisioned for color-sensitive photodiodes [43], luminescent devices [42], and sensors [16, 44-48]. A detailed review of these activities can be found in [49].

Here mid and far IR optical filters based on mesoporous silicon are described. Mesoporous silicon filters also offer significant advantages if these filters require cooling to cryogenic temperatures (e.g. for most of astronomical and defense applications). The benefit of mesoporous silicon filters in such applications is the absence of thermal or mechanical stresses between the individual layers. Since the layers are “all-silicon”, they are mechanically and thermally perfectly matched. In contrast, common interference filters are always composed of layers with dissimilar mechanical properties and thermal expansion coefficients, causing considerable problems when cooled (not to mention that common interference filters for wavelengths exceeding 24 μm are not available at all due to a number of fabrication problems (the required multilayer structure is getting to thick for conventional deposition technologies).

Examples of SEM images of far IR mesoporous silicon filter cross-sections are provided in Fig. 2.1. High porosity (low refractive index, typically in a range of 1.9 - 2.3) mesoporous

silicon layers have darker contrast due to less silicon (meaning less charging); vice versa low porosity (high refractive index, typically in the range of 2.7 - 3) mesoporous silicon layers have lighter contrast. In Fig. 2.1a the structure of a quarter wave Bragg reflector centered around $63\ \mu\text{m}$ is given, while Fig. 2.1b shows the magnified SEM image of the filter of Fig. 2.1a, indicating the very good quality of the interface between layers with low and high porosity (an important parameter in optical filter fabrication). Fig. 2.1c gives the SEM cross-sectional image of the 100-layer wide band mesoporous mirror reflecting above 90 % from $2.5\ \mu\text{m}$ to $10.5\ \mu\text{m}$. Different thicknesses of mesoporous silicon layers in Fig. 2.1c are created intentionally.

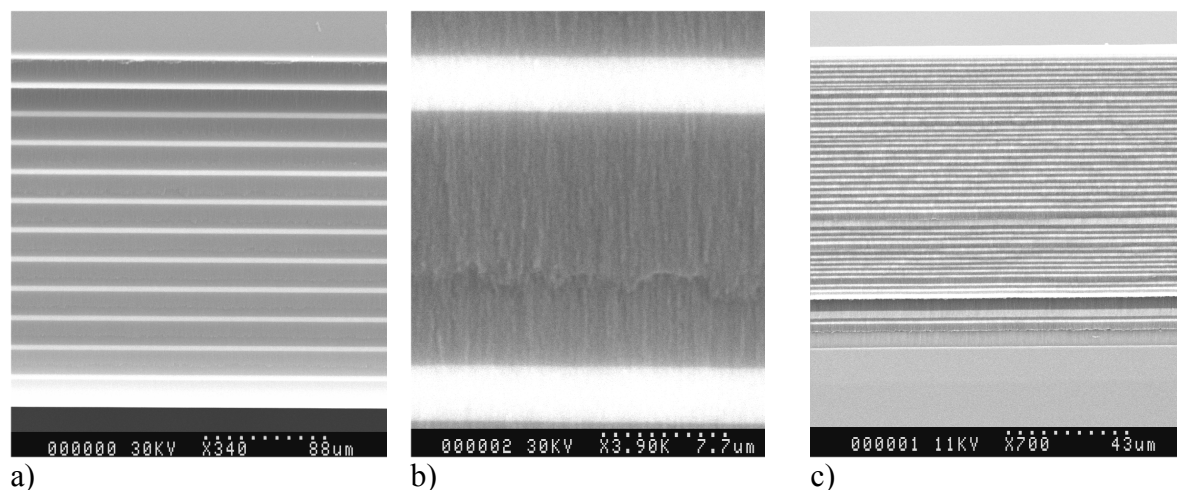


Figure 2.1. SEM images of cross-sections of different mesoporous silicon multilayers etched on (100)-oriented p⁺-doped wafers in HF/Ethanol-based electrolytes.

Depending on the wavelength range that is targeted, the overall thickness of the mesoporous silicon superlattice can vary from as thin as $2\ \mu\text{m}$ (for visible-range filters) to as thick as 200-300 μm multilayers (for far IR filters). While porous silicon superlattices can be formed on both p and p⁺ doped silicon wafers, p⁺ doped wafers are preferred if high refractive index contrast and/or thick multilayer structures are to be fabricated. Mesoporous silicon superlattices can be fabricated on n and n⁺ doped wafers as well, although not as thick and mechanically stable as those made on p⁺ doped wafers (25 μm -thick mesoporous multilayer structure etched on n⁺ doped wafer is the thickest etched so far). Thus, commonly, (100)-oriented Boron-doped wafers with resistivities in the range of 1 to 100 $\text{m}\Omega\text{-cm}$ are used for these purposes (although differently orientated wafers were also used in order to achieve optical anisotropy of mesoporous silicon layers for some applications [18-21]). Typically HF: Ethanol: H₂O electrolytes are used. The sharpness of the edge between the high- and low-porosity layers depends on the temperature of anodization (see, e.g., [50]), and etching at as low as $-20\ ^\circ\text{C}$ temperature was shown to be beneficial for some applications [51]. The achievable current modulation contrast (and through that the porosity contrast) strongly depends on the total thickness of the structure to be etched and on the number of layers. In general high porosity contrast structures are mechanically weaker (it turns out that the weakest points in such a structure are the porosity interfaces).

Another fabrication issue is associated with drying mesoporous silicon multilayers with high-porosity contrast. The capillary forces in pores quite frequently result in loss of the mechanical integrity of mesoporous silicon samples during drying process. Two quite effective solu-

tions were proposed so far: supercritical drying [52], and use of a low surface tension liquid (e.g., Pentane). It should be noted that the “cracking” problem is not that pronounced with mesoporous silicon as it is with microporous silicon, and that in most cases using Pentane (much cheaper and simpler option than supercritical drying) is sufficient to solve the problem.

The attractive features of porous silicon filters and mirrors were stated to be 1) simplicity and a low-cost fast fabrication process, 2) possibility of tailoring the refractive index, 3) compatibility to existing silicon technology [53]. However, some problems with porous silicon filters/mirrors were soon encountered, too. The main problems are environmental instability of mesoporous silicon layers (see, e.g. [54]) and absorption in the highly-doped silicon substrate usually used for mesoporous silicon filter fabrication. These problems and possible solution shall be addressed in the remainder of this section.

2.4.2. Environmental Instability Problem

Environmental instability of mesoporous silicon originates from the very high surface area of mesoporous silicon ($600 - 700 \text{ m}^2/\text{cm}^3$ for microporous and $200 - 250 \text{ m}^2/\text{cm}^3$ for mesoporous silicon [55, 56]); it causes the following unwanted effects: i) blue-shift of the filter wavelength; ii) degradation of the filter performance (quarter wavelength matching of the layers get destroyed); iii) decrease of reflectivity. In infrared transmission-type filters a strong degradation of the transmission is also observed. In general, two different causes are responsible for the effects listed above.

The blue-shift of the filter wavelength and degradation of the quarter-wave matching (causing some decrease of the reflectivity as well) is tied to the relatively slow formation of native silicon dioxide on the pore walls [53]. It is well known that at room temperature and ambient environment about 7 nm of native oxide can be formed with time. Due to the very large surface area of mesoporous silicon, the slow formation of native oxide on all the pore walls is causing very strong optical effects.

The loss of transparency of the mesoporous silicon in the mid and far IR range (it is only transparent through all mid and far IR ranges immediately after etching) is associated with the adsorption of polar gas molecules on the freshly etched silicon surface [57], as illustrated schematically in Fig. 2.2. This effect is much faster than the oxide formation effect and a substantial loss of the transparency in mid and far IR can be observed within a couple of hours after the drying of the sample. In about one week this effect reaches saturation. However, this effect is also fully reversible within some time after etching (for at least two weeks) as also illustrated in Fig. 2.2a.

During the last decade several approaches were suggested for solving the environmental instability problem. This includes the pre-oxidation of mesoporous silicon sample either chemically (by boiling in HNO_3) or thermally (see, e.g. [53]). The reported results suggested that none of these techniques succeeded in a complete prevention of the aging effect. For thermal oxidation a set of conditions exists (at quite elevated temperatures) at which the process is slowed down to acceptable levels for most applications. It should be noted, however, that such a processing results in very substantial shifts and reshaping of the reflection and transmission characteristics of the mesoporous silicon multilayer. Also, due to a substantial lattice mismatch of silicon dioxide and silicon, thermally oxidized layers (especially thick ones, such as required for mid and far IR filters) exhibit large stresses even at room temperatures (caus-

ing considerable bowing of the wafer) and the effect is even stronger at cryogenic temperatures.

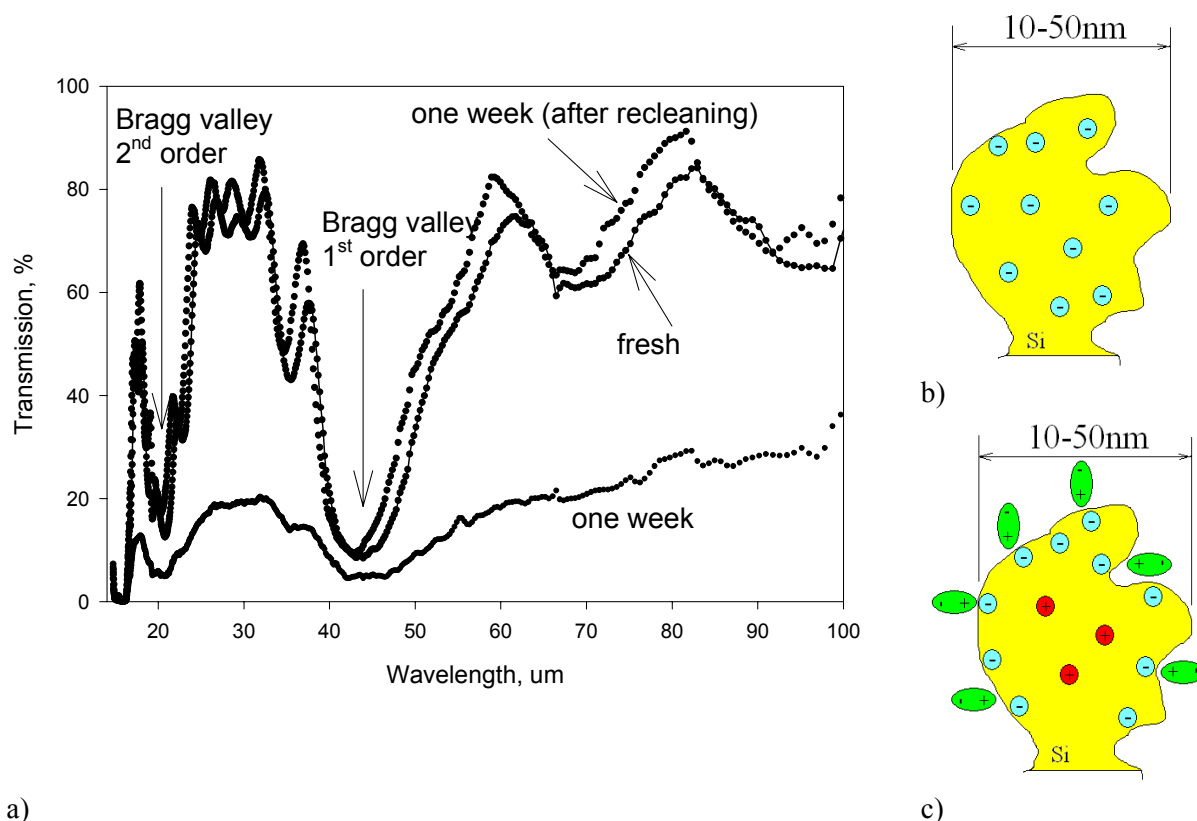


Figure 2.2. a) Transmission spectra through a mesoporous silicon multilayer membrane taken after etching, after 1 week aging in ambient atmosphere and after recovering the membrane in wet chemical solution.; b) - c) schematic drawings illustrating the increase of the absorption in mesoporous silicon (yellow) due to reversible adsorption of polar gas molecules (green), attracting electrons (blue), thus creating uncompensated charge carriers (red) in the mesoporous silicon.

Considerable efforts were devoted towards the stabilizing porous silicon with organic compounds. The basis of these efforts is the replacement of the relatively unstable hydrogen termination of the Si surfaces of pore walls (Si-H bonds) by more stable carbon termination (Si-C bonds). A quite thorough review can be found in [58]. Various techniques were employed for this purposes, including hydrosilylation [59-61], the electrochemical grafting [62] and the method based on alkyl halides [63], to name a few. The methods were mainly devoted towards a stabilization of the optical properties of porous silicon in the visible spectral range. In the far infrared spectral range the advantages of these methods are still to be proven, since FTIR studies show the appearance of additional absorption bands associated with Si-C bonds and (sometimes) other bonds related to the particular composition of pore wall coverage.

Another possible solution for the stabilization of the mesoporous silicon multilayer is the use of a sintering process. Sintering of the mesoporous silicon is usually performed in oxygen and water vapor-free hydrogen or hydrogen/inert gas atmosphere at elevated temperatures (up to 1100 °C and above), and results in a complete closure of the pores at the top surface of the mesoporous silicon layer and sometimes at the porosity interfaces (see, e.g. [64-67]). My experience with this process showed that such a technique could accomplish a substantial stabi-

lization of the mesoporous silicon multilayer, indeed, while offering a substantially reduced mechanical stress level as compared to thermally oxidized wafers. This is no surprise, of course, since the mesoporous silicon layers are still all-silicon after the sintering process. However, the reshaping/shifting of the spectral characteristics of the samples were still considerable and quite comparable to thermally oxidized samples.

Coating the mesoporous silicon surface with layers of SiO_2 deposited at relatively low temperatures by Plasma Enhanced Chemical Vapor Deposition (PECVD) or by Low Pressure Chemical Vapor Deposition (LPCVD) was suggested in [68]. In the same reference, spin-coatable PMMA layers were also suggested for the protection of mesoporous silicon mirrors from moisture, and it was observed that PMMA is actually better suited for moisture protection, while PECVD deposited SiO_2 is better suited for coating of mesoporous silicon membranes. However, I was not able to observe a substantial improvement in some experiments performed in this direction.

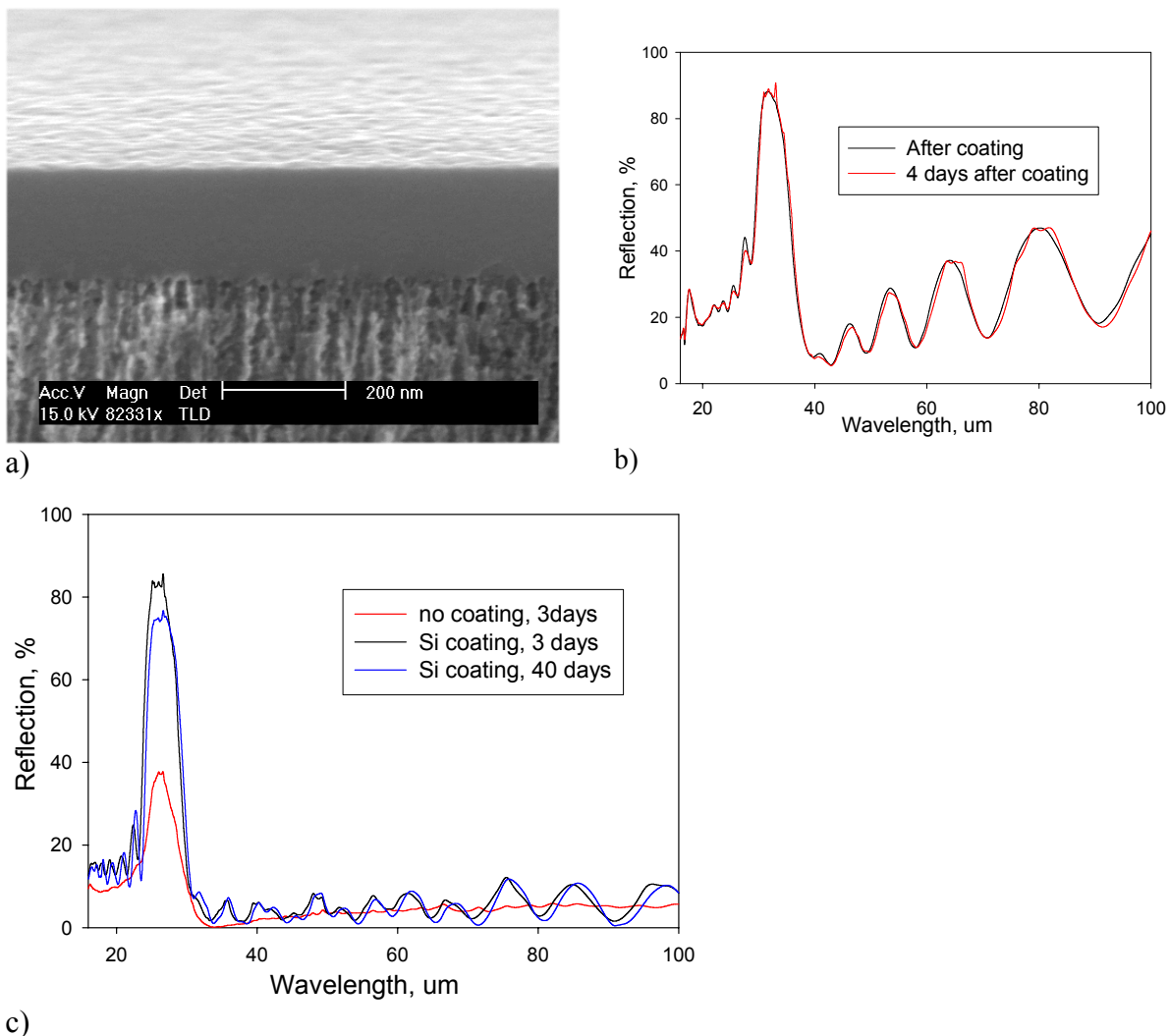


Figure 2.3. a) SEM image of a silicon-encapsulating layer sputtered onto the mesoporous silicon surface. b) Reflection spectra of a mesoporous silicon filter with surface encapsulated with 200 nm Si taken at different times after the deposition. c) Reflection spectra of a mesoporous silicon filter with and without a 200 nm Si layer on the mesoporous silicon surface taken under three days aging conditions and under forty days aging conditions.

Here it is proposed to use a magnetron-sputtered silicon layer on the mesoporous silicon surface as a method of improving the environmental stability of the far IR filters. The advantage of such an approach is based on the fact that the thermal expansion coefficient of a sputtered silicon layer will be the same or close to that of the mesoporous silicon multilayer and silicon substrate. In other words, the filter structure will be all-silicon.

Here I show the results of this method. A SEM image of such a filter structure is given in Fig. 2.3a. The good quality of the silicon layer on the top of the mesoporous silicon multilayer is apparent. Optical testing of the filters confirmed that for a sputtered silicon layer with a thickness of 200 nm or larger, the environmental stability of the filter improves considerably. This statement is illustrated by Figs. 2.3b and 2.3c. As follows from Fig. 2.3b, no change in the reflection from a mesoporous silicon quarter wave stack is detectable three days after the deposition, while the reflectivity of the uncoated sample at the Bragg wavelength degrades strongly as shown in Fig. 2.3c. However, forty days aging in ambient atmosphere resulted in some degradation of the reflectance, indicating that some further optimization of the encapsulation is still required; suitable experiments are currently under way.

2.4.3. Substrate Absorption Problem

As mentioned previously, a big problem with mesoporous silicon IR filters in the transmission mode comes from free carrier absorption (also known as multiphoton absorption) in the silicon substrate still present beneath the mesoporous layer. Highly doped silicon wafers with resistivities in the range of 1 m Ω cm to 20 m Ω cm are totally opaque in most of the mid IR and far IR spectral range at room temperature.

While at cryogenic temperatures transparency can be restored in part of the mid IR region, for room temperature applications the only solution offered for the last ten years has been the removal of the mesoporous silicon multilayer from the unetched silicon substrate by means of a current spike at the end of the etching process, which “lifts off” the mesoporous silicon filter structure [69], i.e. produces a free-standing mesoporous silicon membrane. However, while some mesoporous silicon membranes are relatively robust and flexible (if sufficiently thick, as for far IR filters) many membranes would not survive this rather violent process. In particular, thinness or high porosity renders freestanding membranes unacceptably brittle for practical applications.

Here a new approach is suggested. Instead of a homogeneously doped silicon wafer, a “two layer” silicon wafer composed of a highly doped Si layer with the proper thickness for the intended mesoporous layer bonded to low-doping density “handle” wafer is used. This provides the high carrier concentration necessary for mesoporous multilayer formation on silicon that is highly transparent throughout the far IR range. A schematic drawing of such a bonded structure is shown in Fig. 2.4a.

The key point in choosing a wafer bonding technique suitable for these purposes is a uniform and generally high conductivity across the bonding interface. A fusion bonding technique is capable of meeting this requirement. In fusion bonding, two polished sides of silicon wafers of proper doping, thickness and orientation are brought into contact in a clean environment and then annealed under some pressure across the interface to increase the bond strength [70].

The absence of native oxide on the wafer surfaces is a must to insure good conductivity across the bonding interface.

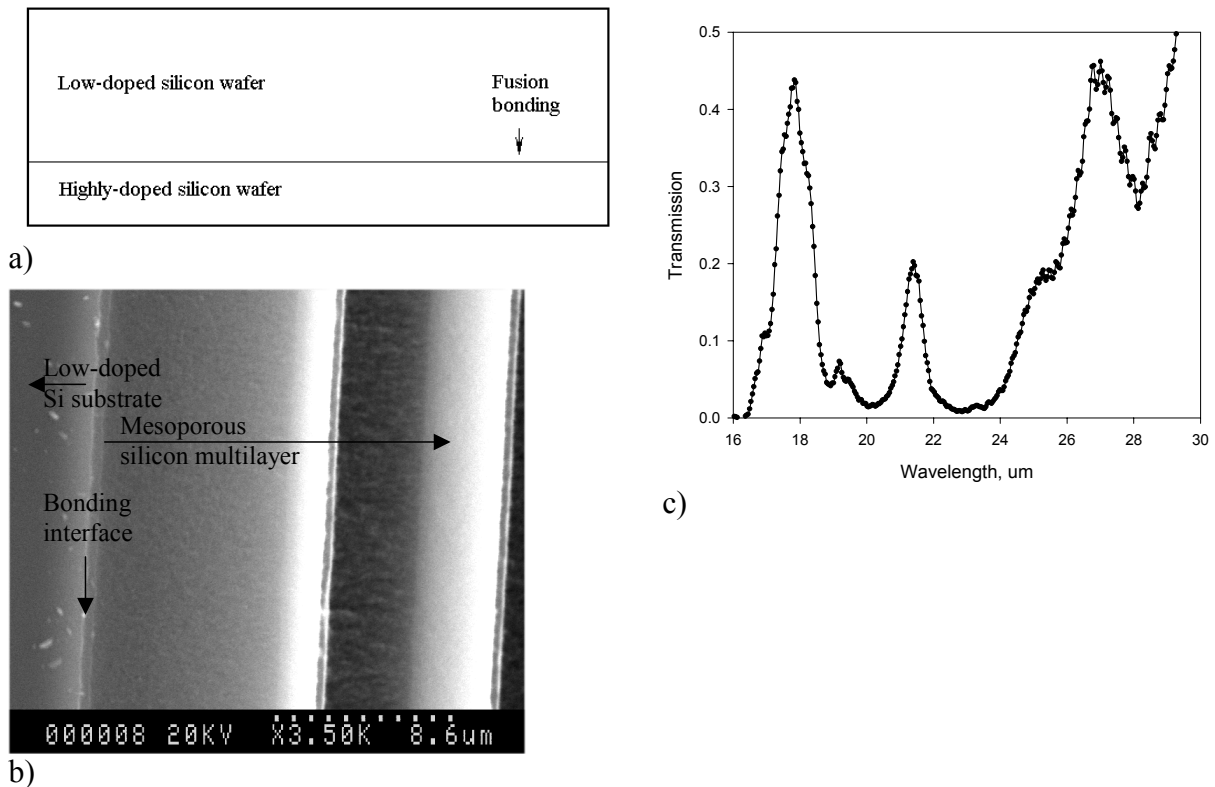


Figure 2.4. a) Schematic drawing of the fusion bonded silicon wafer used for fabricating transmission-type mesoporous silicon IR filters. b) SEM image of a bonded wafer cross section after electrochemical etching up to the bonding interface. The bonding interface is indicated; only the last three layers of the mesoporous multilayers are shown. c) Transmission spectrum taken through a mesoporous silicon filter etched on a bonded wafer at angle of incidence $\sim 14^\circ$ from normal at room temperature.

The backsides of the bonded wafers were metallized and wafers were electrochemically etched. The etching was stopped exactly at the bonding interface, which was made possible by monitoring the current/voltage characteristics of the system. An SEM image of a portion of the mesoporous silicon filter around the bonding interface is given in Fig. 2.4b. In order to prove the transparency of the mesoporous silicon multilayer with a handle wafer, one of the etched wafers was examined in an FTIR at room temperature. The transmission spectrum is shown in Fig. 2.4c. One can see that the structure is indeed transparent in the far IR range. The lower than expected level of transmission within the narrow transmission band is actually caused by losses in the mesoporous silicon multilayer itself, originating from the environmental instability of the mesoporous silicon as described above. The FTIR measurements were performed some time after etching without using the protective methods described above.

It should be noted that while the improvements described above for a mesoporous silicon filter fabrication process in principle resolved all the critical issues, such filters are still not commercially available. The only (but very significant) problem that is still not resolved is the reliable supply of silicon wafers with tight specifications on resistivity (i.e. doping density) and impurity (mainly oxygen) concentration. While this is not considered to be a problem for

large volume applications, for a niche market like far and mid IR filters, the volume is too low to convince silicon wafer suppliers to guarantee the needed quality of silicon wafers.

2.5. Macroporous Silicon Long Wave Pass Filters

Random arrays of macropores in Si scatter the light at wavelengths below the average pore-to-pore distance. In this part of Chapter 2 it is proposed to use this property to make an infrared long-wave pass filter (LWPF) that would scatter the light with wavelengths below an edge wavelength that is defined by the porous layer morphology, but transmit the light effectively and uniformly for wavelengths above this edge. Infrared LWPFs have a number of important applications. They are used both in combination with narrowband pass filters (in order to achieve a narrow pass band with wide and deep rejection bands) and by themselves in applications where the radiation from shorter wavelengths should be suppressed in order to improve the signal-to-noise performance of detectors (as in astronomy, Fourier transform spectroscopy, etc).

In the visible, near IR, and mid IR spectral ranges, LWPFs are usually made as interference filters or as a combination of an absorbing material with a multilayer stack [71]. However, in the far IR this approach is not as successful as in the visible range because the low number of transparent materials that can be used for multilayer stacks, and because of the large thickness of the required multilayers. For the far IR range a scattering-type filter was already proposed in [72], utilizing a layer of diamond particles (or other transparent materials) of suitable sizes, which are spread on a surface of a sheet or substrate of a material that is transparent in the desired IR region (e.g. polyethylene, quartz or sapphire). Light with wavelengths around or below the size of the particles in the “active” layer is blocked by means of scattering, while the light with wavelengths above the size of the particles is transmitted. Such filters are truly long wave pass filters, i.e. the transmission above the rejection edge is uniform over the wavelengths where substrate and particles are transparent. Such filters can be used both in room temperature and cryogenic applications. However, the mechanical stability of such filters is usually poor, since the active layer can be easily peel or flake off. Moreover, the versions made with thin polymer films cannot withstand large pressure differentials very well, thus requiring slow pumping time. Another drawback with particle-based filters is that in order to fabricate filters with a specific rejection edge position, particles of specific size are needed, which are not always commercially available. Also, in order to efficiently scatter the light the particles should have a fairly high refractive index, which makes polystyrene particles (which are inexpensive and widely available) not suitable for such applications.

From the MPS point of view, silicon has a sufficiently high refractive index in the IR spectral range (around 3.5) and the pores, if etched on a flat, unstructured surface, form a random array with a relatively narrow distribution of pore sizes that can be easily fine-tuned in a wide range by choosing suitable substrate and etching parameters [24]. Hence, one can expect that such a material will exhibit long wave pass behavior similar to diamond particle filters [72]. The principle of operation is schematically illustrated in Fig. 2.5a: light with wavelengths labeled 2.3 is long enough compared to the average interpore distance and is transmitted through the filter 2.1 (with some reflection losses), since it “sees” the macroporous layer 2.2 as an effective medium. The light with wavelengths lower than the average interpore distance (2.4) experiences strong scattering (2.5) and thus is effectively blocked.

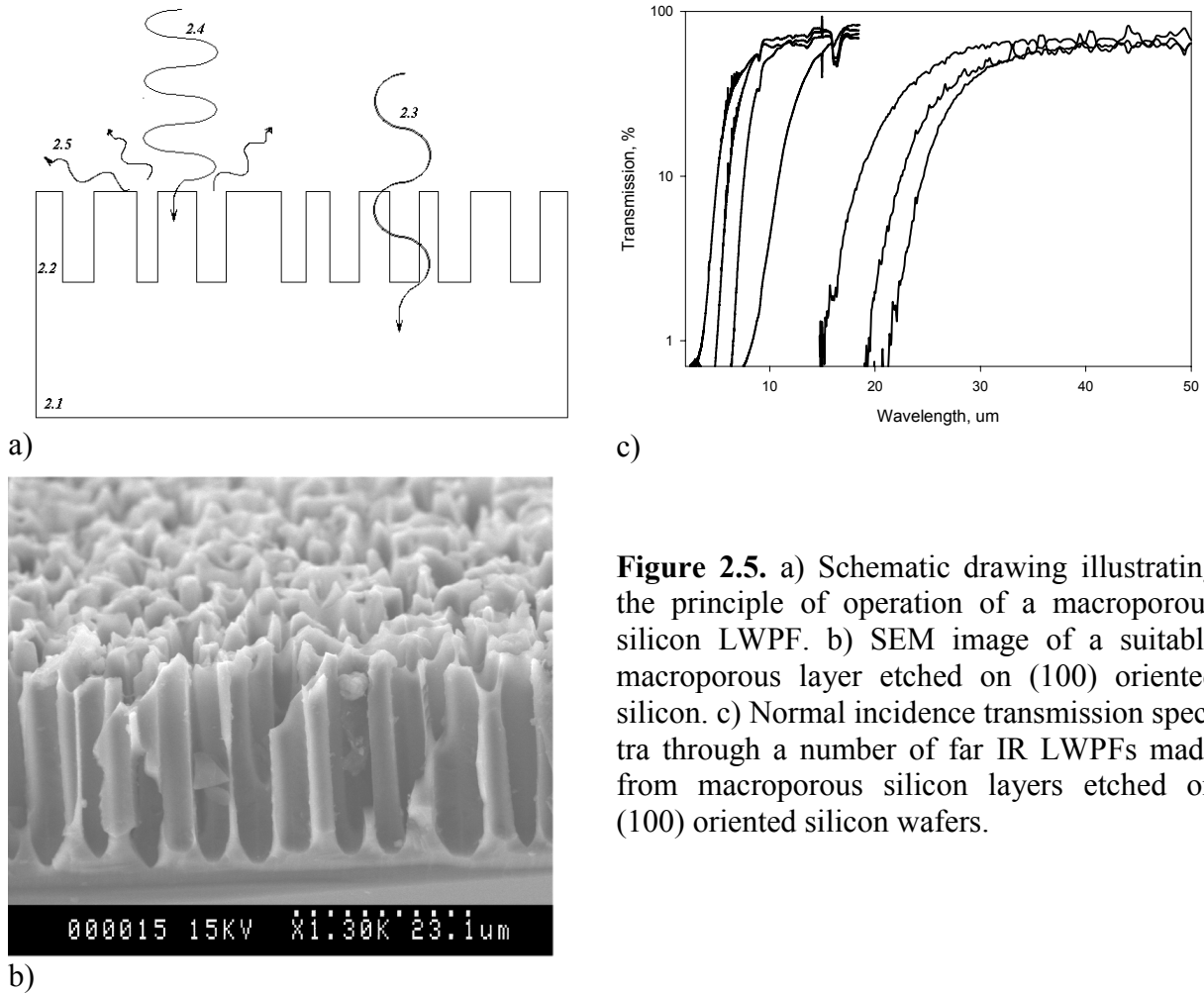


Figure 2.5. a) Schematic drawing illustrating the principle of operation of a macroporous silicon LWPF. b) SEM image of a suitable macroporous layer etched on (100) oriented silicon. c) Normal incidence transmission spectra through a number of far IR LWPFs made from macroporous silicon layers etched on (100) oriented silicon wafers.

Initial efforts were devoted toward the realization of a LWPF on p-doped (100)-oriented silicon wafers. An SEM image of a random MPSi array etching in organic electrolyte is presented in Fig. 2.5b). An optical evaluation (see Fig. 2.5c) confirmed that random MPSi arrays etched on (100) p-doped wafers indeed exhibit well pronounced long wave pass behavior. It was found that by changing the silicon doping, electrolyte concentration, current density and temperature during the electrochemical etching process, it is possible to fabricate good-quality (optically and mechanically) long wave pass filters with edge positions anywhere from $\sim 3 \mu\text{m}$ to $35 \mu\text{m}$.

The sharpness of the rejection edge could also be controlled within wide limits by adjusting the total thickness of the MPSi layer and by optimizing (usually lowering) the temperature during electrochemical etching. Temperature control also allows to some extent to influence the spread of the average pore distance distribution in the array.

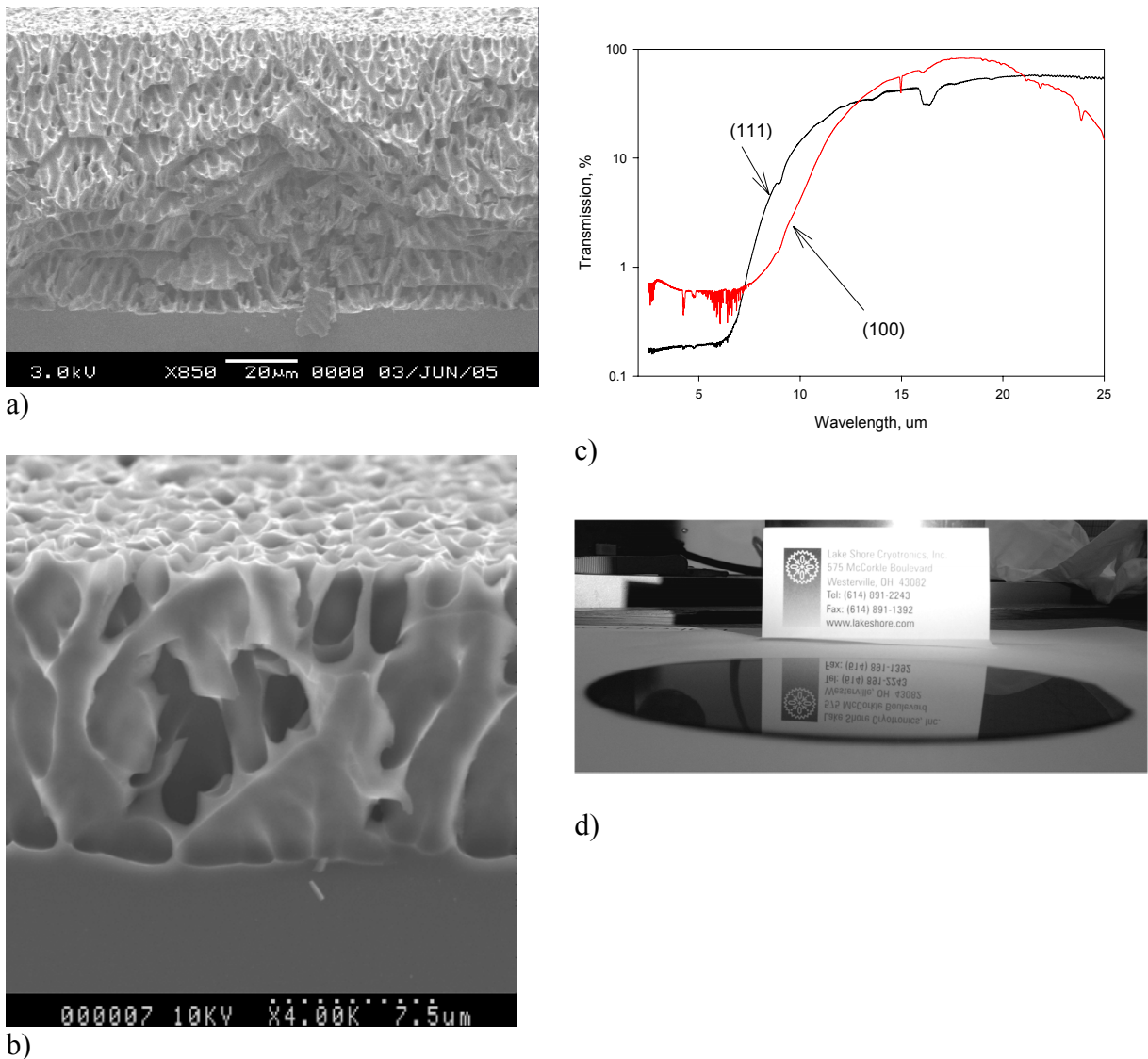


Figure 2.6. a)-b) SEM cross-sectional views of a MPL formed on p-doped (111)-oriented silicon wafers. c) Normal incidence transmission spectra through a number of far IR LWPFs made from MPL etched on (100) oriented silicon wafers. d) Photo of the far IR MPSi LWPF (at glancing angle), illustrating the good surface quality of macroporous silicon.

In addition to LWPF fabricated out of (100)-oriented p-doped silicon, the (111) substrate orientation was evaluated as well. Macropores on (111)-oriented wafers do not grow straight and perpendicular to the wafer surface, but rather in the three equivalent $\langle 113 \rangle$ directions [15]. They also show considerable branching. Since the basis of MPSi LWPF is light scattering, such layers should be beneficial for LWPF applications. Several random MPSi arrays were fabricated and tested. The results are shown in Fig. 2.6. As expected, the branchy structure of MPSi layers on (111) substrate caused much more effective scattering indeed, as illustrated in Fig. 2.6c, where the same thickness of an MPSi array provided stronger rejection and sharper edge on a (111)-oriented wafer as compared to a (100)-oriented wafer. A somewhat unexpected side benefit was a better mechanical behavior and an improved surface quality (see Fig. 2.6d) obtained with the (111) orientation.

An MPSi layer can be easily formed on both sides of the wafer. This not only helps to better control the transmission characteristics of the filters, but also provides the opportunity to reduce the reflection losses within the pass band (which can be considerable due to high refractive index of the silicon).

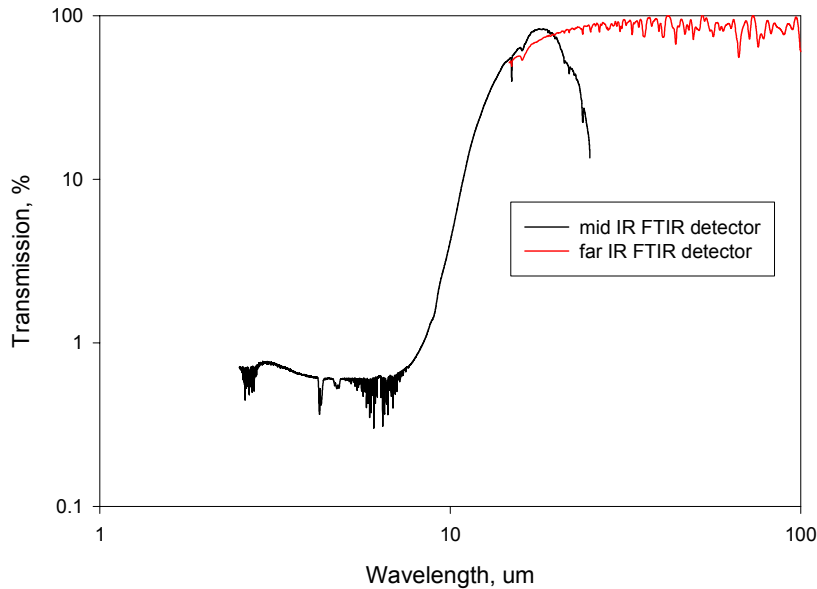


Figure 2.7. Log-log plot of the transmission through the MPSi LWPF etched on (100)-oriented substrate.

The pass band of MPSi LWPF filters was found to be flat up to a wavelength of 100 μm at room temperature, as illustrated by the normal incidence transmission spectrum shown in Fig. 2.7. The reason for this is that the silicon wafers used for fabrication of LWPF are typically low doped, thus the free-carrier absorption is relatively low. Moreover, the number of vibronic bands in silicon is relatively small compared to that of polymers, which have been used with LWPFs based on colloidal diamond [72].

In addition, LWPFs made from MPSi layers are mechanically stable and “all-silicon”, and thus can be operated in a wide temperature range, including “bake-out” to cryogenic temperatures.

As a summary, macroporous silicon long wave pass infrared filters offer a number of important advantages compared to other kinds of long wave pass IR filters. The technology is already sufficiently developed and the filters were introduced to the market in 2005. This is, to best of the author’s knowledge, the first commercially marketed optical product based on porous Si.

2.6. Optical Components Based on Normal Waveguide Mode Propagation Through Macroporous Silicon

Waveguide mode propagation through porous silicon is possible at certain geometries of macroporous silicon arrays along the direction of pore growth. Let’s consider a system that is made of an array of waveguides made in the form of a macroporous silicon (MPSi) layer

where silicon (refractive index $n_{Si} = 3.5$) islands between the pores serve as waveguide cores above the silicon absorption edge, i.e., at $\lambda > 1100$ nm, while the air-filled pores ($n_{Air} = 1$) serve to optically decouple these waveguides. Such arrays are schematically shown in Fig. 2.8. Three physical processes affect the transmission through such a system: coupling of light into the structure at the first MPSi layer interface, propagation of light through the structure, and outcoupling at the second MPSi structure interface.

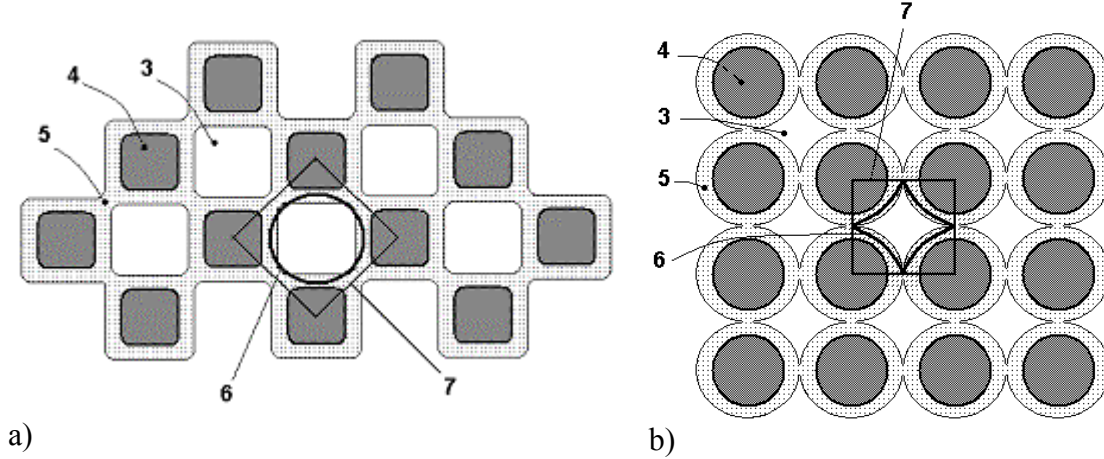


Figure 2.8. Cross-sectional schematic drawings of the waveguide array made out of ordered macroporous silicon array. The pores (4), waveguide mode volume (6) and array's unit cells are schematically shown (7). (5) indicates an (optional) oxide layer. Possible realizations of cubic-symmetry MPSi array are illustrated: a) cubic symmetry, near-square pores; b) cubic symmetry, circular pores.

Three physical processes affect the transmission through such a system: coupling of light into the structure at the first MPSi layer interface, propagation of light through the structure, and outcoupling at the second MPSi structure interface. The total transmission T through the “waveguide only” mode of propagation through the MPSi structure has the following form:

$$T(\lambda, \theta, \theta') \Big|_{\text{Near IR, IR}} = \Sigma DE_{i,j}^W(\lambda, \theta') P_{i,j}^W(\lambda, \theta) \exp(-\alpha_{i,j}^W(\lambda) l) \quad (2.1)$$

where $P_{i,j}^W(\lambda, \theta)$ is the coupling efficiency into the (i,j) waveguide mode of the structure at the angle of incidence θ ; $DE_{i,j}^W(\lambda, \theta')$ is the outcoupling efficiency into the “angle of observation” θ' ; $\alpha_{i,j}^W(\lambda)$ is the loss coefficient of the (i,j) waveguide mode, and l is the thickness of the MPSi layer. It should be noted that in general the angle of incidence and the angle of observation are not in the same plane.

The efficiency, $P_{i,j}^W(\lambda)$, for the waveguide modes of the coupling of normally incident light at the first MPSi layer interface into the MPSi structure is calculated as

$$P_{i,j}^W(\lambda) = \frac{\int E_{i,j}^W(s, \lambda) \cdot E_{i,j}^{*W}(s, \lambda) \cdot ds}{\sqrt{\int E_{i,j}^W(s, \lambda) \cdot (E_{i,j}^W)^*(s, \lambda) \cdot ds \cdot \int E_{i,j}^W(s, \lambda) \cdot E_{i,j}^{*W}(s, \lambda) \cdot ds}} \quad (2.2)$$

where $E_{i,j}^W(s, \lambda)$ is the electric field of the $(i,j)^{\text{th}}$ waveguide mode at the plane of the first MPSi layer interface; $E_I(s, \lambda)$ is the electric field of the incident wave on the MPSi layer per-

pendicular to the mode propagation direction; and λ is a wavelength of light. If a plane-parallel beam of light is normally incident on the first MPSi layer interface, for the fundamental waveguide mode the Equation (2.2) can be roughly approximated as:

$$P_{0,0}^W(\lambda) \approx \frac{4n_{Si}(\lambda) \cdot n_I}{(n_{Si}(\lambda) + n_I)^2} \cdot \frac{S_{uc} - S_p}{S_{uc}} \quad (2.3)$$

where S_p is the area of each pore (see Fig. 2.8), which for the circular pore cross section is equal to $\pi \phi^2/4$, where ϕ is the diameter of the pore, and for near-square pores the cross section is $\sim d^2$, where d is the characteristic cross section size; and S_{uc} is the area of an MPSi array's unit cell (which could be introduced for ordered MPSi arrays only), and where $n_{Si}(\lambda)$ is the refractive index of the silicon at the wavelength λ and n_I is the refractive index of the incident medium. For the most common case of air, expression (2.3) can be rewritten as

$$P_{0,0}^W(\lambda) \approx \frac{4n_{Si}(\lambda)}{(n_{Si}(\lambda) + 1)^2} \cdot \frac{S_{uc} - S_p}{S_{uc}}. \quad (2.4)$$

In other words, to some approximation, $P_{0,0}^W(\lambda) \approx 0.69(1 - p)$, where p is the porosity of the MPSi layer. It should be noted that the cross-coupling between neighboring waveguides is so far ignored (if the cross-coupling is significant, Eq. 2.4 has a different form).

At the second surface of the MPSi layer, the light from each end of each waveguide is emitted with a divergence governed by the numerical aperture of the waveguide, NA , and the wavelength. In the far field, the destructive and constructive interference of all light sources provided by the facets of waveguides takes place. In the case of an ordered MPSi array, this leads to a number of diffraction orders, and this number is in general defined by the pore array geometry (by the relationship between pore size and pore-to-pore distance) and the wavelength of light. For optical filters applications utilizing filters in the far field of the receiver (or light coupling device), only the 0th diffraction order, the efficiency of which is denoted in the following discussion as $DE_{0,0}^W(\lambda)$, is of interest. The only application that is not sensitive to the outcoupling of light to higher diffraction orders is that of the filter mounted directly on top of photodetector (i.e., in the receiver is in the near field of a filter). In all other cases, the outcoupling losses at the second MPSi layer interface can be estimated as $1 - DE_{0,0}^W(\lambda)$ for the waveguide array, since the main source of such losses is the redistribution of light into higher diffraction orders. Such losses are sensitive on both the wavelength and the pore array geometry. They are more pronounced at short wavelengths due to the higher number of diffraction orders.

The optical losses $\exp(-\alpha_{ij}^W(\lambda) l)$ of the normal waveguide mode (i.e. during the propagation of light through the structure) are small in the mid IR range if no absorptive layer or absorptive filling is used in the pores. This is due to the high transparency of the silicon typically used for macroporous silicon fabrication. However, waveguides are known to exhibit the Bragg reflection phenomenon when their effective refractive indices are periodically modulated in the direction of waveguide mode propagation. Modulation of effective refractive indices in silicon island waveguides in the MPSi layer is possible through modulation of the porosity (or, in other words, modulation of macropore diameters) of the MPSi layer with its depth. Different ways to fabricate such MPSi layers are discussed in the next section. The modulation of the porosity of an MPSi layer will modify the spectral dependence of the

transmission through each silicon island waveguide. This modification can be taken into account by introducing an additional term T_{ij}^{BG} in expression (2.1):

$$T(\lambda, \theta, \theta') = \sum DE_{i,j}^W(\lambda, \theta') P_{i,j}^W(\lambda, \theta) T_{i,j}^{BG} \cdot \exp(-\alpha_{i,j}^W(\lambda) l) \quad (2.5)$$

Since Bragg reflections take place during waveguide mode propagation through the waveguide, under the assumption of the independence (i.e., low cross coupling) of waveguides in the waveguide array, this process is independent on angle of incidence. Hence, if the Bragg grating part T_{ij}^{BG} of (2.5) is the main contributor for the overall transmission spectral shape of MPSi layers, this shape will be independent on angle of incidence.

The particular shape of the spectral dependence of T_{ij}^{BG} is a function of the silicon islands shape, size, wavelength, waveguide mode losses, and so on. This means that uniform silicon island sizes and shapes are required. The spectral dependence of T_{ij}^{BG} is different for different orders and polarizations of waveguide modes. Hence, silicon islands should be single-mode waveguides around the central filtering wavelength. Single mode requirement is also important to ensure independence of the transmission spectral shape on the angle of incidence due to different dependences of the coupling and outcoupling efficiencies for different-order waveguide modes. This effect is similar to the one discussed for the leaky waveguide case that will be considered later in this Chapter. However, unlike leaky waveguides, where losses dramatically increase with the number of modes, the losses of waveguide modes are generally small, so in the case of the multimode nature of waveguide, higher-order mode transmission cannot be neglected. To summarize, for an MPSi array to act as an omnidirectional filter, it should be ordered, and silicon island waveguides should be independent (low cross-coupling) and single-mode. Light transmission through such MPSi arrays other than by waveguide modes should be suppressed. In this case expression (2.5) for 0th diffraction order will take the form

$$T(\lambda, \theta) = DE_{0,0}^W(\lambda, \theta) P_{0,0}^W(\lambda, \theta) T_{0,0}^{BG} \exp(-\alpha_{0,0}^W(\lambda) l) \quad (2.6)$$

since for the ordered array of waveguides and zero diffraction order $\theta = \theta'$.

The coupling efficiency at the first MPSi layer surface can be estimated as

$$P_{0,0}^W(\lambda, \theta) = P_{0,0}^W(\lambda, \theta = 0) \exp(-(\theta/\theta_{ac})^2) \quad (2.7)$$

where $P_{0,0}^W(\lambda, \theta = 0)$ is the coupling efficiency in the waveguide array of plane-parallel beam incident normally to the MPSi layer (which can be estimated according to Eq. 2.4), and θ_{ac} is the acceptance angle of the silicon island waveguide. It should be noted that the porosity (i.e., macropores diameters) is not constant across the MPSi layer. As was discussed above, for narrow-band-pass, band-pass, or band-blocking filter applications, the MPSi porosity has to be modified in a periodic fashion through the MPSi layer depth. Moreover, the porosity at both surfaces of the MPSi layer can be minimized within some limits to maximize the coupling and outcoupling efficiencies of the silicon islands waveguide array. Hence, (2.7) can be rewritten as

$$P_{0,0}^W(\lambda, \theta) = 0.69(1 - p(0)) \exp(-(\theta/\theta_{ac})^2) \quad (2.8)$$

This opens the opportunity to minimize the coupling losses by minimizing the porosity at the surfaces of MPSi layer.

The particular value of the acceptance angle strongly depends on the waveguide structure. For silicon island waveguides and air-filled pores, the $\sin\theta_{ac}$ estimation will be $[(n_{Si})^2 - 1]^{1/2} = 3.35$; meaning that the acceptance angle of silicon island waveguides (and through the MPSi layer as a waveguide array) will be $\pi/2$. Such a wide acceptance range of the MPSi layer at IR wavelength range means that spectral filters based on the MPSi layer will be truly omnidirectional.

As mentioned above, the absence of the cross-coupling between neighboring silicon waveguides in the MPSi layer is essential. However, the calculations showed that with pure MPSi layers the cross-coupling is too strong. The simplest way to suppress the cross-coupling is to partially oxidize the MPSi layer so the silicon island waveguides will be physically separated by either air pores or silicon dioxide bridges. This is schematically illustrated in Fig. 2.8, where thermally grown SiO_2 layer (5) is shown.

Before estimating cross-coupling between neighbor waveguides, let us first find the silicon island size and silicon dioxide layer thickness ranges needed to guarantee the single-mode character of the silicon island waveguides.

In Fig. 2.9 the numerically calculated dependences of effective refractive indices of TE polarization waveguide modes on the silicon island cross-section are presented for the cubic-symmetry array of near square pores. The wavelength of light was assumed to be 1550 nm. One can see that the silicon island waveguides become multimode starting at about 300 nm of silicon island cross-section. For other wavelengths the maximum silicon island cross-section needed can be found by scaling.

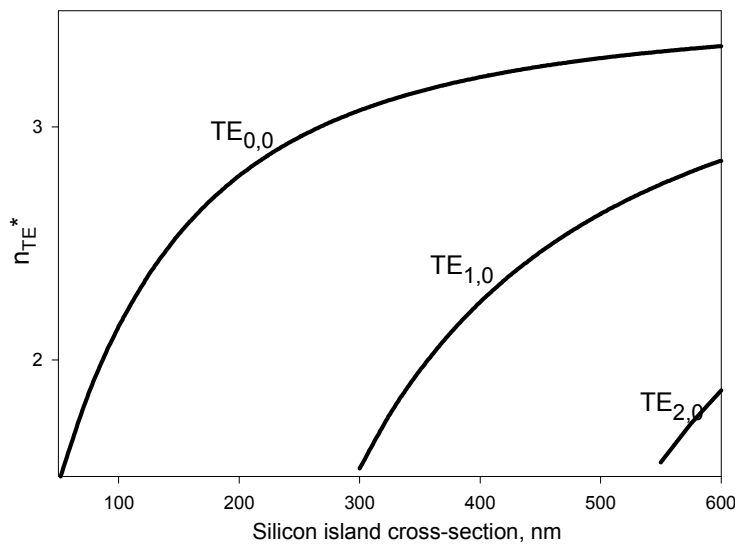


Figure 2.9. Numerically calculated dependences of effective refractive indices of TE polarization waveguide modes on the square silicon island cross-section (side of the square).

The SiO_2 layer thickness affects both the cross-coupling suppression and the number of modes in the silicon island waveguide for constant silicon island cross-section. In Fig. 2.10a the numerically calculated dependences of effective refractive indices of TE polarization

waveguide modes on the silicon dioxide layer thickness are given for the MPSi layer of Fig. 2.8a. The wavelength of light was assumed to be 1550 nm, while the silicon island cross-section was assumed to be 275 nm. One can see that even for such a silicon island cross-section the thickness of the silicon dioxide layer covering the pore walls has to be less than approximately 300 nm. Now having the silicon island size, the silicon dioxide layer thickness, and the geometry of the MPSi array, we can estimate the cross-coupling coefficient between neighbor waveguides. In Fig. 2.10b the numerically calculated dependence of the cross-coupling coefficient on the silicon island separation is given for fundamental waveguide mode. The wavelength was assumed to be 1550 nm, the silicon island cross-section was assumed to be 275 nm, the silicon dioxide layer thickness was assumed to be 300 nm, and the MPSi layer structure was assumed to be the same as in Fig. 2.8a.

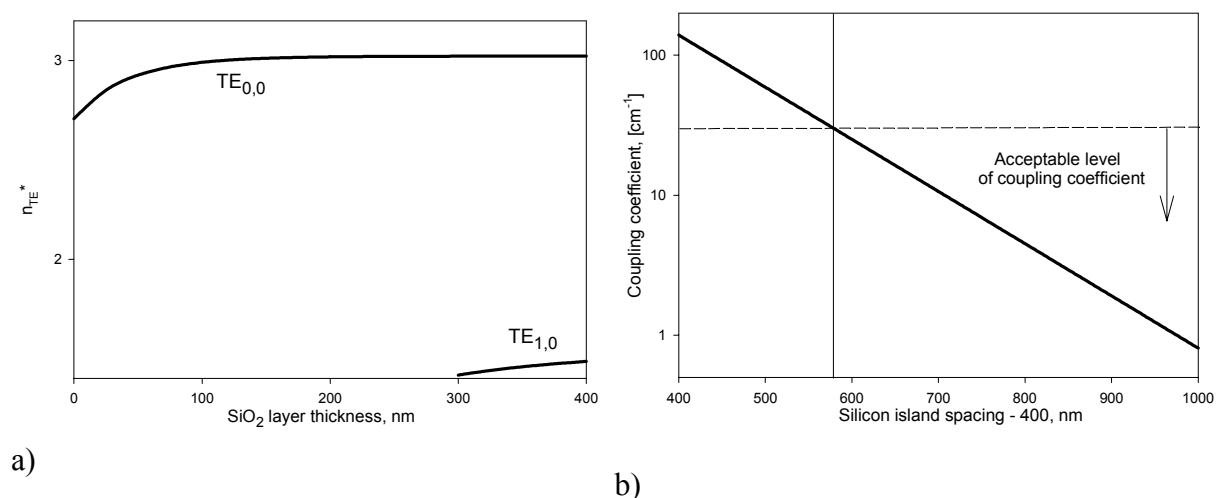


Figure 2.10. a) Numerically calculated dependences of effective refractive indices of TE polarization waveguide modes on the silicon dioxide layer thickness for the structure of Fig. 2.8a; b) numerically calculated dependences of cross-coupling coefficients of fundamental waveguide modes on the silicon island separation.

As expected, the coupling coefficient decreases exponentially as the silicon island spacing decreases. To provide omnidirectionality of the transmitted light, the coupling length, which is equal to the inverse coupling coefficient, should be less than the thickness of the MPSi layer. Taking into account that the typical MPSi layer thickness is in the range of 50 to 300 μm , while the thickness of the MPSi layer with modulated pores diameters will not exceed 200 μm , it will be safe to set the upper limit of the coupling coefficient at about 20 cm^{-1} .

According to Fig. 2.10b, the cross-coupling coefficient will be suitable for providing omnidirectionality of the transmittance spectrum for a silicon island spacing starting at ~ 980 nm. The MPSi array is assumed to be of cubic symmetry; hence, the unit cell area in this case will be about 1 μm^2 (see Fig. 2.8a). The waveguide mode area will be 0.16 μm^2 for the 1550 nm wavelength. Hence, the coupling losses at the first MPSi layer interface (if pores and hence silicon islands are constant across all MPSi depth) will be around 84 %. Such a value is not suitable for most of optical filter applications. Even modification of the porosity of the MPSi layer near both interfaces will not boost the potential transmittance to more than 25 to 35 %. Hence, a better way of suppressing the cross-coupling while keeping coupling losses at a reasonable level is needed. It is possible by making further modifications in MPSi layer structure.

One relatively simple way to modify the MPSi layer structure to suppress cross-coupling while keeping the potential transmittance at a reasonable level is to fill the pores with highly reflective material, such as metal. A thin layer of low refractive index material (for example, thermally grown silicon dioxide) is still needed between the metal filling the pores, and silicon island waveguides to suppress the propagation losses in the waveguides. Such a design will also suppress other modes of light propagation through the MPSi structure than through waveguides.

Lets again consider the MPSi array of cubic symmetry and near-square macropores as in Fig. 2.8a. Before investigating the particular values of coupling efficiencies and cross-coupling coefficients, we need to define the sizes of silicon islands and the thickness of the silicon dioxide layer needed to maintain single-mode operations of silicon island waveguides and the metal-caused propagation losses on a sufficiently low level.

The silicon island cross-section can be estimated from the previously given consideration (see Fig. 2.9). Hence, we can set the maximum silicon island cross-section to be around 300 nanometers to ensure single-mode waveguiding at 1550 nm. However, we need to pay additional attention to propagation losses, absent in previous case, but considerable here. As an example, in Fig. 2.11 the numerically calculated dependences of loss coefficients of TE-polarized waveguide modes on the silicon island cross-section are presented. The MPSi layer structure was assumed to be of cubic symmetry; the silicon dioxide layer thickness was assumed to be 200 nm, and calculations were made for 1550 nm wavelength. In the calculations the metal was assumed to be nickel.

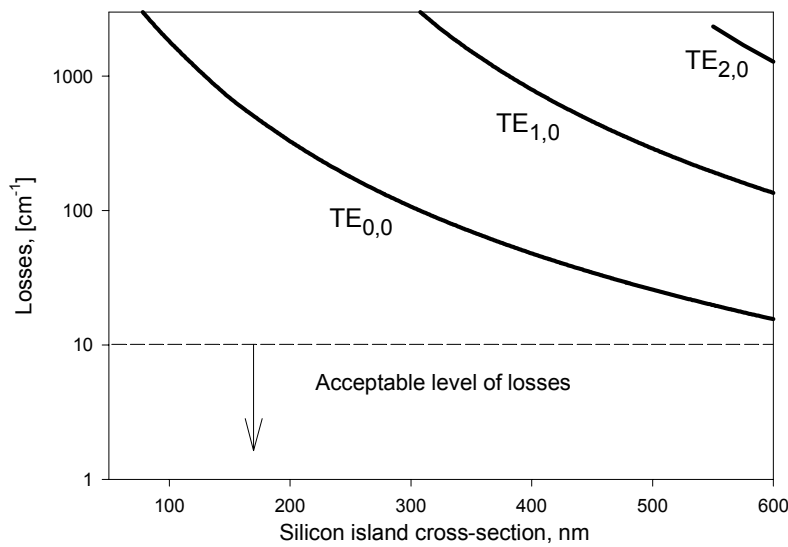


Figure 2.11. Numerically calculated dependences of loss coefficients of TE polarization waveguide modes on the silicon island cross-section.

The waveguide mode losses decrease for each mode with the increase of the silicon island cross-section. It happens due to the increase of the localization of the waveguide mode in the silicon island and, hence, the decrease of the localization of the waveguide mode near the metal/silicon dioxide boundary when the waveguide parameters are getting further from the cut-off conditions. The important question here is the acceptable level of losses that are suffi-

cient to provide a reasonable performance of narrow-band-pass, band-pass, or band-blocking filter, based on such an MPSi layer. From one point of view, the coupling losses at the first MPSi layer interface will be dominating (probably not less than 20 to 30 %): even the losses of 10 % of coupled intensity due to propagation losses will not cause the dramatic change of the performance of the MPSi-based filter. Taking into account that the MPSi layer thickness will not exceed 300 μm , it will give maximum acceptable propagation losses of around 10 cm^{-1} . From another point of view, the quality of waveguide Bragg resonances is a function of the level of losses in the waveguide: high losses will be prohibitive in obtaining a really narrow pass band (in the case of narrow-band-pass filter) or steep edges of pass-band (in the case of band-pass or band-blocking filters). However, these filter parameters are unique for each filter design, as is the acceptable level of waveguide mode propagation loss. Hence, we can set the level of maximum acceptable losses at 10 cm^{-1} .

It is obvious that for the MPSi structure of Fig. 2.11 the losses are higher than what is desired. However, the losses are known to drop exponentially with the buffer (silicon dioxide in this case) thickness. As an example, figure 4.12 gives the numerically calculated dependences of loss coefficients of TE polarization waveguide modes on the silicon dioxide layer thickness. The MPSi layer structure was assumed to be of cubic symmetry; the silicon island cross-section was assumed to be 275 nm, and calculations were made for 1550 nm wavelength. In the calculations the metal was assumed to be nickel. In this particular example the losses became acceptable for a silicon dioxide layer thick enough to cause the appearance of a second waveguide mode. However, unlike the MPSi layer with pores not filled with metal, it will not cause problems due to very high losses of this mode (two orders higher than that of fundamental mode). Hence, we can conclude that the optimal MPSi layer structure for 1550 nm filter should be as follows: the silicon island cross-section should be not more than 300 nm, and silicon dioxide thickness should be not less than 300 nm.

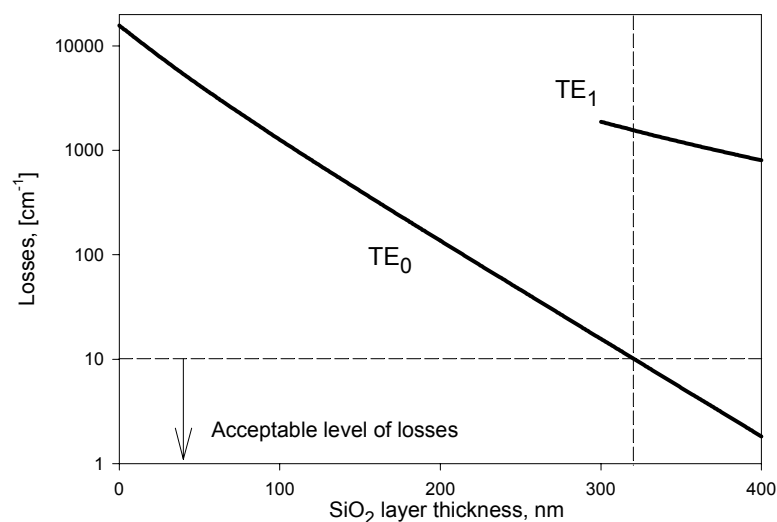


Figure 2.12. Numerically calculated dependences of loss coefficients of TE polarization waveguide modes on the silicon dioxide layer thickness.

With these parameters in mind, we are now ready to estimate the level of cross-coupling and get the approximate sizes of MPSi array. In Fig. 2.13 the numerically calculated dependence of cross-coupling coefficient on the silicon island separation is given for the fundamental waveguide mode. The wavelength was assumed to be 1550 nm, the silicon island cross-

section was assumed to be 275 nm, the silicon dioxide layer thickness was assumed to be 300 nm, and the MPSi layer structure was assumed to be the same as in figure 2.8a with pores filled with nickel. By comparing Figs. 2.10b and 2.13 one can see that metal in the pores indeed suppress the cross-coupling between neighboring silicon island waveguides. Cross-coupling suppression is not very strong. However, it should provide better potential coupling efficiency at the first MPSi layer interface due to a smaller acceptable value of porosity at the same or better cross-coupling. We can estimate it to be the same as in the air-filled MPSi layer case: according to Fig. 2.13, the minimum acceptable (from the viewpoint of the cross-coupling suppression) silicon island spacing of 910 nm corresponds to the area of such an MPSi array unit cell of $\sim 0.82 \mu\text{m}^2$. The waveguide mode area will be $0.2 \mu\text{m}^2$ for the 1550 nm wavelength. Hence, the coupling losses at the first MPSi layer interface, if pores and hence silicon islands have constant sizes across all MPSi depth, will be $\sim 75\%$. With the modification of the porosity of the MPSi layer near both interfaces the potential transmittance can be increased to about 40 to 50 %.

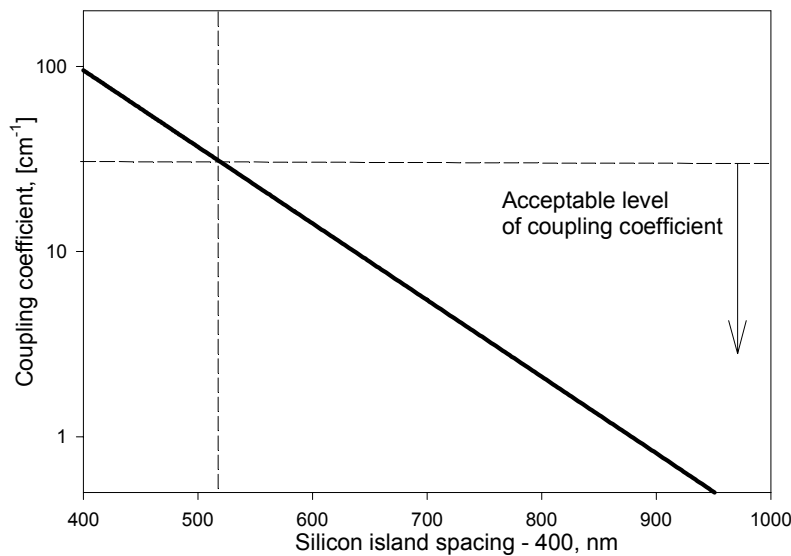


Figure 2.13. Numerically calculated dependences of cross-coupling coefficients of the fundamental waveguide modes on the silicon islands separation for metal-filled pores.

This value of potential transmittance is already acceptable for some applications, but it is lower than what is needed for e.g. telecommunication applications. The appearance of metal-caused propagation losses in this design is negative from the viewpoint of quality of Bragg resonance. However, since the value of propagation losses is very different for different orders of waveguide modes, it is possible to utilize two-mode waveguides in such an MPSi layer, since a second-order mode will dissipate due to high losses. It provides an opportunity to utilize higher than 300 nm (for 1550 nm wavelength) cross-sections of silicon island waveguides for the same area of an MPSi array unit cell (i.e., it increases the coupling efficiency at the first interface of MPSi layer).

The numerically calculated spectral dependences of the coupling, outcoupling, and propagation losses of a nickel-filled cubic MPSi array with period (pore-to-pore distance of 1500 nm) pore diameters (after oxide layer growth step) of 750 nm and a 300 nm oxide layer covering the pore walls is presented in Fig. 2.14. One can see that propagation losses are expected to be considerably less than coupling losses for such a filter.

The metal-filled MPSi array of Fig. 2.8a clearly can find some applications, since despite a considerably low level of transmittance, it can offer narrow-band-pass, band-pass, or band-blocking filters with an independence of transmittance spectral shape on angle of incidence. However, further suppression of losses can expand the potential markets for such a filter.

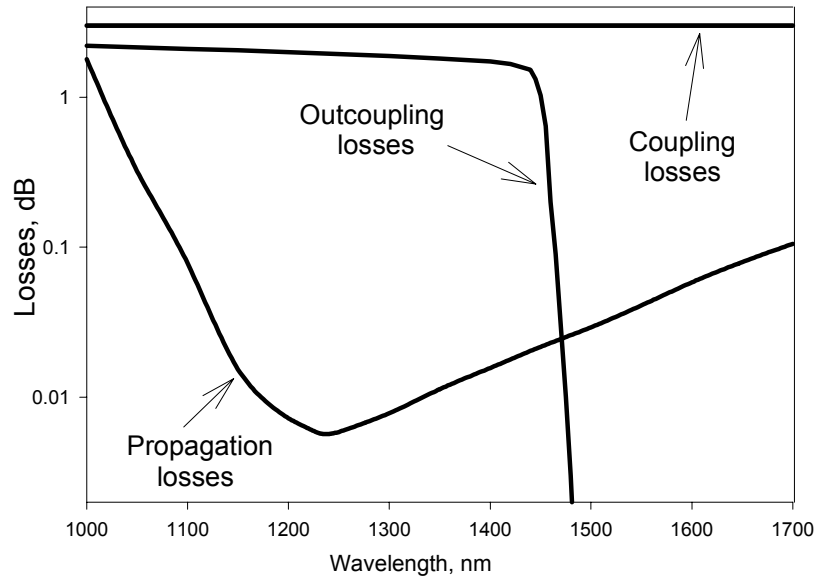


Figure 2.14. Numerically calculated coupling, propagation, and outcoupling losses for the structure with parameters given in the text.

Another solution of this tradeoff between cross-coupling and coupling losses is to create MPSi arrays of more complex symmetries. The examples of such MPSi array cross-sections are given in Fig. 2.15. In Fig. 2.15a the advanced hexagonal symmetry MPSi array is presented, while in Fig. 2.15b the advanced cubic symmetry MPSi array is presented. In both cases the macropores are of circular cross-section. Both the array unit cells and the silicon island waveguide mode profile are schematically shown. One can see that for MPSi layers in Fig. 2.15 the ratio of silicon island waveguide mode to MPSi array unit cell is considerably higher than that of the MPSi layers of Fig. 2.8. It should be noted that macropores in advanced-symmetry MPSi structures could be also filled either with air or with metal (if more suppression of cross-coupling is required).

The required dimensions of the MPSi layer can be transferred at some extent from the previous discussion. The cross-section of silicon islands should be less than 300 nm for 1550 nm wavelength. The size of macropores and the thickness of the silicon dioxide layer covering the pore walls should be found according to cross-coupling suppression requirement. In Fig. 2.16 the numerically calculated dependences of cross-coupling coefficients of fundamental waveguide modes on the silicon islands separation are given for the MPSi layer of Fig. 2.15a. The wavelength was assumed to be 1550 nm, the pores were assumed to be circular, and the thickness of the silicon dioxide layer was assumed to be equal to half of the macropore diameter. As follows from Fig. 2.16 the cross-coupling coefficient between neighbor silicon island waveguide fundamental modes reaches acceptable levels at the silicon island separation of 790 nm.

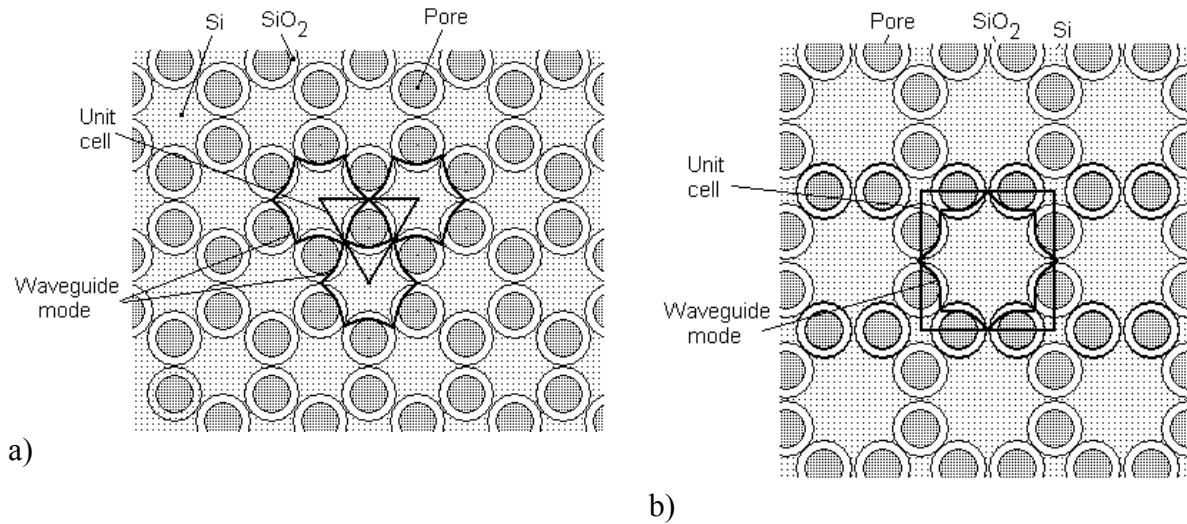


Figure 2.15. Possible symmetries of an MPSi array: (a) advanced hexagonal symmetry; (b) advanced cubic symmetry. In both cases the macropores are of circular cross-section.

By taking simple geometrical calculations and taking into account the single-mode requirement we can find that the needed macropore diameter should be around 180 nm and the needed thickness of the silicon dioxide layer should be at least 120 nm. The unit cell area for an MPSi layer with such dimensions will be $0.26 \mu\text{m}^2$, while the silicon island waveguide mode cross-section will be around 0.16 to $0.2 \mu\text{m}^2$. Hence the coupling losses at the first MPSi layer interface will not exceed 30 %. It is expected that by reducing the porosity of the MPSi layer (i.e., by reducing the macropore diameters) near both interfaces of the MPSi layer it is possible to increase the potential transmittance of such a structure over 75 %. The same as for simple symmetries of MPSi arrays discussed previously, the macropores in the MPSi arrays of Fig. 2.15 can be filled by metal. In this case the cross-coupling between neighbor silicon island waveguides is expected to be even smaller (i.e., the ratio of waveguide mode area to unit cell area can be increased). For such an array the potential transmittance is expected to exceed 85 %, which is suitable for most of applications of IR narrow-band-pass, band-pass, or band-blocking filters.

It should be noted that in all discussions in this section the coupling efficiency at the first interface of the MPSi layer was calculated as a ratio of the waveguide mode area to the MPSi array unit cell area. However, as it follows from expression (2.3) or (2.4a) the reflectance at the air/silicon boundary (as well as the reflectance at the silicon/air boundary during outcoupling at the second MPSi layer interface) strongly degrades the coupling (and outcoupling) efficiency. Due to the high refractive index of silicon, reflection losses are expected to reach 31 % at each MPSi layer interface at normal incidence. It means that even for optimized MPSi array symmetries (like the ones shown in Fig. 2.15) the transmittance through such an MPSi array would not exceed 30 to 40 %. Fortunately, the high reflection loss problem can be solved by coating of both surfaces of the MPSi layer with an antireflection coating. It can be a single-layer antireflection coating, like silicon monoxide or multilayer antireflection coating.

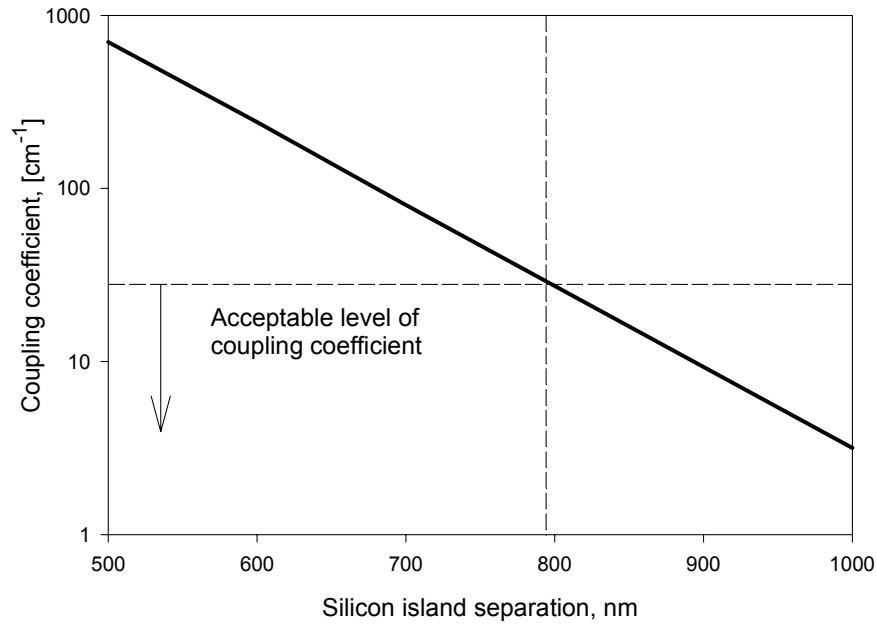


Figure 2.16. Numerically calculated dependences of cross-coupling coefficients of fundamental waveguide modes on the silicon island separation for the MPSi layer of figure 4.13a.

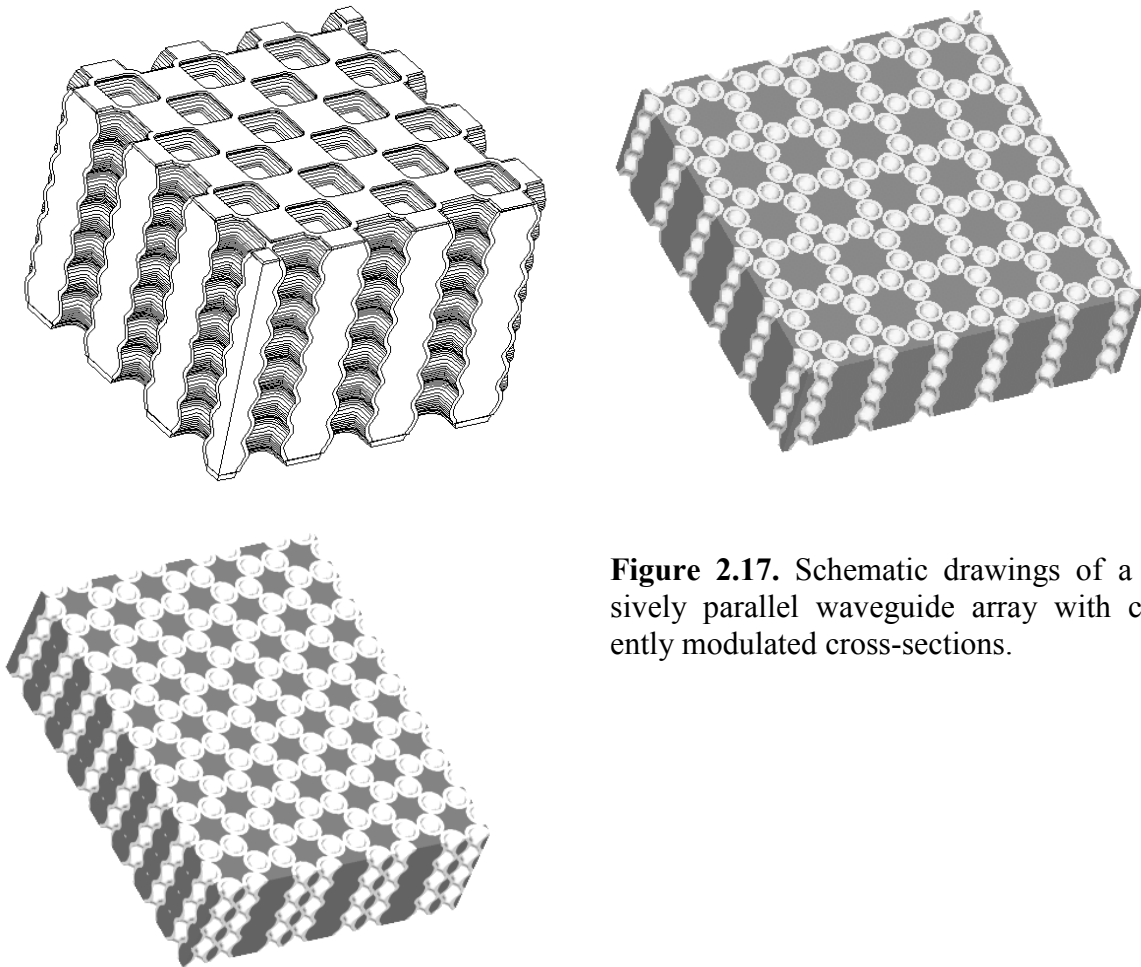


Figure 2.17. Schematic drawings of a massively parallel waveguide array with coherently modulated cross-sections.

To summarize, the optimal structure of MPSi array to perform as an omnidirectional optical component in the IR spectral range should be as that artistically shown in Fig. 2.17.

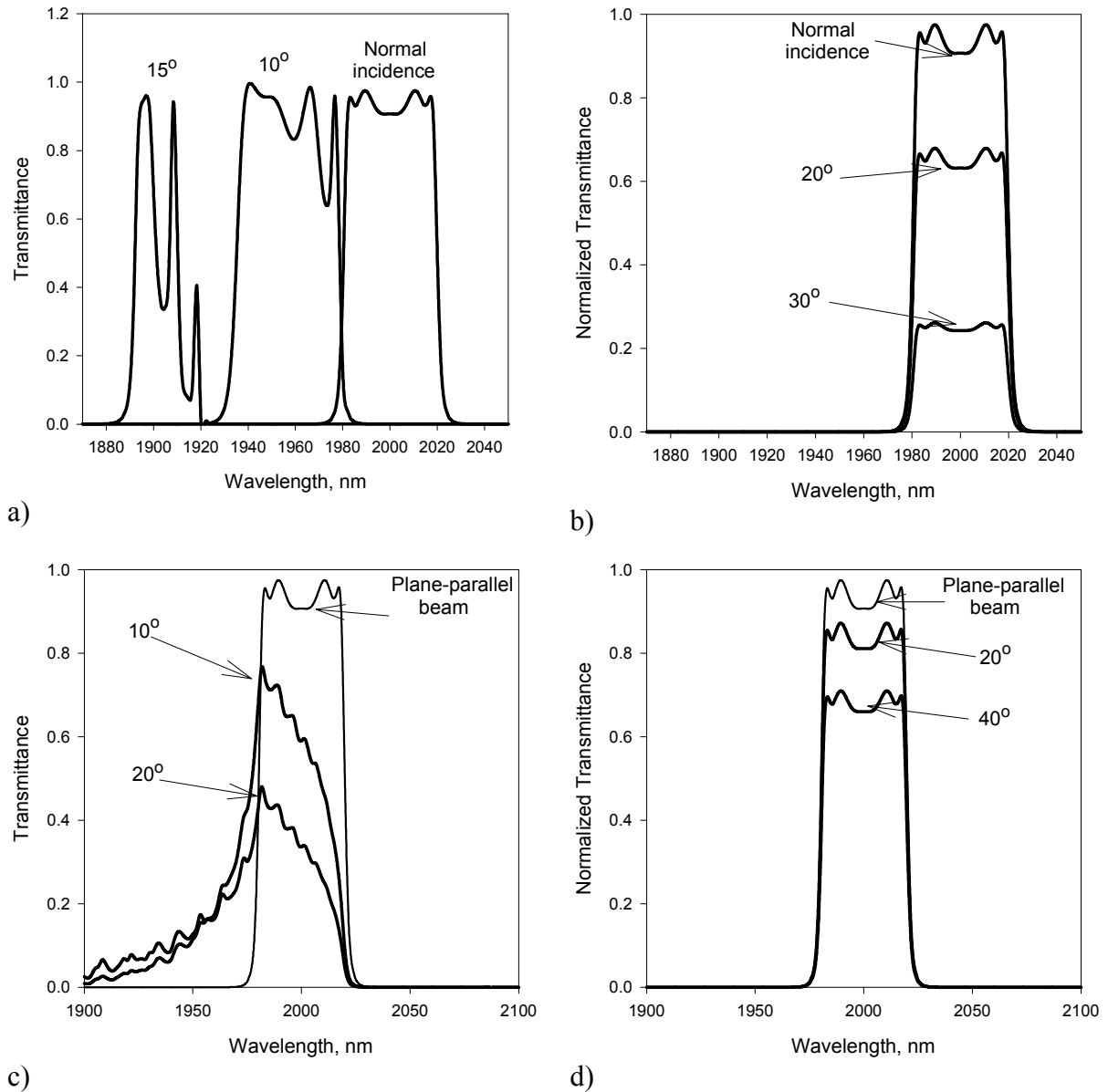


Figure 2.18. Numerically calculated transmission spectra through a thin-film interference filter (a) and through an MPSi filter (b) for different angles (light incident at 0, 10 and 15 deg. from normal) of incidence; numerically calculated transmission spectra through a thin-film interference filter (c) and through an MPSi filter (d) for different divergences of Gaussian beams.

To illustrate the expected advantages of the spectral filter based on this design with respect to common interference filters, numerical calculations are presented in Fig. 2.18. Fig. 2.18a gives the simulated transmittance spectra through a seven-cavity narrow-band-pass multilayer dielectric filter for normally incidence and 10° and 15° tilted plane-parallel beams. The wavelength shift of the pass-band position together with the degradation of the pass-band shape is rather pronounced. In Fig. 2.18b, the normalized transmittance spectra through a multiple-cavity MPSi-array-based filter are presented for normal incident and 20° and 30° tilted plane-

parallel beams. The transmittance in this case is presented in a normalized form since the maximum transmittance is defined by the particular MPSi layer structure. Fig. 2.18c presents the simulated transmittance spectra through the narrow-band-pass multilayer dielectric filter of Fig. 2.18a for normally incident beams with different divergences: plane-parallel beam (0-divergence angle) and Gaussian beams with 10° and 20° divergence angles. The degradation of both the pass-band shape and the out-of-band rejection that are common to multiple-cavity all-dielectric multilayer filters are demonstrated. In Fig. 2.18d, the calculations for normalized transmittance spectra through the multiple-cavity MPSi filter of Fig. 2.18b are presented for 0°, 20°, and 40° divergent, normally incident Gaussian beams.

2.6.1. Fabrication

The general formation of MPSi was reviewed in some detail in a previous sections of this Chapter. In this section the discussion will be focused on some peculiarities of the fabrication process originating from the particular symmetries of pore arrangements required by filter design.

The peculiar (“chess-board”) arrangement of Fig. 2.8 was achieved with the help of common photolithographic equipment and anisotropic etching of Si in a KOH solution, providing well developed inverted pyramids as nuclei. The pore diameter modulation was obtained by periodic variations of the current density during the electrochemical etching of p-doped (100)-oriented silicon wafers in organic electrolyte. Fig. 2.19 shows SEM images of different cross-sections of MPS arrays having modulated macropore diameters and a pore geometry as shown in Fig. 2.8a. While a fair matching to the initial design goals was achieved, up to now the proper pore modulation parameters could not be achieved. This prevented an experimental proof of the feasibility of the discussed filter design. However, much progress in pore diameter modulation etching has been achieved in the meantime by the Halle group [73, 74], and it is believed that further optimization of the electrochemical etching process will enable the fabrication of functional omnidirectional IR filter structure using MPSi.

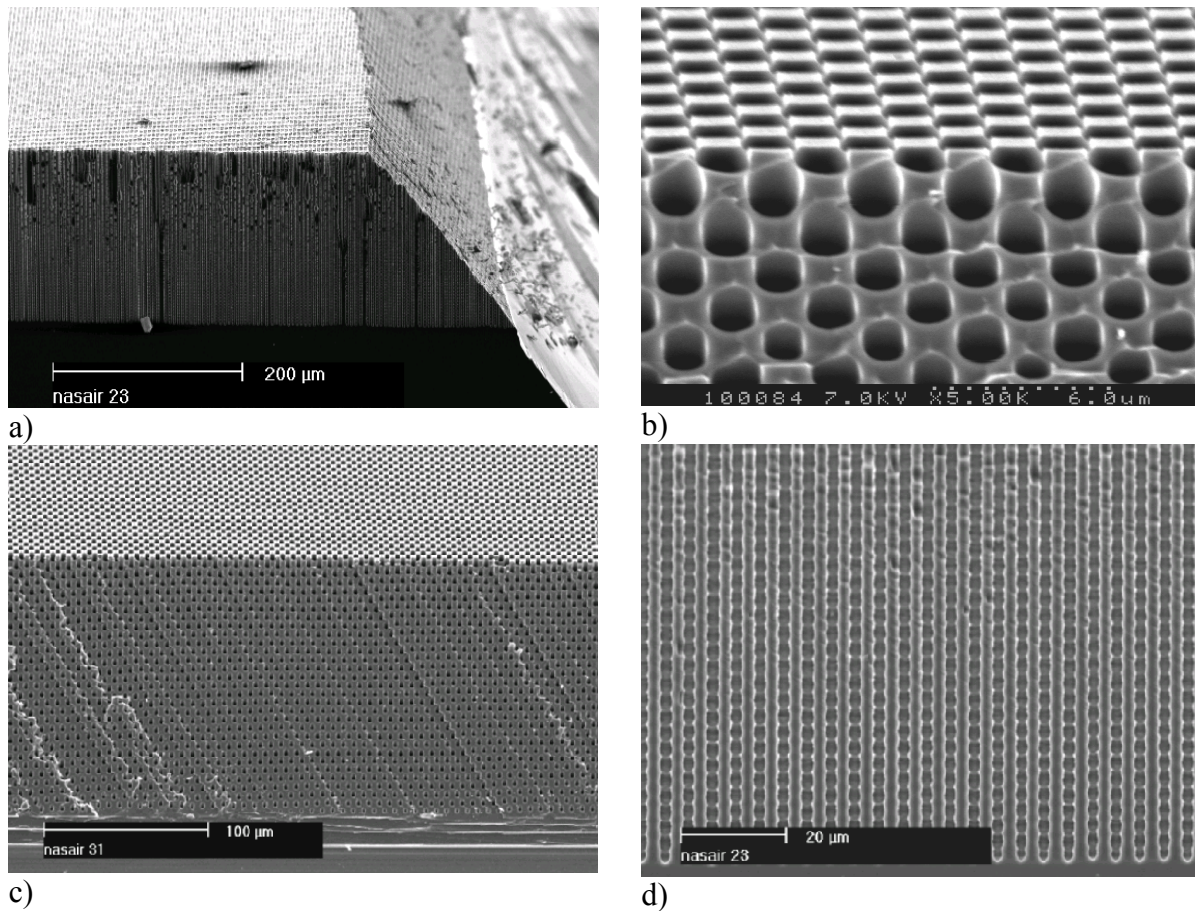


Figure 2.19. SEM images of an MPSi layer having the structure of Fig. 2.8. a)-b) Tilted views at different magnifications. The top surface of the MPSi layer corresponds to the (100) crystallographic orientation, while the front surface is (111) orientated; c) tilted view with two cleaved faces; d) magnified cleaved face showing pore diameter modulations.

MPSi arrays with advanced symmetries as shown in Fig. 2.15 were fabricated as well. The SEM images of an array with an “advanced hexagonal” symmetry is shown in Fig. 2.20; the pattern symmetry is preserved down to at least 200μm. While so far such arrays were successfully fabricated only on n-doped (100)-oriented silicon substrates with back-side illumination, it is believed that careful optimization of electrochemical etching condition can permit fabrication of similar MPSi arrays on p-doped (100)-oriented silicon substrates as well. No modulation of the macropore diameters in advanced symmetry arrays were attempted so far at all.

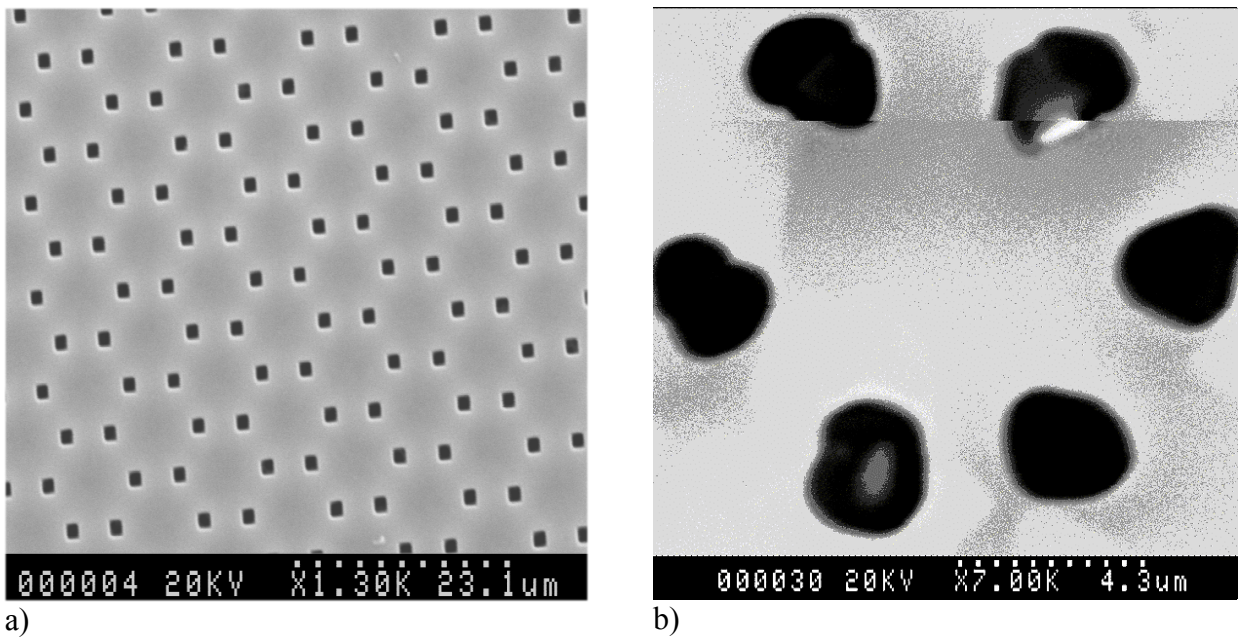


Figure 2.20. SEM images of the advanced hexagonal symmetry MPSi array. a) Front surface. b) Back surface (200 μm deep), opened by chemical etching.

Some experiments with metal filling of the pores by electro-plating were performed as a proof of principle as well. Plating was performed on unoxidized MPSi layers right after the anodization. A chamber similar to that used for silicon anodization was used for plating. It was found to be necessary to insure that the current is flowing only through the MPSi layer. Otherwise plating was mostly observed in the areas surrounding the MPSi layer.

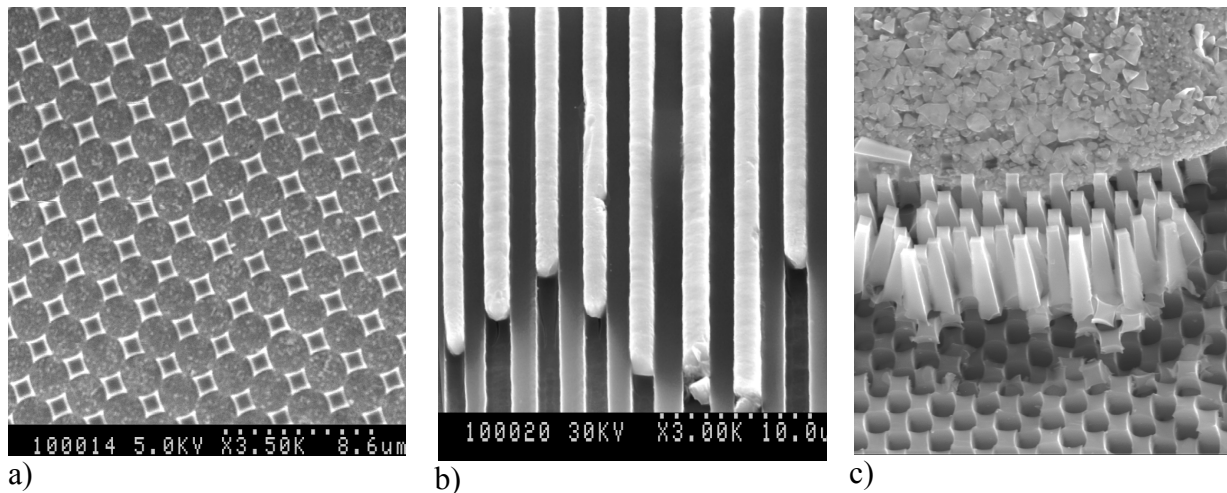


Figure 2.21. SEM images of the copper-plated MPSi arrays.

In such an electro-plating geometry the plating process works essentially inverse to the anodization process – i.e. sharp pore tip “focuses” current lines at the bottom of the pores so the plating initiated exactly at the bottom, not on the pore walls, and the plated metal continuously fills the pores from the bottom and up. Such plating provided very good quality, voidless filling of the pores. Copper and permalloy (Fe/Ni alloy) were plated so far, although it is believed that many other metals can be plated into the pores equally well. For copper plating, Cubath® SC makeup provided by Enthone OMI was used as an electrolyte. The current

density was $10\text{mA}/\text{cm}^2$; the system was run in a DC mode. Fig. 2.21 gives SEM images of the electroplated MPSi layers with copper completely filling the pores. Fig. 2.21a shows the top view of the MPSi layer that was electroplated for ~ 1 hour, so the copper almost completely filled the pore, but unplated silicon “islands” were left on the filter “surface”. Fig. 2.21b gives an SEM image of the cleaved edge of the MPSi layer. Good quality of the pore-filling copper is clearly demonstrated. The uneven filling of the pore was not due to the bad plating but rather occurred during the cleavage of the wafer – copper has quite poor adhesion to silicon and during cleavage part of the pore-filled copper was left on one side of the cleaved wafer while other part of pore-filled copper was left on another part of the cleaved wafer. It also should be noted that all the pores were filled uniformly. Fig. 2.21c shows an SEM image of the MPSi layer surface near the cleavage for the MPSi layer that was severely over-plated (2 hours), so a thick layer of copper was formed over all the surface of the MPSi layer. It should be noted that cleaving such a wafer was difficult because of the malleability of copper; so multiple bending of the copper layer was required prior to separating the pieces. During this procedure, part of the copper was removed from the pores, as illustrated in the image. One can see that not only the copper columns were uniform, but also the quality of the copper in the columns was considerably better than that covering the MPSi layer from the top. This is another indication of the good-quality plating achieved.

Note also that the copper-plating process used here is suitable for plating only pure silicon MPSi layers attached to the non-porous part of the Si wafer and cannot be used with MPSi layers having pores coated by non-conductive materials or free-standing MPSi layers. For such layers, the electro-plating process must be modified.

Such work is currently in progress with the goal to fabricate the functional omnidirectional IR MPSi filter and to prove the feasibility of theoretical predictions made above.

2.6.2. Omnidirectional Filters for Visible Wavelengths

The spectral filters for the IR range based on the MPSi layer structures discussed above promise significant advantages over dielectric multilayer-based filters. However, these designs cannot be directly transferred into the visible and near IR spectral ranges (400 to 1100 nm wavelengths) due to the absorption of the silicon, which would cause unreasonable propagation losses in silicon column waveguides. Nevertheless, visible and near IR spectral ranges are of great commercial importance and omnidirectional narrow-band-pass, band-pass, and band-blocking spectral filters are clearly needed for these wavelengths.

An ordered array of waveguides with a coherently modulated cross-section made of materials that are transparent at visible spectral range (similar to the MPSi layer discussed above) would serve such purposes. Here it is suggested to use a *completely oxidized MPSi layer (COMPSi)* for the visible wavelength range. Lehmann has shown that it is possible to completely oxidize MP membranes [75], and the considerations for MPSi IR filters can be directly transferred to COMPSi layers, except for some normalization caused by a lower refractive index of silicon dioxide than that of silicon. In particular, the reflection losses during coupling should be about 4 % at each interface of a freestanding COMPSi layer and the acceptance angle of silicon-dioxide-based waveguides should be also considerably less than that of silicon.

As with an MPSi layer, silicon dioxide waveguides in a COMPSi layer cannot be considered independent of each other. In order to obtain visible-range, omnidirectional, narrow-band-pass, band-pass, or band-blocking filters based on the COMPSi layer, the structure of the COMPSi layer should be modified to suppress cross-coupling between neighboring silicon dioxide waveguides. Again, this can be done by coating the pore walls with a metal layer.

Another design of omnidirectional filters for the visible wavelength range can be realized by coating the walls of MPSi layer with modulated pore diameters with a transparent layer having a low refractive index, and then to fill the pores (with small openings in the center) with a transparent higher refractive index material. This can be done in principle by Atomic Layer Deposition (ALD) techniques (or by a combination of thermal oxidation and an ALD technique) discussed in more detail in relation to UV filters in following sections of this Chapter.

Of course, the fabrication of such structures is more challenging than the fabrication of omnidirectional MPS structures for the IR range and the feasibility of such designs needs still to be proven experimentally.

2.7. Optical Components Utilizing Leaky Waveguide Modes of Light Propagation Through Macroporous Silicon

This mode of light propagation was first observed by Lehmann et al. [30], who reported the short-wave pass filtering by a macroporous silicon membrane. The experimental findings, however, were only explained by the spectral dependency of light diffraction at a small aperture, which falls somewhat short of the task. Nevertheless, a thin sheet of macroporous opaque material works as a short pass optical filter. The correct explanation in terms of leaky waveguide mode transmission is given here.

2.7.1. Light Transmission Through Macroporous Silicon in the UV- Near IR Spectral Region

The short-pass filters based on leaky waveguide mode propagation were suggested for 100 μm and longer wavelengths (far IR spectral range); examples can be found in [76-78]. These short-pass filters were based on the array of metallic leaky waveguides (see Fig. 2.22). The manufacturing of such filters was based on drilling uniform holes in thin metal plates. By drilling such holes with a high density, the overall transmission of such filters can be made sufficiently high. This approach though is obviously not scalable for the UV spectral range.

Later and independently, in [30] a free-standing macroporous silicon (MPSi) array was observed to exhibit short-pass filtering in UV. A reasonable transmission was shown down to 180 nm wavelengths, and it was predicted that the pass-band will extend to far and even extreme UV (down to several tens of nanometers; see Fig. 2.23). However, such short-pass filters have not provided truly short-pass behavior - the spectrum showed transmission in the near IR, which was unexpected to Lehmann et al. [30].

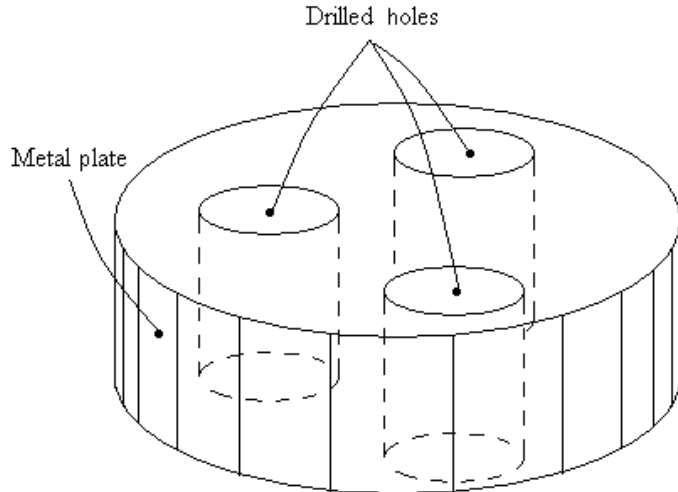


Figure 2.22. Waveguide mode cut-off IR short-pass filter design.

In order to better understand the performance of such filters (denoted in the future consideration as *Lehmann's filter*), let us consider the optical effects that take place during light transmission through the MPSi array. It should be noted that such principles are very similar to the metal waveguides filters discussed above.

The structure of the Lehmann's filter is schematically shown in figure 2.24. Such a filter consists of air- or vacuum-filled macropores electro-etched into the silicon wafer host. The macropores are forming an ordered uniform array (in [30] the array was of cubic symmetry). The pore's ends are open on both the first and second interfaces of silicon wafer.

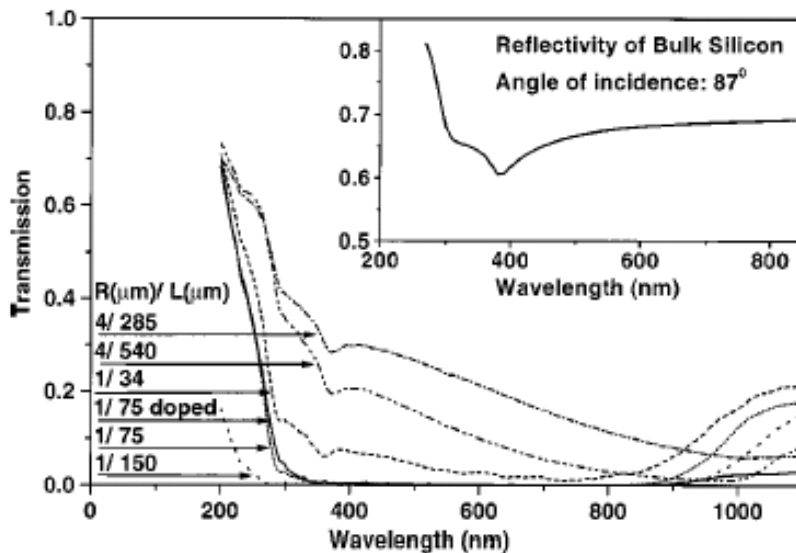


Figure 2.23. Measured transmittance (corrected for porosity) of MPSi array with pore radius R , pore length L , and the pore axis parallel to the light beam. Inset shows the spectral reflectivity of bulk silicon for a large angle of incidence (after [30]).

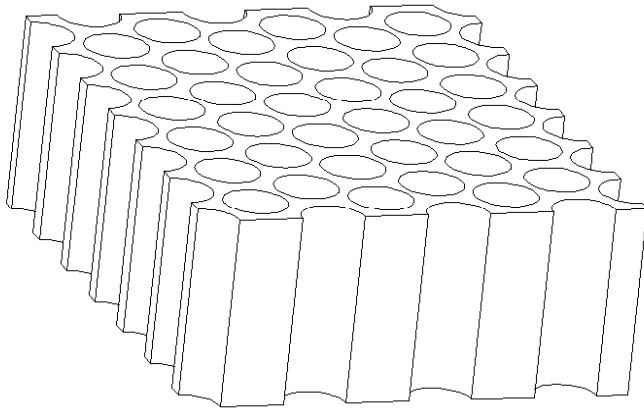


Figure 2.24. The short-pass MPSi filter structure of [30].

In the UV and visible spectral range, the transmission through such a structure obviously takes place through the pores (since silicon is opaque at these wavelengths, as follows from Fig. 2.25). Each pore in such a material can be considered as a waveguide. The waveguides, with cores formed by the pores, are essentially leaky as long as light can penetrate into a higher index cladding.

Optical filtering in long pores is mainly provided by wavelength dependent propagation losses. Using a simplified geometrical picture, a short-wavelength fundamental mode in a pore waveguide is presented by a ray trajectory with a shallow angle almost parallel to the pore walls, while a trajectory corresponding to long-wavelength mode would make a larger angle with respect to the pore walls. This causes more reflection events per unit of length as well as a smaller reflection, which results in higher optical losses for longer wavelengths.

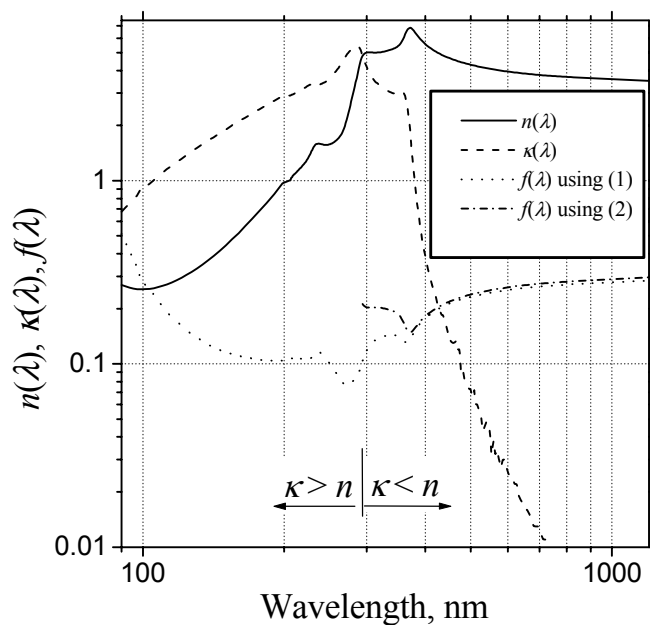


Figure 2.25. The optical constants of silicon (from [79]) and the wavelength-dependent factor $f(\lambda)$ for optical losses calculated using (2.1) and (2.2).

This explanation can be supported by an estimation of losses in a waveguide formed by metallic-like boundaries surrounding a dielectric core (e.g. vacuum). This approach can be used at short wavelengths ($\lambda < 294$ nm) where the optical properties of silicon resemble those of metals ($\kappa > n$, where κ and n are the imaginary and real parts of the refractive index, Fig. 2.25). An analytical solution is possible for a waveguide with flat boundaries. While it is not exactly the geometry of the pores, it gives a reasonable estimation of how the optical losses depend on the wavelength. For the N -th order ($N = 0, 1, 2, \dots$) transverse electric (TE) mode in a vacuum slab between the metal mirrors ($\kappa \gg n$, $\kappa \gg 1$) separated by a distance $d \gg \lambda$ this estimation is (after [80])

$$\alpha_{metal}^{TE} \approx (N+1)^2 \frac{\lambda^2}{d^3} \frac{n}{n^2 + \kappa^2}, \quad (2.9)$$

In the wavelength range $\lambda > 294$ nm the real part of the index is greater than the imaginary part; $n > \kappa$. Waveguiding in the pores is still provided by the same mechanism, high reflection for a shallow incident angle. The difference with the metallic mirrors is in the electromagnetic field structure in the waveguide claddings. In the case of metallic claddings, the field is strongly decaying while in the high index dielectric cladding, the waveguide mode loses energy to waves propagating in the cladding, i.e. the waveguide becomes leaky. Due to the high absorption of silicon in this spectral range, the leaking waves are eventually absorbed in any case. Optical losses due to leakage only ($\kappa \ll n$, $d \gg \lambda$) are estimated as follows (after [81]):

$$\alpha_{leakage}^{TE} \approx (N+1)^2 \frac{\lambda^2}{d^3} \frac{1}{\sqrt{n^2 - 1}} \quad (2.10)$$

Leaky modes have been studied [82] in application to high power fiber transmission systems using hollow fibers in the mid-infrared spectral region (CO_2 lasers).

Both equations (2.9) and (2.10) predict similar dependence of optical losses on wavelength, waveguide thickness, and the mode order. Moreover, equations (2.9) and (2.10) predict almost identical values of losses for $\lambda > 380$ nm. Hence, (2.9) can be used over the entire spectrum for practical estimations. The transmission through the waveguide of length L is proportional to an exponential factor such as $\exp(-\alpha L)$, which transfers a quadratic dependence of losses versus wavelength into a steep function with strong filtering of light with longer wavelengths. The macroporous material becomes a short-pass filter. However, at wavelengths $\lambda > 1100$ nm silicon is transparent, resulting in higher transmission for MPSi. To create a true short-pass filter (with cut-off in the UV or deep UV), one must block the infrared transmission. In fact, as it is shown below, absorption in silicon becomes lower than the leakage losses at approximately $\lambda \approx 700$ nm – 800 nm, which further restricts the applicability of the simple analysis presented in this paragraph.

For simplified practical estimations we note that for a particular material – silicon - the factors in (2.9) and (2.10) depend on the optical indices and do not change considerably across the UV and visible spectrum. The index factor

$$f(\lambda) = \begin{cases} n(\lambda)/(n(\lambda)^2 + \kappa(\lambda)^2) & \text{if } n(\lambda) < \kappa(\lambda) \\ 1/\sqrt{n(\lambda)^2 - 1} & \text{if } n(\lambda) > \kappa(\lambda) \end{cases} \quad (2.11)$$

calculated using published data for the optical constants of silicon is shown in Fig. 2.25. Note that (2.9) and (2.10) are valid if $n \ll \kappa$ and $n \gg \kappa$ respectively, which may result in a discontinuity in (2.11) when $n \approx \kappa$. The function $f(\lambda)$ does not change much across the entire spectral range of interest. Moreover, only the fundamental mode ($N = 0$) is essential because of the rapid increase of losses with N increasing. As long as the excitation of odd modes is unlikely due to a vanishing overlapping integral of the incident flat wave and the modal field, the next mode after the fundamental mode is the mode with $N = 2$. Losses for this mode are almost one order of magnitude ($(N+1)^2 = 9$) higher. This reduces (2.9) and (2.10) to a very simple and practical formula such as

$$\alpha = f_0 \lambda^2 / d^3. \quad (2.12)$$

By comparing losses calculated using (2.12) (at the assumption of $f_0 \approx 0.09$) with exact numerical calculations for a slab waveguide, one can find that (2.12) gives surprisingly good ($\pm 10\%$ accuracy) estimation in the 90 nm – 300 nm wavelength range, despite of the fact that at the short wavelengths the condition $\kappa \gg 1$ is violated (Fig. 2.26).

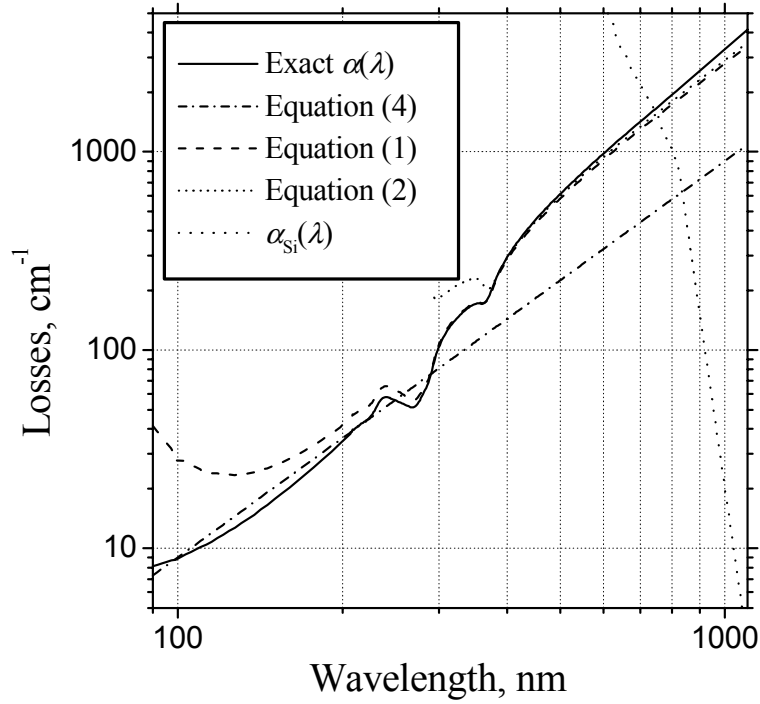


Figure 2.26. Spectrum of optical losses in a vacuum slab between silicon walls calculated using an exact numerical algorithm and estimated using (2.9) and (2.10), and (2.12).

In the visible range, exact calculations give slightly higher losses. For wavelengths longer than 500 nm, equ. 2.12 must be used with $f_0 \approx 0.28$. The absorption in silicon is also shown in Fig. 2.25 to emphasize the necessity of additional filtering at $\lambda > 800$ nm. The simplified loss formula allows the determination of the filter's cutoff wavelength (at $-3dB$ level) λ_{-3dB} and the rejection wavelength (e.g., at $-20dB$ level):

$$\lambda_{-3dB} = \sqrt{\ln(2) \cdot \frac{d^3}{f_0 \cdot L}}, \quad \lambda_{-20dB} = \sqrt{\ln(100) \cdot \frac{d^3}{f_0 \cdot L}}. \quad (2.13)$$

The ratio $\lambda_{-20dB}/\lambda_{-3dB}$ characterizing the sharpness of the filter becomes a constant $\sqrt{\ln(100)/\ln(2)} \approx 2.6$. Interestingly, the sharpness does not depend on the pore size and length. This sharpness might be acceptable for some applications: e.g. at $\lambda_{-3dB} = 150nm$, one gets $\lambda_{-20dB} = 390nm$, indicating that the visible spectrum is strongly suppressed. Sharper transmission characteristics, however, may be required for other challenging applications. Another interesting observation is that UV filters of this type do not necessarily require narrow pore size. Both the $3dB$ cut-off and $20dB$ rejection wavelengths are scaled proportionally to $d\sqrt{d/L}$. This means that with deep enough pores, one can achieve short-wavelength operation of the filter even with relatively large pore diameter. For example, from equ. 2.13, even at $d = 2 \mu m$ one can get $\lambda_{-3dB} = 200nm$ (that is, one tenth of d) if pores with $L = 1.4$ mm are used. This, however, seems to be rather challenging from a technological point of view.

Assuming that a practically achievable aspect ratio is $d/L \approx 1/100$, the cut-off wavelength becomes $\lambda_{-3dB} = d\sqrt{\ln(2)/100f_0} \approx 0.28d$.

The overall efficiency of MPSi filters is also affected by the light coupling to the pore waveguides. A simple estimation can be done for the rectangular ($a \times b$) cross section pores. In the deep UV range, where optical constants of silicon are almost metallic, we can assume that the modal field has a sinusoidal profile:

$$E_{N,M}(x, y) = \sin((N+1)\pi x/a) \sin((M+1)\pi y/b) \quad (2.14)$$

where $N, M = 0, 1, 2, 3 \dots$ are the mode order indices. The beginning of the Cartesian coordinate system is placed at the corner of the rectangular pore. The squared overlapping integral (similar to one in Eq. (2.2)) of this field with plane incident wave becomes equal to

$$I_{N,M} = \frac{64}{\pi^4} \frac{1}{(N+1)^2} \frac{1}{(M+1)^2} \text{ if } N \text{ and } M \text{ are even; } 0 \text{ otherwise} \quad (2.15)$$

Thus, in addition to the porosity factor determined as the relative area covered by pores, one has to apply an additional coupling factor for the fundamental mode equal to $64/\pi^4 \approx 0.66$. High order modes have much smaller coupling: e.g. $I_{2,0} = I_{0,2} = (1/9)I_{0,0}$; $I_{4,0} = I_{0,4} = (1/25)I_{0,0}$; $I_{2,2} = (1/81)I_{0,0}$ etc. They also experience stronger attenuation (see (2.9) and (2.10)). Total coupling to all the modes in a very wide pore supporting a large number of modes equals 100 % (if not counting the porosity factor) due to a mathematical identity

$$\sum_{p=0}^{\infty} \sum_{q=0}^{\infty} \frac{1}{(2p+1)^2} \frac{1}{(2q+1)^2} = \frac{\pi^4}{64} \quad (2.16)$$

As mentioned above in relation to omnidirectional IR filters made of macroporous silicon in the near IR and IR wavelength range, the nature of the transmission through the MPSi layer of Fig. 2.24 changes. Silicon becomes less opaque at wavelengths of 700 to 900 nm and becomes transparent at wavelengths starting at approximately 1000 nm. The light in these wavelength ranges can pass through the MPSi layer not only through the pores, but also through the silicon host (silicon “islands”). Due to the “islands” nature of the silicon host in the MPSi layer, the transmission at the wavelengths above ~ 700 nm will take place through waveguide modes confined in the silicon “islands”. As a high refractive index material, silicon can support waveguide modes if surrounded by a lower refractive index material (air or vacuum in the MPSi filter of Fig. 2.24). Close packing of the pores is essential for efficient transmission through the MPSi layer in the UV and deep UV ranges. Hence, the MPSi layer can be considered in the near IR, mid IR and part of the far IR ranges as an array of silicon waveguides in an air host.

Fig. 2.27 shows numerically calculated spectral dependences of the optical fundamental leaky waveguide and waveguide modes loss coefficients for $1 \times 1 \mu\text{m}^2$ near-square vacuum-filled pores in silicon. According to Fig. 2.27, transmission through the pore leaky waveguides is dominant up to ~ 700 nm, the transmission through the silicon host waveguides is dominant starting from ~ 800 nm, while at 700 to 800 nm both transmission mechanisms compete with each other.

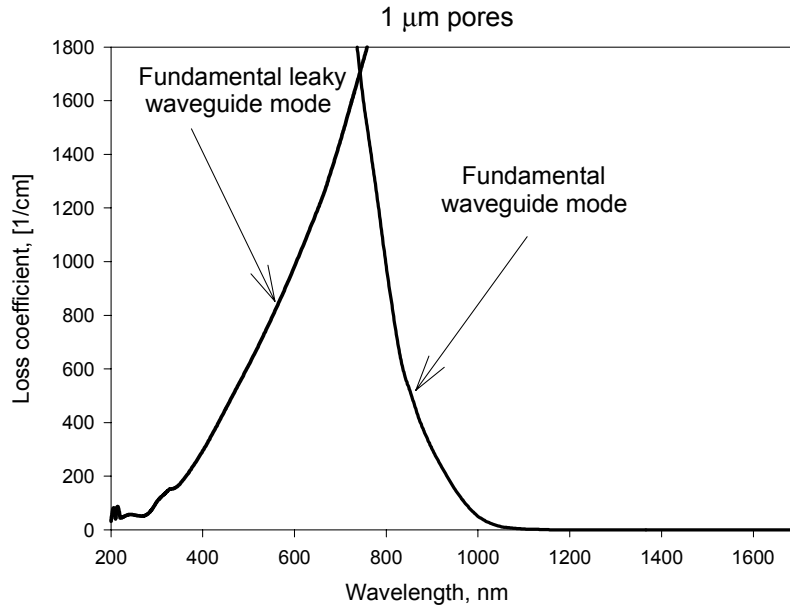


Figure 2.27. Numerically calculated spectral dependences of the optical fundamental leaky waveguide and waveguide modes loss coefficients for $1 \times 1 \mu\text{m}^2$ near-square pore in silicon.

The outcoupling process in a leaky waveguide array is essentially similar to that of a normal waveguide array, as considered in relation to omnidirectional IR filters previously in this Chapter.

In Fig. 2.28 the plot of the spectral dependence of transmission through an MPSi array of cubic symmetry, $50 \mu\text{m}$ thickness, and $1 \mu\text{m}$ pore diameter is given, numerically calculated according to the formalism presented above. Close matching with the experimental data of [30], as given in Figure 2.23 validates the model discussed above.

Fig. 2.27 shows numerically calculated spectral dependences of the optical fundamental leaky waveguide and waveguide modes loss coefficients for $1 \times 1 \mu\text{m}^2$ near-square vacuum-filled pores in silicon. According to Fig. 2.27, transmission through the pores leaky waveguides is dominant up to $\sim 700 \text{ nm}$, the transmission through the silicon host waveguides is dominant starting from $\sim 800 \text{ nm}$, while at 700 to 800 nm both transmission mechanisms compete with each other.

A MPSi-based short-pass filter design has considerable advantages with respect to existing deep and far UV filters. These include transparency down to the far UV spectral range, omnidirectionality of the transmitted spectral shape within the acceptance angles of the leaky waveguides, and other features. However, such a short-pass filter design does not provide enough control over the steepness and the position of the rejection zone edge. Also, band-pass filters (another important class of filters for many applications) cannot be obtained from such a layer.

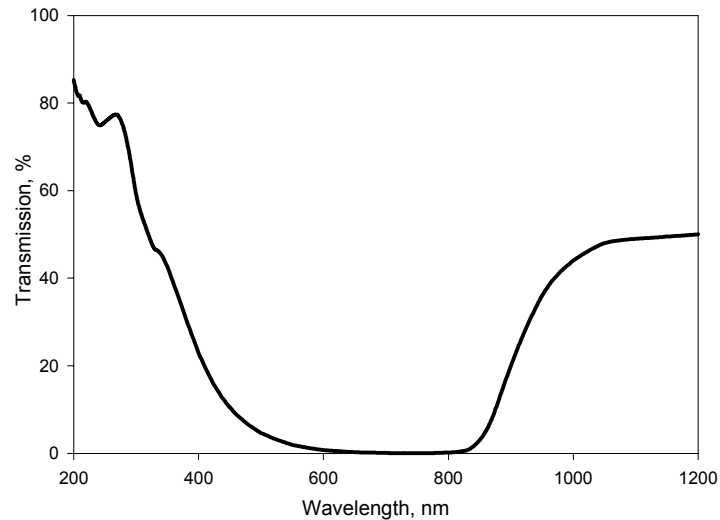


Figure 2.28. Numerically calculated spectral dependence of transmission through MPSi array of cubic symmetry, 50 μm thickness, and 1 μm pore diameter.

Fortunately, the transmission characteristics of an MPSi layer in the leaky waveguide mode can be further optimized by managing the α^{LW} term. This can be done by covering the pore walls with a transparent dielectric multilayer, that is, by creating a multilayer leaky waveguide array.

2.7.2. Coated MPSi Array

The simplest realization of a multilayer leaky waveguide array is a free-standing MPSi layer with pore walls uniformly coated by a single layer of transparent dielectric material, as is shown in Fig. 2.29. Such a layer will strongly modify the spectral dependences of leaky waveguide loss coefficients by means of constructive and destructive interference of the leaky waveguide mode inside this layer.

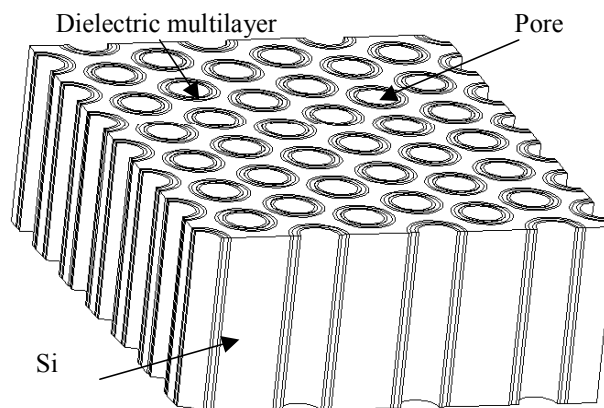


Figure 2.29. Freestanding macroporous silicon uniform pores array with one layer of transparent dielectric material uniformly covering pores walls.

The main purpose of covering the pore walls with a multilayer is to modify the spectral dependence of the leaky waveguide mode loss coefficient ($-\alpha^{LW}(\lambda)$). The multilayer coating can be arranged as a high-dielectric reflector inside the pass band. To provide optimal performance, the materials comprising a multilayer coating do not have to be transparent over the pass band, rejection band and rejection edge. Hence, silicon nitride, silicon dioxide and other materials transparent in at least part of the UV range can be used for deep and far UV filters. As an example, Fig. 2.30 gives the numerically calculated spectral dependences of the transmission through the MPSi membrane with different numbers of layers in the pore wall coating. The pores were assumed to be 350 μm deep and originally 1.5 μm in diameter (i.e., the pore diameter decreased with the increase of the thickness of the dielectric coating on the pore walls). In the calculations the dispersions of the real and imaginary parts of the refractive indices of silicon, silicon dioxide and silicon nitride were taken into account. One can see that while the silicon nitride absorption edge is located approximately at the 290 nm wavelength, substantial transmission in the deep UV is possible.

One of the most attractive properties of the MPSi-based UV filters is the very strong level of rejection that can be obtained. As follows from Fig. 2.30b, even for a single-layer coated MPSi filter the level of rejection can exceed 5 orders of magnitude over the rejection range. With a higher number of layers on the pore walls (or with a higher aspect ratio in the pores) the rejection edge can be made even sharper and the rejection even deeper.

In order to demonstrate the capability of meeting the most demanding requirements on the long wavelength blocking (such as needed in certain applications of solar-blind filters), I have done some preliminary designs of the solar blind filter with unfilled pores. By means of a thorough optimization, it was found that the following pore structure provides sufficiently deep rejection, sufficiently sharp edge, and acceptable levels of transmission (listed radially inward from the pore wall): {Si pore wall/57 nm, HfO₂/73 nm, SiO₂/7 nm, HfO₂/111 nm, SiO₂/18 nm, HfO₂/33 nm, SiO₂/52 nm, HfO₂/91 nm, SiO₂/800 nm air-filled pore}.

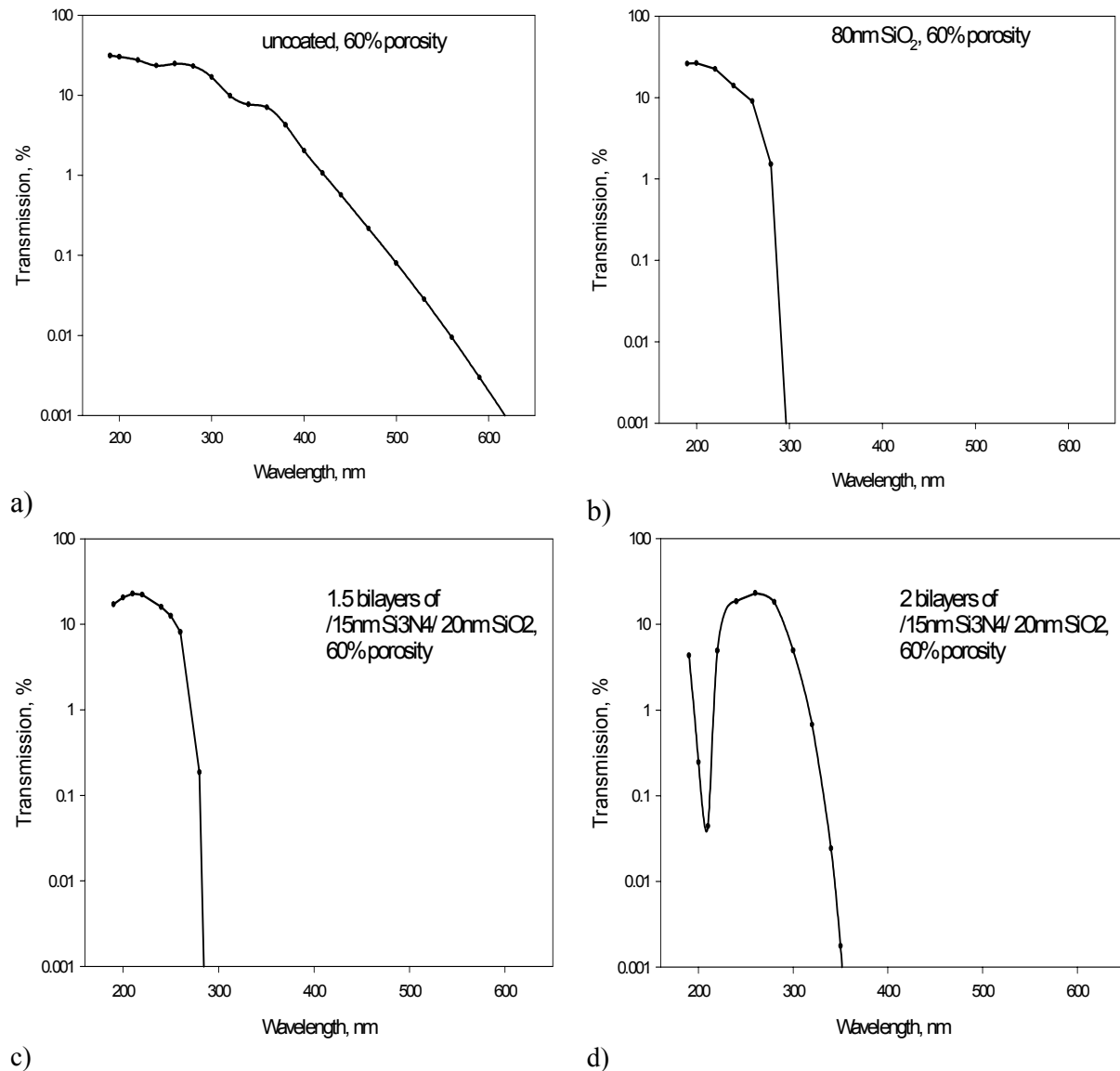


Figure 2.30. Numerically calculated spectral dependences of the transmission through the MPSi membrane with different numbers of layers in the pore wall coatings. The transmission is on a logarithmic scale.

The numerically calculated transmission spectra through MPSi filter with such coatings are given in Fig. 2.31. Fig. 2.31a shows the calculated transmission spectra on a linear scale, while Fig. 11b gives the calculated transmission spectra on a logarithmic scale. The inserts in both figures provide magnified portions of the plots in a UV region of spectrum. Black curves on both figures correspond to the calculated transmission through the MPSi layer with perfectly uniform pores and pore wall coatings along the pore depth, 300 μm thick porous layer and 150 nm metal coating on both sides of the porous layer. No tapering of the pore walls was assumed (hence there is room for improving the transmission through the filter). Green curves correspond to 300 μm thick MPSi layer with the same structure without metal coating of the surfaces and with 5 % random nonuniformity in layers on pore walls (quite a reasonable number as preliminary experiments with ALD pore wall coating have shown). The red curve corresponds to a 300 μm -thick MPSi layer with metal coating and with 5 % nonuniformity assumed. The blue curve corresponds to the MPSi layer with 400 μm thickness, 5 % nonuni-

formity and the same metal coating on the surface. One can see that, at least according to numerical calculations, such a design not only offers a filter performance considerably exceeding the most demanding specifications, but also permits reasonable latitude in MPSi layer parameters. The relatively few (eight) layers of pore wall coating, sufficient for reaching the program specifications, not only should provide a reasonably low cost for the filters, but also should insure the absence of problems typical for interference filters, such as growth of the columnar structure and scattering of light at the imperfect interfaces. It should be also noted that, since the reflection of light from the pore walls will occur at glancing angles (above 80° from the normal to the pore wall), the influence of pore wall or pore wall coating roughness will be thus minimized.

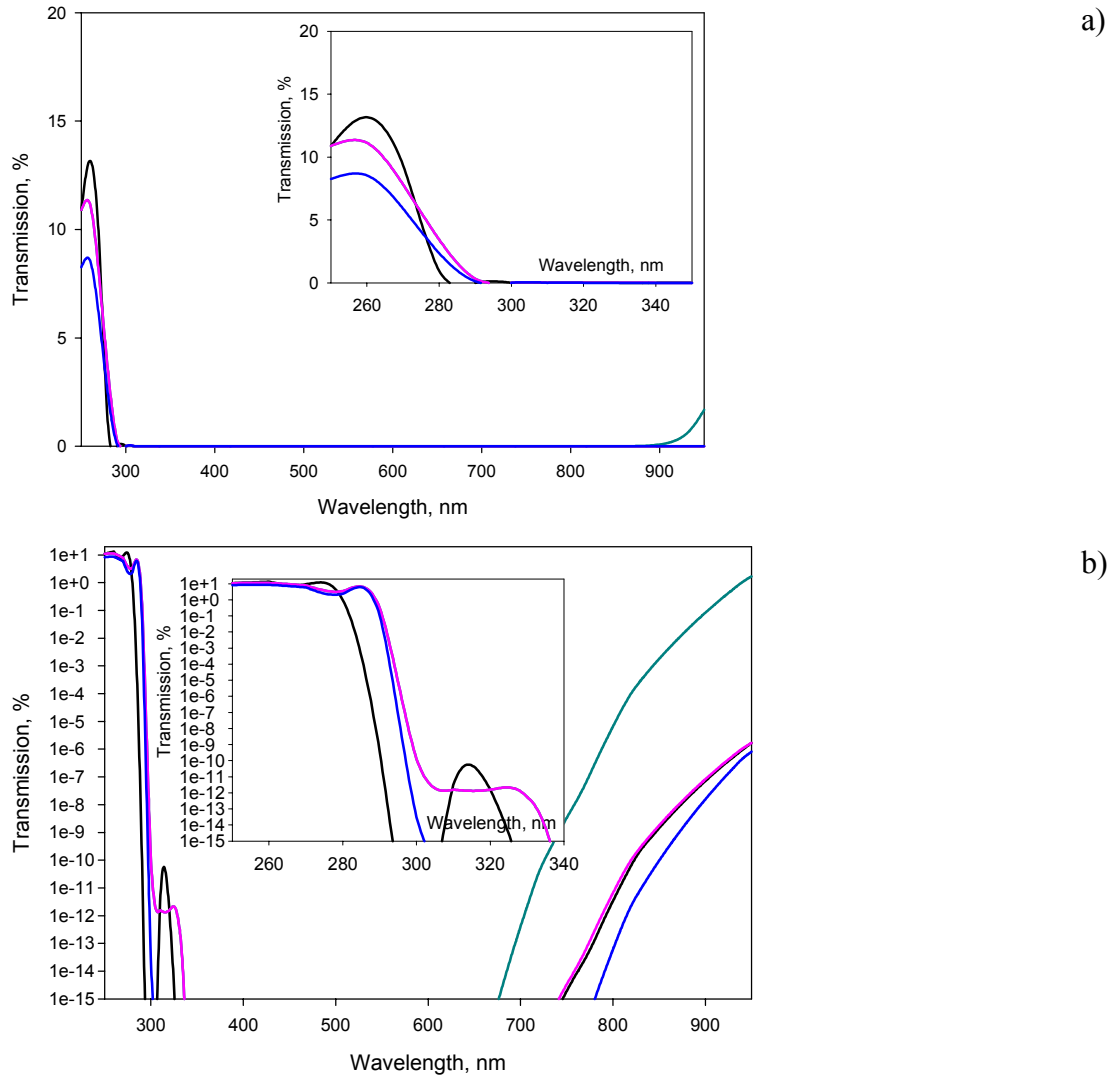


Figure 2.31. Numerically calculated transmission spectra through an MPSi membrane with an eight-layer pore wall coating. The transmission (y-axis) is shown in a) on a linear scale and in b) in logarithmic units. The inserts show the magnified portions of the spectra in UV region. See text for differences in curves.

Besides the short-pass type of filter, it is possible to fabricate a band-pass filter based on coated MPSi layers as well. Fig. 2.32 gives the numerically calculated spectral dependences

of the transmission through an MPSi membrane with a five-layer silicon dioxide/silicon nitride pore wall coating. The band-pass shape of the transmission is clearly apparent.

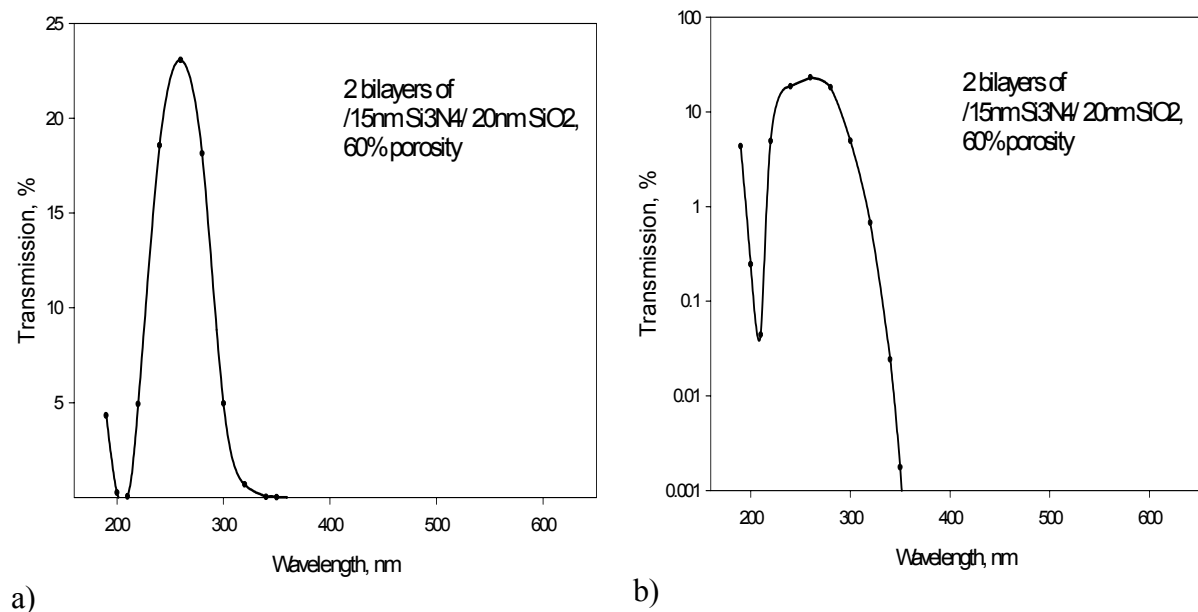


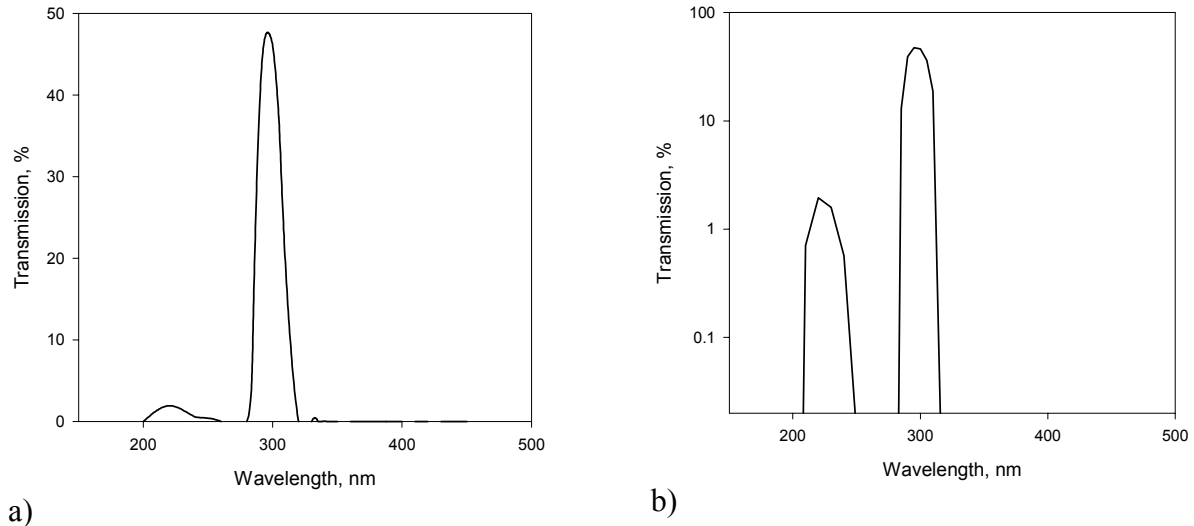
Figure 2.32. Numerically calculated spectral dependences of the transmission through an MPSi membrane with a five-layer pore wall coating. The transmission in a) is given on a linear scale and in b) on a logarithmic scale.

Narrow band-pass filters based on coated MPSi membranes are feasible as well. The peculiarities of the MPSi filter structure are such that, in order to exhibit narrow bandpass behavior, the coating on the pore walls should act as a narrow band reflector at an almost glancing angle of incidence (depending on a pore geometry at angles between 80° and 86°). As it is well known, in order to form such a reflector one needs to use a substantial number of layers of materials with adequately close indices of refraction. This is because the width of the band in this case is determined by the index contrast - the higher the contrast, the wider the band. This calls for the “engineering” of the refractive index of the layers in the multilayer stack, since the choice of transparent, environmentally stable and depositable materials is quite limited in the deep UV range. As will be shown later there is considerable potential for multilayers of “engineered” materials with some of the deposition techniques mentioned.

As an example, Fig. 2.33 gives the numerically calculated spectral dependences of the transmission through an MPSi membrane with a 9.5-bilayer pore wall coating. It is designed as a narrow bandpass filter with the band centered at 300 nm. In the calculations the refractive indices of the layers were assumed to be 1.75 and 1.9. The dispersion of the dielectric constants in the pore wall coating was neglected. Such refractive indices are close to those of an Al₂O₃ and Al₂O₃/TiO₂ nanolaminated stack, discussed later in this Chapter. In the calculations an MPSi membrane with an aspect ratio of 150 was used (such an aspect ratio is well within the limits of the technology). The narrow bandpass transmission of such a structure is clearly demonstrated.

One should note that in addition to a quite high level of transmission within a reasonably narrow band such a structure should exhibit high levels of rejection at wavelengths above the center of the band despite a parasitic transmission peak at ~ 220 nm resulting from theory ne-

glecting absorption. However, this peak should be strongly suppressed in reality since it is located at wavelengths below the TiO_2 absorption edge (i.e., the TiO_2 portion of a multilayer will be opaque).



2.33. Numerically calculated spectral dependences of the transmission through an MPSi membrane with a 19-layer pore wall coating designed as a narrow bandpass filter with band centered at 300 nm. a) Transmission on a linear scale. b) Transmission on a logarithmic scale with more details.

It was observed and explained above that a free-standing MPSi array, in addition to the pass band in the UV, also shows pass-bands throughout the near IR and IR (starting from approximately 1100 nm). For some applications, this channel of transmission should be suppressed. Recalling the discussion above, the transmission at near IR and IR spectral ranges takes place through waveguide modes confined inside the intrapore silicon islands. It is possible to suppress the transmission through waveguide modes completely by covering first, second, or both surfaces of the MPSi layer by thin (100 to 200 nm) metal film. In this case the coupling efficiency of light to waveguides will be completely suppressed. By doing that one can obtain a truly short-pass or band-pass deep UV filter: rejection of the wavelengths longer than the rejection edge would be very strong (6 orders of magnitude or more) up to the limit of the waveguide transmission channel (usually in the far IR).

It should be noted, however, that the covering of MPSi layer surfaces with a metal layer will sacrifice both coupling and outcoupling efficiencies. This will also somewhat suppress the coupling efficiencies. It will be caused by decreasing the open area of each leaky waveguide by the area of the multilayer coating cross-section. Fortunately, most of the leaky waveguide mode energy is concentrated within the air (or vacuum) core of the leaky waveguide. Fig. 2.34 illustrates the numerically calculated fundamental mode intensity and electric field distribution across the pore cross-section for the fundamental TE-polarized leaky waveguide mode for the MPSi layer with pore walls covered by the five-layer coating at the wavelength of 250 nm (central wavelength of the pass-band of MPSi layer).

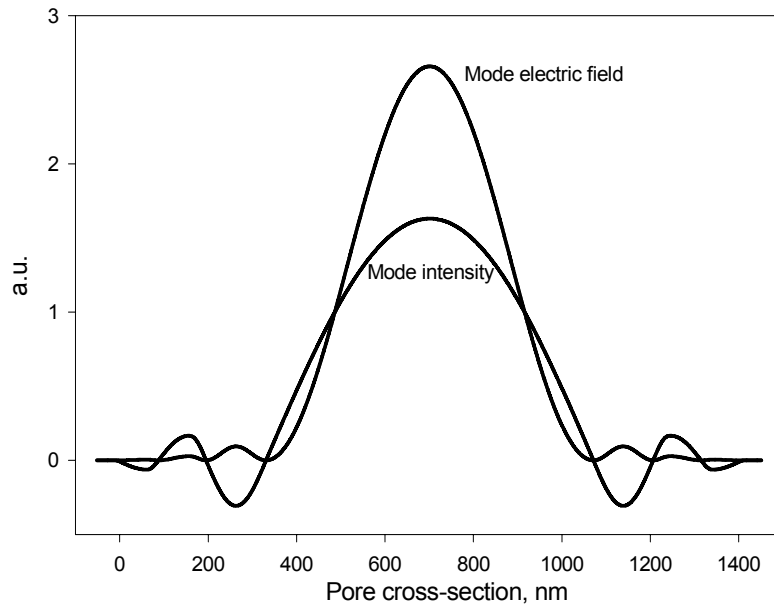


Figure 2.34. Numerically calculated fundamental mode intensity and electric field distribution across the pore cross-section for fundamental TE modes for the MPSi layer with pore walls covered by a five-layer high-reflectance at 250 nm coating. Pores were assumed to have near-square cross-section. The wavelength was assumed to be 250 nm.

Such a multilayer coating of the MPSi layer pore walls will provide the following advantages over ordinary short-pass filters: the steepness of the rejection edge will be increased (due to multiple reflections that the light-waves experience during propagation through leaky waveguide), the rejection level will be higher by many orders of magnitude, and the transmission spectrum will be independent of the angle of incidence due to the independence of the coupling/outcoupling and filtering processes. Although the mechanism of improving the transmission spectra of the MPSi layer with multilayer-coated pore walls is interference-based, the MPSi layer will not suffer from the disadvantages of the usual interference filters, such as the dependence of the spectrum on angle of incidence.

Fig. 2.35a shows the numerically calculated transmittance spectra through the typical interference short-pass filter for normal incident, 10° and 20° tilted plane-parallel beams. The wavelength shift of the pass-band edge position common to all interference edge filters is demonstrated. Fig. 2.35b presents the normalized transmittance (as was discussed above, maximum transmittance will be defined by the particular filter structure and can vary from $\sim 40\%$ to 75%) spectra through an MPSi layer with a five-layer coating for normal incident, 20° and 30° tilted plane-parallel beams. As follows from Figs. 2.35a and 2.35b, a coated MPSi layers should provide considerable advantages over interference edge filter designs and will provide the opportunity to use short-pass filters at different angles of incidence ($\pm 20^\circ$ at least). Fig. 2.35c illustrates the numerically calculated transmittance spectra through the interference short-pass filter of Fig. 2.35a for normal incident beams with different convergence: plane-parallel beam (0-convergence angle) and Gaussian beams with 20° and 40° convergence angle. The degradation of both the band-edge shape and out-of-band rejection, common to the interference short-pass filter, are demonstrated. Fig. 2.35d presents the normalized transmittance spectra through an MPSi layer with 5-layer coating for 0, 20° and 40° convergent normally incident Gaussian beams. It follows from Figs. 2.35c and 2.35d, that the MPSi layer with pore

walls coated by a dielectric multilayer will provide the opportunity to use multiple-cavity narrowband-pass filters at convergent or divergent beams ($\pm 40^\circ$ at least).

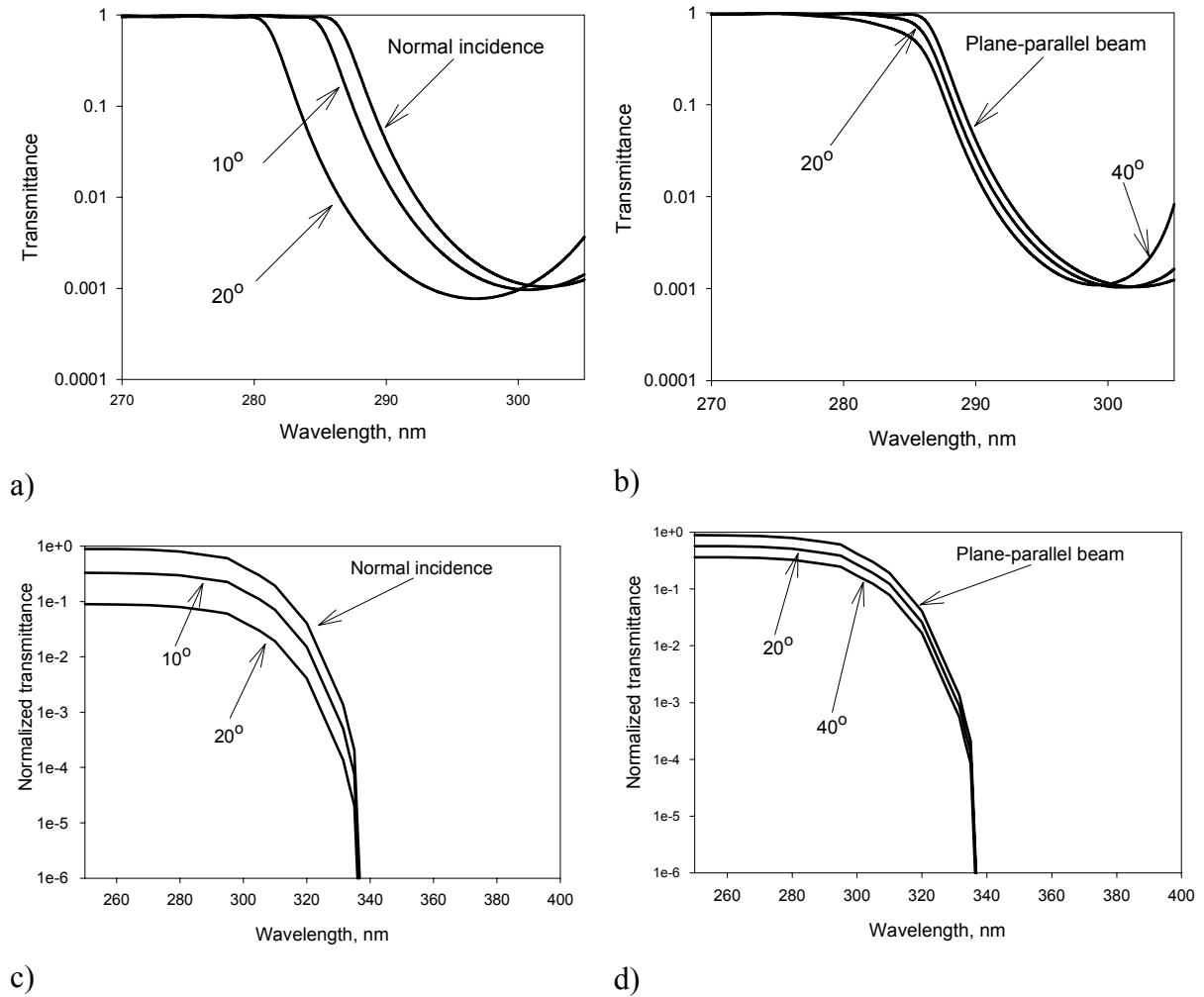


Figure 2.35. a)-b): Numerically calculated transmission spectra through an interference short-pass filter a) and through a five-layer coated MPSi layer b) for different angles of incidence. c)-d): Numerically calculated transmission spectra through an interference short-pass filter c) and through a five-layer coated MPSi layer d) for different diversions of Gaussian beam.

2.7.3. Wide Field-of-View Design

The MPSi UV filter design presented in the previous paragraph offers absence of the spectral shifts or degradation of the shape of the passed or blocked spectral bands with the angle of incidence, thus permitting operation in tilted and divergent light beams as long as the angle of incidence does not exceed the acceptance angle of the pore structure. If the pores are left unfilled as in the designs discussed (Fig. 2.36a), such a filter can be transmissive down to the far-UV or even in the extreme UV spectral range. However, as will be shown in the experimental section of this chapter, the acceptance angle of such filters is quite narrow (between 10 and 20 degrees, depending on the MPSi layer parameters).

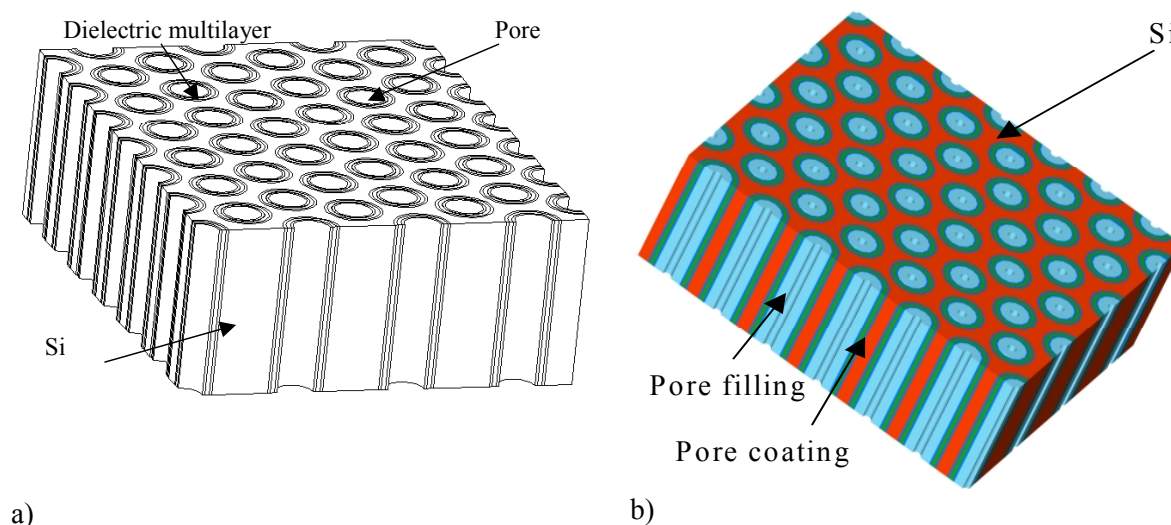


Figure 2.36. Schematic drawing of the pore structure for the a) omnidirectional narrow field-of-view UV filter design and b) omnidirectional wide field-of-view UV filter design.

Omnidirectional UV filters with wider field-of-view are also possible in the design utilizing pores almost completely filled with transparent material (as shown in Fig. 2.36b). Calculations show that such structures are possible and the field-of-view can be indeed enlarged by a factor, which is approximately equal to the refractive index of pore-filling material. For deep UV filters the choice of pore filling materials is limited to the materials that are sufficiently transparent at these wavelengths. HfO_2 (refractive index 2.3), Al_2O_3 (refractive index 1.7), for example, according to the preliminary calculations, can provide the sufficient transmission while increasing the angular range of the filter by a factor of 2.3 and 1.7 respectively. Such materials can be deposited by, for example, Atomic Layer Deposition techniques (ALD) or Low Pressure Chemical Vapor Deposition technique (LPCVD).

There are other factors that have to be accounted for while designing the “filled” MPSi UV filters. One of them is that the average refractive index of the coating should exceed the effective refractive index of the leaky waveguide mode, i.e. it has to exceed the refractive index of the pore-filling material (otherwise the pore embodies a regular waveguide instead of a leaky waveguide, and no modification of the transmission spectrum will be possible). This limits the possible range of materials to be used for pore coating and pore filling. For the case of LP CVD, where the possible materials are limited to polysilicon, silicon dioxide and silicon nitride, it causes the necessity to use polysilicon in a multilayer coating (which is opaque at

such wavelength). However, numerical calculations (Fig. 2.37) show that even with such materials it is possible to design deep UV filters.

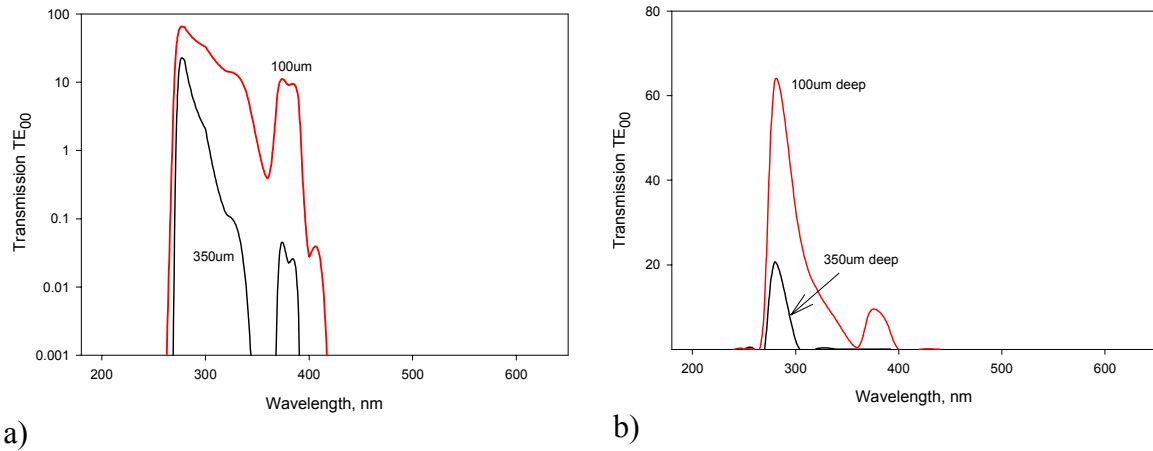


Figure 2.37. Numerically calculated spectral dependences of the transmission efficiency by TE₀₀ leaky waveguide mode through 100 μm (red curve) and 350 μm (black curve) deep MPSi membranes with 5-layer coated (50 nm SiO₂/14 nm Si) pores (900 nm diameter after coating), filled with Si₃N₄ (with 25 nm diameter unfilled area in the center. a) shows the transmission in logarithmic scale, while b) shows a linear scale.

2.7.4. Fabrication and Results

The formation of MPSi was reviewed in some detail earlier in this chapter, so it will not be repeated here. The focus of this section will be on the other processes required to make a functional UV filter from an MPSi layer or membrane. First, as mentioned above, a freshly etched MPSi layer should be made into a freestanding membrane in order to gain any kind of transmittance through it at UV wavelengths. Membrane formation requires removing the un-anodized part of the silicon wafer from the backside. This can be done, e.g., by inductively coupled reactive ion etching (RIE) or by chemical etching in hot KOH solutions [30]. Fig. 2.38 shows an SEM image of a cleaved, freestanding MPSi layer fabricated by backside chemical etching. In order to protect pore walls from chemical species during chemical back etching, a thin protective layer of Si₃N₄ was deposited by a CVD process onto the pore walls in this case, which after the process was removed in hot phosphoric acid.

The next process needed is pore wall coating. The simplest process for obtaining a single-layer pore wall coating is thermal oxidation of the MPSi membrane. However, in order to obtain multilayers of different dielectric materials on the pore walls, a different technique has to be used. Here it is shown that a LPCVD process can be used for these purposes. Several MPSi filters with up to seven layers coating the pore walls were successfully fabricated by a Low Pressure CVD technique by MEMS Precision Instruments, Inc. SEM images of the LPCVD-coated MPSi layer cross-section are given in Fig. 2.39, which gives the image of the single-layer silicon nitride-coated MPSi membrane in a), while b) shows the image of the five-layer coated MPSi membrane. In both cases, a thin layer of polysilicon was deposited by an LPCVD technique after finishing the dielectric coating in order to obtain a better contact of the SEM images. Samples were polished down from the top for these pictures and the cross sections shown were made at a depth of ~200 μm down from the original MPSi layer surface.

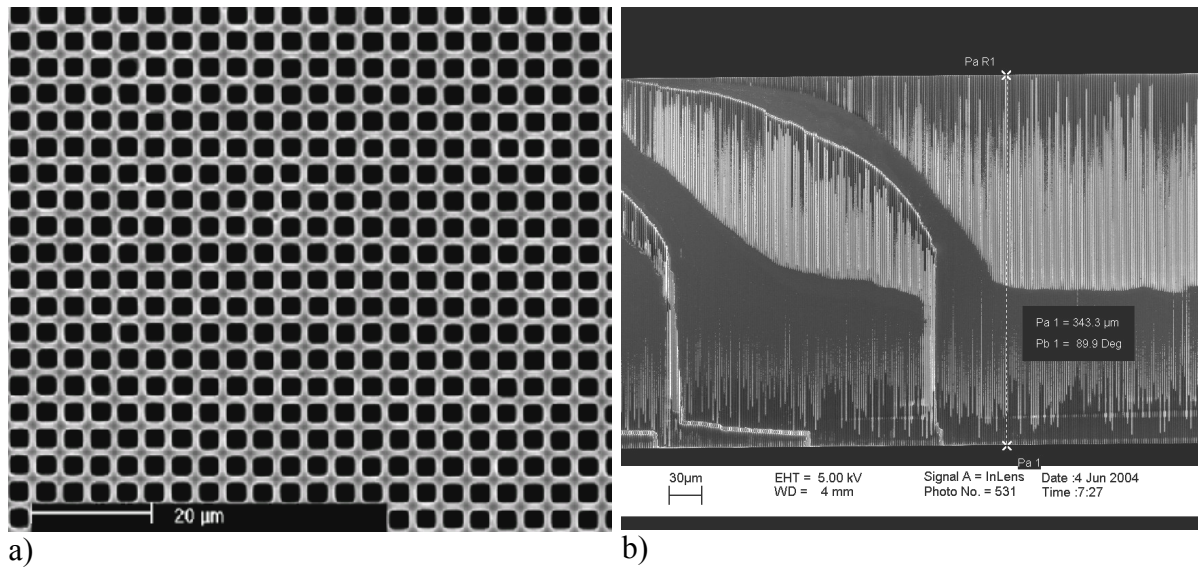


Figure 2.38. SEM images of the MPSi arrays. a) Top view, b) cross-sectional view of the MPSi membrane.

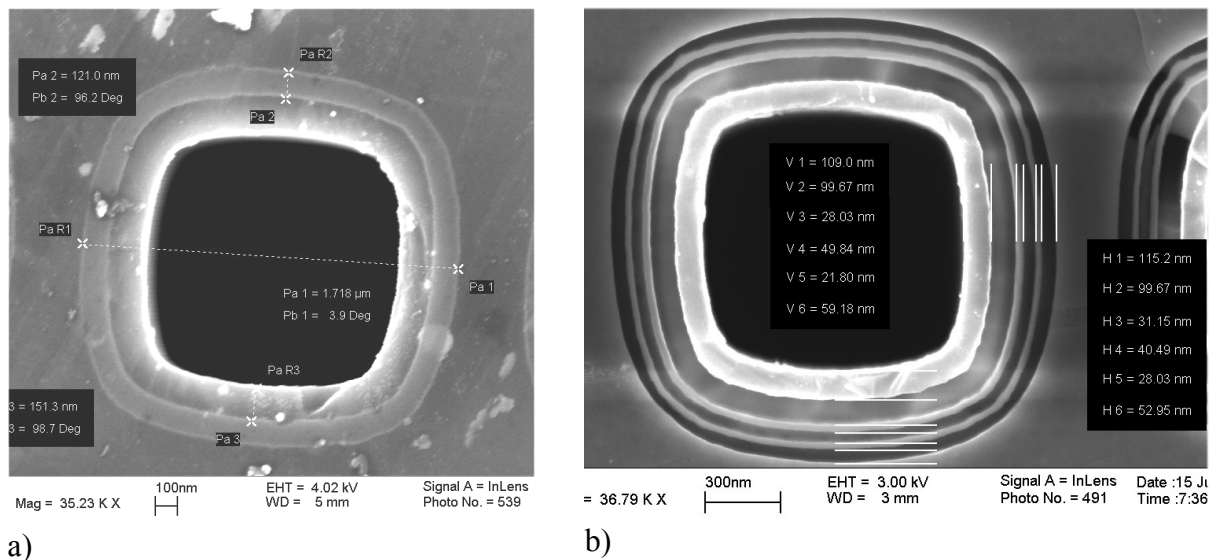


Figure 2.39. Cross-sectional SEM images of the MPSi layer with pore walls coated by: a) A single layer of dielectric material. b) 5 layers of dielectric materials.

However, using LPCVD techniques, it may be difficult to obtain the necessary uniformity of the individual layer thicknesses along the pore length. In addition, stresses in the films were found to be quite large, causing various problems (such as a severe sample bowing). An Atomic Layer Deposition (ALD) technique might be a better process for pore wall coating.

ALD is a deposition technique that puts down films sequentially, one atomic layer after the other [83-85]. ALD films have the proven ability to coat the toughest three-dimensional structures conformally. In addition, the layer-by-layer mechanism allows reproducible film engineering at the atomic level. Film engineering is a key process in enabling continuous growth of ALD films over a variety of substrates wherein typically the incompatibility of the film with the substrate is overcome by providing an ultrathin (several monolayers only) interface

layer that is compatible with both the substrate and the film. Film engineering has also been proven to modify and improve film properties such as the suppression of the growth of disadvantageous polycrystalline films [83]. Amorphous films are an important property for narrow bandpass filter fabrication, as was assumed in the previous sections of this Chapter.

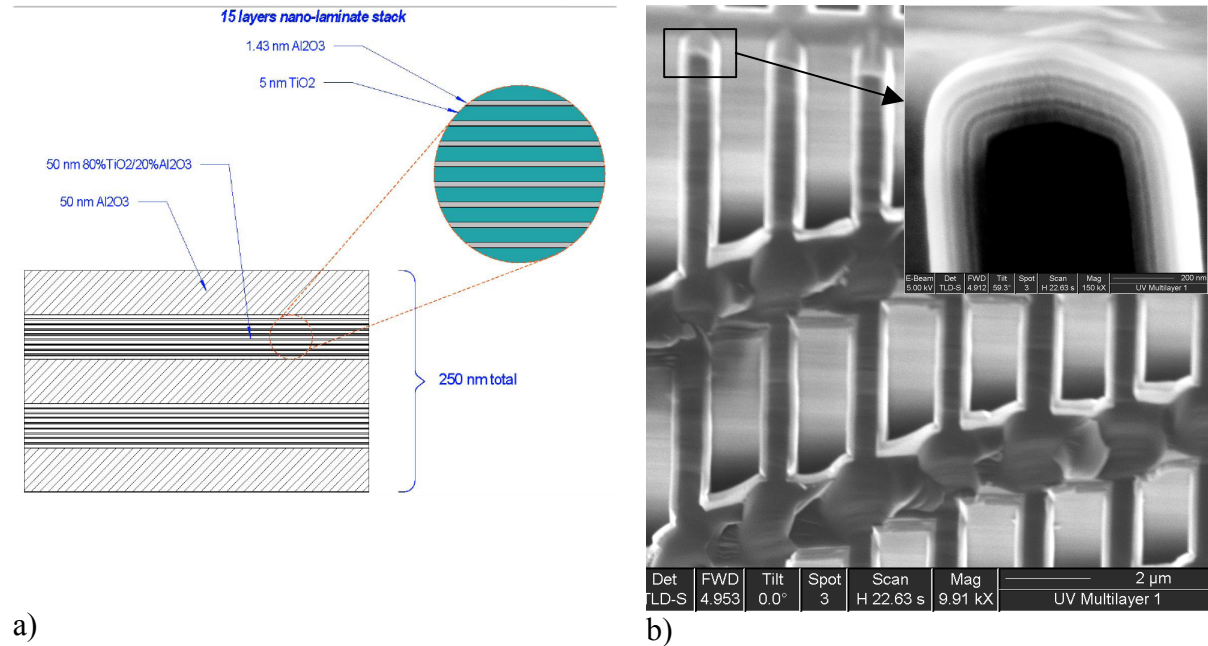


Figure 2.40. a) Schematic cross-sectional drawing of the pore wall coating structure used in the experiment. b) Cross-sectional SEM images of an ALD-coated MPSi membrane with an $\text{Al}_2\text{O}_3/\text{TiO}_2$ multilayer with the structure as in Fig. a).

To check the feasibility of an ALD technique for the UV filter fabrication, a 250 nm thick ALD film stack was deposited over a MPSi sample using five alternating bilayers consisting of a pure Al_2O_3 layer and an alumina-titanate layer, each 50 nm thick. The individual alumina-titanate layer comprises fifteen nanolaminated layers of 5 nm thick TiO_2 and 1.43 nm thick Al_2O_3 resulting in a 4:1 $\text{TiO}_2:\text{Al}_2\text{O}_3$ composition ratio that is sufficient to suppress the natural, disadvantageous agglomeration of TiO_2 , while achieving a relatively high optical index (see Fig. 2.40a for a schematic illustration of the layer-stack). The ALD coating was performed by Sundew Technologies, Inc. (Colorado, USA). The resulting conformal coating is apparent in the SEM images of Fig. 2.40b), indicating the feasibility of robust and reproducible multilayer growth with the required conformality over challenging MPSi substrates. The SEM picture clearly indicates that the 250 nm thick stack is highly conformal. The high resolution SEM highlights the 5 layers stack, although sample charging effects blur the borders between the layers and do not allow to reveal individual nanolayers of 5.0 nm TiO_2 and 1.43 nm thick Al_2O_3 . The feasibility of using ALD for the engineering of pore wall coating is thus clearly demonstrated.

Fig. 2.41 shows a less challenging multilayer pore wall coating: Fig. 2.41a) shows a 5-layer $\text{TiO}_2/\text{Al}_2\text{O}_3$ coating, while Fig. 2.41b) shows a 7-layer $\text{TiO}_2/\text{Al}_2\text{O}_3$ coating.

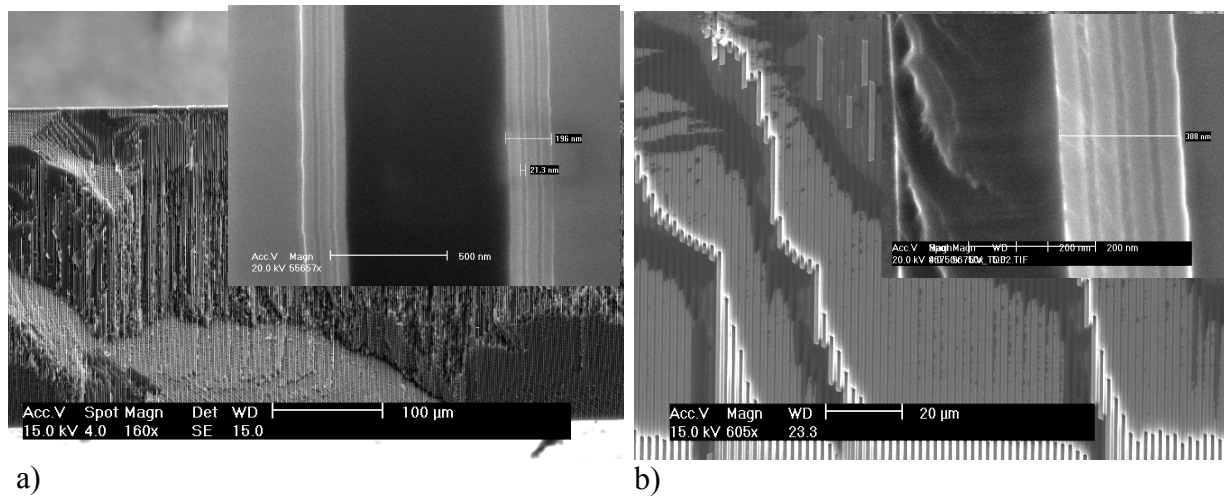


Figure 2.41. SEM cross-sectional images of: a) Five-layer and b) seven-layer $\text{TiO}_2/\text{Al}_2\text{O}_3$ coating on the pore walls of MPSi membrane. Magnified images are shown as inserts on both figures. Scales on insert in a) are 500 nm, 196 nm and 21.3 nm, from largest to smallest, respectively. Thickness of multilayer on insert in b) is 308 nm.

It should be noted that other pore-wall coating materials (such as HfO_2 and SiO_2) were successfully deposited by ALD onto the pore walls as well.

2.7.5. Optical Testing

In order to confirm the theoretical predictions, a number of MPSi samples were fabricated, partially coated, and tested. As a confirmation of the theoretically predicted high rejection level over the wide spectral band, the transmission spectrum through an MPSi membrane with an adequately high aspect ratio (200) is given in Fig. 2.42a). One can see that the rejection in uncoated sample exceeds 5 “O.D. units” (O.D. = optical density) from 300 nm and at least up to 800 nm (i.e. over part of the UV range, over all the visible part of the spectrum, and over at least part of near IR range). The transmission in the near IR was in the order of the noise level of the IR detector (which was much noisier than the UV-sensitive detector). Metal coating of one or both surfaces of the MPSi membrane (a 49 nm thick ion-beam sputtered Ta layer) enables even more spectacular rejection levels. As follows from Fig. 2.42a), the level of IR transmission through the MPSi membrane (up to 3300 nm) was suppressed down to the spectrometer detection limit, while the UV transmission band stayed unchanged (all curves exactly match).

Imaging properties of the MPSi UV filters are demonstrated in Fig. 2.42b). This figure presents the image of a coin taken through the filter. Fig. 2.42c) demonstrates that the (nano)roughness of the pore walls is an important factor for the achievable transmission levels.

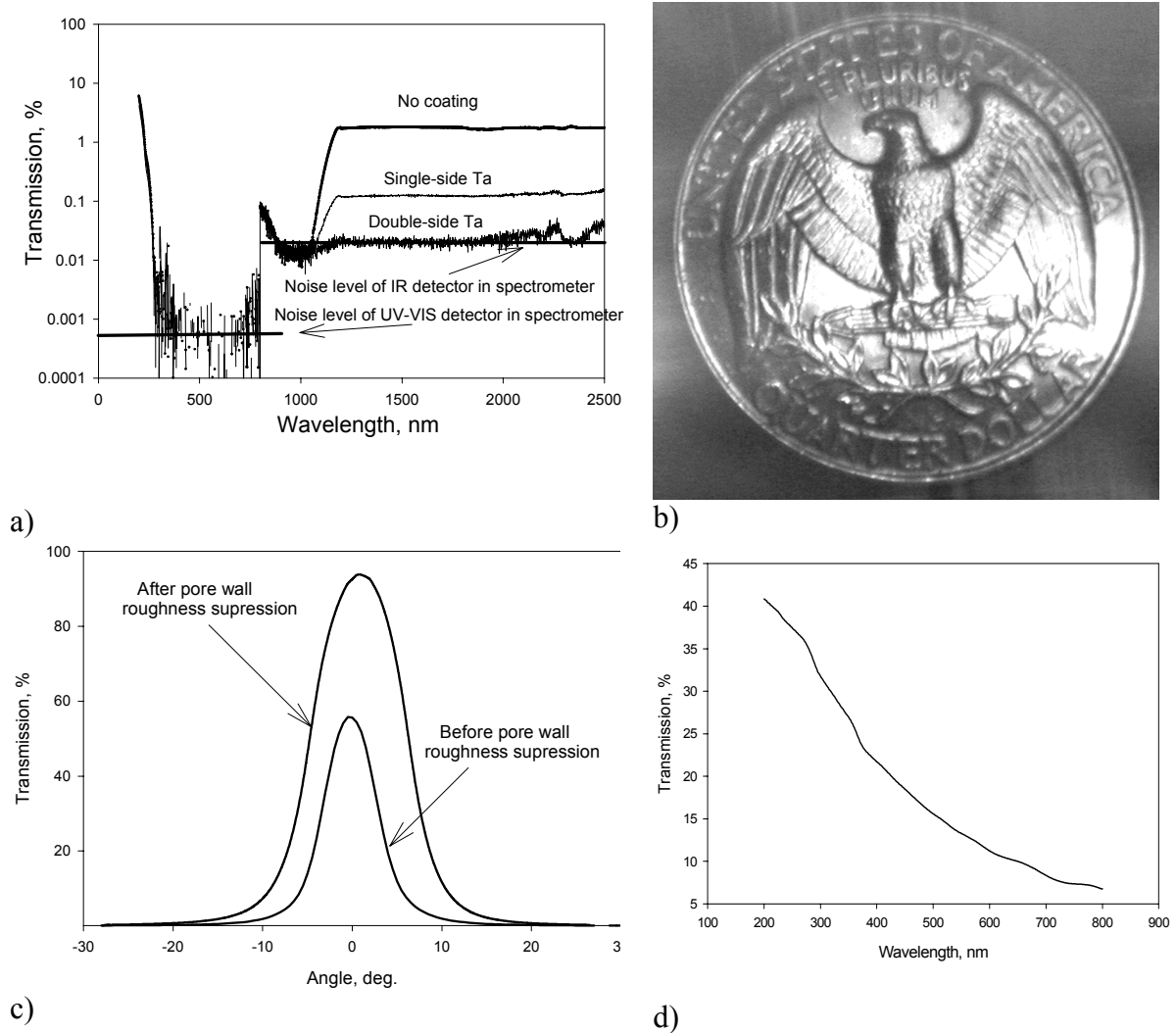


Figure 2.42. a) Far field transmission spectrum through an MPSi membrane with and without metal coatings on one or both surfaces. b) Photo of a quarter taken through the MPSi filter (so the CCD array is effectively in the far field). c) Experimental angular dependences of the near-field transmission through an MPSi UV filter at 248 nm wavelength. d) Far field transmission spectrum through another MPSi membrane.

Experimental plots given in Figs. 2.42c) and 2.42d) illustrate high achievable levels of near- and far- field transmission efficiency. One can see that in the deep UV (300 nm and below) over 35 % far field transmission and up to 90 % near field transmission are possible.

The effect of the dielectric multilayer pore wall coating on the transmission spectrum of the MPSi membrane is illustrated in Fig. 2.43. Fig. 2.43a) gives the far field transmission spectra through an MPSi membrane with a 5-layer pore wall coating at different angles of incidence (the plots were scaled), while Fig. 2.43b) gives the result of numerical calculations of such a structure. While the measured and calculated shapes of the curves are fairly close, the width of the experimental peak is lower than that predicted by theory. The explanation for such a discrepancy is fairly simple: in theoretical modeling the refractive indices of pure silicon dioxide and pure silicon nitride were used. However, silicon nitride deposited by LPCVD is not a pure Si_3N_4 , but rather an oxynitride (i.e. mixture of Si_3N_4 and SiO_2). Thus, the refractive index contrast in experimentally obtained multilayer was substantially less than that used in

numerical calculations. It is well known that the width of the Bragg peak is proportional to the refractive index contrast in a multilayer stack, which explains the discrepancy between experiment and theoretical predictions.

Fig. 2.43 not only confirms the major theoretical prediction that transmission through an MPSi membrane can be increased over a wavelength band due to the Bragg reflection phenomenon in pore wall coatings, but also confirms the omnidirectionality of the filters. Such a property is very important for narrow bandpass applications.

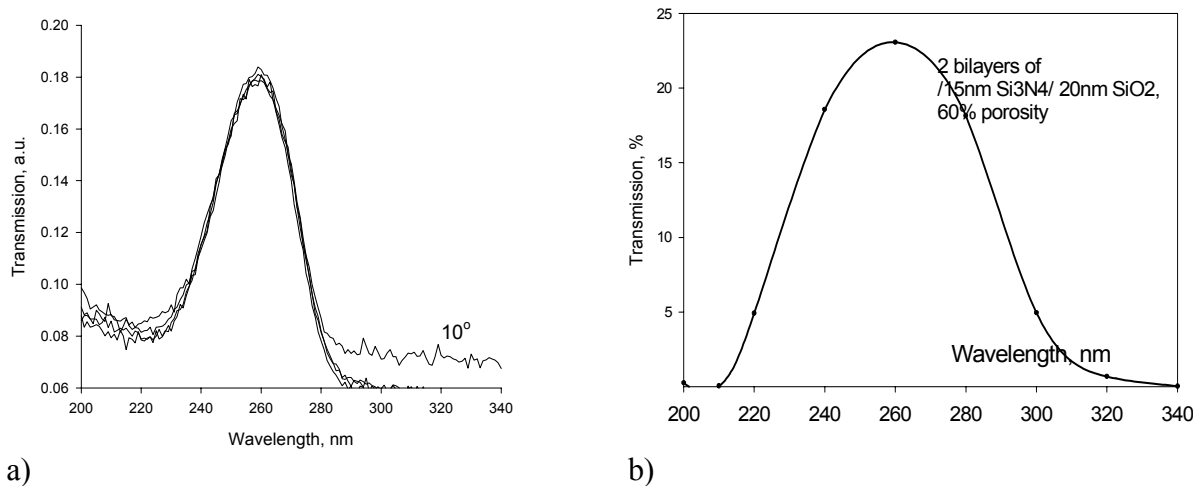


Figure 2.43. a) Far field transmission spectra through an MPSi membrane with a 5-layer SiO₂/Si₃N₄ coating on the pore walls, taken at different angles of incidence and scaled in order to visualize the omnidirectionality of the filter. The 4 curves correspond to angles between 0° and 10°. b) Numerically calculated transmission spectrum through an MPSi membrane with 2 SiO₂/Si₃N₄ bilayers covering the pore walls.

2.8. Polarization Components for the UV Spectral Range

Optical polarization components are used in numerous applications that include photography, liquid crystal displays, polarimetry, astronomy, defense, sensing and photolithography, to name just a few. There are multiple types of polarizers and polarization components currently available. Polarizers based on metal wires, birefringence in crystals and on specially designed dielectric multilayers are among the widest spread (although the variety of known polarizers is by no means limited to these technologies). While polarizers oriented for the visible and near IR wavelengths ranges perform well, that is not the situation in the UV, especially for deep and far UV. Inexpensive plastic polarizers, e.g., are not useable at UV wavelengths since the plastics are not sufficiently transparent. The high-end UV polarizers (such as those based on birefringence (Glan-Thompson) or on multilayers (cube beam-splitters)) are more expensive than the same types designed for the visible and near IR range. In addition, their performance degrades substantially at the shorter wavelengths of light. For example, deep UV polarizers designed to work at 248 nm offer just an extinction of 100-1000, compared to 100,000 for visible polarizers, but demand a high price even for a small working area. In addition, the performance of almost all current types of polarizers capable of performing at deep UV and shorter wavelengths are strongly dependent on the angle of incidence of light on the polarizer. For example, with the tilt of the incident light beam from normal, the extinction de-

grades considerably and/or the preferred polarization may rotate. Far UV polarizers are available only by special order, are extremely expensive and offer fairly poor performance compared to polarizers for the visible spectrum.

Departing from conventional technology, an entirely new concept for a UV optical polarizing material is proposed here that promises solutions to the problems described above. These new polarizers consist of ordered, macroporous silicon (MPSi) with the pore walls covered by dielectric multilayers, similar to the MPSi-based UV filters considered in detail in the previous section of this Chapter. The polarizing behavior in this case originates from the elongated shape of the pores, which provides for the selection of one preferential linear polarization from the transmitted light as described below.

2.8.1. Theoretical Considerations

The MPSi considered so far in this Chapter has either a random structure (as with LWPF) or a symmetrical pore shape (either square or round). Because of this symmetry, the structures did not alter the polarization state of the transmitted beam and were functional only as optical filters. Albeit classical macropores have a circular or quadratic shape, it is possible to generate rectangular slit shapes by arraying the pores in lines combined with a chemical over etch [86]. The so-called Ottow technique [87] allows even to structure porous arrays in arbitrary shapes, but necessitates a complex post-etch structuring process. Recently it was shown [88], that MPSi arrays could be fabricated in a much richer variety of shapes even in a one-step-etch-process, including MPSi arrays with long asymmetrical pores.

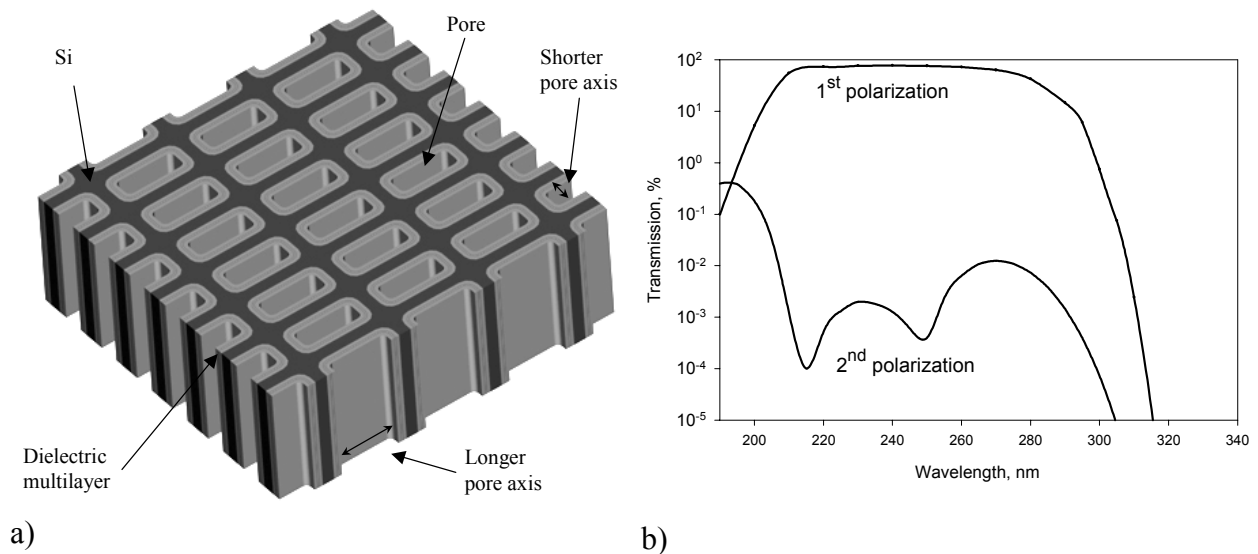


Figure 2.44. a) Schematic drawing of an MPSi-based UV polarizer; b) numerically calculated spectral dependences of the transmission of light with two orthogonal polarizations through an MPSi structure similar to that in a). 1st polarization corresponds to the electric field vector aligned along the longer pore axis, while the 2nd is along the shorter pore axis.

A freestanding MPSi membrane with rectangular or elliptic pores exhibits polarizing behavior in transmission. This behavior originates from the higher propagation losses of the leaky waveguide modes for electric field vectors directed along to the shorter pore axes (see Fig. 2.44a) compared to those of leaky waveguide modes with their electric field vectors directed

along the longer pore axis. This statement can be supported by an estimation of losses in a waveguide formed by metallic-like boundaries surrounding a dielectric core (e.g. vacuum or other transparent relatively low refractive index material).

The theoretical treatment of such a material is quite similar to that in the previous section. Denoting the length of the longer pore axis with a and the length of the shorter pore axis with b , it follows that at short wavelengths ($\lambda < 294$ nm) the difference in the loss coefficients of the modes polarized along the shorter and longer pore axes can be estimated from formula (2.9) as

$$\Delta\alpha \approx (N+1)^2 \lambda^2 \frac{n}{n^2 + \kappa^2} \left(\frac{1}{b^3} - \frac{1}{a^3} \right). \quad (2.17)$$

Similarly, in the wavelength range $\lambda > 294$ nm, from Eq (2.10) it follows that

$$\Delta\alpha \approx (N+1)^2 \lambda^2 \frac{1}{\sqrt{n^2 - 1}} \left(\frac{1}{b^3} - \frac{1}{a^3} \right) \quad (2.18)$$

Both equations (2.17) and (2.18) predict a strong increase in the polarizing behavior of the MPSi layer with the increase of the difference in the length of the pore axis, number of the mode and the wavelength. However, it should be noted that equations (2.17) and (2.18) are limited by the loss coefficient of the TM mode, which is generally considerably larger than that of TE. This manifests itself in a saturation of the anisotropy at some specific value of the difference in pore axis $a - b$. The important property of an MPSi membrane with elongated pores is the exponential increase of the extinction (defined as usual as the ratio of the transmittances for the two orthogonal polarizations) with the depth of the pores. Hence, high extinction is possible for deep pores over a wide wavelength range, including far UV.

An important factor that affects the applicability of the polarizing material to real applications is not only the extinction but also the transmission of the preferred polarization. Hence, not only $\Delta\alpha$ is of importance, but also $\Delta\alpha/\alpha$. For realistic values of the pore parameters for uncoated MPSi layers, this ratio is limited to about an order of magnitude, meaning that it is impossible to achieve high levels of extinction (in excess of 1000) at reasonable levels of transmission of the preferred polarization. This problem can be solved by applying once more a dielectric multilayer coating to the pore walls, as in the UV filters discussed in the previous section of this Chapter. A schematic drawing of such an MPSi-based polarizer is given in Fig. 2.44a). It consists of a freestanding MPSi membrane with elliptical or rectangular pores coated with a dielectric multilayer having a specially designed structure. Fig. 2.44b) gives a numerically calculated plot of the transmission spectral dependences through a 200 micrometer thick MPSi layer, as described below. In this example, the pores were assumed to have 1.3 x 0.7 micrometer cross-sections and a 5-layer coating on the walls. The coating had the following structure: {Silicon pore wall/10 nm SiO₂/33 nm Si₃N₄/ 60 nm SiO₂/ 41 nm Si₃N₄/ 95 nm SiO₂}. As can be observed from theory, a wavelength band of over 80 nm is predicted with better than 5000:1 extinction between orthogonal polarizations of the transmitted light while a high level of transmission for the preferred polarization (in excess of 50 %) is still preserved. It should be noted that the center wavelength of the band could be tuned over a wide range (through the far UV to near IR spectral ranges) by scaling the dimensions of the pores and tuning the structure of the multilayer coating on the pore walls. The extinction of

the polarized material can also be increased by either increasing the aspect ratio of the pores or by increasing the number of layers on the pore walls.

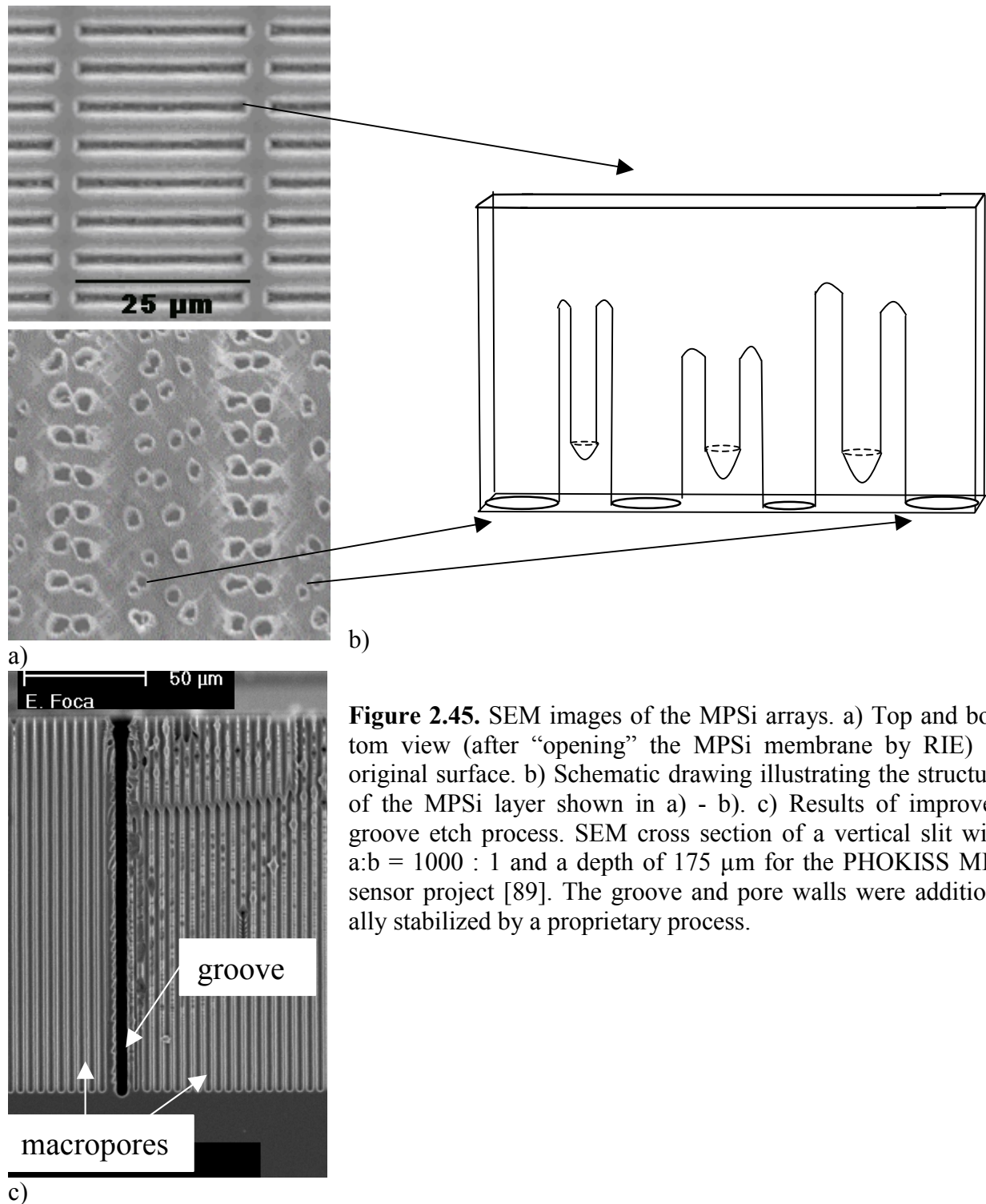


Figure 2.45. SEM images of the MPSi arrays. a) Top and bottom view (after “opening” the MPSi membrane by RIE) of original surface. b) Schematic drawing illustrating the structure of the MPSi layer shown in a) - b). c) Results of improved groove etch process. SEM cross section of a vertical slit with $a:b = 1000 : 1$ and a depth of $175 \mu\text{m}$ for the PHOKISS MIR sensor project [89]. The groove and pore walls were additionally stabilized by a proprietary process.

For optical demonstration of the polarization behavior, an MPSi membrane with elongated pores was made. The fabrication of the random MPSi array is essentially similar to that reviewed in detail in previously except that the etch pits that were intentionally made with an elongated shape. The SEM image of the surfaces of MPSi layer used for optical testing is given in Fig. 2.45. It should be noted that the design goal (see Fig. 2.44a) was not met yet and

more optimization of the electrochemical etching process is required. The pore structure of the sample that was fabricated looks like that shown schematically in Fig. 2.45c). Meanwhile, in the framework of the German BMBF research project “Phokiss”, established to develop a novel MIR gas sensor, deep elongated groove etching has been further improved, in the context to develop a superior coupling facet to a photonic crystal. While grooves normally decompose after etching of some ten microns into individual pores (cf. [88]), an optimized process makes it possible to etch well-defined grooves up to depths of 170 microns and more.

2.8.2. Optical Testing

To prove the theoretical predictions, MPSi membranes (oxidized and uncoated) were tested in a VARIAN CARY 500 UV-VIS-near IR spectrophotometer. A commercial polarizer in the visible was used to analyze the polarization. Fig. 2.46a) shows transmission spectra of the uncoated MPSi membrane for two states of polarization of the incident light. It should be noted that the nonuniformity of the transmission for each polarization (“peaks” at ~300 nm and ~400 nm) are caused by the spectral non-uniformity of the extinction of the commercial polarizer. The spectral dependence of the extinction of this sample is given in Fig. 2.46b). One can see that the sample indeed showed some polarization behavior, as predicted by theory. Another conclusion that can be made from Fig. 2.46b) is that the extinction of the MPSi membrane increases with the wavelength approximately parabolically, in agreement with theoretical predictions.

Fig. 2.46c) shows the transmission spectra of the same MPSi membrane, but with a thin layer of SiO₂ grown on the pore walls by thermal oxidation for two states of polarization of the incident light. The spectral dependence of the extinction in this case is given in Fig. 2.46d). The transmission peaks and valleys due to the oxide presence on the pore walls are masked by much stronger spectral variations of the commercial polarizer. However, the oxide on the pore walls manifests itself as a strong peak of the extinction centered ~350 nm. Hence, it may be concluded that the theoretically predicted enhancement of the extinction due to dielectric coating of the pore walls was demonstrated.

The experimentally achieved values of extinction for the MPSi-based polarization component were far less spectacular than those predicted by theory. This is well understandable, however, since the quality of the tested MPSi layer was quite far from the design goals and in reality only the upper part of the sample was responsible for obtaining the polarization properties.

It should be also noted that the deep and far UV polarizing properties of the material weren’t tested due to the absence of a reference polarizer with both good transmission and good extinction within these spectral ranges. The commercial polarizer used showed a transmission cut-off at about the 260 nm wavelength. However, since the experimental results confirm the main predictions of the theory, good polarizing properties of better quality MPSi material in the deep and far UV ranges can be expected.

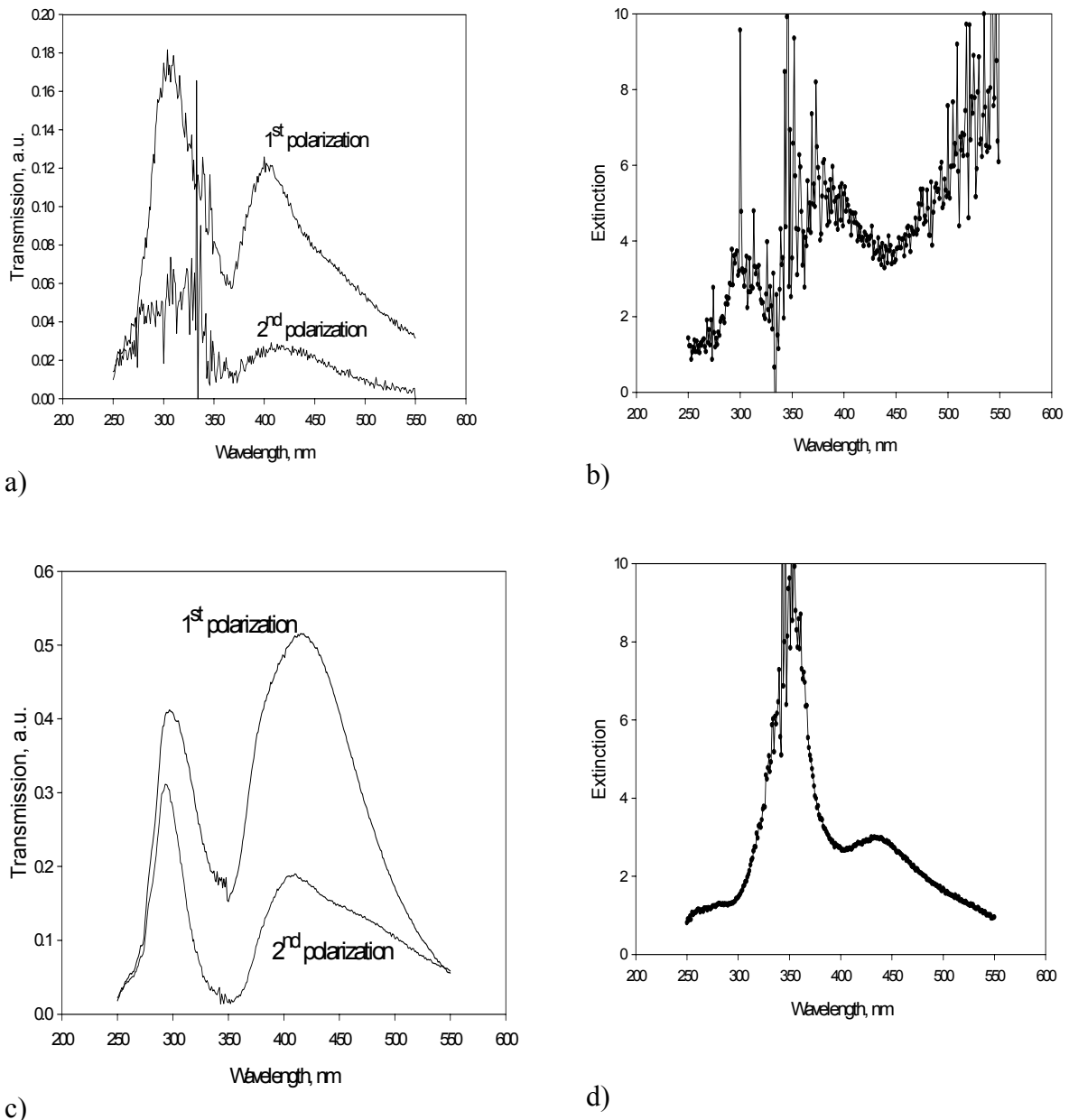


Figure 2.46. a) Transmission spectra of an uncoated MPSi membrane for two states of polarization of incident light (notations are the same as introduced regarding Fig. 2.44a). b) Spectral dependence of the extinction of the same sample as in a). c) Transmission spectra of the MPSi membrane with a thin layer of SiO₂ grown on the pore walls for two states of polarization of incident light. d) Spectral dependence of the extinction of the same sample as in c).

2.9. Retroreflection Suppression Plate

Infrared sensors have been called "the eyes of the digital battlefield" [90]. Military applications dominate the requirements today, especially for IRFPAs (infrared focal plane arrays, which are optical sensors placed at the focal plane of an IR optical system such as a camera, night vision system or night gun sight). In addition to the many military applications for IR

systems such as target acquisition, search and track and missile seeker guidance, there is also great potential for IR systems in the commercial marketplace. IR systems can enhance automobile and aircraft safety, medical diagnosis and manufacturing quality and control. Uncooled long wavelength infrared range (LWIR) FPA's, i.e. those not requiring cryogenic cooling equipment, have enjoyed significant recent advances, making them lighter, simpler and easier to install and maintain. These sensors are now being considered for many "Future Combat System" platforms to meet target acquisition, navigation and surveillance requirements. However, the reflectivity of current uncooled LWIR sensor technology is unacceptably high due to high refractive index semiconductors used in the FPA: If they are used in an otherwise "invisible" airplane, they can be seen, e.g. by CW search lasers as illustrated in Fig. 2.47a). In military applications it is therefore very important to minimize the signature of sensors in certain wavelength regions without compromising performance. Thus, it is highly desirable to reduce the reflectivity of uncooled imaging sensors.

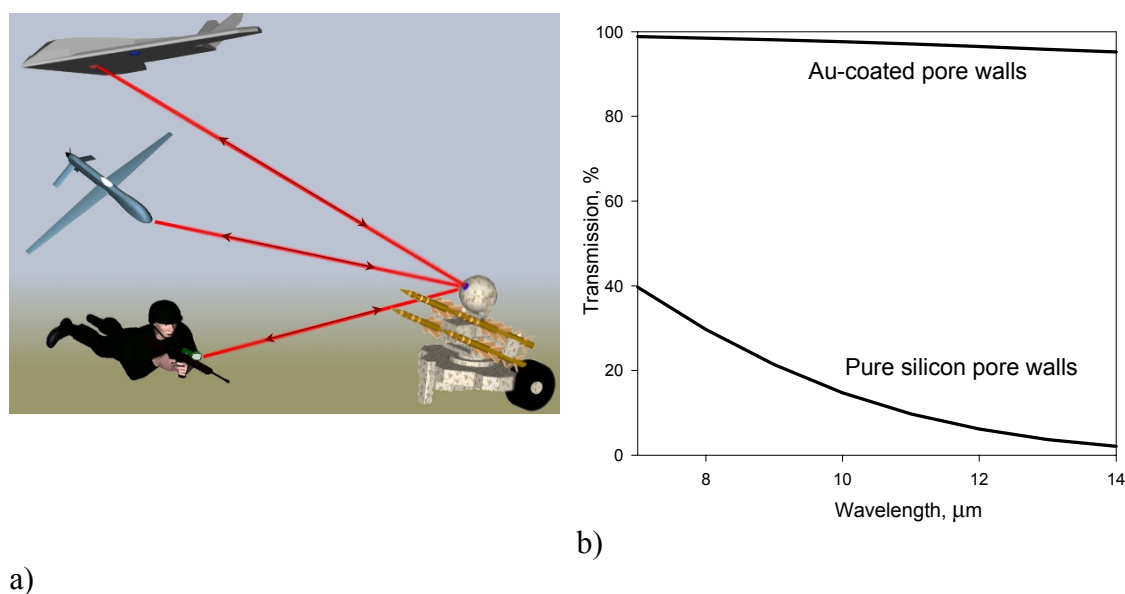


Figure 2.47. a) Schematic drawing illustrating the possible detection of friendly forces by an enemy vehicle employing laser scanning because of uncooled LWIR FPAs. b) Numerically calculated near-field transmission (corrected for porosity) through a 500 μm-thick MPSi layer having pore diameters of 20 μm. Cases for pure silicon MPSi and for a 200 nm-thick layer of gold uniformly covering the pore walls are shown.

This goal can be accomplished by several approaches. For example, the angle of incidence of the incoming radiation may be diverted optically so as to minimize the retroreflection, or the incoming image may be modified by use of optical or image processing techniques to render it out of focus, followed by re-imaging for display. Both of these approaches may provide sufficient results, but the former requires additional optics and a longer light path, thus making the FPA optical system bigger, heavier and more complex, while the latter has the disadvantage of leading to a decrease of the FPA's resolution and lengthens the time for signal processing. A third method to accomplish the suppression of retroreflection from an FPA is to place a special retroreflection suppression plate in the vicinity of the FPA surface, which will not disturb the image transmission in the direction towards the FPA, but will strongly and uniformly scatter all the retroreflected light. The last method will be reviewed here.

The severe difference between the far- and near-field transmission efficiencies occurring while transmitting through random MPSi arrays in the leaky waveguide transmission mode (as reviewed in Section 2.8) is the basis of the method discussed here for the suppression of retroreflection. If a LWIR FPA is placed into the near field of a random MPSi array (as shown in Fig. 2.48a), the light incident on the upper surface of the MPSi plate will be mostly transmitted through massively parallel leaky waveguides to the FPA array, while light retroreflected from the FPA array will be scattered during reemission from the non-coherent (disordered) leaky waveguides. Thus the retroreflection will be effectively suppressed. The main difference between this retroreflection suppression plate design and prior art light diffusing elements is that the coupling of light into such a plate does not introduce any scattering, only the outcoupling does. This is true no matter from which side of the plate light is incident because the reflection from the plate itself is minimal and no scattered light is transmitted through the plate. For example, if a prior art diffuser (such as described in [91] and references therein) were to be used instead of an MPSi-based plate, the scattering at the upper surface of the diffuser would erase or strongly blur the image (assuming the thickness of the diffuser exceeded the FPA pixel-to-pixel distance). Another important advantage of the proposed retroreflection suppression plate is the wide range of angles and wavelengths over which it suppresses retroreflection.

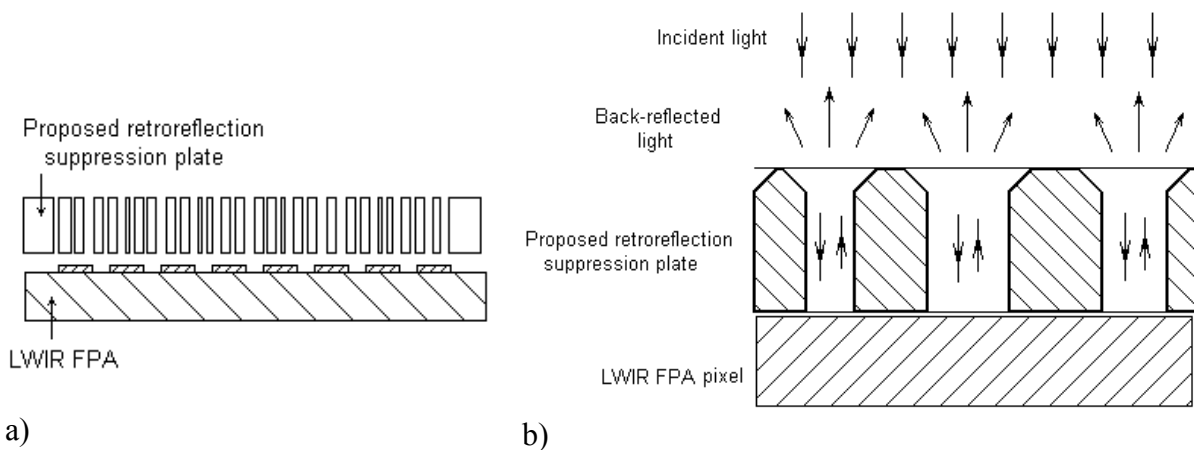


Figure 2.48. Reduction of the retroreflection from uncooled LWIR FPA with the help of a MPSi membrane: a) A random free-standing MPSi layer is placed on the top of LWIR FPA in near-field; b) the same assembly magnified showing schematically the path of light rays.

2.9.1. Theoretical Considerations

To maximize the performance of MPSi-based retroreflection suppression plates, the following conditions should be satisfied:

- i) The near-field transmission efficiency should be maximized.
- ii) The retroreflection suppression should be maximized (i.e., the far-field transmission should be minimized for a wide range of angles and wavelengths).
- iii) The image captured by the FPA should be not distorted.

In order to design the retroreflection suppression plate one has to define first the spectral band of interest (i.e. wavelengths at which the retroreflection needs to be suppressed while the near field transmission have to be maintained at high levels). Since the leaky waveguide mode of

transmission through the MPSi layer has to be utilized, the results of the theory presented in section 2.8 will be used. Let's, for example, estimate the pore dimensions and other MPSi layer properties that would provide an optimized performance in the 8 to 12.5 μm long wavelength infrared range (LWIR, according to US military specifications). As was shown in Section 2.8, both the 3dB cut-off and 20dB rejection wavelengths of uncoated MPSi arrays used in leaky waveguide modes scale proportionally to $d\sqrt{d/L}$ (where d is the diameter of the pore and L is the length of the pore). This means that for the LWIR range and an MPSi thickness of 500-700 μm (common thickness of silicon wafers as supplied by vendors), the pore diameter d should be around 30 μm . However, such large pores present a considerable challenge in fabrication. Fortunately, the transparency range of the MPSi layer may be enlarged and the transmission efficiency within the transparency range may be improved while keeping the pore sizes at more reasonable levels if a thin metal coating is introduced into the pore walls. This is illustrated by Fig. 2.47b) where the numerically calculated near-field transmission (corrected for porosity) through a 500 μm -thick MPSi layer is shown for uncoated and coated pores with 20 μm diameter. The feasibility of ALD-coating of the pore walls of an MPSi array with dielectrics was shown in section 2.8, while the feasibility of metal deposition by ALD was shown in a number of references (see e.g., [92]). It is apparent from that an MPSi layer consisting of pores having 20 μm diameters and 200 nm of Au or Ag on the pore walls would satisfy the requirement of the transparency in the 7.5 μm - 12.5 μm wavelength range.

The second point is a combination of two additional conditions: i) low far-field transmission across a wide spectral range (from UV to CO₂ laser wavelengths, since such wavelengths may be employed by the enemy's detection equipment) and ii) low far-field transmission across reasonably wide angles. The condition a) is automatically satisfied if condition b) is satisfied (provided the pore size is smaller than the wavelength of light by at least 5 times). This is the case here since the proposed pores are 20 μm in diameter while the CO₂ wavelength is just 10 μm). The condition ii) basically means that not only long-range order in the pore positions should be avoided, but that short-range order should also be minimized. The latter requirement is necessary to avoid rings of diffracted light, which might be observed by an enemy. Random pores optimized by proper adjustment of the anodization parameters (such as temperature and current during the pore nucleation and reorganization stage) [93] meet these conditions, alternatively specially constructed random arrays of pores, as, e.g. used in [86] may be employed. The first option is preferred since it reduces the number of necessary processing steps.

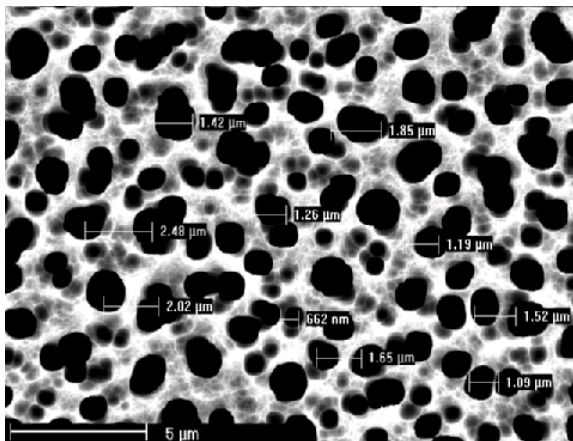


Figure 2.49. SEM image of random pores with neither long nor short range order used for demonstrating retroreflection suppression.

For optical demonstration of the retroreflection suppression an MPSi membrane with parameters suitable for retroreflection suppression in the UV spectral range was made. The fabrication of the random MPSi array is essentially similar to that reviewed previously in this chapter and will not be repeated here. The SEM image of the top surface of MPSi layer used for optical testing is given in Fig. 2.49.

2.9.2. Optical Testing

For the demonstration of the retroreflection suppression the fabricated uncoated MPSi membrane shown in Fig. 2.49 was mounted on the surface of an Al mirror and the normal incidence reflection from such a structure was recorded in a spectrometer within the “far” field of 20 cm next to the Al mirror/MPSi membrane surface. The result of the measurement is presented in Fig. 2.50a). One can see that even at 20 cm the retroreflection was suppressed by 5 orders of magnitude. For a comparison, the near field transmission (recorded by mounting the sample directly on a detector in the spectrometer) is also plotted in Fig. 2.50. It should be noted that at realistic distances from the shielded FPA to an enemy detector of over 1 km (in most situations), more than 10 orders of magnitude of retroreflection suppression can be expected. One should note that the reflection was suppressed quite uniformly over the wide spectral range. As explained above, by coating the pore walls with metal the near field transmission can be increased even further.

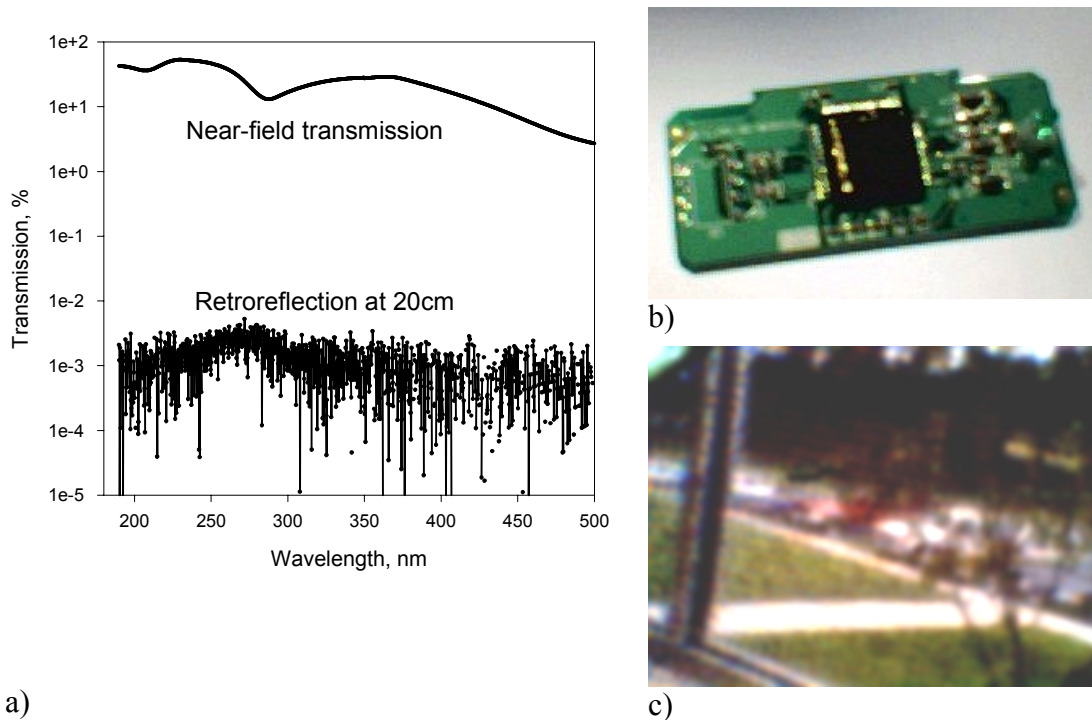


Figure 2.50. a) Spectral dependences of near field and far field retroreflection of the aluminum mirror/MPSi membrane structure. b) Photo of the camera with the MPSi membrane mounted on the top. c) Image of a parking lot obtained with the camera and the MPSi membrane.

In order to investigate the imaging properties of the detector array when used with MPSi retroreflection suppression plate, the MPSi membrane with larger pores (sufficiently large to provide good transmittance in visible spectral range) was mounted on the top of a commercially available CCD camera (as illustrated in Fig. 2.50b). The image of a parking lot obtained

through such a structure is presented in Fig. 2.50c). The (inferior) resolution of the (very cheap) camera could essentially be maintained.

2.10. Discussion and Conclusion

It has been shown that the interaction of light propagating in the direction of the pores with the “metamaterial” porous Si provides for a plethora of interesting phenomena, all of which are useful in the context of advanced optical engineering. If one were to include other geometries, too, as for example light propagation perpendicular to pores in (two-dimensional) photonic crystals or in either direction in homogeneous but optically anisotropic porous Si devices, porous Si can serve as a paragon for an advanced optical meta-material. In particular, porous Si proved to be even useful for photon energies far above the band gap energy of the bulk material.

Since defined pore structures are not limited to Si, but can also be produced (within specific limits) in other semiconductors [11,17,], the potential for novel optical elements is larger yet, including for example, also new features for non-linear optics [28,29].

It has been shown that the existing theoretical framework is sufficient to predict and analyze a large variety of phenomena. That theoretical guidance is needed for the design and production of novel optical elements is clear from what has been presented. Unfortunately, the theory of pore etching is far less clear-cut than that for the optical properties of the devices produced, and this is a major obstacle for the development and production of optical devices.

Many examples in this chapter demonstrated that more progress in pore etching would be essential, be it in the precise control of known and easily produced pore structures, or in the ability to etch structures not easily obtained at all, e.g. deep trenches as outlined in Section 2.8. There is, however, constant and substantial progress in pore etching, and there can be little doubt that all structures discussed in the preceding sections can be made with sufficient precision now or in the near future. The fact that a first product based on porous Si is on the market right now bears testimony to this statement.

A production process has to meet two more conditions: i) reliable electrochemical etching of standard size Si wafers (e.g. with 200 mm diameter) in an automated and tightly controlled way, and ii) suitable (automated) pre- and post-processing processing like lithographical pattern transfer, pore coating, or membrane production. Both conditions have been met in principle: A large-area etcher capable of meeting most if not all requirements is available in the marketplace, and all the other processes mentioned exist, albeit as part of (expensive) clean-room equipment. While it is rather difficult to produce, e.g., the omnidirectional filters introduced in this chapter in a laboratory environment, it would not be an insurmountable problem in a running clean-room facility.

While more work is needed to realize all novel optical devices discussed here, some are hopefully will find applications in the near future, while other (such as long wave pass filters) are already used in industry and research institutions internationally.

Chapter III

Effective Medium Approach for Calculations of Linear and Nonlinear Optical Properties of Porous Semiconductor Materials

3.1. Introduction

Engineering the optical properties of a given material by suitable modifications of its structure is a very attractive area of science and technology. Porous semiconductor materials (see, for example, [11] and references therein) are important cases of such structured “metamaterials”. Semiconductors are usually turned porous by electrochemical (or photoelectrochemical) etching of the nonporous semiconductor substrates in some suitable electrolytes. To date, it has been shown that many types of semiconductors can be made in a porous form by this method. The most popular example is porous silicon, which allows tailoring the pore geometry from micropores, via mesopores to macropores. Electrochemically etched pores have also been obtained in Ge and III-V compound semiconductors, e.g. InP, GaP, GaAs, GaN; and porous layers with many kinds of morphologies could be demonstrated [11]. The usefulness of such materials for various optical components was already outlined in [18, 40, 94]. In most cases the research has been devoted to the isotropic properties of porous semiconductors. However, recently it has been shown [18-21, 39] that mesoporous silicon obtained from a (110) oriented substrate offers optical anisotropy properties that may be of practical importance. A remarkable result is that in the infrared spectral range such a metamaterial offers larger values of optical birefringence than that of any commonly known natural material. Further, the combination of the value of the birefringence in the mid to far infrared range with the transparency of these materials at the wavelengths mentioned makes these findings even more attractive for possible applications and theoretical studies.

In this chapter I will present the modified effective medium formalism for calculation of linear and nonlinear optical properties of porous semiconductors and composites based on porous semiconductors. First, the modification of the Maxwell-Garnett (MG) approach will be developed to evaluate linear optical properties of mesoporous silicon etched on (110)-oriented substrate and porous Ge and III-V compound semiconductors. Then, based on the qualitative predictions of the MG-based approach, the modification of the Bruggeman effective medium theory will be developed and applied to the optical anisotropy of metal-filled mesoporous silicon etched on (110) oriented substrate. Finally, a formalism of qualitative evaluation of nonlinear optical effects (second harmonic generation in particular) in porous semiconductors will be presented.

3.2. Effective Optical Properties of Porous Semiconductor Materials

The method presented in this chapter provides answers to the following questions: What other porous materials besides already investigated mesoporous silicon etched on (110)-oriented substrate can offer optical anisotropy? What kind of optical anisotropy can be expected from different porous materials? How can this anisotropy be controlled by material parameters (such as the porosity of materials, crystal orientation of the substrate, etc.)? In addition, the theoretical method developed here could help to obtain a more direct understanding of the optical effects, which is clearly lacking so far.

A method will be presented for calculating the effective dielectric constants and refractive indices of different porous materials. This method will be applied to several materials already successfully fabricated by an electrochemical etching process of various semiconductors. Previously [18-21], a somewhat generalized Bruggeman “Effective Medium Approach” (EMA [14] was used for calculations of the optical effects in these materials. However, while this generalization of the EMA provides fair estimates for mesoporous (110)-oriented Si, is not applicable for more complex structures, e.g. multiple pore lattices, or for materials containing pores with noncircular cross sections. Moreover, even for the case of mesoporous silicon, which consists of a network of pores with circular cross sections growing in some preferential directions, the referenced generalization of the Bruggeman method was not sufficient to provide a full and correct explanation for some of the observed effects. The so-called Looyenga formulation [37] was also applied to calculations of effective dielectric constants of porous silicon [95], however, this method is not applicable to the case of anisotropic media (it would at least need some modification). In contrast, the method presented in this Chapter has the capability to analyze such structures in a relatively simple fashion. The porous semiconductor medium is treated as macroscopically homogeneous and is assigned a dielectric permittivity tensor. Effective dielectric permittivity tensor elements depend on the dielectric constant of the semiconductor host, the dielectric constants of pore-filling materials, and the pore shape, orientation and filling fraction (porosity).

3.3. Effective Permittivity Tensor Calculations

In order to implement the effective medium approximation, several assumptions have to be made, which also indicate the limitations of the model presented here. First, pores are represented by “air voids”; e.g. by air-filled cavities with elongated elliptical shapes; cf. Fig. 3.1. Second, it is assumed that these air voids are uniformly and randomly distributed in the semiconductor material such that the air voids belonging to one of M lattice subsets have their axes essentially parallel to each other. Third, it is assumed that the bulk semiconductor material is isotropic and has a relative dielectric permittivity ϵ_B . Next, it is assumed that neighboring pores or air holes, respectively, affect each other only through the depolarization factor. This is a strong assumption that limits the validity of the method to relatively small porosities (an expanded method for calculation of optical properties of some of porous semiconductors with higher porosities will be presented later in this Chapter). It should be noted, however, that while this latest assumption is not strictly correct for some porous semiconductor materials, the accuracy of the approximation presented here is still good enough for a basic understanding of the optical effects taking place in such materials. Finally, it is also assumed that the wavelength of the electromagnetic wave considerably exceeds the cross sectional dimensions of the pores.

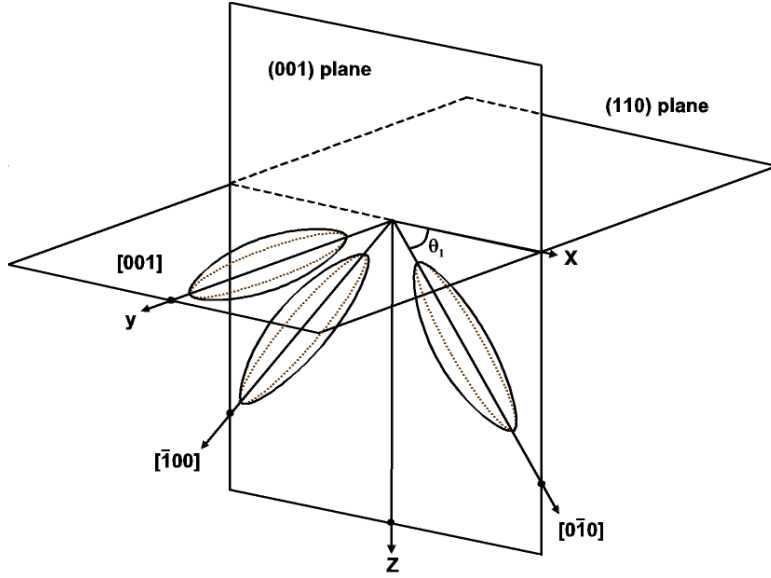


Figure 3.1. Pore structure of the mesoporous silicon grown on (110)-oriented substrate. Orientations of three major pore lattice subsets are shown. A pore would consist of a string of ellipsoids extending in one direction.

An electromagnetic wave with the electric field vector \vec{E} gives rise to a displacement vector \vec{D} in the porous semiconductor material, given by

$$\vec{D} = \epsilon_B \vec{E} + \vec{P} \quad (3.1)$$

where \vec{P} is the effective polarization of all the particles (a pore can always be thought of as a particle in the form of an air void in semiconductor crystal) in a unit volume. With the assumptions as listed above, the porous semiconductor effective dielectric permittivity tensor

$$\hat{\epsilon}^{(eff)} = \begin{pmatrix} \epsilon_{xx}^{(eff)} & \epsilon_{xy}^{(eff)} & \epsilon_{xz}^{(eff)} \\ \epsilon_{yx}^{(eff)} & \epsilon_{yy}^{(eff)} & \epsilon_{yz}^{(eff)} \\ \epsilon_{zx}^{(eff)} & \epsilon_{zy}^{(eff)} & \epsilon_{zz}^{(eff)} \end{pmatrix} \text{ can be defined as follows:}$$

$$\vec{D} = \hat{\epsilon}^{(eff)} \vec{E} \quad (3.2)$$

From (3.1) and (3.2) it follows:

$$\hat{\epsilon}^{(eff)} \vec{E} = \epsilon_B \vec{E} + \vec{P} \quad (3.3)$$

Within the assumptions from above the porous semiconductor material can be considered as an assembly of M electromagnetically separated pore lattice subsets. Hence, the polarization of the porous layer is equal to the vector sum of the polarizations of each lattice subset considered separately, or $\vec{P} = \sum_{i=1}^M \vec{P}^{(i)}$, where $\vec{P}^{(i)}$ is the polarization of the i^{th} lattice subset. In this case (3.3) can be rewritten as:

$$\hat{\epsilon}^{(eff)} \bar{E} = \epsilon_B \bar{E} + \sum_{i=1}^M \bar{P}^{(i)} \quad (3.3a)$$

The polarization of each pore is assumed to be a linear isotropic function of the local electric field of the electromagnetic wave, hence:

$$\bar{P}^{(i)} = N^{(i)} \alpha^{(i)} \bar{E}_L^{(i)} \quad (3.4)$$

$N^{(i)}$ is the density of the pores of the i^{th} lattice subset of porous semiconductor layer, $\alpha^{(i)}$ is the polarizability of a pore in the i^{th} lattice subset, and $\bar{E}_L^{(i)}$ is the local electric field as “seen” by each pore of the i^{th} lattice subset.

The local field $\bar{E}_L^{(i)}$ is given by Yaghjian [96] for arbitrary shaped inclusions as

$$\bar{E}_L^{(i)} = \bar{E} + \frac{\hat{L}^{(i)} \bullet \bar{P}^{(i)}}{\epsilon_B} \quad (3.5)$$

where $\hat{L}^{(i)}$ is the depolarization factor that depends on the shape of the pore; it is a tensor of second rank. Under the assumptions made in the beginning of this section, the polarizability of each pore is a tensor that is always diagonalizable in a coordinate system, in which one

axis coincides with the pore growth direction, i.e., $\hat{\alpha}^{(i)} = \begin{pmatrix} \alpha_{1,1}^{(i)} & 0 & 0 \\ 0 & \alpha_{2,2}^{(i)} & 0 \\ 0 & 0 & \alpha_{3,3}^{(i)} \end{pmatrix}$.

The polarization of the i^{th} lattice subset in the coordinate system associated with said lattice subset then is

$$\tilde{\bar{P}}^{(i)} = \epsilon_B \hat{M}^{(i)} \tilde{\bar{E}}^{(i)} \quad (3.6a)$$

where

$$\hat{M}_{j,j}^{(i)} = \frac{N^{(i)} \alpha_{j,j}^{(i)}}{\epsilon_B - L_{j,j} N^{(i)} \alpha_{j,j}^{(i)}}, j = 1, 2, 3; \text{ and } \hat{M}_{j,k}^{(i)} = 0, \text{ if } j \neq k.$$

$\tilde{\bar{E}}^{(i)}$ is the electric field of the electromagnetic wave in the coordinate system associated with the i^{th} lattice subset. If the coordinate transformation matrix is introduced between the reference coordinate system (which can be associated with the crystallographic axes of the semiconductor host or anything else) and the coordinate system of i^{th} lattice subset

$$\hat{A}^{(i)} = \begin{pmatrix} \cos\psi^{(i)} \cos\phi^{(i)} - \cos\vartheta^{(i)} \sin\psi^{(i)} \sin\phi^{(i)} & -\sin\psi^{(i)} \cos\phi^{(i)} - \cos\vartheta^{(i)} \cos\psi^{(i)} \sin\phi^{(i)} & \sin\vartheta^{(i)} \sin\phi^{(i)} \\ \cos\psi^{(i)} \sin\phi^{(i)} + \cos\vartheta^{(i)} \sin\psi^{(i)} \cos\phi^{(i)} & -\sin\psi^{(i)} \sin\phi^{(i)} + \cos\vartheta^{(i)} \cos\psi^{(i)} \cos\phi^{(i)} & -\sin\vartheta^{(i)} \cos\phi^{(i)} \\ \sin\vartheta^{(i)} \sin\psi^{(i)} & \sin\vartheta^{(i)} \cos\psi^{(i)} & \cos\vartheta^{(i)} \end{pmatrix}$$

where ϕ, ψ and θ are Euler angles, the relations $\tilde{\bar{E}}^{(i)} = \hat{A}^{(i)-1} \bar{E}$ and $\bar{P}^{(i)} = \hat{A}^{(i)} \tilde{\bar{P}}^{(i)}$ hold where \bar{E} and $\bar{P}^{(i)}$ are in the main coordinate system. Hence

$$\vec{P}^{(i)} = \epsilon_{mp} \hat{A}^{(i)} \hat{M}^{(i)} \hat{A}^{(i)-1} \vec{E} \quad (3.6b)$$

By substituting (3.6) into (3.3a) the effective dielectric permittivity tensor of the porous semiconductor layer is obtained as

$$\hat{\epsilon}^{(eff)} = \epsilon_B \left[\hat{I} + \sum_{i=1}^M \hat{A}^{(i)} \hat{M}^{(i)} \hat{A}^{(i)-1} \right] \quad (3.7)$$

where $\hat{I}_{i,j} = \delta_{i,j}$.

The polarizability tensor $\hat{\alpha}$ and, in principle, the depolarization tensor \hat{L} of individual pores, need to be calculated numerically for the particular pore shape. In [97] the internal field approach combined with Finite Element Method (FEM) has been implemented to find the polarizability tensor elements for circular, square, rectangular and triangular shape of the inclusions and here this approach will be followed.

According to the assumptions listed in the beginning of this section, the pore cross section is assumed to be much less than the wavelength of electromagnetic wave (quasi-static approximation). The internal field approach, in which the polarizability is obtained by determining the internal field of the pore, is used so the dipole moment \vec{d} of the air-filled pore in semiconductor material is calculated as

$$\vec{d} = \int_V (1 - \epsilon_B) \vec{E} dV \quad (3.8)$$

and the integration is carried out only within the volume of the pore.

From another point of view, the dipole moment \vec{d} is defined as the product of the polarizability α and the local field \vec{E}_L . Since it was assumed that the pores are electromagnetically separate, the approximation of a single pore in an infinite medium is accurate enough and, by using the results presented in [98], the dipole moment can be written as:

$$\vec{d} = (1 - \epsilon_B) V \frac{\int \vec{E}_{INT} dV}{V} \quad (3.9)$$

where the internal electric field is integrated within the pore. In the dipole approximation, the electric field vector in the pore has x-, y-, z-components, but its integral over the volume of the pore will have only a component for symmetric pores aligned with respect to the electric field. Let's define β as integral of the internal electric field over the pore volume divided by

said volume and the external field: $\beta_i = \frac{\int (\vec{E}_{INT} \cdot \vec{n}_i) dv}{V \cdot |\vec{E}_{EXT}|}$, where \vec{n}_i is a unit vector collinear to

i^{th} coordinate axis direction. In the case of electric field alignment along the Cartesian direction j , the dipole moment can be written as:

$$d_j = (1 - \varepsilon_B)V \beta_j \vec{E}_{EXT,j} \quad (3.10)$$

The integral β is thus independent on both pore volume and the external electric field of the electromagnetic wave. It can be determined either numerically or analytically. Replacing α_i in (3.7) by $(1-\varepsilon_B)V \beta_i$, the final expression of the dielectric permittivity tensor of porous semiconductor material will be

$$\hat{\mathcal{E}}^{(eff)} = \varepsilon_B \hat{I} + \sum_{i=1}^M \hat{A}^{(i)} \left[\begin{array}{ccc} \frac{f_i(1-\varepsilon_B)\beta_1^{(i)}}{\varepsilon_B - L_{11}f_i(1-\varepsilon_B)\beta_1^{(i)}} & 0 & 0 \\ 0 & \frac{f_i(1-\varepsilon_B)\beta_2^{(i)}}{\varepsilon_B - L_{22}f_i(1-\varepsilon_B)\beta_2^{(i)}} & 0 \\ 0 & 0 & \frac{f_i(1-\varepsilon_B)\beta_3^{(i)}}{\varepsilon_B - L_{33}f_i(1-\varepsilon_B)\beta_3^{(i)}} \end{array} \right] \hat{A}^{(i)-1} \quad (3.11)$$

where f_i is the ‘‘porosity’’ of the i^{th} pore lattice, and $\sum_{i=1}^M f_i = p$, $0 < p < 1$, where p is the total porosity of the porous semiconductor layer.

3.4. (110)-oriented Si Containing Mesopores

The method developed above is first applied to analyze the optical effects on mesoporous Si, which can be formed by an electrochemical etching process on (otherwise unusual) (110)-oriented silicon substrates. This porous material has been obtained recently [19] and was intensively investigated with regard to its optical properties (see, for example, [18-21, 39]). Particularly, strong in-plane birefringence (i.e. optical anisotropy) of such layers has been observed for IR wavelengths. These experimental findings were the basis for several proposed photonic devices based on such a material. For example, dichroic Bragg reflectors have been realized by Diener et al. [18], while optical polarizers have been reported in [21] and [39].

The optical anisotropy of mesoporous silicon fabricated on (110)-oriented substrates has been explained in [19] by different filling fractions of layers in different directions (i.e., anisotropic porosity). Similar arguments have been presented in [18] to explain the different values of birefringence (i.e. optical anisotropy). In particular, the difference of the porosity in different directions ([001] and $[\bar{1}\bar{1}0]$ crystallographic directions particularly) is proportional to the etching current during mesoporous silicon formation, i.e., proportional to the overall porosity of the sample. Drawing on the formalism developed in the previous section, let’s follow a different approach towards a better understanding of the optical anisotropy in mesoporous Si formed on (110)-oriented substrates, which appears to match the experimental results better than the explanation given in [18].

In order to apply the model developed in the previous paragraph, the structure of the mesoporous silicon layer grown on (110) substrate has to be identified first. As was shown in

[99], pores in mesoporous Si propagate preferentially in equivalent $\langle 100 \rangle$ crystallographic directions independently of the substrate orientation. Hence, it can be represented as a mixture of three lattice subsets of pores collinear to the crystallographic directions mentioned. However, not all $\langle 100 \rangle$ directions are equivalent; $\langle 100 \rangle$ directions more in line with the electrical field are preferred. This is certainly due to the fact that the electric field strength at the tip then is enlarged, enabling avalanche breakdown [100] and enhancing the electrochemical dissolution reaction at the pore tip.

The three pore lattice subsets found in mesoporous silicon grown on (110) wafers are approximated by a suitable distribution of ellipsoids as shown in Figure 3.1. For such a material the $[\bar{1}00]$ and $[0\bar{1}0]$ pore directions are equivalent since they have identical projections in the direction of the current flow. The $[001]$ direction, however, is perpendicular to the applied current direction, since it lies in (110) crystallographic plane.

In the presented analysis it is thus assumed that the pores in each lattice can be represented as distribution of ellipsoids, which are elongated in the direction of each pore lattice. Such an assumption is in agreement with extensive XRD investigations of different porous layers presented in [101]. In this case equation (3.11) takes the following form:

$$\hat{\epsilon}^{(eff)} = \epsilon_{Si} \left[\hat{I} + \sum_{i=1}^3 \hat{A}^{(i)} \hat{M}^{(i)} \hat{A}^{(i)-1} \right] \quad (3.12)$$

The pore lattices collinear to the $[0\bar{1}0]$, $[\bar{1}00]$, and $[001]$ crystallographic directions have been assigned the index (1), (2), and (3); respectively. It is further assumed that the individual pores represented by ellipsoids are of the same shape and volume, however, the filling fraction of the pores of the first and second pore lattices exceeds that of the third pore lattice due to the current flow direction, i.e., $f^{(1)} = f^{(2)}$ and $f^{(3)} < f^{(1)}$. With this assumption, the depolarization factors and the polarizabilities for each pore lattice are the same.

Let's introduce the local pore lattice coordinate system such that the x-axis is parallel to the pore lattice direction and the y-axis lies in the (110) plane. The depolarization factor for the longer axis of the ellipsoid L_{11} depends on the ratio $x = c/a$ ($a > b = c$) between the axes lengths as (see [102]):

$$L_{11} = \frac{x^2}{(1-x^2)^{3/2}} \left[\text{arcth}(\sqrt{1-x^2}) - \sqrt{1-x^2} \right] \quad (3.13)$$

Due to the circular cross section of the pores in mesoporous Si, $L_{22} = L_{33} = (1 - L_{11})/2$.

If the reference coordinate system is introduced as shown in Fig. 3.1 (X-axis is directed in the $[\bar{1}\bar{1}0]$ direction and Y-axis in $[001]$), the coordinate transformation matrices will be as follows:

$$\hat{A}^{(1)} = \begin{pmatrix} \frac{\sqrt{2}}{2} & 0 & -\frac{\sqrt{2}}{2} \\ 0 & 1 & 0 \\ \frac{\sqrt{2}}{2} & 0 & \frac{\sqrt{2}}{2} \end{pmatrix}, \hat{A}^{(2)} = \begin{pmatrix} -\frac{\sqrt{2}}{2} & 0 & \frac{\sqrt{2}}{2} \\ 0 & -1 & 0 \\ \frac{\sqrt{2}}{2} & 0 & \frac{\sqrt{2}}{2} \end{pmatrix}, \hat{A}^{(3)} = \begin{pmatrix} 0 & 1 & 0 \\ -1 & 0 & 0 \\ 0 & 0 & 1 \end{pmatrix}$$

If the porosity of the mesoporous silicon layer is p and a coefficient r is introduced to describe the ratio of filling fractions between the [001] pore lattice and other lattices, the electrical polarization matrices for each lattice will be as follows:

$$M_{1,1}^{(1)} = M_{1,1}^{(2)} = \frac{(p-p \cdot r)(1-\epsilon_{Si})\beta_1}{2\epsilon_{Si} - L_{11}(p-p \cdot r)(1-\epsilon_{Si})\beta_1},$$

$$M_{2,2}^{(1)} = M_{2,2}^{(2)} = M_{3,3}^{(1)} = M_{3,3}^{(2)} = \frac{2(p-p \cdot r)(1-\epsilon_{Si})\beta_2}{4\epsilon_{Si} - (1-L_{11})(p-p \cdot r)(1-\epsilon_{Si})\beta_2}$$

$$M_{1,1}^{(3)} = \frac{p \cdot r \cdot (1-\epsilon_{Si})\beta_1}{\epsilon_{Si} - L_{11} \cdot p \cdot r \cdot (1-\epsilon_{Si})\beta_1}, \quad M_{2,2}^{(3)} = M_{3,3}^{(3)} = \frac{2p \cdot r \cdot (1-\epsilon_{Si})\beta_2}{2\epsilon_{Si} - (1-L_{11}) \cdot p \cdot r \cdot (1-\epsilon_{Si})\beta_2}$$

The values of the coefficients β_1 and β_2 according to [102] are:

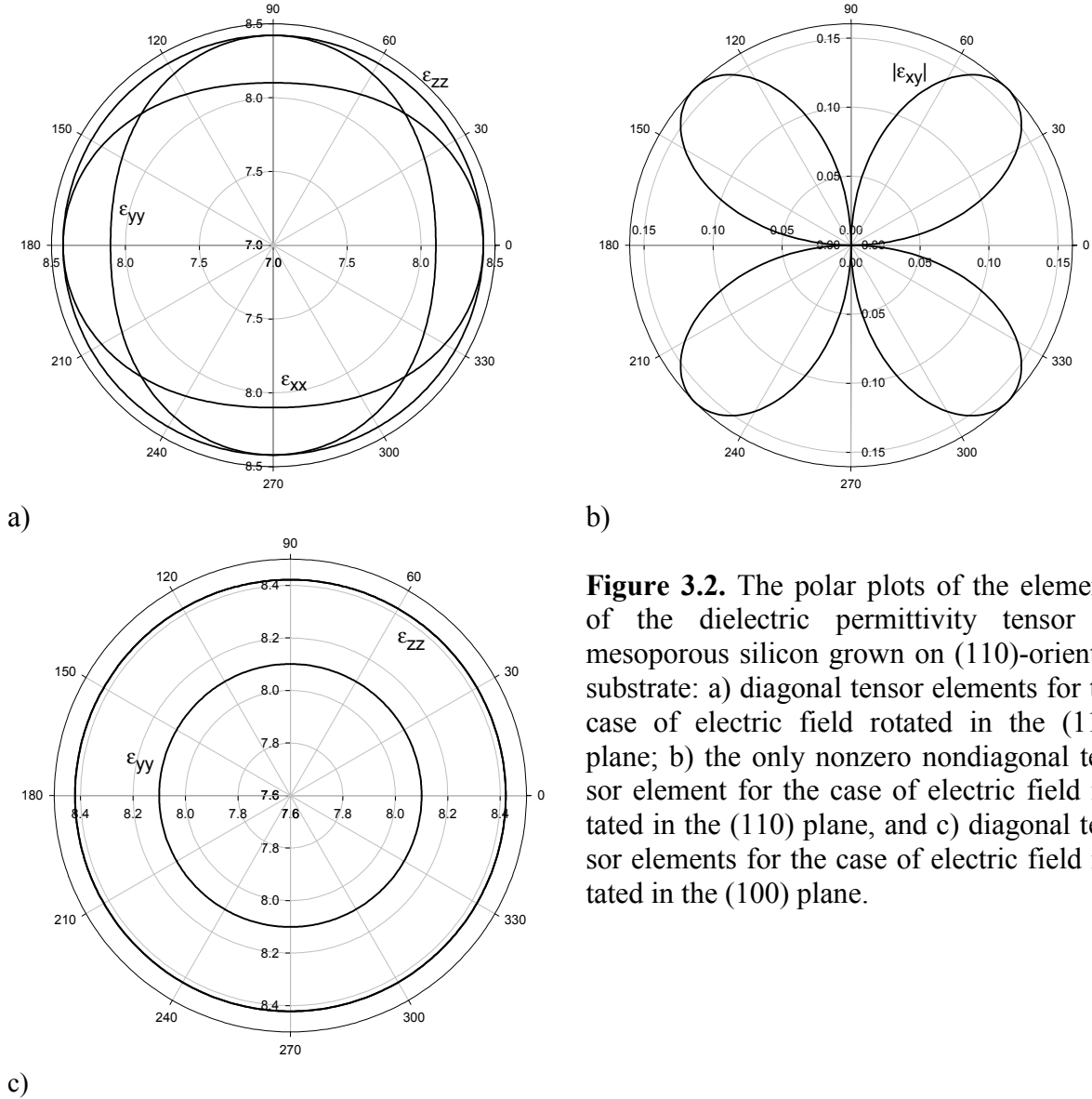
$$\beta_1 = \frac{\epsilon_{Si}}{\epsilon_{Si} - (\epsilon_{Si} - 1) \cdot L_{11}} \quad \beta_2 = \frac{\epsilon_{Si}}{\epsilon_{Si} - (\epsilon_{Si} - 1) \cdot L_{22}} = \frac{2\epsilon_{Si}}{2\epsilon_{Si} - (\epsilon_{Si} - 1) \cdot (1 - L_{11})}$$

Let's now determine the dielectric properties of mesoporous silicon layer grown on (110) substrate for the following assumptions: the overall porosity is 25 %, the aspect ratio of the pore ellipsoids is 0.5 (i.e. longer axis of the ellipsoid is twice longer than other two axes), and the parameter r is 0.1. The refractive index of Si is assumed to be 3.5 with zero imaginary part (which is true for wavelengths exceeding the band edge of Si around 1100 nm and smaller than free carrier absorption edge). Substituting the parameters into (3.12) gives the following value of the dielectric permittivity tensor in the coordinate system as shown in Fig. 3.1:

$$\hat{\epsilon}^{(eff)} = \begin{pmatrix} 8.421 & 0 & 0 \\ 0 & 8.1 & 0 \\ 0 & 0 & 8.421 \end{pmatrix}.$$

This result based on the effective medium model presented in the previous section means that mesoporous silicon grown on (110)-substrate will be a negative uniaxial crystal with an optical axis that coincides with the <001> direction. The angular dependence of the numerically calculated dielectric permittivity tensor components of such a material is given in Figure 3.2. Suffice it to state that the model anisotropy type predicted by the theory presented is in complete agreement with experimental findings as reported in [18] and [19].

3. EFFECTIVE MEDIUM APPROACH FOR CALCULATIONS OF LINEAR AND NONLINEAR OPTICAL PROPERTIES OF POROUS SEMICONDUCTOR MATERIALS



b)

Figure 3.2. The polar plots of the elements of the dielectric permittivity tensor of mesoporous silicon grown on (110)-oriented substrate: a) diagonal tensor elements for the case of electric field rotated in the (110) plane; b) the only nonzero nondiagonal tensor element for the case of electric field rotated in the (110) plane, and c) diagonal tensor elements for the case of electric field rotated in the (100) plane.

The optical anisotropy of such a material is well known (see, for example, [81]). In such crystals for any direction of the electric field in the electromagnetic wave, two eigensolutions of the secular equation exist, which are called ordinary and extraordinary waves and described by refractive indices usually denoted n_o and n_e . In the coordinate system as drawn in Figure 3.1, $n_o = \sqrt{\epsilon_{xx}^{(eff)}} \equiv \sqrt{\epsilon_{zz}^{(eff)}}$, while $n_e = \sqrt{\epsilon_{yy}^{(eff)}}$. The normal surface of the electromagnetic waves in this case consists of a sphere and an ellipsoid of revolution, contained in the sphere. For any direction of light propagation in such a crystal two waves with different refractive indices exist that have two different polarization states: an ordinary wave, which always has the refractive index n_o and is polarized such that the electric field of the electromagnetic wave is in the (001) plane, and an extraordinary wave which has a refractive index as defined by:

$$\frac{1}{n_e^2(\theta)} = \frac{\cos^2 \theta}{n_o^2} + \frac{\sin^2 \theta}{n_e^2},$$

where θ is the angle between the electromagnetic wave propagation direction and the [001] crystal axis. The direction of polarization for the extraordinary electric field for the case of

the plane of incidence being the $(1\bar{1}0)$ plane, is given by

$$\begin{pmatrix} 0 \\ \frac{\cos \theta}{n_e^2(\theta) - n_o^2} \\ \frac{\sin \theta}{n_e^2(\theta) - n_o^2} \end{pmatrix}.$$

The value $(n_o - n_e)/n_o$ of the relative optical anisotropy depends on the porosity of the sample, on the relative filling fraction of the [001] pore lattice subsets, and on the pore ellipsoid aspect ratio. The plots of these dependences are given in Figure 3.3. In all the pictures the porosity of the sample was assumed to be 25 %, the aspect ratio of the pore ellipsoids is 0.5, and the relative filling fraction of the [001] pore lattice subset is 0.1 if it is not stated otherwise. One can see that the dependence of the relative optical anisotropy of the material is linearly proportional to the porosity of the sample if both other parameters are assumed to be constant. However, it is highly likely that both parameters can change with experimental conditions that create different porosities in the material. Unfortunately, no extensive experimental investigation of the relative optical anisotropy vs. porosity of the sample is published to date. Such data, interpreted with the formalism presented here, could provide straightforward information on the changes of the morphology of the mesoporous Si layers with porosity.

In any case, based on the results following from the formalism presented in the previous paragraph, it is safe to state that optical anisotropy in the mesoporous silicon etched on the (110)-oriented substrate is not due to the anisotropic porosity of the material, but rather due to:

- 1) Anisotropic polarizability and depolarization factors of the pores in each pore lattice.
- 2) Preferential ordering of the pores into three distinct lattices.
- 3) Smaller filling ratio of the pores aligned into [001] lattice compared to those aligned into [100] and [010] lattices.

The relative optical anisotropy of the material is expected to increase with the porosity of the material, even if the relative filling fraction of the [001] pore lattice stays the same. With more experimental data available, the effective medium method theory developed here could help to bring more insights into the pore morphology. The anisotropy of the mesoporous silicon etched on differently oriented substrates can be also easily investigated with the methodology presented here.

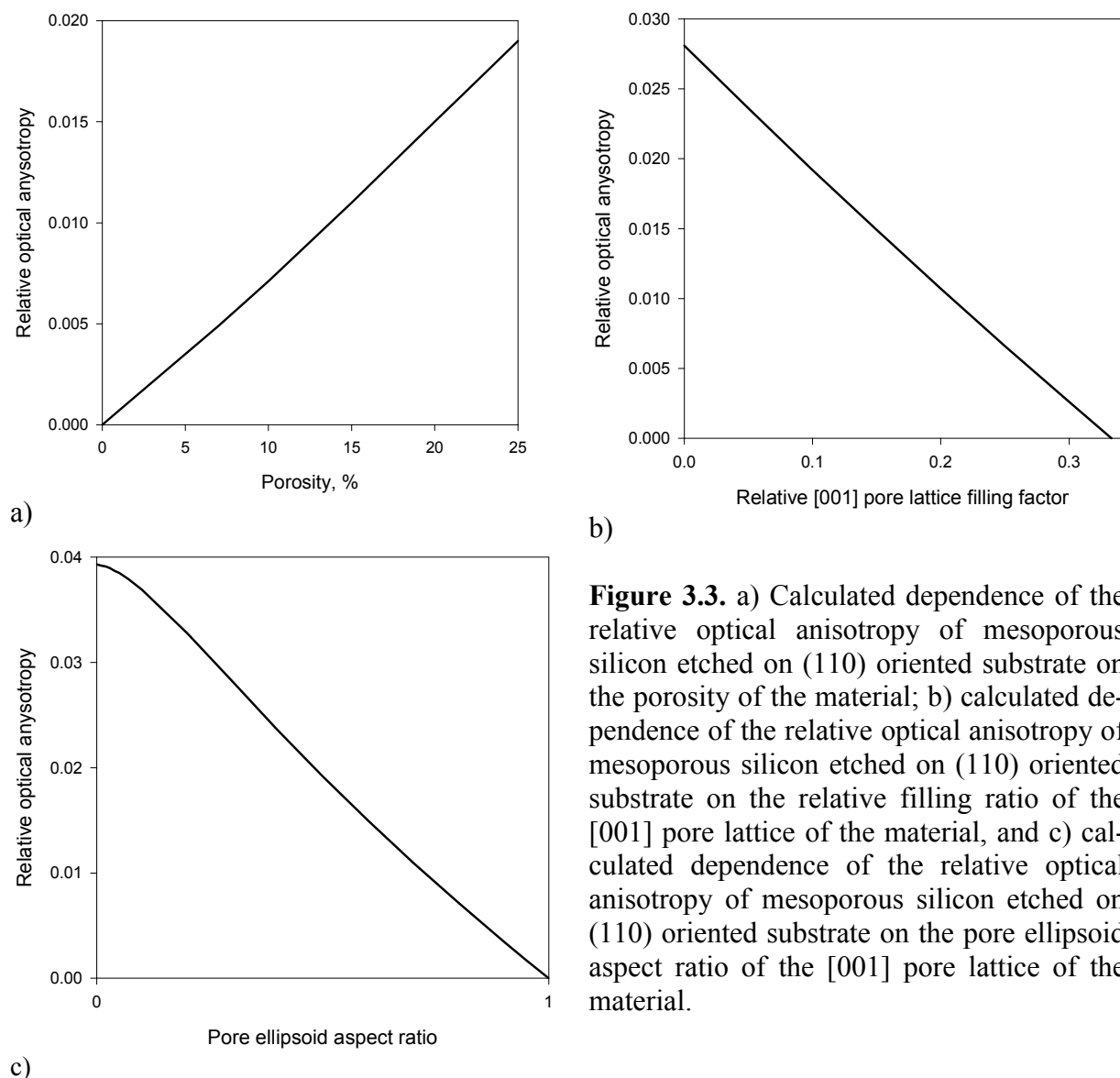


Figure 3.3. a) Calculated dependence of the relative optical anisotropy of mesoporous silicon etched on (110) oriented substrate on the porosity of the material; b) calculated dependence of the relative optical anisotropy of mesoporous silicon etched on (110) oriented substrate on the relative filling ratio of the [001] pore lattice of the material, and c) calculated dependence of the relative optical anisotropy of mesoporous silicon etched on (110) oriented substrate on the pore ellipsoid aspect ratio of the [001] pore lattice of the material.

3.5. (100)-Oriented III-V Compound Semiconductors Containing Crystallographic Pores

Other interesting examples of porous materials are porous InP [11, 103-104] and porous GaAs [11, 104-105] with crystallographically oriented pores. In the following analysis I will consider the case of GaAs, but it should be understood that the analysis of InP material could be done in exactly the same way by just adjusting the refractive index of host material in numerical calculations.

The crystallographically oriented pores in porous GaAs have the $\langle 111 \rangle_B$ crystallographic direction as definite growth direction. The zincblende lattice of the III-V compounds consists of double layers with alternating short (three bonds) and long (one bond) distances, and the layers are occupied by A (Ga) or B (As) atoms. The $\langle 111 \rangle_B$ direction runs from B to A lay-

ers along the shortest distance between A and B planes (or from B to A along the longest distance between the A and the B planes). It is important to note that A planes are generally more stable against electrochemical dissolution than B planes. The so-called $\langle 111 \rangle_A$ directions can be represented as $-Ga \equiv As - Ga \equiv As -$, while the second set ($\langle 111 \rangle_B$) can be represented as $-As \equiv Ga - As \equiv Ga -$ (- means one bond). For an (100)-oriented GaAs wafer, four $\langle 111 \rangle$ crystallographic directions are thus possible for pore growth. The number of $\langle 111 \rangle_B$ directions that will be expressed in the pore lattices depends on the nucleation conditions for the pores. Two general types of pore nucleation have been observed [11, 106]: uniform and non-uniform nucleation. Non-uniform nucleation usually resulted in formation of “pore domains” on the surface of the sample resulting from pores more or less equally distributed along all $\langle 111 \rangle$ directions in the bulk. Uniform nucleation, on the contrary, causing the majority of the pores to grow just in the two $\langle 111 \rangle$ direction being in the same plane and going “downwards”, while in second pair of $\langle 111 \rangle$ directions (going “upwards”) the density of pores is considerably smaller than that of first pair. Figs. 3.4a-3.4c show cross section SEM micrographs of the pores in GaAs. It should be noted, that the pore cross-section in such GaAs layers has a triangular shape.

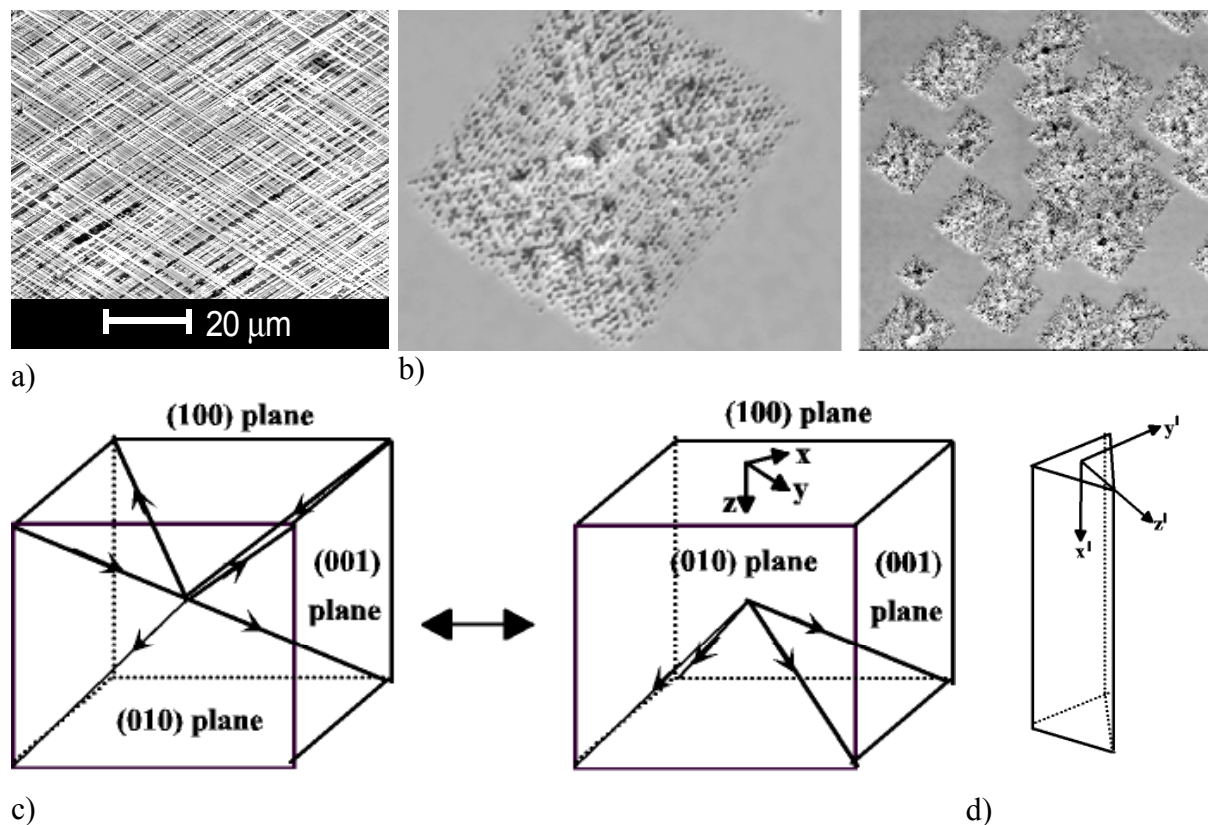


Figure 3.4. a), b) SEM images of the porous GaAs layer with crystallographic pores; c) the schematic drawing showing the pore lattices accounted by the model for the case of porous GaAs or InP electrochemically etched on (100) oriented substrates, and d) the coordinate system associated with the pore lattice.

In the model presented it is assumed that porous GaAs material can be represented by four sublattices of air voids in the bulk of semiconductor material such that the air voids in each sublattice have their axes essentially parallel to each other. It is further assumed that the bulk GaAs material is isotropic and has the dielectric permittivity ϵ_{GaAs} . Further on, it is assumed that the pores are separated from each and affect each other only through the depolarization

factor (this limits the validity of the used method to relatively small porosities). It is also assumed that the wavelength of electromagnetic wave considerably exceeds the pore cross section.

To apply the effective medium method presented here, one needs to consider four pore lattices, as shown in Figure 3.4c. In this case equation (3.11) takes the following form:

$$\hat{\boldsymbol{\epsilon}}^{(eff)} = \boldsymbol{\epsilon}_{GaAs} \left[\hat{I} + \sum_{i=1}^4 \hat{A}^{(i)} \hat{M}^{(i)} \hat{A}^{(i)-1} \right] \quad (3.14)$$

Simple geometrical derivations lead to the following coordinate transformation matrices, if the reference coordinate system is introduced as shown in Figure 3.4c. The X- and Y- axes are collinear to the projections of pore growth directions ($\langle 111 \rangle$ directions) on the (100) plane:

$$\hat{A}^{(1)} = \begin{pmatrix} \frac{\sqrt{2}}{\sqrt{3}} & 0 & -\frac{1}{\sqrt{3}} \\ 0 & 1 & 0 \\ \frac{1}{\sqrt{3}} & 0 & \frac{\sqrt{2}}{\sqrt{3}} \end{pmatrix}, \hat{A}^{(2)} = \begin{pmatrix} 0 & 1 & 0 \\ -\frac{\sqrt{2}}{\sqrt{3}} & 0 & \frac{1}{\sqrt{3}} \\ \frac{1}{\sqrt{3}} & 0 & \frac{\sqrt{2}}{\sqrt{3}} \end{pmatrix}, \hat{A}^{(3)} = \begin{pmatrix} -\frac{\sqrt{2}}{\sqrt{3}} & 0 & \frac{1}{\sqrt{3}} \\ 0 & -1 & 0 \\ \frac{1}{\sqrt{3}} & 0 & \frac{\sqrt{2}}{\sqrt{3}} \end{pmatrix},$$

$$\hat{A}^{(4)} = \begin{pmatrix} 0 & -1 & 0 \\ \frac{\sqrt{2}}{\sqrt{3}} & 0 & -\frac{1}{\sqrt{3}} \\ \frac{1}{\sqrt{3}} & 0 & \frac{\sqrt{2}}{\sqrt{3}} \end{pmatrix}$$

To understand how the triangular shape of the pores affects the optical anisotropy of the porous GaAs material, let's calculate first the dielectric permittivity tensor as if the pores had circular cross section. In this case [102], $\beta_{22} = \beta_{33}$ and $L_{22} = L_{33} = (1 - L_{11})/2$;

$L_{11} = \frac{x^2}{(1-x^2)^{3/2}} \left[\text{arcth}(\sqrt{1-x^2}) - \sqrt{1-x^2} \right]$, where x the ratio between the axes length $x = c/a$

($a > b = c$); $\beta_{11} = \frac{\boldsymbol{\epsilon}_{Si}}{\boldsymbol{\epsilon}_{Si} - (\boldsymbol{\epsilon}_{Si} - 1) \cdot L_{11}}$; $\beta_{22} = \beta_{33} = \frac{2\boldsymbol{\epsilon}_{Si}}{2\boldsymbol{\epsilon}_{Si} - (\boldsymbol{\epsilon}_{Si} - 1) \cdot (1 - L_{11})}$. As follows from

the SEM images (see Fig. 3.4a), the pores in GaAs are best represented as cylinders, or as the limiting case of ellipsoids with $x \rightarrow 0$.

The results of the dielectric permittivity tensor elements calculations are presented in Fig. 3.5 (dashed lines). The electromagnetic wave was assumed to propagate along the $\langle 100 \rangle$ direction with the electric field vector of the electromagnetic wave coinciding with the $\langle 011 \rangle$ crystallographic direction. A 30 % overall porosity of the GaAs layer is assumed. Calculations show that in this case a porous GaAs layer would exhibit a biaxial anisotropy for all relative filling fractions of two pore lattice pairs except for the case of equal filling, where it would behave as an optically isotropic material.

To take into account the triangular shape of the pore cross-section, one needs to reevaluate the values of the L_{ii} and β_i coefficients. Since the ratio of pore length to pore cross-section for porous GaAs is very high, with good accuracy, $L_{11} = 0$ and $\beta_{11} = 1$. For equilateral triangular shape inclusions [102] $L_{22} = 0.5 \Rightarrow L_{33} = 1 - L_{22} = 0.5$. In my calculations the β_2 was assumed to be 1.82, while $\beta_3 = 1.86$.

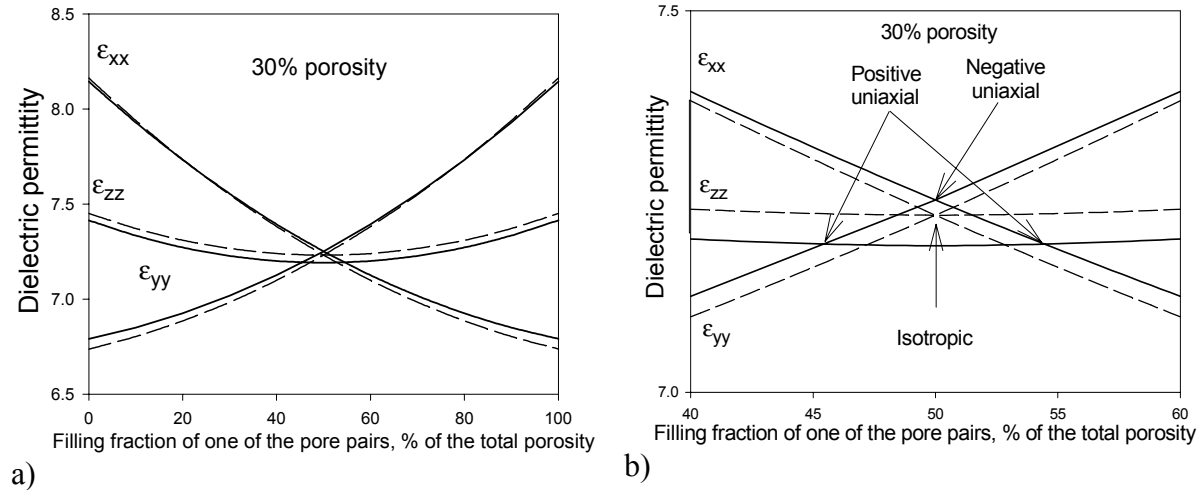


Figure 3.5. Numerically calculated dielectric tensor elements of the porous GaAs layer with crystallographic pores etched in a (100)-oriented substrate as a function of the relative filling fraction of one of the pore lattice pairs: a) general view; b) magnified view near the 50 % filling fraction. The overall porosity of the sample is 30 %. Dashed lines indicate the results of calculations for the case of the pores with circular cross section, solid lines indicate the results of calculations with the account of the triangular cross sections of crystallographic pores in GaAs.

These corrections account for the triangular shape of the pore cross sections and allow calculations of the dielectric permittivity tensor elements of porous GaAs layer with the same set of parameters as used for the calculations for the circular pore cross section. The results of such calculations are also presented in Fig. 3.5. The triangular shape of the pore causes quite interesting effects, which can be viewed better in Fig. 3.5b. For example, for pore lattice pairs with identical representation or “weight”, i.e. a relative filling fraction of 50 %, porous GaAs no longer exhibits isotropic behavior, but rather becomes a negative uniaxial crystal with an optical axis that coincides with the $\langle 100 \rangle$ crystallographic direction. Besides the case of both pore lattice pairs being equally represented, two more points of non-biaxial behavior appear. For the parameters of the porous GaAs layer as used for the calculations, these points correspond to filling fractions of roughly 45.5 % and 54.5 %. At these points the porous GaAs layer will exhibit positive uniaxial behavior with optical axes aligned along the two perpendicular $[011]$ crystallographic directions, respectively. In all other cases the porous GaAs layer will exhibit biaxial behavior. Hence, porous GaAs provides the unique capability to control not only the optical anisotropy value, as, for example, in mesoporous silicon etched on (110) oriented substrates [18-21,39], but also the optical anisotropy type (uniaxial or biaxial), and even the direction of the optical axis by modifying the etching parameters.

The challenge is to develop the right porosity, cross-section, and filling factors of the pore lattices of the porous GaAs for the desired optical properties. The morphology of a porous

semiconductor depends on the electrochemical etching conditions used. Beside parameters like electrolyte composition, applied current density or etching bias, the nucleation process plays a critical role for the overall morphology. The overall current density defines the amount of dissolved material, which can be used to define the porosity. For example in case of porous silicon the applied current determines under certain etching conditions directly the porosity of the layer. In case of GaAs this approach is not as straightforward because pores in GaAs can nucleate in form of pore-domains or homogeneous on the surface. As mentioned, the pores in both cases are crystallographic and propagate along $\langle 111 \rangle_B$ directions. In both cases from one primary nucleation point on the (100) surface of the sample two primary crystallographic pores start to grow. If the primary nucleation points are dense enough, no branching of the two nucleated pores is observed, and a uniform 3D structure will develop. The “cross-hatched” structure occurs because crystallographically oriented pores are able to intersect each other without changing their direction of growth [106]. On the other hand, if the nucleation points are less dense, multiple branching of the two initially nucleated pores and of the secondary pores created by branching will occur, the result is a pore domain with a particular structure. For a homogeneous nucleation it is necessary to obtain a high density of nucleation points on the surface of the sample, which can be arrived by a two-step anodization process [107]. Filling factor other than 50 % might be obtained by starting with a substrate that is slightly off the (100) orientation, because the growth direction more steeply inclined is often favored in pore growth. Further details on the different anodization conditions of porous GaAs can be found elsewhere [11, 106-109].

3.6. Introduction to Surface Plasmon Enhancement of the Optical Anisotropy in Porous Silicon/Metal Composites

Metal filling of the pore arrays through, e.g., electroplating or electroless plating techniques has been already demonstrated (see, for example, Chapter II, or [110-111]). Some of the metals, e.g. silver, gold, aluminum, copper, are known as good providers of surface plasmons (SPs), with non-radiative waves existing on the metal-semiconductor interfaces. SPs are known to be responsible for large enhancements of the electromagnetic field and to influence or dominate the scattering cross-section of metal colloids [112], Raman scattering, higher harmonic generation [113], etc. The question arises on how the linear optical properties (e.g. anisotropy) of the porous semiconductor (such as for example mesoporous silicon etched on (110) substrate) will change if the pores will be filled with SP-active metals.

To answer this question, I present here a method for calculating the effective dielectric constants and refractive indices of metal-filled porous materials.

3.7. Effective Permittivity Tensor Calculations

The structure of the mesoporous silicon layer grown on (110) substrate was discussed previously in this Chapter. First, let's apply the theory presented earlier in this chapter, which was developed for multiple sub-lattices of weakly polarizable inclusions. Equation (3.11) then will take the form

$$\hat{\epsilon}^{(eff)} = \epsilon_B \left[\hat{I} + \sum_{i=1}^3 \hat{A}^{(i)} \hat{M}^{(i)} \hat{A}^{(i)-1} \right] \quad (3.15)$$

where ε_m is the dielectric permittivity of the metal filling the pores. If the porosity of the mesoporous silicon layer is p and the coefficient r will be introduced to describe the ratio of filling fractions between the [001] metal-filled pore lattice and other two lattices, the electrical polarization matrices $M^{(i)}$ for each lattice will be as follows:

$$M^{(1)} = M^{(2)} = \begin{pmatrix} \frac{(p-p \cdot r)\alpha_{4,1}^{(i)}}{2\varepsilon_{Si} - L_{1,1}(p-p \cdot r)\alpha_{4,1}^{(i)}} & 0 & 0 \\ 0 & \frac{2(p-p \cdot r)\alpha_{2,2}^{(i)}}{4\varepsilon_{Si} - (1-L_{1,1})(p-p \cdot r)\alpha_{2,2}^{(i)}} & 0 \\ 0 & 0 & \frac{2(p-p \cdot r)\alpha_{3,3}^{(i)}}{4\varepsilon_{Si} - (1-L_{1,1})(p-p \cdot r)\alpha_{3,3}^{(i)}} \end{pmatrix}$$

$$M^{(3)} = \begin{pmatrix} \frac{p \cdot r \cdot \alpha_{4,1}^{(3)}}{\varepsilon_{Si} - L_{1,1} \cdot p \cdot r \cdot \alpha_{4,1}^{(3)}} & 0 & 0 \\ 0 & \frac{2p \cdot r \cdot \alpha_{2,2}^{(3)}}{2\varepsilon_{Si} - (1-L_{1,1}) \cdot p \cdot r \cdot \alpha_{2,2}^{(3)}} & 0 \\ 0 & 0 & \frac{2p \cdot r \cdot \alpha_{3,3}^{(3)}}{2\varepsilon_{Si} - (1-L_{1,1}) \cdot p \cdot r \cdot \alpha_{3,3}^{(3)}} \end{pmatrix}$$

If the metal inclusions in different subsets have the same shape and volume but different orientations, as was assumed originally, $\alpha_{i,j}^{(k)} = \alpha_{i,j}^{(l)}$. To determine these coefficients $\alpha_{i,j}^{(k)}$ I will use the result of Kuwata [112] for calculations of the normalized (by volume) polarizabilities of metal ellipsoids, which states

$$\alpha_{i,i}(\varepsilon) = \frac{1}{\left(L_{i,i} + \frac{\varepsilon}{\varepsilon_m - \varepsilon}\right) + A_{i,i}\varepsilon_m x_i^2 + B_{i,i}\varepsilon_m^2 x_i^4 - i \frac{4}{3} \cdot \pi^2 \varepsilon_m^{2/3} \frac{V}{\lambda^3}} \quad (3.16)$$

where $x_1 = \pi a/\lambda$; $x_2 = x_3 = \pi b/\lambda$; $x = a/b$; $A_{i,i} = -0.4865L_{i,i} - 1.046L_{i,i}^2 + 0.8481L_{i,i}^3$,
 $B_{i,i} = 0.01909L_{i,i} + 0.1999L_{i,i}^2 + 0.6077L_{i,i}^3$; λ is the wavelength.

Equation (3.16), according to [112] is valid for metal inclusion dimensions with sides in the range from just a few nanometers to at least a hundred of nanometers.

The spectral dependences of the polarizability coefficients for the case of a silver elongated ellipsoid with $a = 15$ nm and $b = 10$ nm, embedded into a silicon host was calculated with eq. (3.16); the results are given in Fig. 3.6.

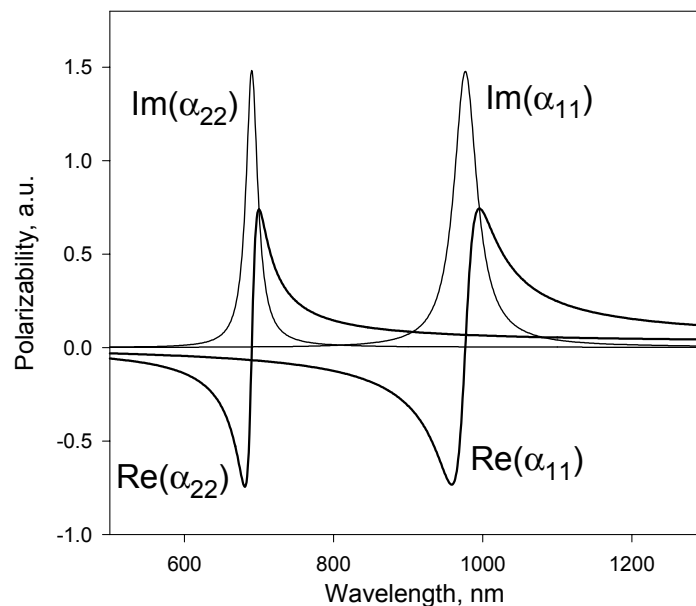


Figure 3.6. Numerically calculated spectral dependences of the polarizability tensor coefficients of the elongated silver ellipsoid with $a=15$ nm and $b=10$ nm, embedded into silicon host.

The dielectric constant of silver was calculated according to the Drude approximation. For the calculations, the imaginary part of the silicon refractive index at the given wavelengths was neglected. The reason for this is that in porous silicon the position of the absorption edge is strongly blue-shifted (see [114]), so such an assumption indeed makes sense. As one can expect, the polarizability resonances of the silver ellipsoids for electric fields of the electromagnetic wave aligned along different ellipsoid axes are located at different wavelengths. These polarizability resonances are related to the excitation of the surface plasmon modes on the ellipsoid surface.

By substituting (3.16) into (3.15) and calculating the coefficients of dielectric permittivity tensor of silver-porous silicon etched on (110) substrate composite one can show that the resultant material will exhibit an uniaxial type of anisotropy with the optical axis coinciding with the $\langle 001 \rangle$ silicon crystallographic direction, the same as for unfilled pores considered previously in this Chapter.

The numerically calculated spectral dependences of the real (n) and imaginary (k) parts of ordinary and extraordinary refractive indices of the material with filling fraction of the silver ellipsoids of just 0.1 volume percent are given in Fig. 3.7. One can see that the model predicts a substantial optical anisotropy of such a material, even for the small filling fractions used, and that the uniaxial anisotropy of the material changes the “sign” (from positive to negative) around the positions of the surface plasmon resonances.

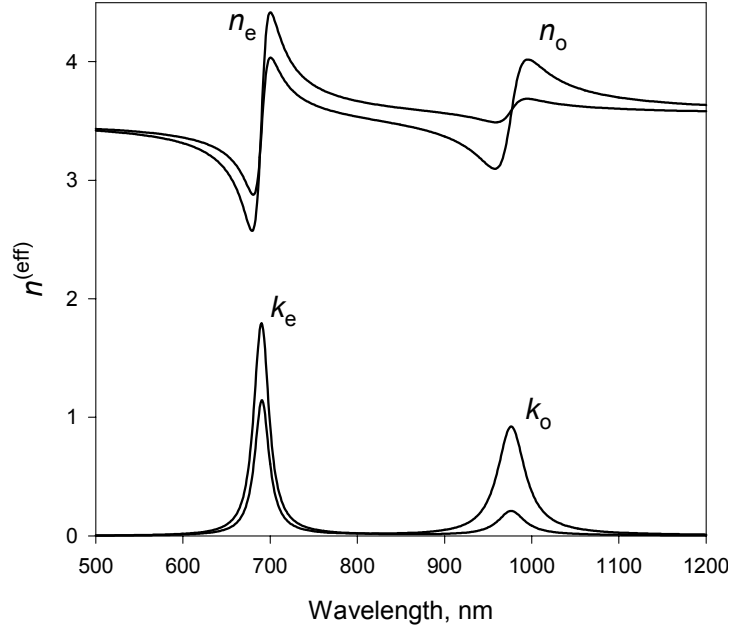


Figure 3.7. Numerically calculated spectral dependences of the real (n) and imaginary (k) parts of ordinary and extraordinary refractive indices of the silver/ porous silicon etched on (110)-oriented wafer with filling fraction of the silver ellipsoids of 0.1 volume percent.

It should be noted that the model presented above can provide reasonable results only for very small filling fractions of metal ellipsoids, especially around the resonances. Moreover, such a model can only predict the dielectric properties of composites consisting of weakly polarizable inclusions fairly realistically; for such highly polarizable inclusions as metal ellipsoids around plasmon resonance excitation conditions, the model is not really adequate. More self-consistent models need to be implemented and the following material is devoted to this task.

Here the generalization of the Bruggeman [14] method for the case of composite consisting of multiple sublattices of inclusions is presented. The main assumption in the Bruggeman method is that the total electrical polarizability of the composite material is equal to zero. In other words, the total polarizability of all the inclusions (in the analyzed case both metal inclusions and silicon “inclusions”) embedded in the medium with effective dielectric parameters should vanish:

$$\sum_{i=1}^3 \tilde{P}^{(i)} + \tilde{P}^{(4)} = 0 \quad (3.17)$$

where $\tilde{P}^{(i)}$, $i = 1, 2, 3$ is the polarization of the i^{th} lattice subset and $\tilde{P}^{(4)}$ is the polarizability of the Si “inclusion” in the matrix. According to the abbreviations introduced above, (3.17) can be rewritten in the analyzed case in the following form:

$$(1-p)\hat{\alpha}^{(4)}\bar{E} + \frac{p-p\cdot r}{2}\hat{A}^{(1)}\hat{\alpha}^{(1)}\hat{A}^{(1)-1}\bar{E} + \frac{p-p\cdot r}{2}\hat{A}^{(2)}\hat{\alpha}^{(2)}\hat{A}^{(2)-1}\bar{E} + p\cdot r\cdot\hat{A}^{(3)}\hat{\alpha}^{(3)}\hat{A}^{(3)-1}\bar{E} = 0 \quad (3.18)$$

Generally, equation (3.18) states a fairly complex problem since it includes the determination of the polarizabilities of the all inclusions in the anisotropic medium with generally speaking unknown orientations of the axes, and thus requires solving a system of six independent equations with six unknowns (according to the number of independent coefficients in the dielectric permittivity tensor of the effective medium). However, in the analyzed case one can simplify the solution of problem (3.18) by using the results obtained by using the generalization of the Maxwell-Garnet model already introduced.

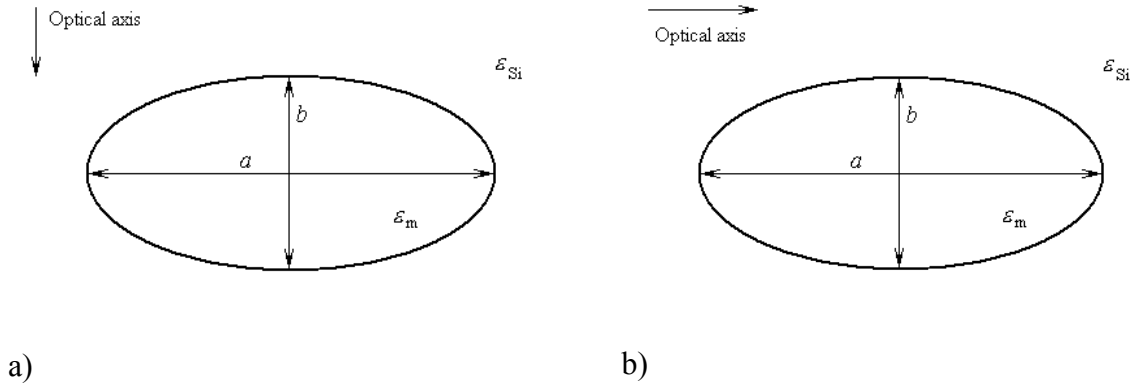


Figure 3.8. Schematic drawing illustrating the orientation of the optical axis of the material consisting of metal-filled porous silicon etched on (110) oriented substrate with respect to the major axis of the meal inclusion ellipsoid (a) for 1st and 2nd inclusion subsets, and (b) for 3rd inclusion subsets.

Although, as mentioned before, this model cannot provide sufficiently accurate quantitative results for the material analyzed here, the qualitative predictions of an uniaxial type of anisotropy with optical axis aligned with the $\langle 001 \rangle$ crystallographic direction can certainly be trusted. Taking this into account, the polarizability tensors of metal inclusions in each lattice subset can be written as:

$$\hat{\alpha}^{(1)} = \begin{pmatrix} \alpha_{1,1}(\epsilon_o) & 0 & 0 \\ 0 & \alpha_{2,2}(\epsilon_e) & 0 \\ 0 & 0 & \alpha_{3,3}(\epsilon_o) \end{pmatrix}, \quad \hat{\alpha}^{(2)} = \begin{pmatrix} \alpha_{1,1}(\epsilon_o) & 0 & 0 \\ 0 & \alpha_{2,2}(\epsilon_e) & 0 \\ 0 & 0 & \alpha_{3,3}(\epsilon_o) \end{pmatrix},$$

$$\hat{\alpha}^{(3)} = \begin{pmatrix} \alpha_{1,1}(\epsilon_e) & 0 & 0 \\ 0 & \alpha_{2,2}(\epsilon_o) & 0 \\ 0 & 0 & \alpha_{3,3}(\epsilon_o) \end{pmatrix}$$

where the $\alpha_{i,j}^{(k)}$ coefficients are determined according to (3.16). This can be done because the optical axis of the effective medium is always aligned with one of the axes of an inclusion ellipsoid for porous silicon etched on (110)-oriented substrate, as illustrated in Fig. 3.8a for inclusions from 1st and 2nd subsets and Fig. 3.8b for inclusions from 3rd subset. Silicon ‘parti-

cles” in this approximation can be assumed to have spherical shape. It makes sense to preserve the reference coordinate system in the silicon “particles” matrix. In this case,

$$\hat{\alpha}^{(4)} = \begin{pmatrix} \frac{\epsilon_{Si} - \epsilon_o}{\epsilon_{Si} + 2\epsilon_o} & 0 & 0 \\ 0 & \frac{\epsilon_{Si} - \epsilon_e}{\epsilon_{Si} + 2\epsilon_e} & 0 \\ 0 & 0 & \frac{\epsilon_{Si} - \epsilon_o}{\epsilon_{Si} + 2\epsilon_o} \end{pmatrix}.$$

Hence, equation (3.18) can be rewritten into a system of two equations with two unknowns (ϵ_o and ϵ_e):

$$\begin{cases} (1-p)\alpha_{1,1}^{(4)} + \frac{p-p \cdot r}{4}(\alpha_{1,1}^{(1)} + \alpha_{3,3}^{(1)} + \alpha_{1,1}^{(2)} + \alpha_{3,3}^{(2)}) + p \cdot r \cdot \alpha_{2,2}^{(3)} = 0 \\ (1-p)\alpha_{2,2}^{(4)} + \frac{p-p \cdot r}{2}(\alpha_{2,2}^{(1)} + \alpha_{2,2}^{(2)}) + p \cdot r \cdot \alpha_{1,1}^{(3)} = 0 \end{cases} \quad (3.19)$$

Since according to the assumptions the metal “particles” in each of the lattices have the same shape and volume, (3.19) can be further simplified to:

$$\begin{cases} (1-p)\alpha_{1,1}^{(4)} + \frac{p-p \cdot r}{2}(\alpha_{1,1}^{(1)} + \alpha_{3,3}^{(1)}) + p \cdot r \cdot \alpha_{2,2}^{(3)} = 0 \\ (1-p)\alpha_{2,2}^{(4)} + (p-p \cdot r)\alpha_{2,2}^{(1)} + p \cdot r \cdot \alpha_{1,1}^{(3)} = 0 \end{cases} \quad (3.20)$$

Equation (3.20) can be easily solved numerically.

Based on this model, Fig. 3.9 gives the numerically calculated spectral dependences of the refractive indices of the ordinary and extraordinary waves for the silver/porous silicon system on (110)-oriented substrate composites. Fig. 3.9a and 3.9c give the spectral dependences of the real parts of the refractive indices for the composites with 1 % and 0.1 % metal filling fractions respectively, while Fig. 3.9b and 3.9d give the spectral dependences of the imaginary parts of the refractive indices (also known as attenuation coefficients). In all the figures the silver ellipsoids were assumed to be of an elongated shape with a longer axis of 15 nm and shorter axes of 10 nm.

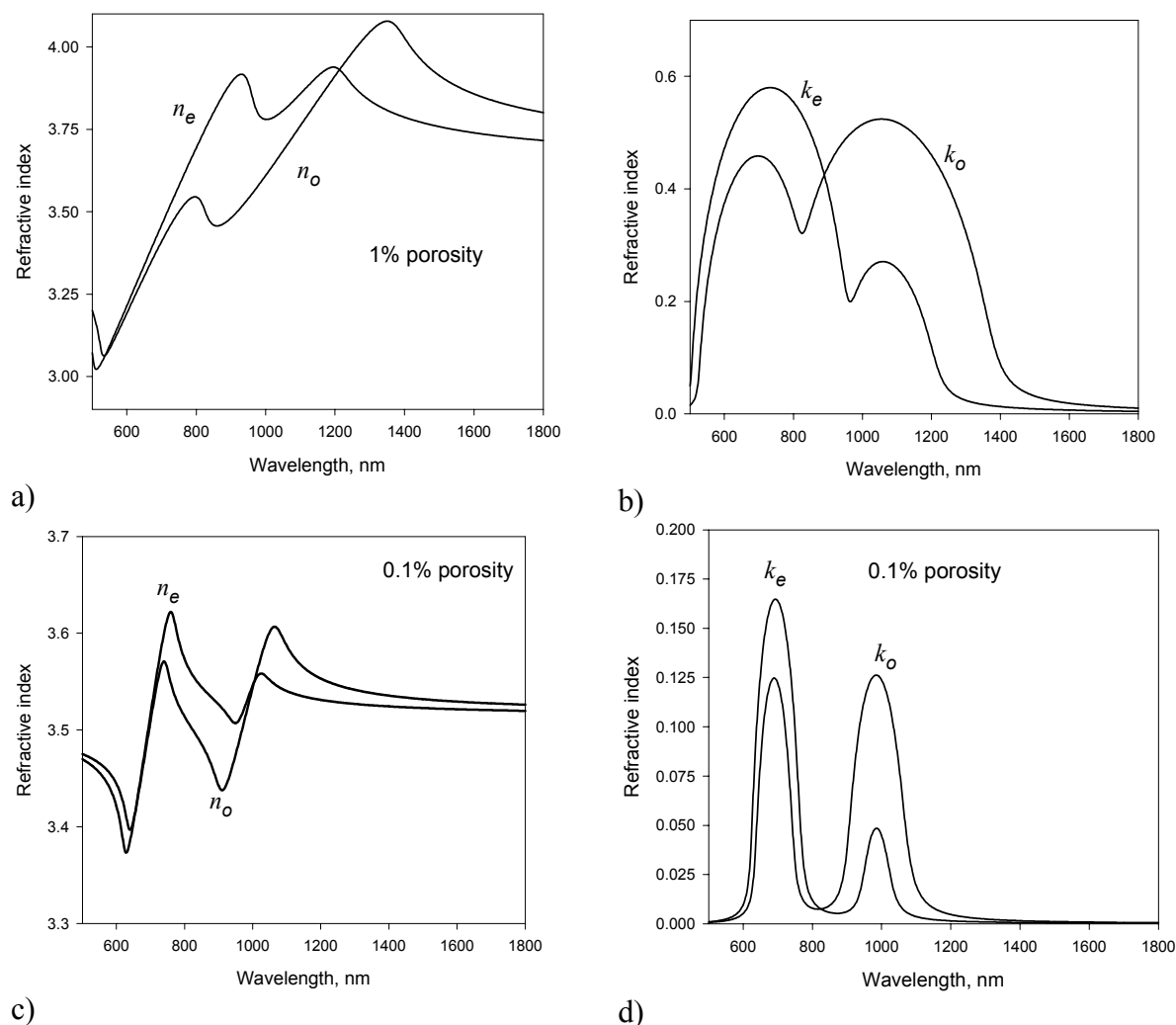


Figure 3.9. Numerically calculated spectral dependences of the a) real and b) imaginary parts of the refractive indices of ordinary and extraordinary waves, and numerically calculated spectral dependences of the c) real and d) imaginary parts of the refractive indices of ordinary and extraordinary waves case for a material composed of silver-filled porous silicon etched on (110)-oriented substrate and a 1 % filling fraction of metal.

The parameter r (see above) was assumed to be 0.1. One can see that the optical anisotropy of such a material is indeed expected to be quite high. While at 0.1 % filling fraction the calculated dependences (Figs. 3.9c and 3.9d) of the refractive indices closely resemble those obtained with the generalized Maxwell-Garnet methodology (Fig. 3.7), for filling fractions still as small as 1 %, the spectral dependences are changing shape dramatically. However, the surface plasmon enhancement of the optical anisotropy at certain wavelengths is still very strong.

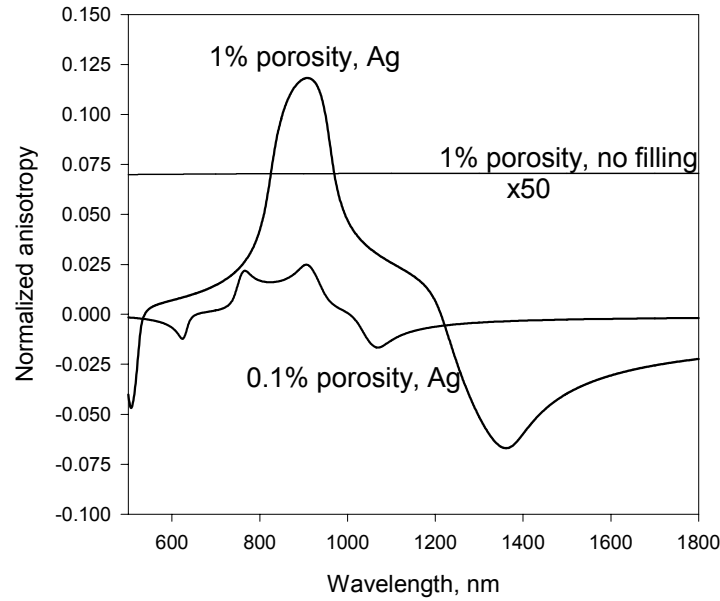


Figure 3.10. Numerically calculated spectral dependences of the relative optical anisotropy of the silver-filled porous silicon etched on (110)-oriented substrate for 0.1 % and 1 % filling fraction of silver and of the air-filled porous silicon etched on (110)-oriented substrate with 1 % porosity (multiplied by 50).

Fig. 3.10 presents the spectral dependences of the relative optical anisotropies ($|n_o - n_e|/n_o$) of the silver-filled porous silicon etched on (110)-oriented substrate for 0.1 % and 1 % filling fraction of silver and of the air-filled porous silicon etched on (110)-oriented substrate with 1 % porosity. One can see that an almost 100-fold enhancement of the optical anisotropy can be achieved due to the surface plasmon resonance on silver ellipsoids.

The analyzed material can also exhibit quite interesting properties at intermediate filling fractions. For example, Fig. 3.11 shows the numerically calculated spectral dependences of the dielectric permittivity tensor coefficients for the silver-filled porous silicon etched on (110)-oriented substrate with 17 % volume fraction of metal. Fig. 3.11a) gives the spectral dependences of the real parts of the effective dielectric permittivity tensor coefficients, while Fig. 3.11b) presents the spectral dependences of the imaginary parts of those. One can see that the theory predicts different signs of the diagonal elements of the effective dielectric permittivity tensor around 1250-1775 nm wavelengths. Materials having these parameters within this spectral range belong to the class of materials with “indefinite” permittivity tensors, using the terminology introduced in [115]. It turns out that “indefinite” materials based on porosity offer quite peculiar optical properties. For example, some of the optical modes (surface or bulk) in such materials exist only for certain directions of propagations, but disappear in other directions, a property that can be used in e.g. spatial filtering. However, it should be noted that according to the model presented here, the losses in the analyzed material within the “indefinite” parameter range will be high (see the large anisotropic imaginary part of the effective dielectric permittivity tensor elements given in Fig. 3.11b). Also, as will be shown in Chapter IV, the quantitative accuracy of the model presented here deteriorates at such concentrations.

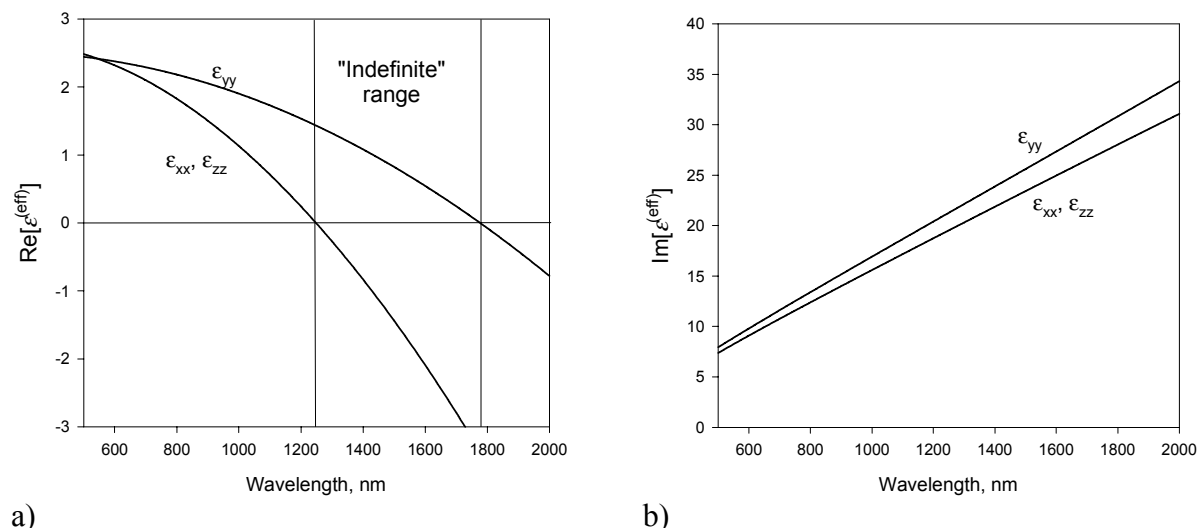


Figure 3.11. Numerically calculated spectral dependences of the a) real and b) imaginary parts of the effective dielectric permittivity tensor coefficients of the material composed of silver-filled porous silicon etched on (110)-oriented substrate for the case of 17 % filling fraction of metal.

Another interesting effect that should take place in the metal-filled porous silicon etched on (110)-oriented substrates is an enhancement of various nonlinear properties such as Raman scattering and higher order harmonic generation (second, third harmonics, etc.). Such effects should be greatly enhanced due to the very strong enhancement of the electromagnetic field in the vicinity of metal inclusions. Moreover, uniaxial anisotropy of the analyzed material should make it possible to achieve phase matching (a must in order to get strong coupling between irradiated and double frequency waves). A more detailed consideration of the nonlinear response of analyzed material is given below.

3.8. Effective Medium Approach for the Estimation of the Second Harmonic Generation in Certain Porous Semiconductor Materials

Porous semiconductors offer the opportunity of engineering not only their linear optical properties (as was described in Chapter II and the preceding part of this Chapter), but nonlinear optical properties as well, as quite recently has been also shown in [11, 29, 116-118]. However, a calculation technique for predicting the nonlinear properties of various porous materials is still missing. In last part of this Chapter, I will present a theoretical approach based on effective medium theory, which permits numerical analysis of such materials.

Nonlinear phenomena in some composite materials were already considered on the basis of the effective medium approaches by a number of authors [120-122]. For example, in [121] composites made by mixing isotropic materials were considered. However, for the inclusions in the composite matrix, a random distribution was assumed. In [120] the case of anisotropic inclusions was treated. However, only two options were discussed: random distribution or alignment of the inclusions.

The class of materials considered here (anisotropic composite consisting of a mixture of isotropic materials) does not belong to any of the cases already considered, and has some dis-

tinct peculiarities requiring separate consideration. Here I will use a (somewhat modified) approach for the third and second order nonlinearity given in [120]

3.9. Effective Nonlinear Susceptibility Tensor Calculations

In anisotropic nonlinear materials the local displacement vector \mathbf{D} is connected to the local electric field vector \mathbf{E} as:

$$D_i = \varepsilon_{ij} E_j + d_{ijk} E_j E_k + \chi_{ijkl} E_j E_k^* E_l + \dots \quad (3.21)$$

where D_i and E_i are the Cartesian components of \mathbf{D} and \mathbf{E} , ε_{ij} , d_{ijk} and χ_{ijkl} are second-, third- and fourth-rank Cartesian tensors. The Einstein convention that repeated indices are summed over will be used from now on. In this consideration, let's limit ourselves to the first and second order terms only, i.e., χ_{ijkl} and higher order susceptibilities will be neglected. Furthermore, only the weakly nonlinear regime will be considered, i.e. d_{ijk} is assumed to be small compared to ε_{ij} .

The material considered is composed of a host medium with isotropic dielectric permittivity $\varepsilon^{(B)}$ and anisotropic second order nonlinear susceptibility $d_{ijk}^{(B)}$, which contains a number of inclusions (such as filled or unfilled pores) having an isotropic dielectric permittivity $\varepsilon^{(I)}$ and an anisotropic second order nonlinear susceptibility $d_{ijk}^{(I)}$. It is further assumed that the inclusions are arranged in N subsets characterized by a special direction, and that the size, shape, and orientation (including orientation of the $d_{ijk}^{(I)}$) are the same in each subset relative to the special direction of the subset. The inclusions are aligned in the special direction of their subset but are otherwise distributed randomly within the composite. In other words, the same material as previously considered in this Chapter is now considered to have some nonzero nonlinear susceptibility.

For the definition of the effective dielectric permittivity $\hat{\varepsilon}^{(eff)}$ and the second order nonlinear susceptibility $\hat{d}^{(eff)}$, the following relation will be used:

$$\langle D_i \rangle = \varepsilon_{ij}^{(eff)} E_j^0 + d_{ijk}^{(eff)} E_j^0 E_k^0 + \chi_{ijkl}^{(eff)} E_j^0 E_k^{0*} E_l^0 + \dots \quad (3.22)$$

Where $\langle \dots \rangle$ denotes a volume average and E_i^0 are the Cartesian components of the electric field vector of the incident electromagnetic wave. Following the approach presented in [120], the local electric field in the composite may be written as:

$$\bar{\mathbf{E}} = \bar{\mathbf{E}}^{(lin)} + \delta\bar{\mathbf{E}} \quad (3.23)$$

where $\bar{\mathbf{E}}^{(lin)}$ is the local electric field that would exist in a linear composite with the same spatial distribution of the dielectric permittivity, but with $d_{ijk} \equiv 0$ everywhere in the composite, and $\delta\bar{\mathbf{E}}$ is the additional electric field due to nonlinearity, which is by definition of at least first order in d_{ijk} . Following derivations similar to those presented in [120] one can obtain the following formulas for the effective dielectric permittivity and for the second order nonlinear permeability:

$$\epsilon_{i,j}^{(eff)} = \frac{\int \epsilon(\bar{x}) E_i^{(lin)} E_j^{(lin)} d^3 x}{V E_i^0 E_j^0}$$

$$d_{i,j,k}^{(eff)} = \frac{\int d(\bar{x})_{i,j,k} E_i^{(lin)} E_j^{(lin)} E_k^{(lin)} d^3 x}{V E_i^0 E_j^0 E_k^0}$$

where the integration is carried out over some volume V . Remembering the assumptions about the analyzed material, these formulas can be written in the following form:

$$\epsilon_{i,j}^{(eff)} = \epsilon^{(B)} \frac{\int E_i^{(lin),B} E_j^{(lin),B} d^3 x}{V E_i^0 E_j^0} + \epsilon^{(I)} \frac{\int E_i^{(lin),I} E_j^{(lin),I} d^3 x}{V E_i^0 E_j^0} \quad (3.24)$$

$$d_{i,j,k}^{(eff)} = d_{i,j,k}^{(B)} \frac{\int E_i^{(lin),B} E_j^{(lin),B} E_k^{(lin),B} d^3 x}{V E_i^0 E_j^0 E_k^0} + d_{i,j,k}^{(I)} \frac{\int E_i^{(lin),I} E_j^{(lin),I} E_k^{(lin),I} d^3 x}{V E_i^0 E_j^0 E_k^0} \quad (3.25)$$

where the integration is now performed over either the bulk (or host) material volume (V_B) or the inclusion volume (V_I). Since both inclusions and the host are considered to have isotropic dielectric permittivity, a coordinate system will exist, in which the effective dielectric permittivity tensor of the composite will be diagonalizable. In this system Equation (3.24) can be rewritten as

$$\epsilon_{i,i}^{(eff)} = \epsilon^{(B)} \frac{\int (E_i^{(lin),B})^2 d^3 x}{V (E_i^0)^2} + \epsilon^{(I)} \frac{\int (E_i^{(lin),I})^2 d^3 x}{V (E_i^0)^2} \quad (3.26)$$

Following the approach presented in [120], the volume average of the squared electric field projections in both the bulk material and inclusions can be estimated from partial derivatives of effective dielectric constant tensor elements. From (3.26) it follows that

$$\frac{\partial \epsilon_{i,i}^{(eff)}}{\partial \epsilon^{(B)}} = \frac{\int (E_i^{(lin),B})^2 d^3 x}{V (E_i^0)^2} + \epsilon^{(B)} \frac{\int 2E_i^{(lin),B} \frac{\partial E_i^{(lin),B}}{\partial \epsilon^{(B)}} d^3 x}{V (E_i^0)^2} + \epsilon^{(I)} \frac{\int 2E_i^{(lin),I} \frac{\partial E_i^{(lin),I}}{\partial \epsilon^{(B)}} d^3 x}{V (E_i^0)^2} \quad (3.27)$$

$$\frac{\partial \epsilon_{i,i}^{(eff)}}{\partial \epsilon^{(I)}} = \frac{\int (E_i^{(lin),I})^2 d^3 x}{V (E_i^0)^2} + \epsilon^{(I)} \frac{\int 2E_i^{(lin),I} \frac{\partial E_i^{(lin),I}}{\partial \epsilon^{(I)}} d^3 x}{V (E_i^0)^2} + \epsilon^{(B)} \frac{\int 2E_i^{(lin),B} \frac{\partial E_i^{(lin),B}}{\partial \epsilon^{(I)}} d^3 x}{V (E_i^0)^2}$$

These equations are too unwieldy for the problem considered, and additional approximations are required. In [120] it was suggested that one could make the following estimation of certain terms in (3.27) within the limits of the Nonlinear Decoupling Approximation (NDA) [121, 123]:

$$\varepsilon^{(I)} \frac{\int_{V_I} 2E_i^{(lin),I} \frac{\partial E_i^{(lin),I}}{\partial \varepsilon^{(I)}} d^3x}{V(E_i^0)^2} + \varepsilon^{(B)} \frac{\int_{V_B} 2E_i^{(lin),B} \frac{\partial E_i^{(lin),B}}{\partial \varepsilon^{(I)}} d^3x}{V(E_i^0)^2} \approx 0 \quad (3.28)$$

Under such an assumption (3.27) takes the following simple form:

$$\frac{\partial \varepsilon_{i,i}^{(eff)}}{\partial \varepsilon^{(I)}} = \frac{\int_{V_I} (E_i^{(lin),I})^2 d^3x}{V(E_i^0)^2}$$

(3.29)

$$\frac{\partial \varepsilon_{i,i}^{(eff)}}{\partial \varepsilon^{(B)}} = \frac{\int_{V_B} (E_i^{(lin),B})^2 d^3x}{V(E_i^0)^2}$$

However, no proof of the validity of approximation (3.28) was published to the best of my knowledge. Here I will provide such a proof:

Equation (3.28) can be rewritten in a following form:

$$\frac{\int_V \varepsilon(\vec{r}) E_i^{(lin)}(\vec{r}) \frac{\partial E_i^{(lin)}(\vec{r})}{\partial \varepsilon^{(I)}} d^3x}{(E_i^0)^2} \approx 0 \Leftrightarrow \frac{\left\langle \varepsilon(\vec{r}) E_i^{(lin)}(\vec{r}) \frac{\partial E_i^{(lin)}(\vec{r})}{\partial \varepsilon^{(I)}} \right\rangle_V}{(E_i^0)^2} \approx 0$$

Within the NDA approximation the following estimation holds:

$$\frac{\left\langle \varepsilon(\vec{r}) E_i^{(lin)}(\vec{r}) \frac{\partial E_i^{(lin)}(\vec{r})}{\partial \varepsilon^{(I)}} \right\rangle_V}{(E_i^0)^2} \approx \frac{\left\langle \varepsilon(\vec{r}) E_i^{(lin)}(\vec{r}) \right\rangle_V}{(E_i^0)} \frac{\left\langle \frac{\partial E_i^{(lin)}(\vec{r})}{\partial \varepsilon^{(I)}} \right\rangle_V}{(E_i^0)} \quad (3.30)$$

In a first order approximation

$$E_i^{(lin),I}(\vec{r}) = E_i^0 - \chi^I \cdot (\varepsilon^{(B)} - \varepsilon^{(I)}) E_i^0 \quad E_i^{(lin),B}(\vec{r}) = E_i^0 + \chi^B \cdot (\varepsilon^{(B)} - \varepsilon^{(I)}) E_i^0 \quad (3.31)$$

where χ^I and χ^B are some positive coefficients (it is so because $\mathbf{E}^{(lin)} = \mathbf{E}^0 + \frac{\overline{\overline{L}}^{(i)} \cdot \overline{\overline{P}}}{\varepsilon_B}$, and

in first order approximation, as was shown in Paragraph 3.3, \mathbf{P} is proportional to $(\varepsilon^{(B)} - \varepsilon^{(I)}) E^0$). Hence,

$$\left\langle \frac{\partial E_i^{(lin)}(\vec{r})}{\partial \mathcal{E}^{(I)}} \right\rangle_V = \left\langle \frac{\partial E_i^{(lin)}(\vec{r})}{\partial \mathcal{E}^{(I)}} \right\rangle_{VI} + \left\langle \frac{\partial E_i^{(lin)}(\vec{r})}{\partial \mathcal{E}^{(I)}} \right\rangle_{VB} = \langle \chi^I \cdot E_i^0 \rangle_{VI} - \langle \chi^B \cdot E_i^0 \rangle_{VB} \quad (3.32)$$

From another point of view as follows from Bruggeman assumption

$$\langle E_i^{(lin)} \rangle_V = E_i^0. \quad (3.33)$$

By substituting (3.31) into (3.33), one can obtain

$$\begin{aligned} & \langle E_i^0 - \chi^I \cdot (\mathcal{E}^{(B)} - \mathcal{E}^{(I)}) E_i^0 \rangle_{VI} + \langle E_i^0 + \chi^B \cdot (\mathcal{E}^{(B)} - \mathcal{E}^{(I)}) E_i^0 \rangle_{VB} = E_i^0 \Leftrightarrow \\ & \Leftrightarrow \langle \chi^I \cdot (\mathcal{E}^{(B)} - \mathcal{E}^{(I)}) E_i^0 \rangle_{VI} - \langle \chi^B \cdot (\mathcal{E}^{(B)} - \mathcal{E}^{(I)}) E_i^0 \rangle_{VB} = 0 \Leftrightarrow \\ & \Leftrightarrow \langle \chi^I \cdot E_i^0 \rangle_{VI} - \langle \chi^B \cdot E_i^0 \rangle_{VB} = 0 \end{aligned} \quad (3.34)$$

By substituting (3.34) into (3.32) the following obtains:

$$\left\langle \frac{\partial E_i^{(lin)}(\vec{r})}{\partial \mathcal{E}^{(I)}} \right\rangle_V = 0 \quad (3.35)$$

and by substituting (3.35) into (3.30):

$$\frac{\left\langle \mathcal{E}(\vec{r}) E_i^{(lin)}(\vec{r}) \frac{\partial E_i^{(lin)}(\vec{r})}{\partial \mathcal{E}^{(I)}} \right\rangle_V}{(E_i^0)^2} \approx \frac{\left\langle \mathcal{E}(\vec{r}) E_i^{(lin)}(\vec{r}) \right\rangle_V}{(E_i^0)} \frac{0}{(E_i^0)} = 0,$$

This means that under the approximation used in (3.30), the following indeed holds true:

$$\mathcal{E}^{(I)} \frac{\int_{V_I} 2E_i^{(lin),I} \frac{\partial E_i^{(lin),I}}{\partial \mathcal{E}^{(I)}} d^3x}{V(E_i^0)^2} + \mathcal{E}^{(B)} \frac{\int_{V_B} 2E_i^{(lin),B} \frac{\partial E_i^{(lin),B}}{\partial \mathcal{E}^{(I)}} d^3x}{V(E_i^0)^2} \approx 0$$

Defining the porosity p as $p = V_I/V \equiv V_I/(V_I+V_B)$, from (3.29) it follows that

$$\frac{\left\langle (E_i^{(lin),I})^2 \right\rangle_I}{(E_i^0)^2} = \frac{1}{p} \frac{\partial \mathcal{E}_{i,i}^{(eff)}}{\partial \mathcal{E}^{(I)}} \quad (3.36)$$

Where $\langle \rangle_I$ means average value over the volume of all the inclusions (filled or nonfilled pores). Similarly,

$$\frac{\left\langle \left(E_i^{(lin),B} \right)^2 \right\rangle_B}{\left(E_i^0 \right)^2} = \frac{1}{(1-p)} \frac{\partial \mathcal{E}_{i,i}^{(eff)}}{\partial \mathcal{E}^{(B)}} \quad (3.37)$$

Returning now to (3.25), let's study the case when only the semiconductor host has a nonzero nonlinear susceptibility. In this case (3.25) takes the following form:

$$d_{i,j,k}^{(eff)} = d_{i,j,k}^{(B)} \frac{\int_{V_B} E_i^{(lin),B} E_j^{(lin),B} E_k^{(lin),B} d^3x}{V E_i^0 E_j^0 E_k^0} \quad (3.38)$$

Let's further assume that only elements with indices $\{i,i,j\}$ or $\{j,i,i\}$ of the semiconductor host second order susceptibility are not equal to zero (which is quite a reasonable assumption for at least some semiconductor materials [119]). In this case (3.38) can be written as:

$$d_{i,i,j}^{(eff)} = d_{i,i,j}^{(B)} (1-p) \left\langle \frac{\left(E_i^{(lin),B} \right)^2 E_j^{(lin),B}}{\left(E_i^0 \right)^2 E_j^0} \right\rangle_B \quad (3.39)$$

Next, let's make the assumption that the signs of the $E_j^{(lin),B}$ and E_j^0 are always the same within semiconductor host, which is a fairly reasonable assumption for air-filled pores and holds for metal-filled pores in the case of a small porosities (i.e., small filling fraction of the metal in the composite material). In this case, $\frac{E_j^{(lin),B}}{E_j^0} = \left| \frac{E_j^{(lin),B}}{E_j^0} \right|$, and one can rewrite

(3.39) as

$$d_{i,i,j}^{(eff)} = d_{i,i,j}^{(B)} (1-p) \left\langle \frac{\left(E_i^{(lin),B} \right)^2 \left| E_j^{(lin),B} \right|}{\left(E_i^0 \right)^2 E_j^0} \right\rangle_B .$$

Within the limits of nonlinear decoupling approximation (NDA), one can obtain:

$$\left\langle \frac{\left(E_i^{(lin),B} \right)^2 \left| E_j^{(lin),B} \right|}{\left(E_i^0 \right)^2 E_j^0} \right\rangle_B \approx \left\langle \frac{\left(E_i^{(lin),B} \right)^2}{\left(E_i^0 \right)^2} \right\rangle_B \left\langle \frac{\left| E_j^{(lin),B} \right|}{E_j^0} \right\rangle_B .$$

By applying NDA again and substituting the results into (3.39), one can obtain the following estimation of the second order effective susceptibility of the composite material:

$$d_{i,i,j}^{(eff)} \approx d_{i,i,j}^{(B)} (1-p) \frac{\partial \mathcal{E}_{i,i}^{(eff)}}{\partial \mathcal{E}^{(B)}} \sqrt{\frac{\partial \mathcal{E}_{j,j}^{(eff)}}{\partial \mathcal{E}^{(B)}}} . \quad (3.40)$$

Equation (3.40) is the main theoretical formula of this paragraph. It allows to estimate the effective nonlinear susceptibilities of composite materials as described (such as porous semiconductors) from the effective dielectric tensor values of said materials, which can be found

reasonably accurately based on effective medium approaches described previously in this Chapter. For the case of second harmonic generation, (3.40) must be evaluated in the form:

$$d_{i,i,j}^{(eff),SH} \approx d_{i,i,j}^{(B),SH} (1-p) \frac{\partial \epsilon_{i,i}^{(eff)}}{\partial \epsilon^{(B)}}(\omega) \sqrt{\frac{\partial \epsilon_{j,j}^{(eff)}}{\partial \epsilon^{(B)}}(2\omega)}. \quad (3.41)$$

where $\frac{\partial \epsilon_{i,i}^{(eff)}}{\partial \epsilon^{(B)}}(\omega)$ stands for the value of the partial derivative of the effective permittivity tensor element at the frequency ω , $\frac{\partial \epsilon_{i,i}^{(eff)}}{\partial \epsilon^{(B)}}(2\omega)$ stands for the value of this partial derivative at twice the frequency 2ω .

3.10. SHG from Silver-filled Pores Etched into a (110) Substrate

In this section I will apply this theory to the case of mesoporous (110)-oriented silicon substrates where the pores have been filled with metals (silver in this case) supporting surface-plasmons, i.e., I will use the results, obtained earlier in this Chapter (paragraph 3.7). Numerically calculated spectral dependences of the refractive indices of the ordinary and extraordinary waves for the silver/porous silicon system on (110)-oriented substrate composites are given in Fig. 3.9.

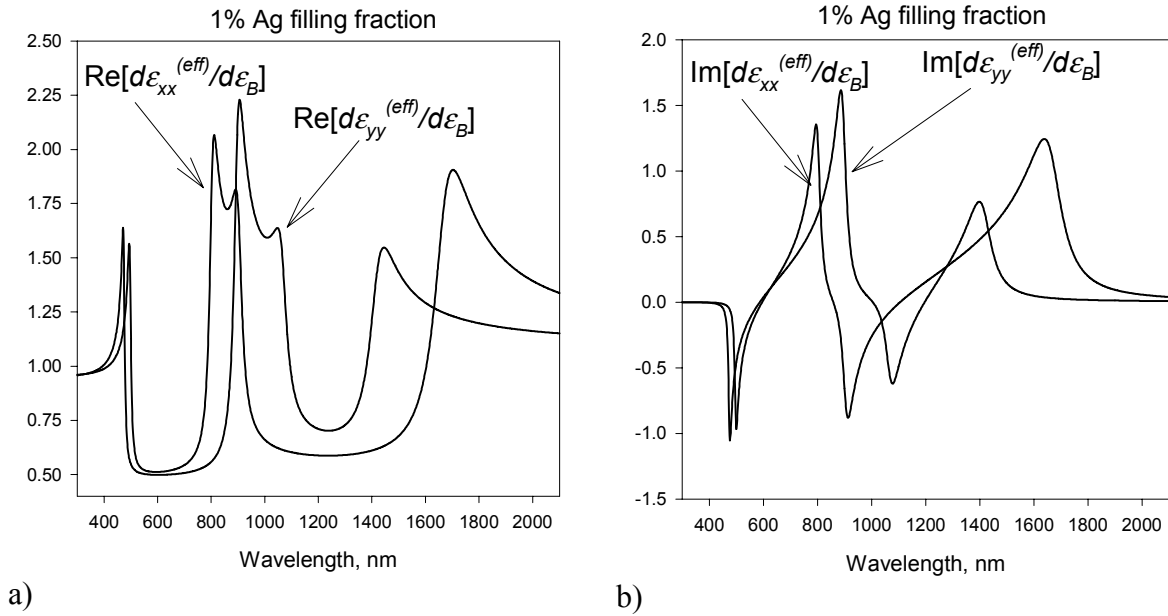


Figure 3.12. Numerically calculated spectral dependences of the a) real, and b) imaginary parts of $\frac{\partial \epsilon_{i,i}^{(eff)}}{\partial \epsilon^{(B)}}$ coefficients of the silver/ porous silicon etched on (110)-oriented wafer with filling fraction of the silver ellipsoids of 1 volume percent.

Fig. 3.12 gives the numerically calculated spectral dependences of the real (Fig. 3.12a) and imaginary (Fig. 3.12b) parts of the $\frac{\partial \epsilon_{i,i}^{(eff)}}{\partial \epsilon^{(B)}}$ coefficients for such a composite. These coefficients, as follows from the theory derived in the previous section (see eqs. (3.40-3.41)) essentially define the second order nonlinear response of the composite material. The surface plasmon-caused peaks are clearly visible. Also, they are spectrally separated for ordinary and extraordinary waves.

By using the results obtained and Eq. (3.41), we now are ready to estimate the SHG coefficients for the composite. Fig. 3.13 shows the numerically calculated spectral dependences of the

$\frac{\partial \epsilon_o^{(eff)}}{\partial \epsilon^{(B)}}(\omega) \sqrt{\frac{\partial \epsilon_e^{(eff)}}{\partial \epsilon^{(B)}}(2\omega)}$ (denoted as *o/e*), $\frac{\partial \epsilon_e^{(eff)}}{\partial \epsilon^{(B)}}(\omega) \sqrt{\frac{\partial \epsilon_o^{(eff)}}{\partial \epsilon^{(B)}}(2\omega)}$ (denoted as *e/o*),
 $\frac{\partial \epsilon_o^{(eff)}}{\partial \epsilon^{(B)}}(\omega) \sqrt{\frac{\partial \epsilon_o^{(eff)}}{\partial \epsilon^{(B)}}(2\omega)}$ (denoted as *o/o*) and $\frac{\partial \epsilon_e^{(eff)}}{\partial \epsilon^{(B)}}(\omega) \sqrt{\frac{\partial \epsilon_e^{(eff)}}{\partial \epsilon^{(B)}}(2\omega)}$ (denoted as *e/e*) coefficients, again for the composite material analyzed in relation to Fig. 3.12. One can see that the strongest enhancement factor is predicted for the $\frac{\partial \epsilon_o^{(eff)}}{\partial \epsilon^{(B)}}(\omega) \sqrt{\frac{\partial \epsilon_e^{(eff)}}{\partial \epsilon^{(B)}}(2\omega)}$ coefficient at around 1700 nm wavelength.

This result can be intuitively understood from the following considerations: due to the elliptical structure of the metal particles and three directions of preferential alignment of these particles, for some frequencies the electromagnetic field of the pump waves and the electromagnetic field of the second harmonic waves get simultaneously enhanced, leading to overall strong enhancement of the SHG. Hence, it can be concluded that the theory presented above is in agreement with the intuitive expectations; a satisfactory result given the somewhat tentative character of the theory considering the many approximations.

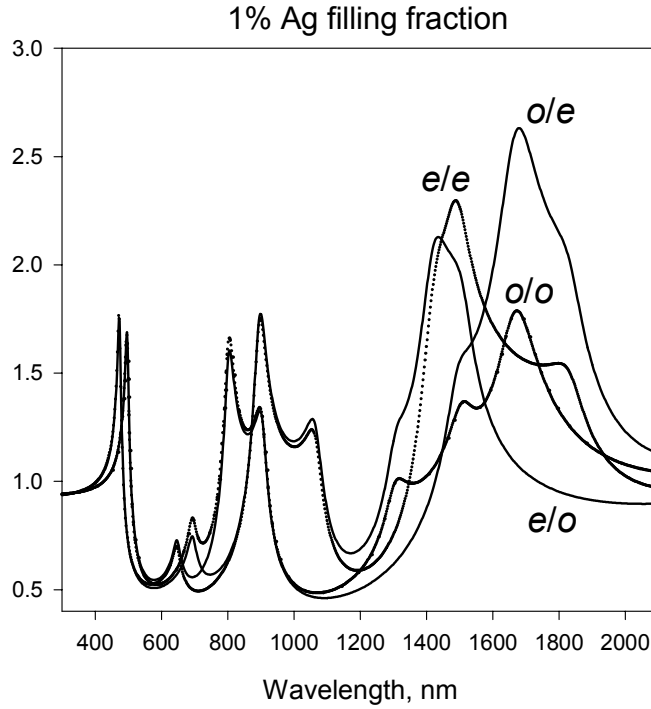


Figure 3.13. Numerically calculated spectral dependences of $\frac{\partial \mathcal{E}_o^{(eff)}}{\partial \mathcal{E}^{(B)}}(\omega) \sqrt{\frac{\partial \mathcal{E}_e^{(eff)}}{\partial \mathcal{E}^{(B)}}(2\omega)}$ (denoted as *o/e*), $\frac{\partial \mathcal{E}_e^{(eff)}}{\partial \mathcal{E}^{(B)}}(\omega) \sqrt{\frac{\partial \mathcal{E}_o^{(eff)}}{\partial \mathcal{E}^{(B)}}(2\omega)}$ (denoted as *e/o*), $\frac{\partial \mathcal{E}_o^{(eff)}}{\partial \mathcal{E}^{(B)}}(\omega) \sqrt{\frac{\partial \mathcal{E}_o^{(eff)}}{\partial \mathcal{E}^{(B)}}(2\omega)}$ (denoted as *o/o*) and $\frac{\partial \mathcal{E}_e^{(eff)}}{\partial \mathcal{E}^{(B)}}(\omega) \sqrt{\frac{\partial \mathcal{E}_e^{(eff)}}{\partial \mathcal{E}^{(B)}}(2\omega)}$ (denoted as *e/e*) coefficients of the silver/ porous silicon etched on (110)-oriented wafer with filling fraction of the silver ellipsoids of 1 volume percent.

3.11. Discussion of SHG in Certain Porous Semiconductor Composites

The quantitative result presented for a complex metamaterials could only be obtained by using a number of approximations and assumptions. Most of these are well understood or quite reasonable and it is generally possible to estimate that they will not significantly question the validity of the results obtained. The main approximation used in presented derivation that possibly limits the applicability of the developed theory, is the Nonlinear Decoupling approximation, introduced in [121], and [123]. This approximation is based on an assumption that the fluctuations of the electric field $\langle |E_j^{(lin)}|^2 \rangle - \langle |E_j^{(lin)}| \rangle^2$ within the j^{th} component are small compared to $\langle |E_j^{(lin)}|^2 \rangle$ itself. This approximation is the most accurate in metamaterials, for which the electric field is nearly uniform within the nonlinear component, and less accurate when those fluctuations are large (such as near the percolation threshold). For the

material examined here, the conditions were quite far from the percolation threshold, so the qualitative and quantitative results obtained should be fairly accurate. It should be also noted that the NDA approximation has been widely accepted, and its use in the present context thus appears to be justified; the more so since the result obtained appear to be quite reasonable from a qualitative point of view.

The theory is easily extend to other hosts and pores geometries. In this context it should be noted that it is generally possible to engineer the pore structures in semiconductors; for example the pore sizes (and, hence the axes of pore ellipsoids) can vary in to large extent by changing electrochemical etching parameters (such as silicon doping level, electrolyte composition, current density during etching, etc.). This, in turn, gives the opportunity to “tune” the theoretically predicted SHG enhancement band over a potentially wide spectral range to the near IR range currently practically important for SHG (e.g. YAG laser, powerful semiconductor lasers).

It should also be noted that the formalism developed here could be used for calculation of other second-order nonlinear processes, such as parametric amplification and frequency up-conversion.

3.12. Conclusions of Chapter III

A number of modifications to an effective medium theory have been made in order to adapt it for the calculation of linear and nonlinear optical properties a certain classes of porous semiconductors and porous semiconductor-based composite materials. In particular, the cases of pores in silicon etched in (110)-oriented substrates, and porous III-V compound semiconductors were considered, together with the case of silver-filled mesoporous silicon etched in (110)-oriented substrates. Optical anisotropy of such materials was explained and the biaxial anisotropy in porous III-V compound semiconductors was predicted at certain anodization conditions. Strong enhancement of the second harmonic generation efficiency was predicted for certain wavelengths in metal-filled mesoporous silicon etched on (110)-oriented substrate.

Chapter IV

Theoretical Analysis of Optical and Magneto-Optical Phenomena in Metal Nanocomposites

4.1. Introduction

While the exploration of the peculiar optical properties of composite materials consisting of metal nanoparticles (or, in another terminology, nanoclusters) embedded into a transparent dielectric matrix dates back to the Middle Ages [1], the first step to an understanding of the metal nanoparticle properties can be attributed to the work of Michael Faraday in the 19th century [2]. Possible applications include sensing [124] (including single-molecule detection [125]), enhancement of nonlinear processes [8], materials with otherwise unavailable optical properties, such as, for example substantial deviation from unity of the magnetic permeability at visible wavelengths [9], and many more. This area of research very recently became “mainstream” in the optical sciences under the heading “plasmonics”, with the goal of creating plasmonic integrated optical components and circuits [10].

Despite of the fact that this area of optics is relatively old, a number of topics in the optics of metal nanocomposites are not yet sufficiently developed. For example, there is still no widely accepted accurate and simple model that permits the calculation of linear optical properties of metal nanocomposites for intermediate metal filling fractions (5 % to 15 %). The theory of magneto-optical properties of metal nanocomposites is even less developed – there are only a few papers addressing some limited cases - despite of the clear promise of metal nanocomposites to enhance magneto-optical effects [126]. This chapter is intended to fill this void in theory and modeling of metal nanocomposites.

In the first part of this chapter a modified effective medium approximation (EMA), accounting for higher order interactions between metal nanoparticles in metal-dielectric composite materials, is presented. An experimental section, which elucidates the details of the composite material preparation, as well as results of the structural and optical characterization of the material, is given first. Next, a modified EMA is introduced, and the theoretical results are applied to a composite material consisting of randomly distributed spherical gold nanoparticles. Finally, the comparison of experimental results and theoretical predictions and analysis is provided. It is shown that the theory presented considerably expands the applicability range of EMA to up to a ~20 % metal filling fraction at very little additional computational expenses. It is also demonstrated that the new theory permits to extract additional information from the optical characterization of the composite material, such as the distribution of interparticle distances in a composite.

Another part of this chapter presents the theoretical formalism needed for the calculation of magneto-optical properties of metal nanocomposites. A number of metal/dielectric nanocomposites comprising magneto-optically active media (either as a magnetic or dielectric part of the composite) are evaluated. In particular, the magneto-optical activity of such composites is theoretically evaluated around the plasmon resonance conditions. A number of compound materials with significantly enhanced magneto-optical activity is proposed.

In the last part of this chapter the calculations of magneto-optical properties of the metal-dielectric composites containing core-shell nanoparticles is presented. With the recent breakthroughs in core-shell nanoparticles fabrication (see [127] and references therein) such composites become available for research and commercial applications. It is theoretically shown that core-shell nanocomposites present a significant promise in magneto-optics as well.

4.2. Linear Optical Properties of Metal Nanocomposites: Background

A considerable number of theoretical models and theories devoted to the optical response of metal particles dispersed in a transparent dielectric material have been developed up to date. At the beginning of the 20th century, Mie already gave a complete solution to the problem of light absorption and scattering from a single metallic particle [128]. Later models accounting for the collective properties of metal particles in composites were developed. Models that became classical are the Maxwell-Garnett (MG) theory [38], and the Bruggeman effective medium approximation (EMA) [14]. Both these models are still actively used today due to the ease with which one may calculate the dielectric constants of the composite - despite of considerable shortcomings of these theories, which limit accurate predictions to low concentrations of the metal. And even for low metal concentrations it was shown that both models fall short of correct predictions of the far infrared absorption [129].

For metal concentrations close to percolation conditions, a number of models were developed as well; such as a scaling approach [130-132] which offers the empirical formulas for the calculation of the divergence of the dielectric function in a close vicinity of the percolation threshold: an approach based on depolarization distribution functions (see, for example, [133, 134]), which is relatively straightforward if accounting for just the dipole polarizabilities and accurate at low concentration limits, but getting complex if accounting higher order polarizabilities; or various cluster-related approaches [135, 136] that are usually limited to some specific distribution of the metal particles in a composite, to name just a few. Calculations of individual fractal clusters were also performed by a number of authors [137, 138] using the Discrete Dipole Approximation (DDA) method. While giving accurate results, DDA is complex, and in most cases requires quite substantial knowledge of the topology of the composites.

In general both the low metal concentration limit and the “close-to-the-percolation” limit are covered quite satisfactorily with the theories already proposed. This is not the case, however, for intermediate metal filling fractions, when the EMA, MG and other models are no longer applicable due to the multi-polar polarizability contributions, while scaling theories are not yet applicable because the conditions are too far off the percolation threshold. While several interesting methodologies were suggested, such as, for example, a diagrammatic approach by Barrera [139, 140], or the method of Grechko [141], both methodologies showed limited reproduction of the experimental results at intermediate metal filling fractions.

Here I present a modification of EMA, capable of accounting for higher order interactions between metal nanoparticles in metal-dielectric composite materials. The approach given considerably expands the applicability limits of EMA, while still keeping the computations simple. In additions, I present a technique allowing to extract additional information from the optical characterization of the composite material, such as the distribution of the interparticle distances in a composite (in addition to the corrected identification of the concentration of the

metal particles). An experimental section is given first, to identify the kind of composite material used for checking the theory, and to validate the reasonableness of the assumptions used.

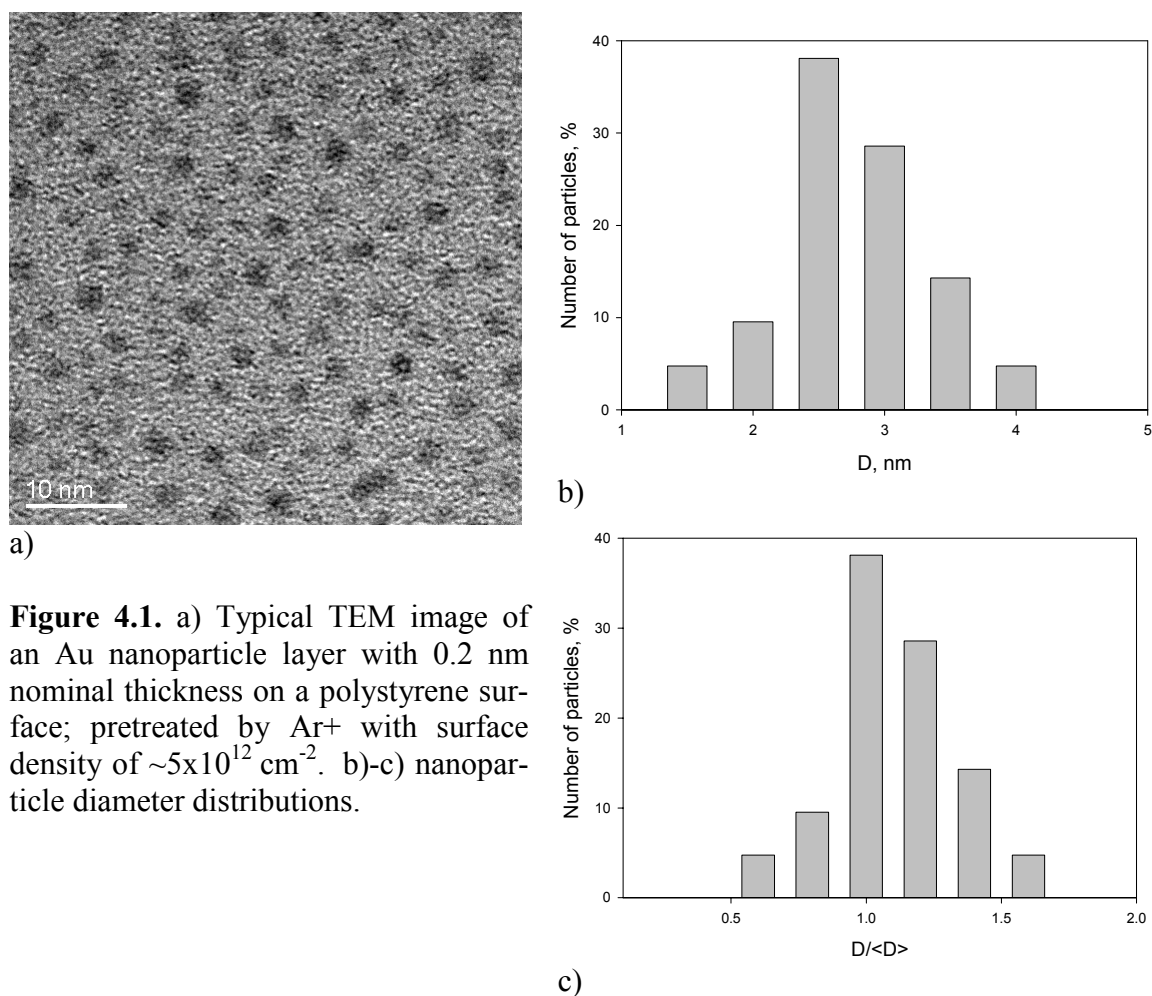


Figure 4.1. a) Typical TEM image of an Au nanoparticle layer with 0.2 nm nominal thickness on a polystyrene surface; pretreated by Ar⁺ with surface density of $\sim 5 \times 10^{12} \text{ cm}^{-2}$. b)-c) nanoparticle diameter distributions.

4.3. Experimental Results

Nanocomposite metal-polymer films prepared by vapor-phase co-deposition of Au and polymers in high vacuum is a good testing system for the optical models, since such a fabrication technique offers unique control not only over the metal filling fraction, nanoparticles size and spacing, but also over the dimensionality of the nanocomposite layer (see [142-145]). Such a method was chosen for the work reported.

Au-polystyrene nanocomposite films were synthesized by vacuum phase deposition of metal and polymer. Due to the extreme difference in cohesive energy between metal and polymer and the small metal/polymer interaction, spherical Au nanoparticles are formed either on the polymer surface or they are embedded into the polymer, as was shown in [143]. The good control over the size and interparticle distance provided by this technique allows a thorough study of how the particle plasmon modes depend on the particle size and distributions. The nanocomposite films were characterized with the different techniques like TEM, EDX, XPS, and UV-Vis spectroscopy as recently described in [142].

The optical properties were studied using an UV/Vis/NIR-spectrometer Lambda900 (Perkin Elmer). To obtain information about the morphology and the particle size and particle distribution in the nanocomposite films, TEM micrographs (Philips CM 30 TEM) were taken after deposition of nanocomposite films on carbon TEM-grids. Thickness measurements and EDX analysis were performed to determine the metal filling factors.

4.3.1.

Two-dimensional planar gold nanoparticle arrays were prepared by deposition of Au directly on a polystyrene surface. The monodisperse polystyrene (PS) ($M_w = 212000$ g/mol, $M_w/M_n < 1.1$) used in the experiments was obtained from Aldrich Chemical Company as a powder. The polymer films (with a thickness of approximately 200 nm) were prepared by dissolving the polymer powder in toluene (27 g/l) and spin coating on a silicon wafer with a native oxide layer. The PS samples were then annealed under UHV conditions for 40 min. at a temperature of 130°C, and then slowly cooled to room temperature with a constant cooling rate of 1K/min. Next, Gold (99.99 % pure, Good Fellow Industries) was evaporated from a heated Mo crucible mounted in the preparation chamber of the XPS spectrometer (Omicron Full Lab). The deposition rate R and the nominal thickness Rt were monitored by a quartz crystal microbalance, which was calibrated gravimetrically. The nominal or equivalent thickness, which is a measure for the amount of metal evaporated onto the surface, was identified by accounting for the condensation (sticking) coefficient of Au atoms on polystyrene, which was determined previously [144].

Noble metals exhibit a strong aggregation tendency during deposition on polymers due to the fact that the cohesive energy of metals is typically two orders of magnitude higher than that of polymers, and the interaction between moderately reactive metals and polymers is generally very weak in comparison to the strong metal-metal binding forces. For these reasons metals of low reactivity like gold do not wet untreated polymer surfaces and form random distributed spherical nanoparticles during vacuum deposition [145]. To avoid various sources of inhomogeneities in particle growth, an Ar ion pre-treatment of the polymer surface was performed. This treatment of the polymer surface with a low ion dose creates a definite number of surface adsorption sites (nucleation centers), the number of which is proportional to the ion flux. As was demonstrated in [145], Au adatoms are diffusing on the surface until being caught at an ion-treatment caused nucleation center. This procedure allows the synthesis of two-dimensional nanoparticle arrays with well-controlled surface density.

During vacuum deposition process the uniformly distributed spherical nanoparticles growth on the surface until they coalesce (around percolation threshold) and then form a continuous film at high metal coverage. Before the percolation the size of nanoparticles increases proportionally to $t^{1/3}$ where t is the nominal (received from quartz monitor) Au thickness. Fig. 4.1a shows a typical TEM image of the two dimensional Au nanoparticle array with nominal Au thickness of 0.2 nm. Au nanoparticle density N_c was $\sim 5 \times 10^{12}$ cm⁻² (average interparticle distance ~ 5.3 nm) and average nanoparticle diameter was 2.7 nm as it is apparent from Fig. 4.1b. The nanoparticle diameter distribution had a nearly-Gaussian shape with 0.5 nm standard deviation. At such a dosage of Ar⁺ treatment (i.e., at such a surface density of nucleation sites) during the deposition of additional Au, the cluster size grows until the nanoparticles coalesce near percolation threshold at ~ 2.2 nm nominal Au coverage.

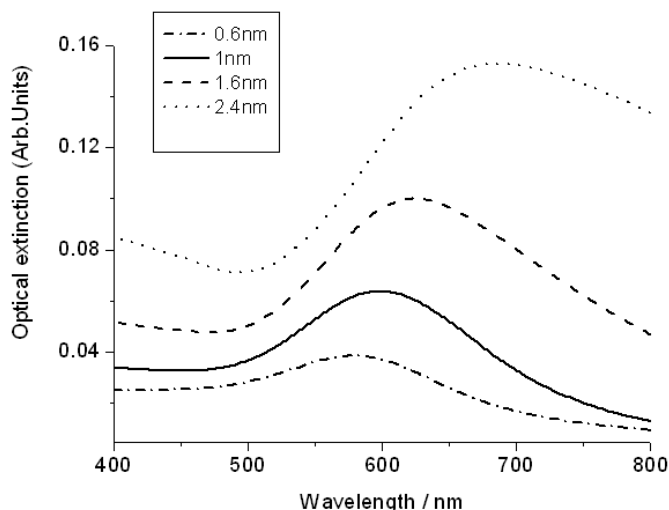


Figure 4.2. Optical extinction data for Au nanoparticles recorded for 4 different nominal Au thicknesses.

The typical extinction UV-Vis spectra at different Au thicknesses are shown in Fig 4.2. Plasmon oscillations are excited within the Au particles, which manifest themselves as a peak in a spectral dependence of the absorption. The spectral position, strength, width and shape of the plasmon resonance (PR) peak strongly depend on the nanoparticle size, interparticle distance and other parameters, thus giving a good testing data for the theoretical model, as will be shown later in this paper.

4.3.2. Three-Dimensional Au-Polystyrene Nanocomposite Films

Three dimensional nanocomposite films were prepared by simultaneous evaporation of gold with Poly(α -methylstyrene) [P(α -MS)] (ALDRICH) on glass substrates at room temperature. XPS shows that the chemical structure of the deposited polymer films was similar to the pristine polymers. Two quartz-crystal monitors were used for independent control of the deposition rates of the metal and organic species. In nanocomposite films synthesized by simultaneous metal-polymer evaporation, metal particles are uniformly dispersed and fixed in a polymer matrix (see TEM images in Fig. 4.3).

The percolation threshold in three dimensional films was identified through the resistance measurements of the nanocomposite, since percolation manifests itself as an abrupt change in the resistance characteristics from the insulation to the conductance regimes. Percolation threshold was observed at metal filling fraction around 20 %. The average values of the ratio of nanoparticle radius to interparticle distance in a case of 3D composite films were estimated in range ~ 0.3 - 0.5 for filling factors between 9.5 % and 21 %. The typical extinction UV-Vis spectra of 3D nanocomposites at different Au filling fractions are shown in Fig. 4.4.

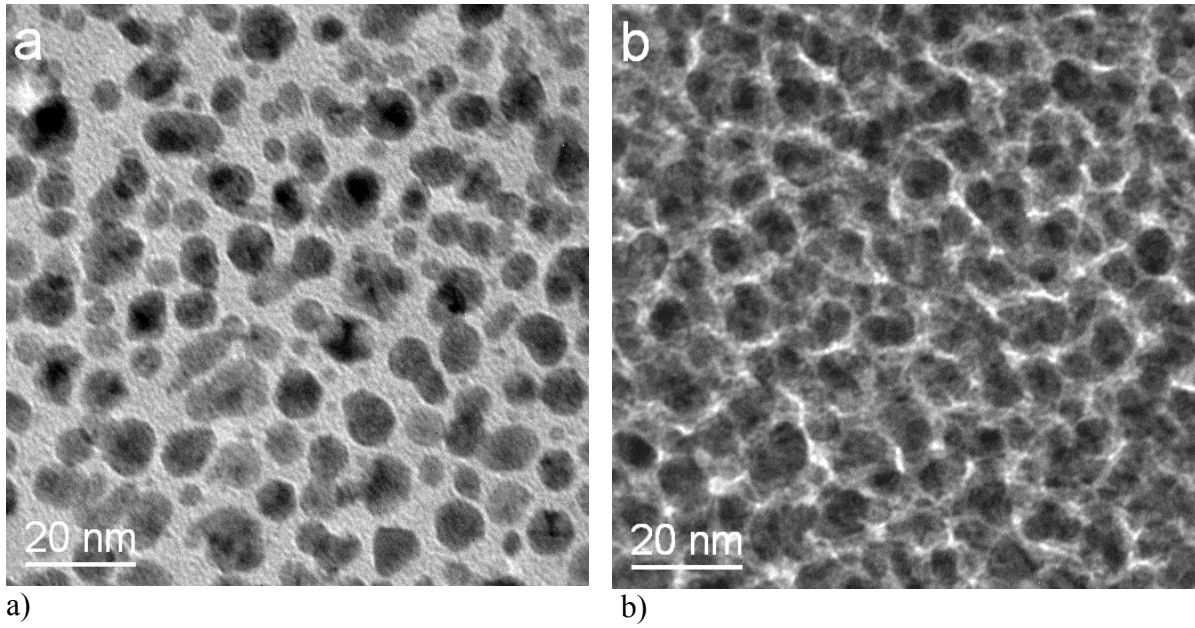


Figure 4.3. TEM micrographs of Au-polystyrene three dimensional nanocomposite films at various Au volume filling factors. a) 5 %, b) percolation – 21 %.

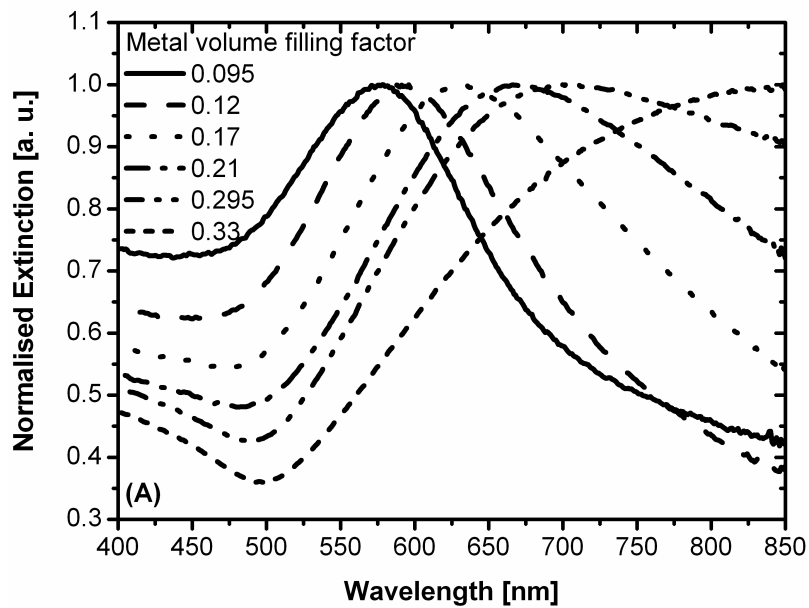


Figure 4.4. Normalized extinction UV-Vis spectra of 3D Au-polystyrene nanocomposite films at different metal filling.

4.4. Modified Effective Medium Approximation

Before deriving the modified EMA it is worthwhile to overview the list of assumptions that can be made in relation to the considered nanocomposite material. It is reasonable to assume that the polymer material has an isotropic dielectric permittivity $\epsilon^{(B)}$, independent on the metal filling fraction. Based on TEM investigation of both 2D and 3D nanocomposite materials it is further reasonable to assume a random distribution of the metal nanoparticles either over the surface of the polymer (as in 2D case) or over some volume (as in 3D case). It is obvious from TEM images that no fractal-like metal structures are formed at least up to a close vicinity of the percolation threshold. It is also reasonable to assume that the dielectric permittivity $\epsilon^{(m)}$ of metal nanoparticles is isotropic. However, the dependence of $\epsilon^{(m)}$ on the nanoparticle size cannot be neglected, especially taking into account the small size of nanoparticles in experimental samples (less than 3 nm in the 2D case and less than 10 nm in the 3D case).

Following [137] we will assume that the size-dependence of the relaxation time γ is dominant and can be approximated as $\gamma(R) = \gamma_\infty + v_F/R$, where v_F is the Fermi velocity, R is the radius of the nanoparticle and γ_∞ is the relaxation time of the bulk gold. From the Drude formula it follows that the dielectric permittivity $\epsilon^{(m)}$ of the gold nanoparticle is given by

$$\epsilon^{(m)}(R) \approx \epsilon_\infty^{(m)} + i \frac{v_F}{R} \frac{\omega}{\omega_p^2 + \gamma_\infty^2} + \frac{v_F}{R} \frac{\gamma_\infty}{\omega_p^2 + \gamma_\infty^2}, \quad (4.1)$$

where $\epsilon_\infty^{(m)}$ is the bulk value of the dielectric permittivity of bulk gold, and ω_p is the plasma frequency of gold. Equation (4.1) is quite convenient since it permits an estimation of the size-dependent correction to the dielectric permittivity, while using the tabulated values of bulk gold (i.e., values taken, e.g., from [146], which deviate from Drude-like behavior at short wavelengths). Such an approximation was used in this work. Fig 4.5 shows the calculated size-dependent corrections to the Au dielectric permittivity for 2 nm diameter nanoparticle according to Eq. (4.1)

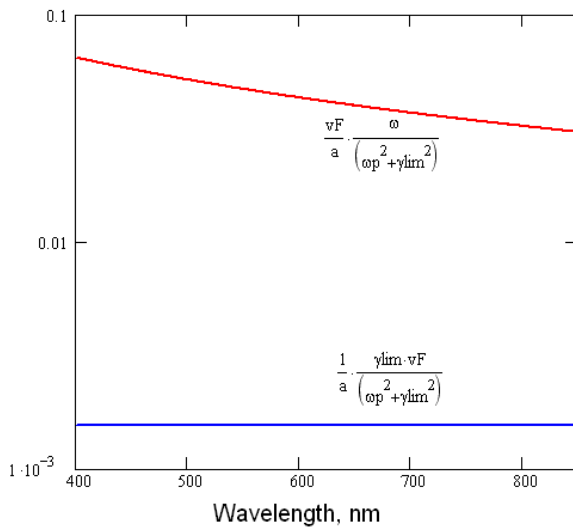


Figure 4.5. Numerically calculated spectral dependences of the size-dependent corrections to the real (blue curve) and imaginary (red curve) parts of the dielectric constant of Au nanoparticle with 2 nm diameter; according to Eq. (4.1).

Another assumption that is made in this work is the spherical shape of nanoparticles (at least till close to percolation threshold conditions). TEM investigations, however, do not provide a

definite confirmation for the validity of such an assumption. Since from another point of view it was shown [127] that a deviation from the spherical shape of the nanoparticles can cause quite a substantial shift and reshaping of the plasmon resonance absorption peak; so this is a crucial point. Fortunately, optical measurements can provide some insight into the problem. The peculiarity of the nanoparticle formation mechanism is such that the formation of elliptically shaped nanoparticles having their major axis oriented at angles different from 0° or 90° to the normal direction of the polymer surface is energetically unfavorable. In other words, if an elliptical shape of the nanoparticles is assumed, such particles would be either prolate or oblate ellipsoids with their axis being normal to the polymer surface. However, a layer composed of such particles would inevitably exhibit uniaxial anisotropy with an axis normal to the polymer surface (see for example [147]). Such an anisotropy would cause a spectral shift of the extinction of the composite film if the angle of incidence deviates from normal direction [147]. In order to validate such an assumption, measurements of absorption through the 2D nanocomposite film were made at different angles of incidence (see Fig. 4.6). One can see that no spectral shift was observed, i.e. the gold nanoparticles must be quite close to perfect spherical shape and the deviation from the spherical shape is randomly oriented, thus not causing any detectable optical effects. Quite interestingly, the results of Fig. 4.6 also demonstrate that the anisotropy due to the induced electrical polarization (image-dipoles) of the polymer underneath the nanoparticles (see [147] and references therein) can be neglected as well.

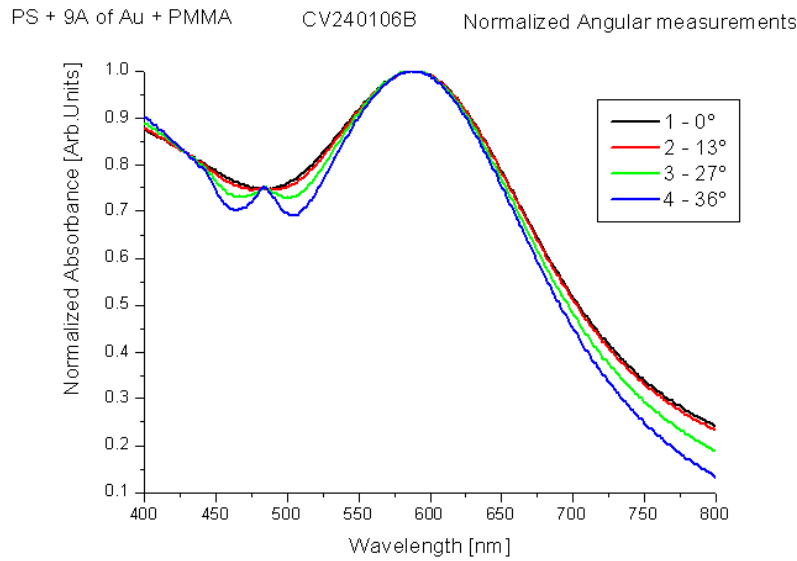


Figure 4.6. Normalized absorption spectra of 2D Au-polystyrene nanocomposite taken at different angles of incidence.

Here I will expand the EMA [14] method to account for the interactions between metal nanoparticles more accurately. The main assumption in the Bruggeman method is that the total electrical polarizability of the composite material is equal to zero. In other words, the total polarization of all the inclusions, embedded in the medium with effective dielectric parameters should vanish. In classical EMA [14] two kinds of inclusions are encountered, metal spherical inclusions with a total polarization of $P_m(\epsilon^{(eff)}) = \frac{\epsilon^{(m)} - \epsilon^{(eff)}}{\epsilon^{(m)} + 2\epsilon^{(eff)}} f_m$, and dielectric inclusions (which are also assumed to be spherical) with a total polarization of

$P_d(\mathcal{E}^{(eff)}) = \frac{\mathcal{E}^{(d)} - \mathcal{E}^{(eff)}}{\mathcal{E}^{(d)} + 2\mathcal{E}^{(eff)}}(1 - f_m)$, where f_m is the metal filling fraction and $\mathcal{E}^{(eff)}$ is the effective dielectric constant of the composite material. The classical EMA equation for $\mathcal{E}^{(eff)}$ is as follows:

$$P_m(\mathcal{E}^{(eff)}) + P_d(\mathcal{E}^{(eff)}) = 0 \quad (4.2)$$

In addition to the polarizabilities of metal and dielectric particles, in my model it is proposed to account also for the polarization originating from metal particle dimers. In order to do that, let's start with the modeling of the polarizability of isolated metal nanoparticle dimers in an insulating (and optically lossless) host.

4.5. Polarizability of Metal Nanoparticle Dimers

Over the last two decades the problem of accurately finding the polarizability of metal nanoparticle dimers was solved at least twice. The latest solution is described in [148] and is based on the so-called plasmon hybridization approach [149]. This method received a lot of attention recently, because it provides the basic understanding of the physics that takes place in the interacting particles. It also can be easily expanded to the case of particles with multiple layers (nanoshells or “nanomatrushkas”) [150]. A rigorous algorithm for the calculation of the optical response of interacting metal particles was developed in 1980th by Gerardy and Auslos (see, e.g. [151-153]), but this method is even more computationally intense than that of Prodan and is much less intuitive. Here I will follow the plasmon hybridization approach for the analysis of polarizability of metal nanoparticle dimer (after [148-150]).

In the plasmon hybridization approach it is assumed that conduction electrons in metal nanoparticles form an incompressible, irrotational, charged fluid sitting on a top of a rigid, uniform and positive background charge ρ_0 , representing the ion cores. The entire particle is assumed to be charge neutral. The dynamics of small deformations of the fluid is determined from the Lagrangian of the system:

$$L = \frac{n_0 m_e}{2} \int \eta \dot{\sigma} dS - \frac{1}{2} \int \frac{\sigma(\vec{r})\sigma(\vec{r}')}{|\vec{r} - \vec{r}'|} dS_{\vec{r}} dS_{\vec{r}'}, \quad (4.3)$$

where σ is the surface charge (“superficial charge”) distribution of the metal particle, η is a scalar function satisfying the Laplace equation $\bar{\nabla}^2 \eta = 0$, n_0 is the electron density of the conduction electrons (i.e. unique for each particle material), m_e is the electron mass. The first term in (4.3) corresponds to the kinetic energy, while the second term contains the potential energy. For a single solid metallic spherical particle the surface charge can be expressed as

$$\sigma(\Omega, t) = n_0 e \sum_{l,m} \sqrt{\frac{l}{R^3}} S_{l,m}(t) Y_{l,m}(\Omega), \quad (4.4)$$

where $Y_{l,m}(\Omega)$ is a spherical harmonic of the solid angle Ω , and e is the charge of the electron. As was shown in [150], the dynamics of the deformation of a single isolated particle embedded in vacuum is described by the Lagrangian:

$$L_S = \frac{n_0 m_e}{2} \sum_{l,m} [\dot{S}_{l,m}^2 - \omega_{S,l}^2 S_{l,m}^2] \quad (4.5)$$

where

$$\omega_{S,l} = \omega_B \sqrt{\frac{l}{2l+1}} \quad (4.6)$$

where $\omega_B = \sqrt{\frac{4\pi e^2 n_0}{m_e}}$ is the bulk plasmon frequency, and $l = 1, 2, \dots$ is the angular momentum of the respective mode.

If retardation effects are neglected (which is permissible in the case considered, since both particle sizes and the inter-particle separation distance are much smaller than the wavelength of light), the potential energy of the dimer contains an additional term characterizing the Coulomb interaction between the surface charges of the particles (after [148]):

$$V^1(x) = \int_{R_1^2} d\Omega_1 \int_{R_2^2} d\Omega_2 \frac{\sigma^1(\Omega_1) \sigma^2(\Omega_2)}{|\vec{r}_1 - \vec{r}_2|}, \quad (4.7)$$

which is a function of the separation distance x between the centers of the spherical particles.

It is fairly straightforward to expand (4.7) to the case of three or more particles. The potential energy term will then have the following form:

$$V^N(x) = \sum_{i,j} \int_{R_i^2} d\Omega_i \int_{R_j^2} d\Omega_j \frac{\sigma^i(\Omega_i) \sigma^j(\Omega_j)}{|\vec{r}_i - \vec{r}_j|}. \quad (4.7a)$$

where the summation is performed over each particle pair in a multi-particle assembly.

For the case of the dimer¹, as was shown in [148], due to axial symmetry, the interaction is diagonal in the azimuthal quantum number m (see Eq. (4.5)), so the Lagrangian can be written for each azimuthal quantum value separately in the following form:

$$L^{(m)} = \frac{n_0 m_e}{2} \sum_{i,j} \left[(\dot{S}_i^2 - \omega_i^2 S_i^2) \delta_{i,j} - \frac{\omega_B^2}{4\pi} V_{i,j}^{(m)}(x) S_i S_j \right], \quad (4.8)$$

where the interaction term $V_{i,j}^{(m)}$ is zero if I and j refer to the same sphere; otherwise we have

$$V_{i,j}^{(m)}(x) = 4\pi \sqrt{l_i l_j R_i^{2l_i+1} R_j^{2l_j+1}} \int d\theta_j \sin\theta_j \frac{P_{l_i}^m(\cos\Theta_i(\theta_j))}{(2l_i+1)X_i(\theta_j)^{l_i+1}} P_{l_j}^m(\cos\theta_j). \quad (4.9)$$

¹ The same will hold for a “linear” trimer, etc.

In Eq. 4.9 l_i and l_j stand for the angular moments of i^{th} and j^{th} particles, R_i and R_j are the radii of the i^{th} and j^{th} particle, and the P_l^m are Legendre polynomials of the second kind:

$$\Theta(\theta_j) = \arctg\left(\frac{R \cdot \sin(\theta_j)}{D - R}\right), \quad X_j = \sqrt{R^2 + D^2 - 2R \cdot D \cdot \cos(\theta_j)}$$

(in both these expressions $D \equiv x$).

From the set of equations $\frac{\partial L^{(m)}}{\partial S_i} - \frac{\partial}{\partial t} \frac{\partial L^{(m)}}{\partial \dot{S}_i} = 0$ one can conclude that the frequencies of the plasmon modes in a particle dimer are eigenvalues of the following equation:

$$\det[A_{i,j}^{(m)} - \omega^2] = 0, \quad (4.10)$$

where the matrix $A(m)$ is defined as:

$$A_{i,j}^{(m)} = \omega_i^2 \delta_{i,j} + \frac{\omega_B^2}{8\pi} (V_{i,j}^{(m)} + V_{j,i}^{(m)}). \quad (4.11)$$

and ω_l is defined according to Eq. 4.6.

Prodan et al. [150] pointed out that the structure of the secular equation (4.10) is entirely analogous to that for molecular levels obtained from atomic orbitals in a two-atom molecule. For example, the case of dimer composed of two identical spheres is entirely analogous to the case of the levels of an H_2 molecule. The matrix elements V_{ij} describes the coupling (hybridization) between the modes I and j and results in separation-dependent shifts in the dimer plasmon modes.

As an illustration, Fig. 4.7 gives the calculated plasmon energies of the lowest order plasmon modes ($m = 0, l = 1$). The slight discrepancy with the results presented in [150] close to the sphere touching point is due to the fact that in my program I truncated the expansion at $l_{\text{max}} = 4$, while in [150] the calculations included sphere plasmons with angular momentum up to $l_{\text{max}} = 50$. It should be noted that such an accuracy is probably not needed in our case because if the average distance between the particle centers approaches $2R$ (the parameter region where such a large number of interacting plasmon modes needs to be taken into account), we are getting very close to the percolation condition, so the accuracy of my model will not be satisfactory anyway in this case.

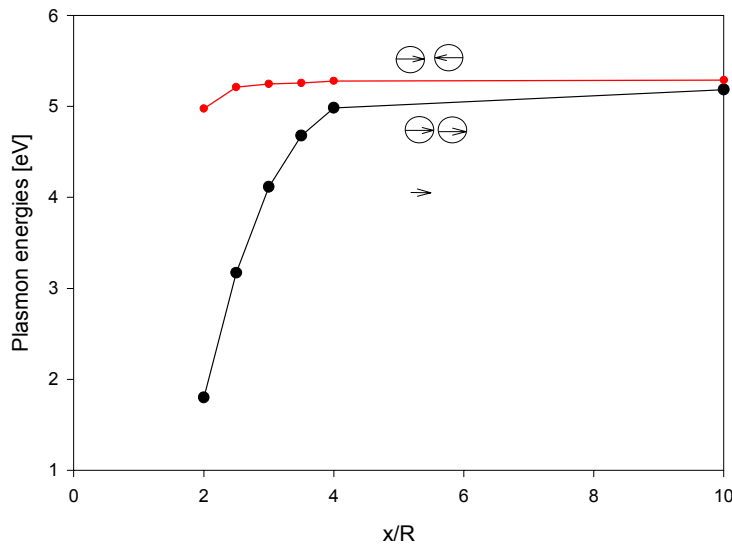


Figure 4.7. Calculated plasmon energies of two lowest order modes ($l = 1$) of a dimer as a function of a normalized particle separation (the radius of both spheres was assumed to be 3 nm) for $m = 0$. The orientation of the particles dipole moments is shown schematically.

The behavior of the plasmon modes in a dimer is schematically illustrated in Fig. 4.8a. All the modes of the individual metal particle split in two, and the value of splitting increases with the decrease of the interparticle separation (as follows from Fig. 4.7).

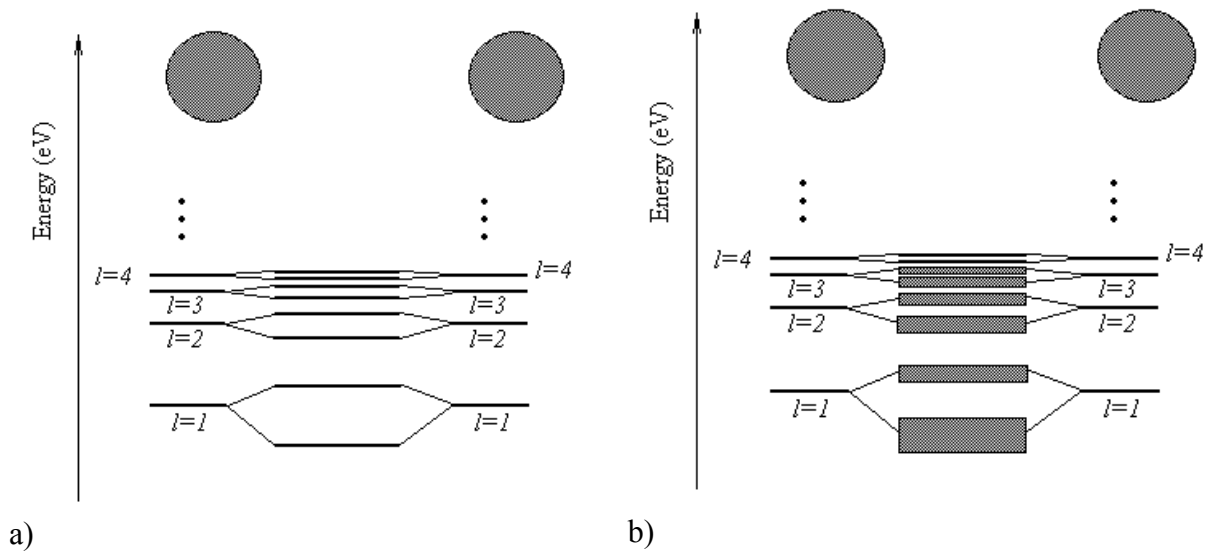


Figure 4.8. a) Plasmon hybridization in a nanoparticle dimer (after [148]); b) Effect of averaging over the distribution of dimers with some dispersion of particle separation.

If we will consider the nanoparticle dimer assembly with some distribution of the interparticle distances in dimers, then due to the averaging over the distribution of interparticle separation, we will get energy bands (instead of energy levels) as schematically shown in Fig. 4.8b). If the interparticle distance is not very close to $2R$, then, as was mentioned in [148], the splitting will be proportional to x^{-3} . The effect of the embedding of the dimer into some effective medium with some effective dielectric permittivity exceeding that of a host medium will result in some blue-shift of the energy levels of the dimer modes.

4.6. Expansion of EMA by Accounting for Dimer Polarizabilities

After an understanding of the electromagnetic interaction of nanoparticle dimers has been developed, we can now incorporate this knowledge into the EMA-type of model. In order to simplify numerical calculations, some more assumptions are needed: In my model it is further assumed that all the particles have the same radius R , and that the interparticle separation distance x obeys a Gaussian distribution law. While such an assumption is not obvious, it greatly simplifies the necessary calculations, but, as will be shown below, still provides quite a reasonable fit to the experimental data. Moreover, I limit the model to the quadrupole order of expansion in interparticle interaction. Analytical formulas for the dimensionless polarizabilities of two optically active modes of the dimer are fairly simple and can be found in [154]:

$$a_{10} = \frac{1}{1 - 3t - 2z^3 - 9z^8 \left(1 - \frac{5}{2}t - 6z^5\right)^{-1}},$$

$$a_{11} = \frac{1}{1 - 3t + z^3 - 3z^8 \left(1 - \frac{5}{2}t + 4z^5\right)^{-1}},$$
(4.12)

where $t = \frac{\epsilon^{(h)}}{\epsilon^{(h)} - \epsilon^{(m)}}$ and $\epsilon^{(h)}$ stands for either the polymer or the effective medium dielectric permittivity, and $z = R/x$, $z \in (0, 0.5)$, is a dimensionless parameter.

As an illustration, Fig. 4.9 gives the numerically calculated spectral dependences of a_{11} (Fig. 4.9a) and a_{10} (Fig. 4.9b) for different values of the ratio of nanoparticles radius to nanoparticles separation in a dimer (z parameter). In these calculations the interparticle material was assumed to be glass, and the bulk value of the Au dielectric constant was used. In such a case the results of the calculations are independent of the nanoparticle dimensions, and are dependent only on the z -parameter.

It is logical to assume a random orientation of the dimers in a composite material. In this case the important parameter for the calculation of the effective properties is the “orientation-averaged” polarizability of the nanoparticle dimer in the form of $\left[\frac{2}{3}a_{1,1} + \frac{1}{3}a_{1,0}\right]$. The numerically calculated spectral dependence of the imaginary part of this term for different values of the z -parameter are plotted in Fig. 4.10. One can see that with an increase of the z -parameter (which corresponds to a decrease of the spacing between the nanoparticles at fixed particle size, or an increase in particle size at a fixed interparticle spacing), an increase in the splitting of the resonance curve occurs with larger effects at the longer wavelength tail of the resonance curve.

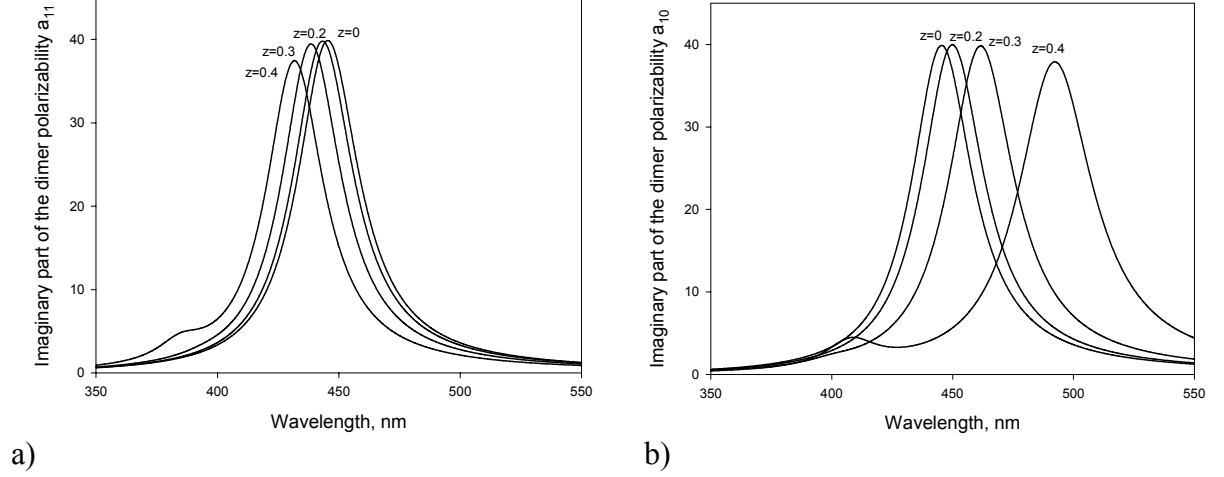


Figure 4.9. Numerically calculated spectral dependences of the imaginary parts of the polarizabilities of the a) a_{11} , and b) a_{10} optically active modes of Au nanoparticle dimer embedded in glass for different values of z -parameter (according to Eq. (4.12)).

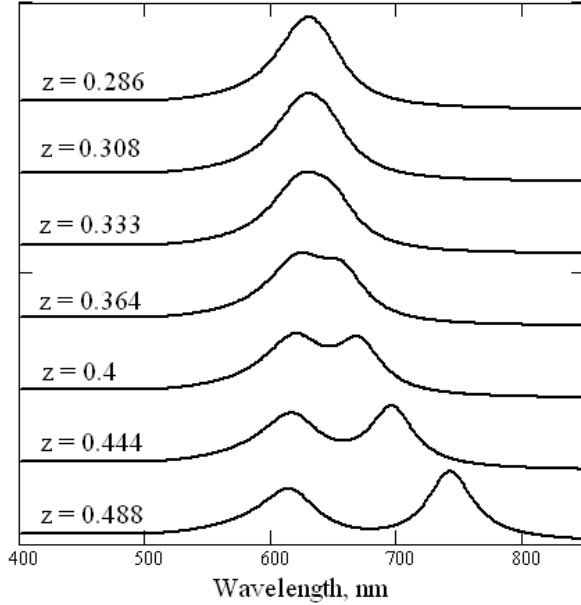


Figure 4.10. Numerically calculated spectral dependences of the “orientation averaged” polarizability of the nanoparticle dimer at different values of the z -parameter. The curves are shifted along the y -axis for easier comparison.

In order to include the nanoparticle dimer-caused contribution described above to the electrical polarization of the composite material in EMA, I propose to rewrite Eq. (4.2) in the following form:

$$A \cdot \int_{x=R}^{\infty} F(x) \cdot \left[\frac{2}{3} a_{1,1}(\mathcal{E}^{(eff)}, x) + \frac{1}{3} a_{1,0}(\mathcal{E}^{(eff)}, x) \right] \cdot dx + \tilde{P}_m(\mathcal{E}^{(eff)}) + \tilde{P}_d(\mathcal{E}^{(eff)}) = 0, \quad (4.13)$$

where $F(x)$ is the distribution function of the interparticle spacing, $\tilde{P}_m(\mathcal{E}^{(eff)}) = \frac{\mathcal{E}^{(m)} - \mathcal{E}^{(eff)}}{\mathcal{E}^{(m)} + 2\mathcal{E}^{(eff)}} \tilde{f}_m$, $\tilde{P}_d(\mathcal{E}^{(eff)}) = \frac{\mathcal{E}^{(d)} - \mathcal{E}^{(eff)}}{\mathcal{E}^{(d)} + 2\mathcal{E}^{(eff)}} \tilde{f}_d$; \tilde{f}_m and \tilde{f}_d are the appropriately reduced filling fractions of the metal nanoparticles and the host material, respectively (by the fraction of metal nanoparticles and the interparticle dielectric material accounted in dimers), and A is the coefficient defining the relative contribution of the dimer polarizability (which

will be found by fitting the experimental data). In general the type of the distribution of nanoparticles in a composite determines the particular dependence of A on the metal filling fraction. For a purely random placement of the particles I assume that it is linearly proportional to the total metal filling fraction f_m .

Equation (4.13) can be solved numerically (with substitution of the integration by a finite sum). However, equation (4.13) can be simplified under the assumption that the dimer-caused polarization contribution is small compared to $P_m(\epsilon^{(eff)})$ and $P_d(\epsilon^{(eff)})$. This corresponds to the case of concentrations reasonably far from the percolation limit. In this case the interaction term in Eq. 4.13 can be assumed to be small in comparison to the other two terms, and the effective dielectric permittivity of the composite can be found through an expansion in the following way. Let's use following abbreviations:

$$P_0(\epsilon^{(eff)}) = P_m(\epsilon^{(eff)}) + P_d(\epsilon^{(eff)}) \quad (4.14)$$

$$P_1(\epsilon^{(eff)}) = \int_{x=R}^{\infty} F(x) \cdot \left[\frac{2}{3} a_{1,1}(\epsilon^{(eff)}, x) + \frac{1}{3} a_{1,0}(\epsilon^{(eff)}, x) \right] \cdot dx, \quad (4.15)$$

where $\epsilon_0^{(eff)}$ is the solution of the equation $P_0(\epsilon^{(eff)}) = 0$, $\epsilon_1^{(eff)}$ is the solution of $P_0(\epsilon^{(eff)}) + P_1(\epsilon^{(eff)}) = 0$, $\delta\epsilon^{(eff)} = \epsilon_1^{(eff)} - \epsilon_0^{(eff)}$. Then the following equation holds to the first order approximation:

$$P_0(\epsilon_0^{(eff)}) + \frac{\partial P_0}{\partial \epsilon^{(eff)}}(\epsilon_0^{(eff)}) \cdot \delta\epsilon^{(eff)} + P_1(\epsilon_0^{(eff)}) = 0 \quad (4.16)$$

or:

$$\epsilon_1^{(eff)} = \epsilon_0^{(eff)} - \frac{P_1(\epsilon_0^{(eff)})}{\frac{\partial P_0}{\partial \epsilon^{(eff)}}(\epsilon_0^{(eff)})}. \quad (4.17)$$

In Eq. 4.17 all the terms can be relatively easily estimated numerically.

4.7. Application of the Modified EMA to Polymer/Gold Nanocomposites

In order to compare the applicability of the model presented above to metal nanoparticle composites, the calculated absorbance spectra of the Au-polystyrene film with ~10 % metal filling fraction were calculated with both the Bruggeman model and my model. The results of the calculations, together with the experimental absorbance spectrum, are plotted in Fig. 4.11. The model parameters (filling fraction in the Bruggeman model, filling fraction, size and z-parameter distribution in my case) were adjusted in order to match the spectral position of the absorbance maximum to the experimentally obtained data. fit with our model up to ~725 nm the actual contribution from dimer modes was overestimated.

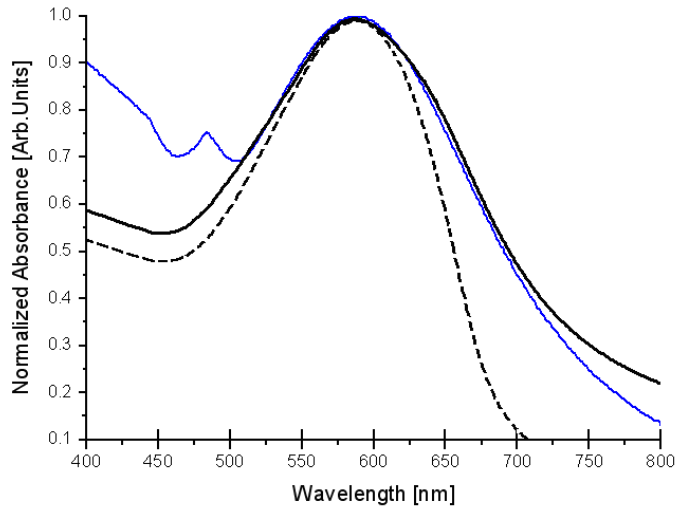


Figure 4.11. Experimentally measured normalized absorbance spectrum of the Au-polystyrene composite (blue curve); numerically calculated absorbance spectrum of Au-polystyrene composite according to the Bruggeman model (black dashed curve), and the model developed here (black solid curve).

One can see that even at such a moderate filling fraction of the metal (less than half of the percolation concentration), there is a substantial deviation between the Bruggeman model predictions and the experiment. On the contrary, my model provides a very close fit of the experimental curve from roughly 500 nm to about 725 nm. I believe that the deviation at wavelengths shorter than 500 nm (higher absorbance than predicted) is due to the losses in polystyrene material (in calculations, I neglected the dispersion of the polystyrene refractive index and assumed polystyrene to be lossless over all the spectral range). The absorption peak centered at ~ 475 nm is clearly due to the polymer material. The degradation of the accuracy of the fit with my model at the long wavelengths tail (>725 nm) is most probably due to the optically active modes excited in nanoparticle clusters with more than two particles. The contributions of such polarizations start to play a role at wavelengths shorter than 725 nm, so in order to get the best fit with my model up to ~ 725 nm, the actual contributions from dimer modes were somewhat overestimated.

In order to illustrate the range of applicability of the model, and to compare the experimentally determined values of z -parameter (through TEM investigations) with the values, providing the best fit to the data, the spectra given in Fig. 4.4 were fitted. The results are presented in Fig. 4.12. One can see that our model provides reasonably good fits up to roughly 19 % metal volume filling factor. Taking into account that the percolation threshold for such films was determined experimentally to be slightly above 20 %, so the range concentrations at which the good fit was achieved was significant. The fitting quality degraded considerably at around percolation condition (21 %), which was expected, since at such concentrations the dimer expansion is clearly insufficient and higher order polarizabilities have to be accounted.

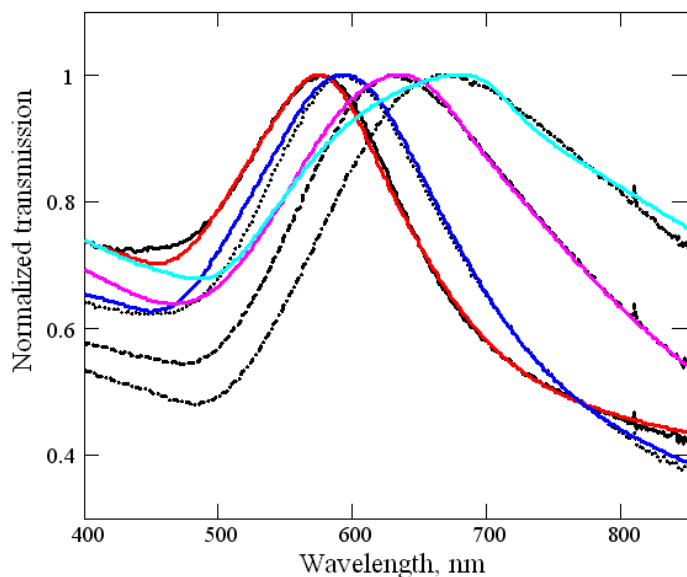


Figure 4.12. *Black curves:* Experimental extinction spectra of 3D Au-polystyrene nanocomposite films at different metal fillings (same as in Fig. 4.4); *colored curves:* numerically calculated extinction spectra according to the model presented here.

The values of z -parameter used for fitting the curves in Fig. 4.12 are given in Fig. 4.13. A Gaussian distribution of the z -parameter in dimers was assumed, while the centroid and the dispersion of the distribution functions were actually fitting parameters. The values deduced from fitting of the z -parameter were within the range of parameters identified in TEM investigations (0.3 - 0.5). Moreover, a widening of the distribution of z -parameters with the metal filling factor was predicted, which is quite consistent with the TEM observations. It thus can be concluded that the proposed model, while approximate, still can provide some additional information from analyzing optical data as compared to classical EMA. Since the necessary computations are quite simple with the technique proposed, the fitting procedure is fast and straightforward as well. I believe that the method can be very useful in studies of metal-dielectric composites below the percolation threshold conditions, since in some instances it provides information otherwise available only from time-consuming and expensive TEM investigations.

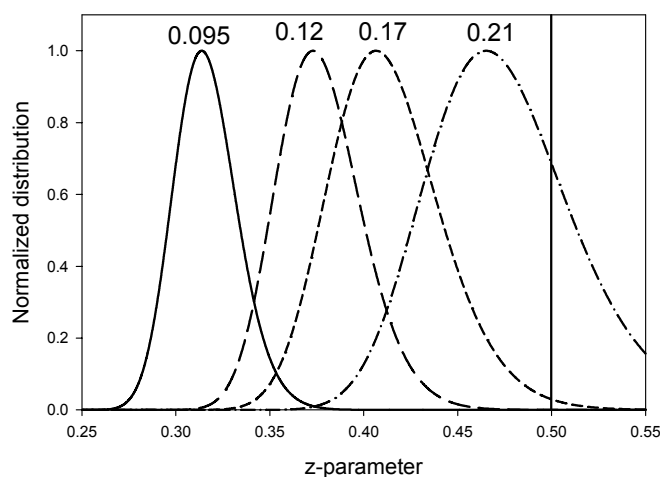


Figure 4.13. Normalized distributions of z -parameter providing the best fit to the experimentally recorded curves used in Fig. 4.12. The metal filling fractions are marked over each curve, while the z -value for a nanoparticle pair collapse is indicated as a black line.

4.8. Magneto-Optical Properties of Metal Nanocomposites: Background

Magneto-optical (MO) effects and magneto-optical materials were known and used since 19th century [155, 156]. The most prominent magneto-optical effects are the *Faraday effect* (which manifests itself in a rotation of the light's polarization plane as it propagates through a medium placed in a longitudinal magnetic field) and the *Voigt effect* (which causes the rota-

tion of the light's polarization as it propagates through a medium placed in a transverse magnetic field). The magnetic field-induced polarization rotation for light reflected from the sample surface is typically called *Kerr effect*, although physically this effect is based on the same principles as the Faraday and the Voigt effects.

The Faraday effect (or the *magneto-optical activity* of the material) is based on the Zeeman splitting of the atomic or molecular levels in the presence of an magnetic field, which leads to a difference in the resonance frequencies (and thus spectral positions and, possibly, intensities, of the absorption bands) for the right-handed and left-handed circular polarizations [157]. This results in a difference of the refractive indices n_r and n_l , respectively (and phase velocities), for light waves with right- and left-handed circular polarizations propagating through the medium, causing the rotation of the polarization. The rotation of the plane of polarization is obeying the following law:

$$\theta_F = \pi(n_r - n_l)\frac{l}{\lambda}, \quad (4.18)$$

where l is the length of the sample, and λ is the wavelength of light.

Magneto-optical effects found a large number of applications, including light modulators, optical switches, optical isolators, circulators, magneto-optical memories, and magneto-optical imagers, to name just a few. All of these applications require material with large magneto-optical activity besides the purely magnetic specifications. Magneto-optical activity was found in a large number of materials, such as magnetic metals, metal oxides, or doped glasses, to name a few. The largest magneto-optical effect is observed in metals, although in this case it is necessarily accompanied by a large absorption, thus limiting the maximal thickness of the material to less than 100 nm if operated in a transmission mode. Doped glasses, while being reasonably transparent, typically exhibit a low level of Faraday rotation per unit length, and require large values of the applied magnetic field. Macroscopically thick (up to several cm) samples are necessary in order to accommodate a 45° or a 90° polarization rotation (such as required in optical components). The range of materials with high enough magneto-optical activity and an absorption lower than that of metals (common specifications for magneto-optical imaging and magneto-optical sensing) is limited more or less to iron garnets (bismuth-doped yttrium iron garnets, in particular Bi:YIGs). However, the supply of such materials became unstable after bubble-memory applications were phased out by the market.

An enhancement of the magneto-optical effects due to surface plasmon excitations was predicted and observed in thin-film multilayer structure (Au/Co) at "Kretschmann and Otto geometries", i.e. through evanescent wave coupling (see, e.g. [158-160]). An enhancement of the polarization rotation in a grating structure on Ag/Bi:YIG interfaces through diffraction coupling was reported in [161]. Magneto-optical effects in composite materials containing metal nanoparticles also were investigated in the past: In [162] the effective dielectric permittivity tensor was derived based on the MG theory in an effort to explain the magneto-optical Kerr effect in cermets or composites in which magnetized spherical particles were embedded in dielectric materials. The Faraday effect in composite material containing metal spheres of a magneto-optically-active metal was theoretically analyzed under Bruggeman EMA assumptions in [126], while the magneto-optic Kerr effect was theoretically evaluated under Maxwell-Garnett assumptions for composite materials containing metal multilayer core-shell nanoparticles in [163]. The application of the Bruggeman EMA to the case of magneto-optical ellipsoids was described in [164], with some improvements made in [165]. However, neither the cases of magneto-optical dielectric core shell-particles, nor cases of medium or near-percolation concentrations were considered. Moreover, for core-shell structures only the

magneto-optical Kerr effect was considered and found to be suppressed since the reflectivity from the composite material at low (1 %) metal concentrations (the limit of applicability of MG approximation used in [163]) was obviously much lower than that of pure magneto-optical metal layer.

The objective of this work is to evaluate theoretically a number of metal/dielectric nanocomposites containing magneto-optically active media (either as a magnetic or dielectric part of the composite). Particularly, the magneto-optical activity of such composites is theoretically evaluated around the plasmon resonance conditions. A number of compound materials with significantly enhanced magneto-optical activity is proposed.

4.9. Faraday Effect in Metal/Dielectric Composites at Low Metal Concentrations

Here I will limit myself to the case of a Faraday geometry (i.e. the magnetization of the magneto-optically active medium is assumed to be along the propagation direction of the electromagnetic wave in the medium). I will further assume that the magnetization of the magneto-optically active medium is uniform throughout all the volume fraction of such a composite. It should be noted that such an assumption is generally incorrect in the case of magneto-optically active medium made from ferromagnetic or ferrimagnetic materials.

Assuming further that the magneto-optically active medium is spatially isotropic, the dielectric permittivity tensor of the magneto-optically active medium has the following form in the Cartesian coordinate system:

$$\hat{\boldsymbol{\epsilon}}^{(c.)} = \begin{pmatrix} \epsilon_{xx} & i\epsilon_{xy} & 0 \\ -i\epsilon_{xy} & \epsilon_{xx} & 0 \\ 0 & 0 & \epsilon_{xx} \end{pmatrix} \quad (4.19)$$

In a left-right-handed circular cylindrical coordinate system, the dielectric permittivity tensor have the following form:

$$\hat{\boldsymbol{\epsilon}}^{(l.r.)} = \begin{pmatrix} \epsilon_{xx} - \epsilon_{xy} & 0 & 0 \\ 0 & \epsilon_{xx} + \epsilon_{xy} & 0 \\ 0 & 0 & \epsilon_{xx} \end{pmatrix}. \quad (4.20)$$

It is easy to see that the transformations between different coordinate systems yield $\hat{\boldsymbol{\epsilon}}^{(l.r.)} = \hat{A} \cdot \hat{\boldsymbol{\epsilon}}^{(c.)} \cdot \hat{A}^{-1}$ and $\hat{\boldsymbol{\epsilon}}^{(c.)} = \hat{A}^{-1} \cdot \hat{\boldsymbol{\epsilon}}^{(l.r.)} \cdot \hat{A}$ in a Faraday geometry can be obtained with the

help of the matrix $\hat{A} = \frac{1}{\sqrt{2}} \begin{pmatrix} 1 & -i & 0 \\ 1 & i & 0 \\ 0 & 0 & \sqrt{2} \end{pmatrix}$. The Faraday rotation per unit length of the material

then is equal to:

$$\theta_F = \frac{\pi}{\lambda} \cdot \frac{\text{Re}[\epsilon_{xy}]}{\text{Re}[\sqrt{\epsilon_{xx}}]}, \quad (4.21)$$

while the ellipticity is given by:

$$\phi = \frac{\pi}{\lambda} \cdot \frac{\text{Im}[\epsilon_{xy}]}{\text{Re}[\sqrt{\epsilon_{xx}}]} \quad (4.22)$$

4.10. Gold Nanoparticles Embedded into a Magneto-Optically Active Dielectric with Magneto-Optical Properties

Let's consider first the case of metal nanoparticles (gold, for example) embedded into a magneto-optical dielectric material. The geometry that I am considering is schematically shown in Fig. 4.14a). Under the assumption of a perfectly spherical shape of the metal nanoparticles the polarizabilities of the gold nanoparticle with radius a for the right- and left-handed circular polarizations ($\alpha^{l.h}$ and $\alpha^{r.h}$, respectively) of an electromagnetic wave will be as follows:

$$\alpha^{l.h} = 4\pi a^3 \frac{\epsilon_{Au} - (\epsilon_{xx} - \epsilon_{xy})}{\epsilon_{Au} + 2(\epsilon_{xx} - \epsilon_{xy})} \quad (4.23a)$$

$$\alpha^{r.h} = 4\pi a^3 \frac{\epsilon_{Au} - (\epsilon_{xx} + \epsilon_{xy})}{\epsilon_{Au} + 2(\epsilon_{xx} + \epsilon_{xy})} \quad (4.23b)$$

The spectral dependences of the normalized polarizability of gold nanoparticles embedded into a magneto-optically active dielectric for the right-handed and the left handed circular polarizations of the incident electromagnetic wave are given in Fig. 4.14b). The dispersion of the diagonal and non-diagonal parts of the dielectric constants of the MO-active material were neglected the same as an absorption in magneto-optically active dielectric material. The diagonal part of the dielectric constant of the MO active material was assumed to be 2.35, while the non-diagonal parts were assumed to be 0.1 (values close to those of Bi:YIG at ~514 nm wavelength). The splitting of the plasmon modes for the two polarizations is demonstrated.

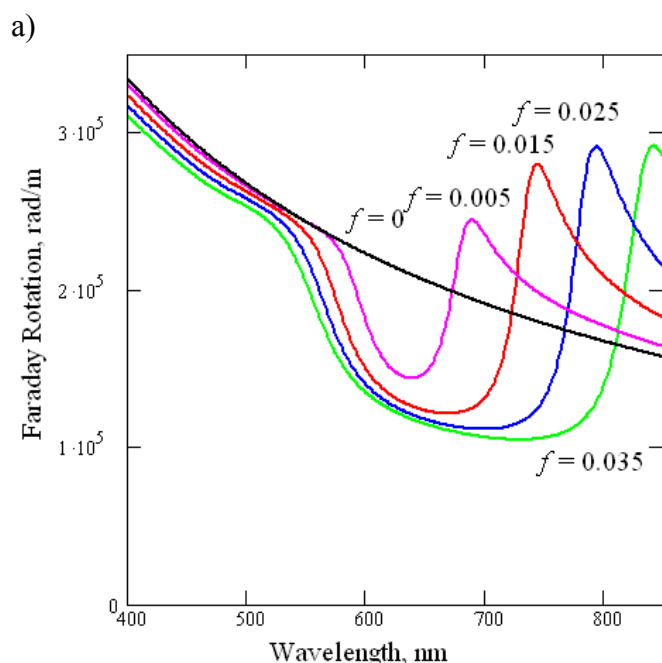
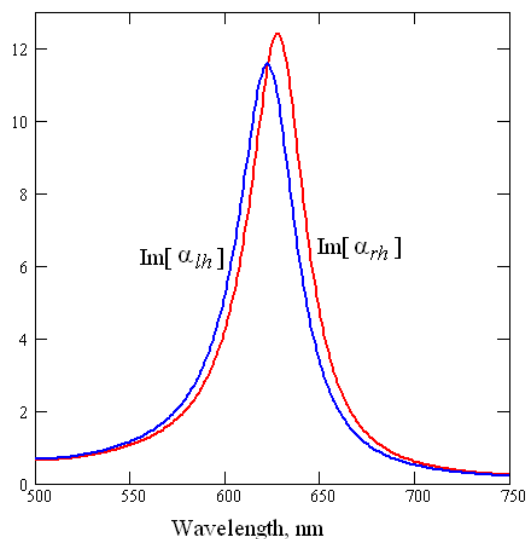
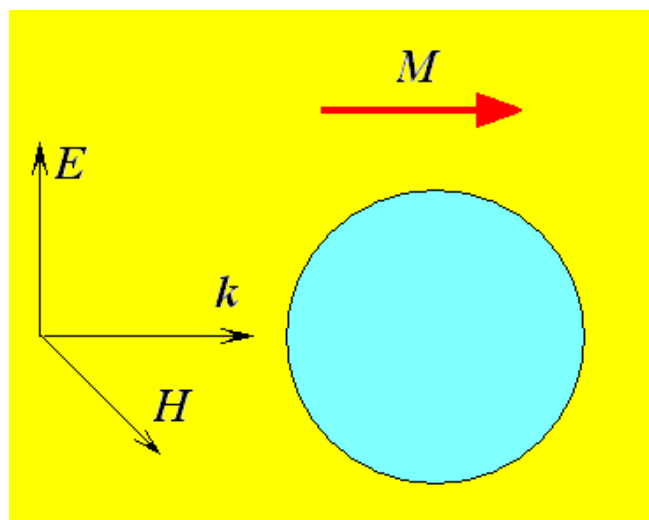


Figure 4.14. a) Schematic drawing of the gold nanoparticle embedded into a magneto-optically active dielectric material. The orientations of magnetization and direction of light propagation are schematically shown; b) numerically calculated spectral dependences of the normalized polarizability of gold nanoparticles embedded in a magneto-optically active dielectric for right-handed and left-handed circular polarizations of the incident electromagnetic wave; c) numerically calculated spectral dependences of the Faraday effect in a composite material consisting of Au nanoparticles embedded into the magneto-optically active dielectric for different filling fractions f of metal.

For calculations of the effective dielectric constant of the composite material, I am further assuming that 1) nanoparticles are small compared to the wavelength (which is a very reasonable assumption), and 2) the distribution of particles in the composite is macroscopically isotropic in all three dimensions. For low (<5 %) and high (above 95 %) concentrations of metal in a composite, the Bruggeman EMA [14] is a reasonably accurate approximation for visible and near infrared spectral ranges. If applied to a magneto-optical medium, Bruggeman's EMA accounts for two kinds of inclusions, metal spherical inclusions with total polarization of

$$\bar{P}_m = f_m (\hat{\epsilon}^{(m)} + 2\hat{\epsilon}^{(eff)})^{-1} (\hat{\epsilon}^{(m)} - \hat{\epsilon}^{(eff)}) \bar{E}_0, \quad (4.24a)$$

and dielectric inclusions (which are also assumed to be spherical) with a total polarization of

$$\vec{P}_d = (1 - f_m)(\hat{\epsilon}^{(d)} + 2\hat{\epsilon}^{(eff)})^{-1}(\hat{\epsilon}^{(d)} - \hat{\epsilon}^{(eff)})\vec{E}_0, \quad (4.24b)$$

where f_m is the metal filling fraction, and $\epsilon^{(eff)}$ is the effective dielectric constant of the composite material, $(\dots)^{-1}$ stands for the inverse matrix of (\dots) , and \vec{E}_0 is the electric field of the propagating electromagnetic wave. The value of $\epsilon^{(eff)}$ can thus be found from equation (4.2).

In a left-right circular cylindrical coordinate system all matrices of the dielectric constants are diagonal, so equation (4.2) transforms into three scalar quadratic equations for the different elements of the effective dielectric constant tensor. Based on such an approach, one can come up with a simple perturbational approach (under the assumption that $|\epsilon_{xy}| \ll |\epsilon_{xx}|$, which is typically the case for all the magneto-optically active materials) for the estimation of the Faraday effect in a composite material (for all the assumptions listed previously, and under the additional assumption that only one component in a composite exhibits magneto-optical activity):

$$\theta_F \approx \frac{\pi}{\lambda} \cdot \frac{1}{\text{Re}[\sqrt{\epsilon_0^{(eff)}}]} \text{Im} \left[\frac{\partial \epsilon_0^{(eff)}}{\partial \epsilon_{MO}} i \epsilon_{xy} \right], \quad (4.25)$$

where $\epsilon_0^{(eff)}$ is the effective dielectric constant of the composite material at zero magnetization (since we assumed isotropy of the composite at the absence of magnetization), ϵ_{MO} is the dielectric constant of the magneto-optically active material at zero magnetization, and $i\epsilon_{xy}$ is the nondiagonal element of the dielectric permittivity tensor of the magneto-optically active material at non-zero magnetization.

Thus, with such a perturbational approach, the enhancement factor Γ_F of the Faraday coefficient in a composite can be estimated as:

$$\Gamma_F \approx \frac{1}{\text{Re}[\sqrt{\epsilon_0^{(eff)}}]} \text{Re} \left[\frac{\partial \epsilon_0^{(eff)}}{\partial \epsilon_{MO}} \right]. \quad (4.26)$$

It is quite interesting to compare the average electrical field enhancement factor Γ_E in a magneto-optically active medium in a composite, which can be roughly estimated at the assumption of low metal concentrations as follows (see [120-121]):

$$\Gamma_E = \frac{\langle E^2 \rangle_{MO}}{E_0^2} \approx \frac{1}{f_{MO}} \text{Re} \left[\frac{\partial \epsilon_0^{(eff)}}{\partial \epsilon_{MO}} \right] \quad (4.27)$$

By comparing (4.26) and (4.27), it is fair to conclude that at low metal concentrations the Faraday coefficient in a nanocomposite material is proportional to the electromagnetic wave intensity enhancement factor due to the plasmon resonance in metal nanoparticles, i.e.

$$\Gamma_F \approx \frac{f_{MO}}{\text{Re}[\sqrt{\epsilon_0^{(eff)}}]} \Gamma_E \quad (4.28)$$

With the formalism developed, one thus may obtain an estimate for the magneto-optical effects, based on the knowledge of the dielectric permittivity of a composite material with no magneto-optically active medium. The problem is now mathematically much simpler, due to a large number of already solved cases for non magneto-optically active composites.

Using such a simple formalism, I calculated the dielectric properties and thus the Faraday rotation of a composite with the same composition as in Fig. 4.14b) under the same assumptions (losses in the magneto-optically active dielectric were neglected, as well as the dispersion of tensor elements of the dielectric permittivity of the dielectric). Results are presented in Fig. 4.14c). One can see that the Faraday coefficient of such a composite exhibit certain peculiarities around the plasmon resonance wavelength, with some enhancement of Faraday coefficients at certain wavelength range exceeding plasmon resonance wavelength and degradation of the Faraday coefficient at certain wavelength range below the plasmon resonance wavelength.

4.11. Magneto-Optically Active Dielectric Nanoparticle Embedded in Gold

Using the same formalism I estimated the Faraday coefficient and dielectric constants of the composite material with high gold concentrations. Physically such a material is made of magneto-optically active dielectric nanoparticles embedded in gold, as schematically shown in Fig. 4.15a). The numerically calculated spectral dependences of the Faraday coefficient and the imaginary part of the diagonal tensor element of effective dielectric permittivity are given in Figs. 4.15b) and 4.15c), respectively. The strong peak of the Faraday rotation corresponds to the so-called cavity plasmon resonance; which is also causing a significant enhancement of the electromagnetic field in the cavities. The peculiarity of such a material is a very high loss coefficient of the material, which probably makes such a material completely impractical in a transmission mode. In a reflection mode, however, such a material may be of interest to some applications, since it combines significant values of the Faraday coefficient (comparable with that of magneto-optically active metals, such as Co or Ni) with the comparatively large reflectivity of gold in the green-red spectral range (in comparison with reflectivities of, e.g., Co and Ni).

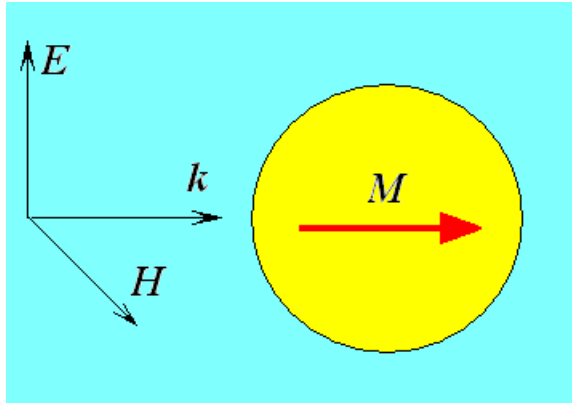
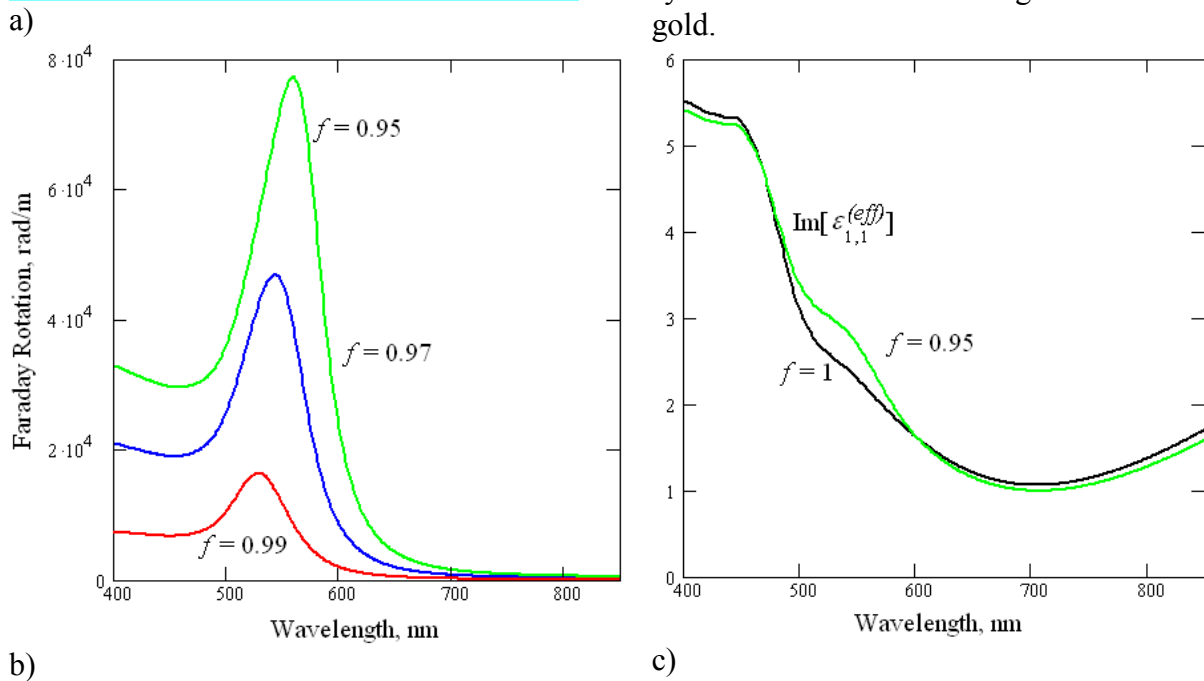


Figure 4.15. a) Schematic drawing of the nanocomposite made from a magneto-optically active dielectric material embedded into gold; b) numerically calculated spectral dependences of the Faraday effect in such a composite for different filling fractions f of gold; c) numerically calculated spectral dependences of the imaginary part of the diagonal element of the effective dielectric constant in a Cartesian coordinate system for different filling fractions of gold.



4.12. Magneto-Optically Active Metal Nanoparticles Embedded in a Dielectric Matrix

Another type of composite material that was evaluated consisted of magneto-optically active metal nanoparticles embedded into the isotropic dielectric material (a schematic drawing is given in Fig. 4.16a). In the calculations the dielectric constants of Co were used. The results of numerical calculations of the Faraday rotation in such a composite material for different Co filling fractions are given in Fig. 4.16b). The plasmon resonance manifests itself by a change in the sign of the Faraday coefficient in the green-red portion of the spectrum. The spectral feature caused by the plasmon resonance in Co nanoparticles is spectrally broad, and virtually no plasmon-caused enhancement of the magneto-optical activity in such a composite is predicted. This is due to the strong damping of the plasmons in Co (due to the close to unity ratio of $\frac{\text{Re}[\varepsilon_{Co}]}{\text{Im}[\varepsilon_{Co}]}$, which defines the quality of plasmon resonance).

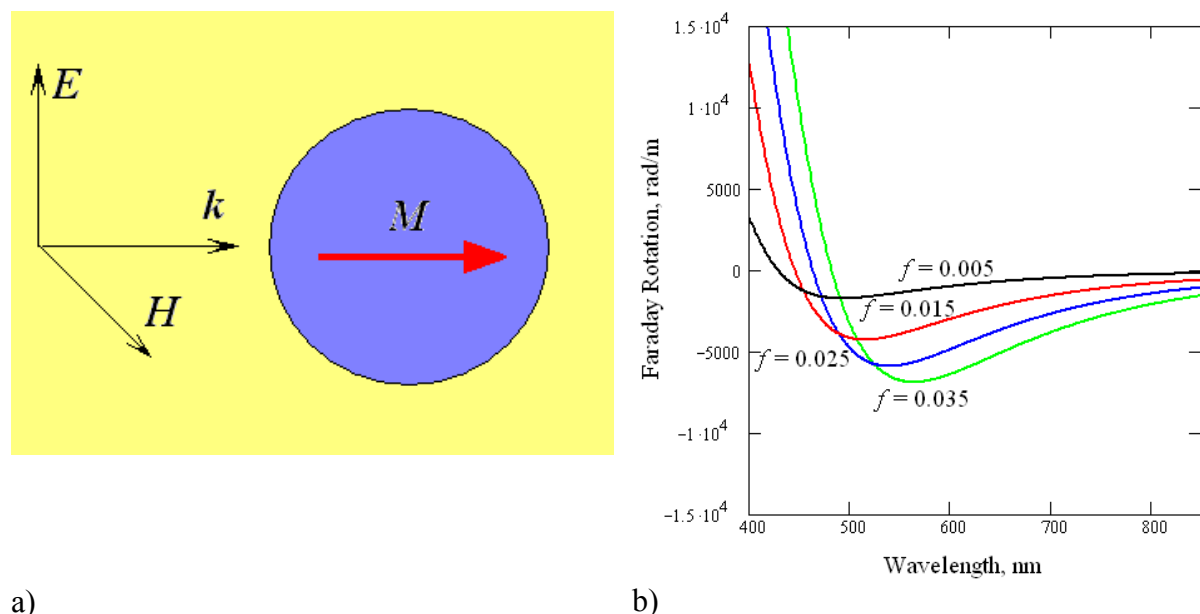


Figure 4.16. a) Schematic drawing of a magneto-optically active metal nanoparticle embedded in glass; b) numerically calculated spectral dependences of the Faraday effect in such a composite material for different filling fractions of the magneto-optically active metal.

4.13. Mixtures of Magneto-Optically Active Metal Nanoparticles and Gold Nanoparticles Embedded in a Dielectric Matrix

An interesting case (that is also and relatively simple to make) is the combination of the “good” plasmon resonance of gold with the “good” magneto-optical activities of metals like Co. This can be achieved in nanocomposites containing gold nanoparticles and magneto-optically active metal nanoparticles embedded in a dielectric loss-less matrix, as schematically shown in Fig. 4.17a). In order to estimate the magneto-optical response of such a composite one can use a similar formalism to that described above (under the same assumptions), with equation (4.2) replaced by:

$$\bar{P}_{Au}(\hat{\epsilon}^{(eff)}) + \bar{P}_{M.O.}(\hat{\epsilon}^{(eff)}) + \bar{P}_d(\hat{\epsilon}^{(eff)}) = 0 \quad (4.29)$$

The numerically calculated spectral dependence of the Faraday rotation for such a composite for different filling fractions of Au and Co nanoparticles are given in Figs. 4.17b)-c), while Fig. 4.17d) gives the normalized value of the Faraday rotation at a fixed Co filling fraction and for different Au filling fractions. The peak at ~675 nm is obviously caused by the change in the sign of the Faraday coefficient in the Co/glass nanocomposite (which was used as a reference point in normalization). However, it also follows that by adding gold nanoparticles into the composite, a substantial enhancement of the magneto-optical can be expected - almost an order of magnitude at near-IR wavelengths!

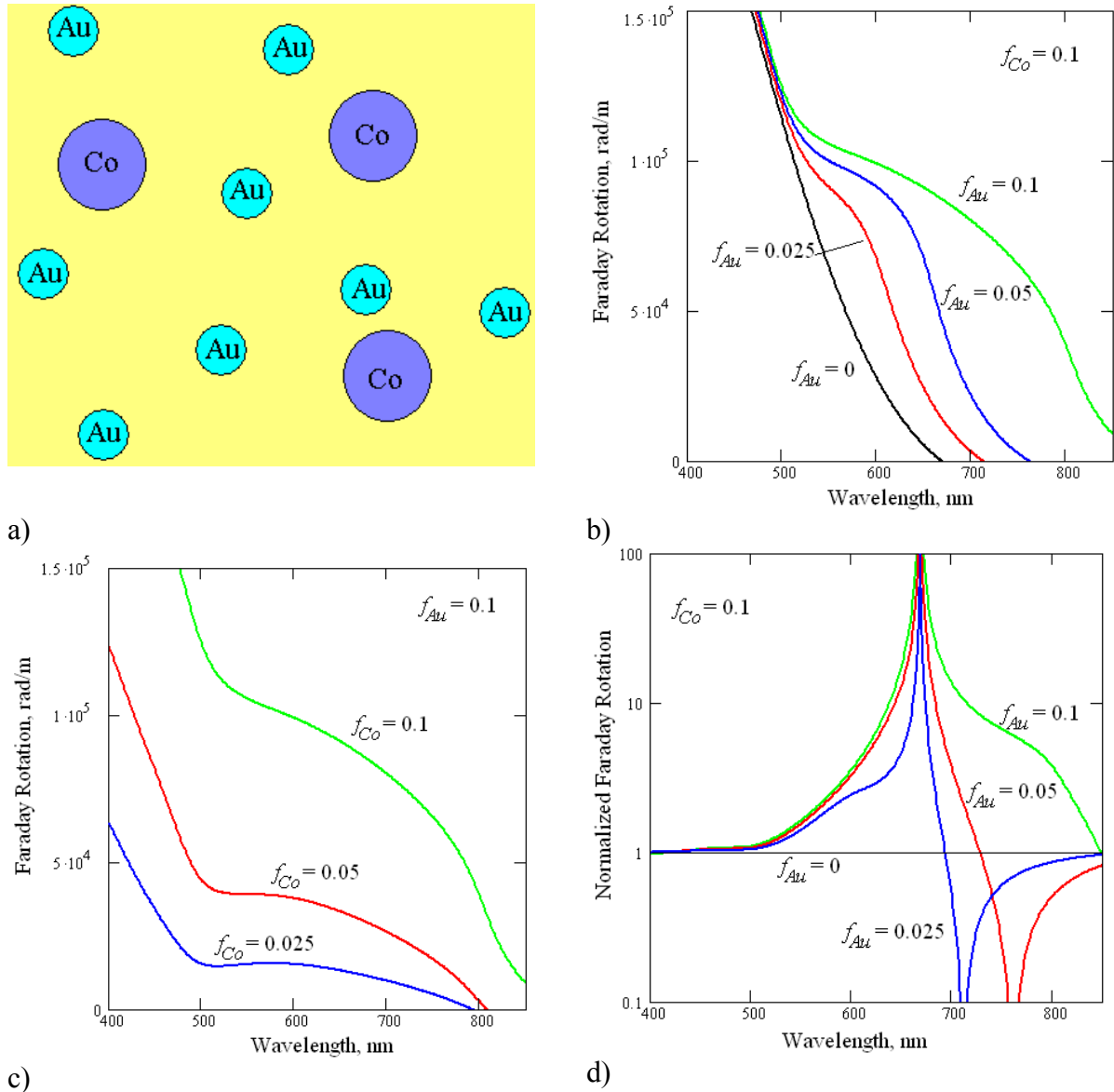


Figure 4.17. a) Schematic drawing of the nanocomposite material consisting of magneto-optically active metal nanoparticles and gold nanoparticles embedded in glass; b) numerically calculated spectral dependence of the Faraday effect in such a composite material for different gold filling fractions at a fixed Co filling fraction (0.1); c) numerically calculated spectral dependences of the Faraday effect in such a composite material for different Co filling fractions at a fixed Au filling fraction (0.1); and d) numerically calculated spectral dependences of the normalized Faraday rotation in such a composite material for different gold filling fractions at fixed Co filling fraction (0.1).

4.14. The Faraday Effect in Metal/Dielectric Composites at Intermediate Metal Concentrations

As already mentioned in this chapter, at intermediate concentrations of metal in a composite (5 %-15 % of metal), the accuracy of Bruggeman's EMA deteriorates, due to multiparticle polarizability contributions; i.e., the polarizability of individual constituents in a composite cannot be estimated according to Eq. (4.24) anymore. Here I will use the method described in the beginning of this chapter.

By applying the formalism developed previously (Equations (4.21-4.25) and related discussion), the polarizabilities of the "orientation-averaged" nanoparticle dimers were calculated for $z = 0.488$. The results are plotted in Fig. 4.18. By comparison with the calculations for the single nanoparticle (Fig. 4.14b) one can see that accounting for the contributions from dimer polarizabilities should provide stronger Faraday effects at longer wavelengths than the plasmon resonance of a single nanoparticle.

By using the perturbational approximation (see Equations (4.14-4.17)), numerical calculations of the imaginary part of the effective dielectric function for an Au-YIG (zero magnetization) nanocomposite were performed. The results are given in Fig. 4.19a) (calculations were done in a quadrupole approximation). One can see that on account of the dimer Polarizability, a red-shift and a strengthening of the plasmon peak is predicted.

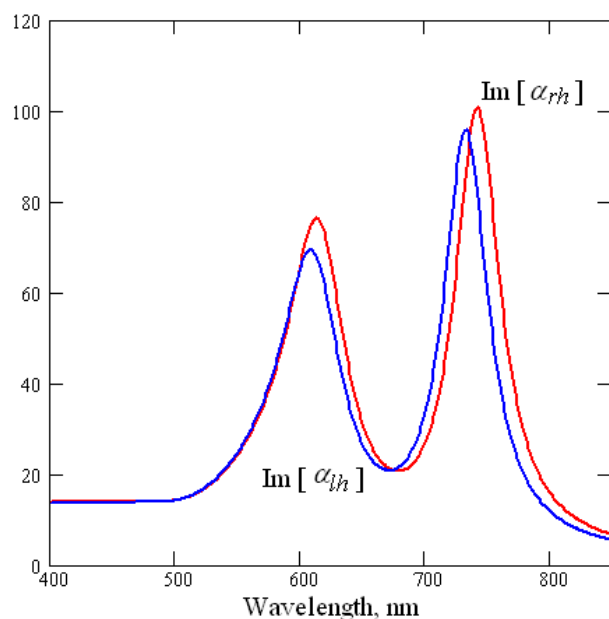


Figure 4.18. Imaginary parts of the normalized orientation-averaged polarizability of the nanoparticle dimer (Au in YIG) for $z = 0.488$, for different polarizations of electromagnetic wave in a quadrupole approximation.

Numerically calculated Faraday coefficients of the Au-YIG nanoparticle composite at intermediate metal filling fractions are given in Fig. 4.19b). As was expected from Fig. 4.18, accounting for interparticle interactions results in a further enhancement of the Faraday coefficient in the near-IR spectral region, although the enhancement is moderate and expected to be in the range of a factor of 2 - 3.

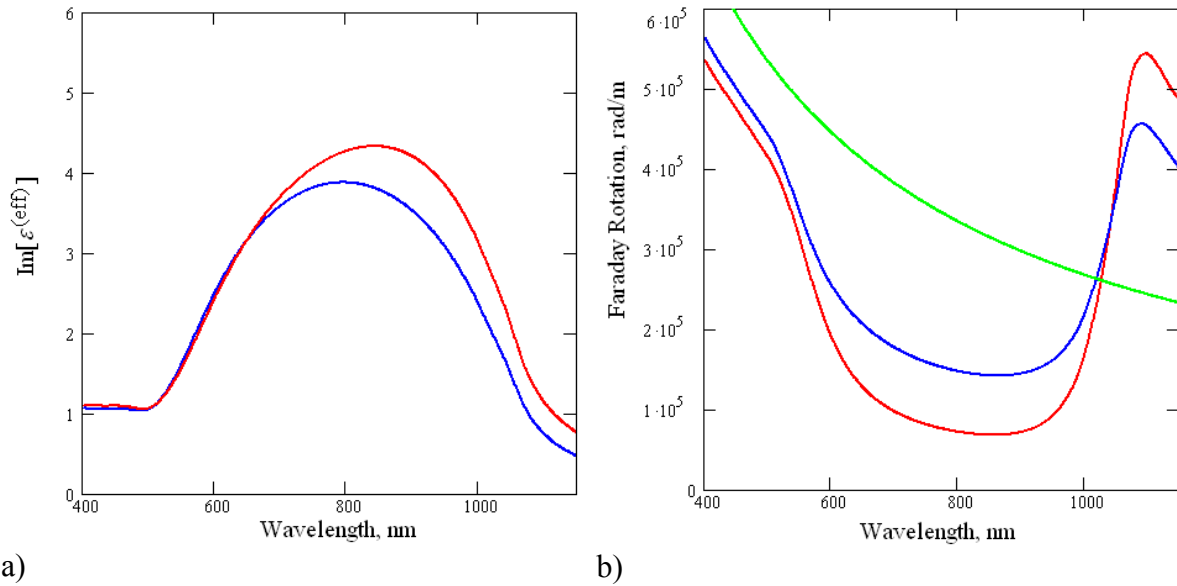


Figure 4.19. a) Numerically calculated spectral dependences of the imaginary part of the effective dielectric constant of an Au-YIG composite (at zero magnetization) for 0.08 filling fraction of Au with Bruggeman's EMA (blue curve), and with taking the interparticle polarizability into account (red curve); b) numerically calculated spectral dependences of the Faraday coefficient in an YIG/Au composite (the same parameters were assumed as in Figs. 4.15-4.16) for 0.08 Au filling fraction, calculated according to Bruggeman EMA (blue curve) and with the dimer approximation (red curve). The Faraday coefficient of the YIG is plotted for comparison (green curve).

Based on the above results one would expect that the enhancement of the Faraday rotation would be higher close to the metal percolation threshold. However, neither Bruggeman EMA [14] nor models accounting for some level of interparticle interactions, are providing the necessary accuracy. Hence, different models have to be used.

4.15. Faraday Effect in Metal/Dielectric Composites Near the Percolation Threshold

For the metal concentrations close to the percolation conditions a number of models were developed for metal-dielectric composites made with isotropic inclusions. Examples are: the scaling approach [130-132], which offers the empirical formulas for calculation of the divergence of the dielectric function in a close vicinity of the percolation threshold; an approach based on depolarization distribution function (see, for example, [133-134]), which is relatively straightforward if accounting just for the dipole polarizabilities (accurate at low concentration limits), but getting complex if accounting for higher order polarizabilities; various cluster-related approaches [135,136] that are usually limited by some specific distribution of the metal particles in a composite; to name reiterate what has been said before. Calculations of individual fractal clusters were also performed by a number of authors [137,138] with a DDA (discrete dipole approximation) method. While giving accurate results, DDA is complex, and in most cases requires a quite substantial knowledge of the topology of the composites.

All of these theories predict very strong enhancements of the local $\left| \frac{\vec{E}(\vec{r})}{\vec{E}_0} \right|$ and of the average $\left\langle \left| \frac{\vec{E}}{\vec{E}_0} \right| \right\rangle$ for electromagnetic fields near the percolation threshold. This explains the huge enhancements observed (up to 14 orders of magnitudes) for nonlinear optical processes (second and third harmonic generation, etc.) near the percolation threshold (see [8] and references therein). As was shown previously in this chapter, at low metal filling fractions the enhancement of the Faraday rotation in a composite is proportional to the electromagnetic field enhancement factor (see Eq. (4.28) and related discussion). However, one should note that the magneto-optical effects that I investigate here are nonreciprocal, unlike the nonlinear optical effects. Thus the local mutual orientation of the magnetization direction, propagation direction and electric field vector may have an effect on the total Faraday effect in a composite material.

In order to evaluate the magneto-optical properties of metal-dielectric composites near the percolation threshold, I will evaluate separately the magneto-optical effect in arrays of ordered metal nanodiscs and nanospheres, since the analytical solution is available for such composites [166], and will then analyze the theoretical predictions based on a scaling theory [130-132].

4.16. Cubic Array of Au Nanodiscs Embedded in YIG

First, let's consider the composite material made of a two-dimensionally ordered array of gold nanocylinders (or nanodiscs) embedded into a magneto-optically active dielectric material (a schematic drawing is given in Fig. 4.20a). Let's assume that the light is propagating parallel to the axis of rotation of these cylinders, which is also the magnetization direction. For the case of zero magnetization one can use the following equation to estimate the value of the effective dielectric constant according to formula derived in [166]

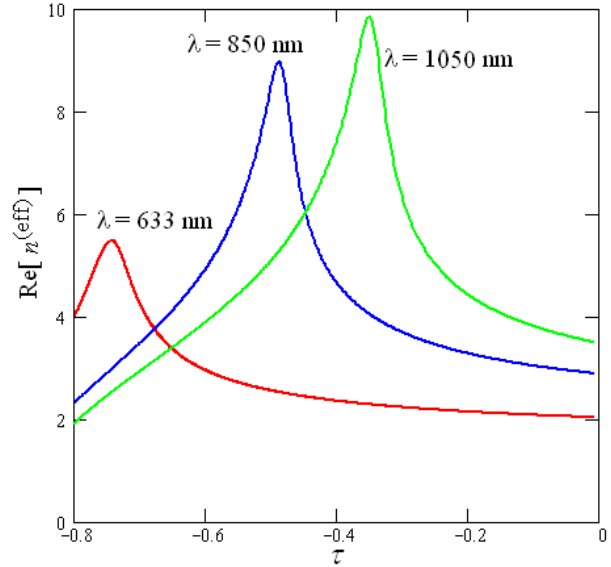
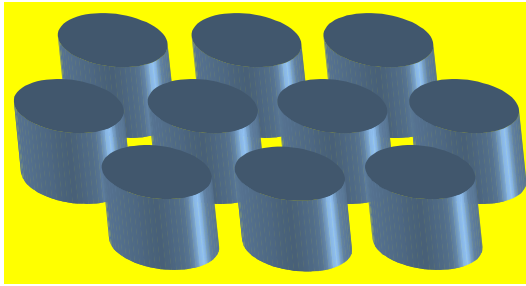
$$\epsilon^{(eff)} \approx \left| \epsilon_m \right| \left(\frac{\pi}{\sqrt{2\kappa(\Delta - i)(W + 1)}} - \frac{(1 + \pi/2)}{(W + 1)} \right), \quad (4.30)$$

where $W = \frac{|\text{Re}(\epsilon_m)|}{\epsilon_d}$, $\Delta = \frac{(W/\gamma - 1)}{\kappa}$, $\kappa = -\frac{\text{Im}(\epsilon_m)}{\text{Re}(\epsilon_m)}$, $\gamma = \frac{2d}{(D - d)}$; D is the period of the array, d is the diameter of the nanodisc. It should be noted that Eq. (4.30) was derived under the assumption of $\kappa \ll 1$ and $\gamma \gg 1$. This corresponds to close to percolation conditions and wavelengths in excess of 600 nm for gold.

The dependences of real parts of the effective refractive index of the composite made of Au nanodiscs embedded into YIG with zero magnetization on the normalized τ parameter ($\tau = \frac{(f_m - p_c)}{p_c}$) for different wavelengths of electromagnetic waves calculated with Eq. (4.30) are given in Fig. 4.20b. The losses in YIG, and the dispersion of the YIG dielectric permittivity were neglected. One can see the sharp spectral peaks corresponding to the plasmon mode excitation in a nanocomposite. The spectral positions and strengths of these peaks

experience red-shift and enhancement as the wavelength increases. The increase of the strength of the peak is due to the improvement of the quality of resonance (decrease in the κ -factor).

By applying the formalism, developed previously (Equations (4.21-4.25) and related discussion), I estimated the Faraday effect in such a composite. The results of numerical calculations are given in Fig. 4.21a, where the normalized (by the value of the Faraday effect in YIG with no metal inclusions) absolute value of faraday rotation is plotted. One can see that the significant (factor of 30) enhancement of the magneto-optical effects is expected around the plasmon resonance (with Faraday coefficient changing the sign exactly at the plasmon resonance wavelength) at certain values of τ -parameter.



a)

b)

Figure 4.20. a) Schematic drawing of the metal-dielectric composite made of ordered metal nanodisks; b) numerically calculated dependences of real parts of the effective refractive index of the same composite on the τ parameter for different wavelengths of electromagnetic waves.

However, the predicted enhancement is significantly smaller than the predicted average electromagnetic enhancement factor \bar{G} (derived in [166]) given by

$$\bar{G} = \left\langle \left| \frac{\vec{E}}{\vec{E}_0} \right|^2 \right\rangle \approx \sqrt{\frac{\pi(W+1)^{7/2}}{2((4-\pi)W+4)\kappa^{7/2}}} \sqrt{\frac{4\Delta^2+9}{(\Delta^2+1)^{3/2}} - \frac{\Delta(4\Delta^4+15\Delta^2+15)}{(\Delta^2+1)^3}}. \quad (4.31)$$

The dependence of \bar{G} on the value of the τ -parameter for the same nanocomposite at different wavelengths is given in Fig. 4.21b.

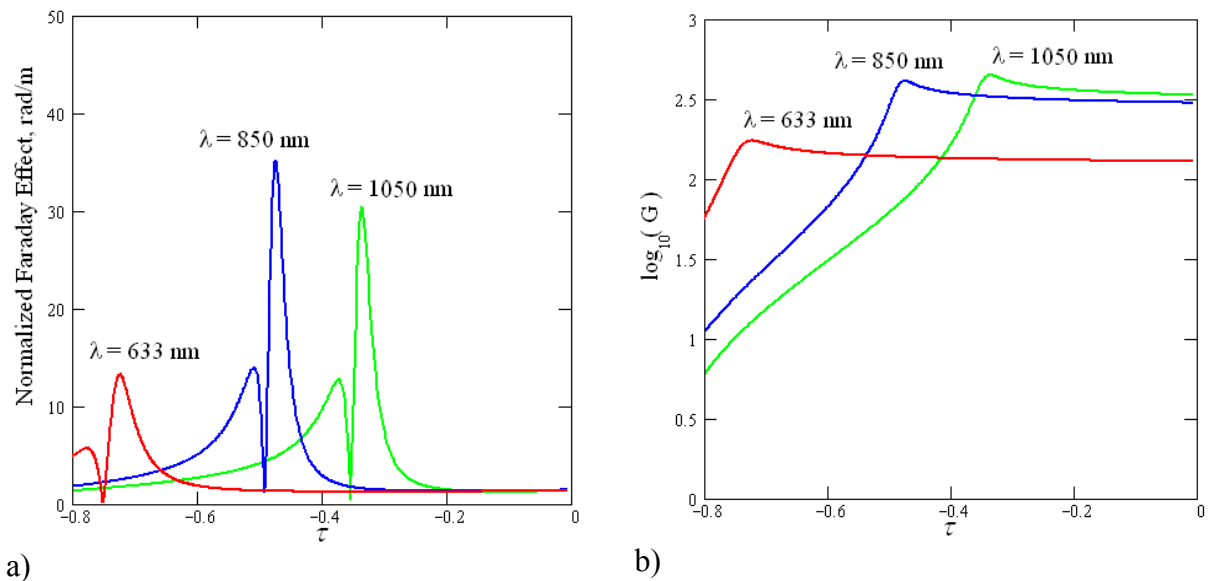


Figure 4.21. a) Numerically calculated dependences of the normalized Faraday coefficient of a composite material as in Fig. 4.20 on the τ -parameter at different wavelengths of the electromagnetic wave; b) average electromagnetic enhancement factor as a function of the τ -parameter for the composite material of Fig. 4.20 at different wavelengths of incident light.

Fig. 4.22 provides the spectral dependences of the real part of the effective refractive index (Fig. 4.22a), normalized Faraday coefficient (Fig. 4.22b) and spatially averaged electromagnetic field enhancement factor \bar{G} (Fig. 4.22c) for different values of τ -parameter.

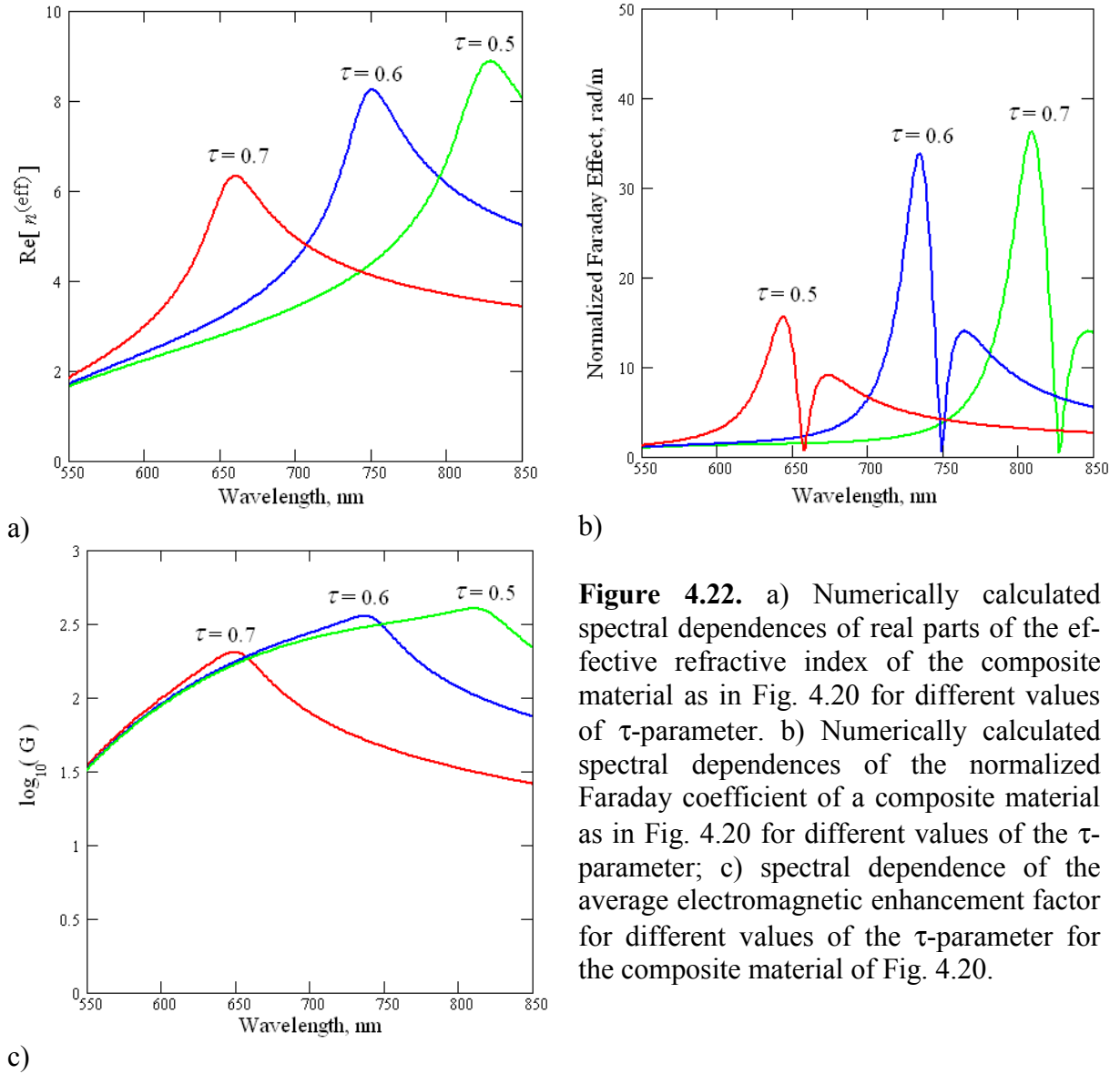


Figure 4.22. a) Numerically calculated spectral dependences of real parts of the effective refractive index of the composite material as in Fig. 4.20 for different values of τ -parameter. b) Numerically calculated spectral dependences of the normalized Faraday coefficient of a composite material as in Fig. 4.20 for different values of the τ -parameter; c) spectral dependence of the average electromagnetic enhancement factor for different values of the τ -parameter for the composite material of Fig. 4.20.

4.17. Square Array of Au Spherical Nanoparticles Embedded in YIG

Let's consider now the ordered array of spherical gold nanoparticles embedded in YIG. I assume cubic symmetry of the nanoparticle array and will neglect the losses in the YIG and the dispersion of the YIG dielectric constants. In such a case (under all the assumptions and limitations as in the case of nanodisc or nanocylinder array considered previously), one can use the following equations to estimate the value of the effective dielectric constant and electromagnetic enhancement factor (see [166]):

$$\varepsilon^{(eff)} \approx 2\varepsilon_d \left(\left(1 + \frac{\kappa\Delta}{W+1} \right) \log \left(\frac{W+1}{\kappa(\Delta-i)} \right) - 1 \right), \quad (4.32)$$

$$\bar{G} \approx \sqrt{\frac{3(W+1)^3}{(W+3)\kappa^3} \left(\frac{\pi}{2} - \frac{\Delta}{1+(\Delta+\kappa)^2} - \tan^{-1}(\Delta+\kappa) \right)}. \quad (4.33)$$

By applying the formalism developed earlier, I have estimated the Faraday effect in such a composite as well. The results of the numerical calculations are given in Fig. 4.23. The predicted enhancement of the magneto-optical effects around the plasmon resonance (with Faraday coefficient changing the sign exactly at the plasmon resonance wavelength) is also predicted; the value of the enhancement factor is expected to be around one order of magnitude. Again, as with the nanodisc array considered above, the magneto-optical enhancement factor (Fig. 4.23b) is by far less spectacular than the electromagnetic field enhancement factor (Fig. 4.23c).

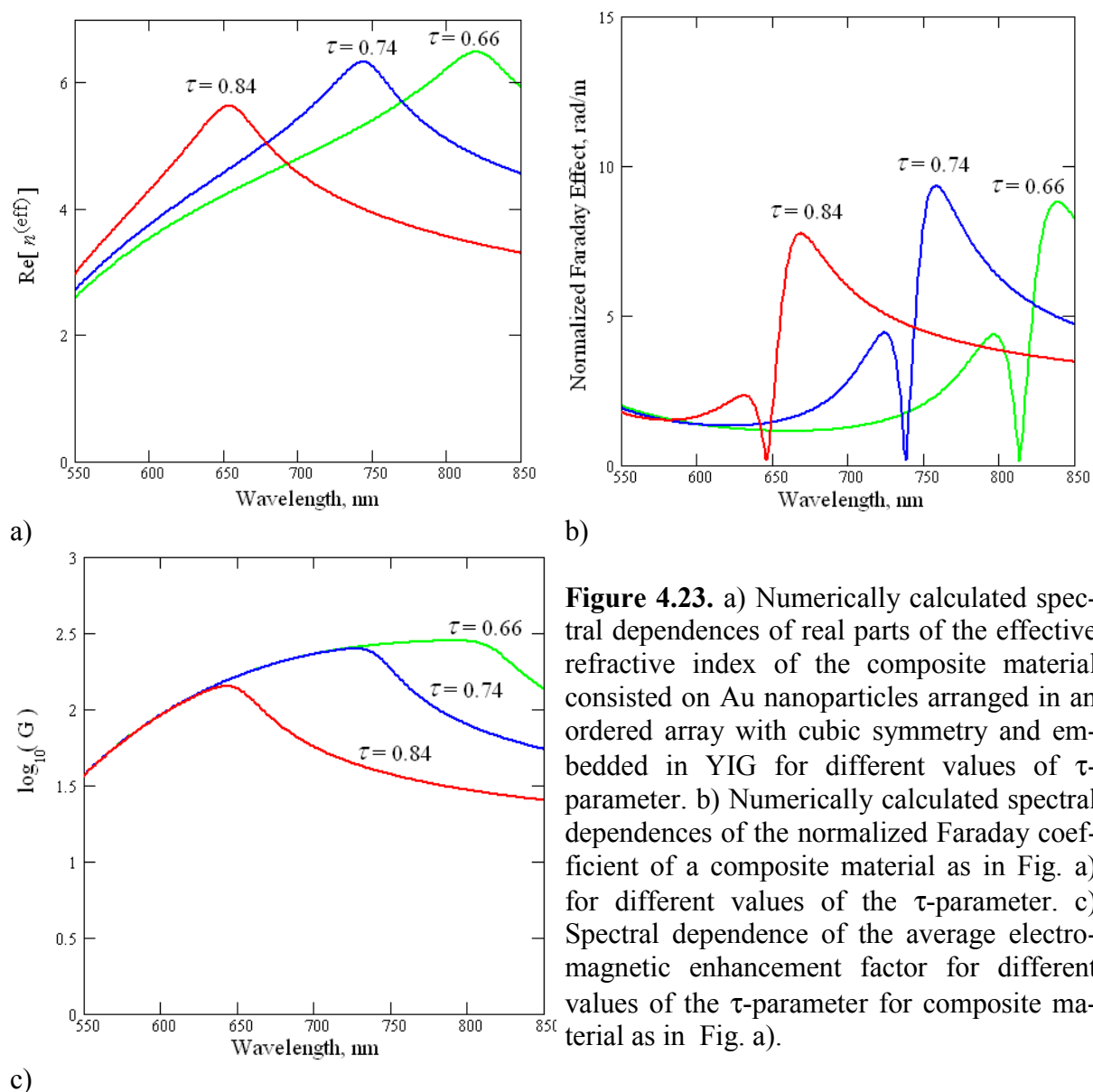


Figure 4.23. a) Numerically calculated spectral dependences of real parts of the effective refractive index of the composite material consisted on Au nanoparticles arranged in an ordered array with cubic symmetry and embedded in YIG for different values of τ -parameter. b) Numerically calculated spectral dependences of the normalized Faraday coefficient of a composite material as in Fig. a) for different values of the τ -parameter. c) Spectral dependence of the average electromagnetic enhancement factor for different values of the τ -parameter for composite material as in Fig. a).

4.18. Magneto-Optical Kerr Effect in Ordered Nanoparticle Arrays

As was mentioned previously, the reflectivity of nanocomposite materials grows significantly in the near IR spectral range as the metal concentration approaches the percolation threshold. On the other hand, it was shown above that the Faraday coefficient also exhibit a significant enhancement close to the percolation conditions in the near IR spectral range. Thus it is logical to predict that the magneto-optical Kerr effect (see Fig. 4.24 illustrating typical Kerr geometry) will also exhibit the local plasmon-caused enhancement in the near IR range. I will limit the consideration to the case of the polar Kerr effect at normal incidence (i.e., the direction of magnetization in a sample is normal to the surface and thus parallel or antiparallel to the incident and reflected radiation).

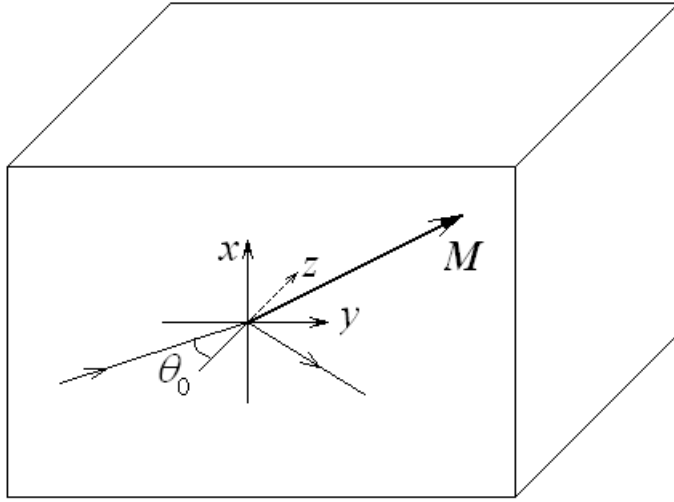


Figure 4.24. Schematic drawing illustrating the geometry of the magneto-optical Kerr effect.

In order to estimate the magneto-optical Kerr effect in metal-dielectric nanocomposites near the percolation threshold, I will use slightly modified abbreviations for the dielectric permittivity tensor of magneto-optical medium as follows.

$$\hat{\epsilon}_{MO} = \epsilon_{xx} \begin{pmatrix} 1 & iQm_z & -iQm_y \\ -iQm_z & 1 & iQm_x \\ iQm_y & -iQm_x & 1 \end{pmatrix}, \quad Q = i \frac{\epsilon_{xy}}{\epsilon_{xx}}. \quad (4.34)$$

In the case of normal incidence and polar Kerr effect ($m_z = 1, m_x = m_y = 0$), the Kerr rotation angle is equal to (see [167, 168])

$$\theta_k = \frac{iQ\sqrt{\epsilon_{xx}\epsilon_0}}{\epsilon_{xx} - \epsilon_0}. \quad (4.35)$$

By following the same arguments as presented in the discussion related to Equations (4.20)-(4.26), and under the assumption of incidence from vacuum, the normal incidence polar Kerr effect can be estimated as

$$\theta_k \approx \frac{\sqrt{\epsilon_0^{(eff)}}}{\epsilon_0^{(eff)} - 1} \frac{\partial \epsilon_0^{(eff)}}{\partial \epsilon_{MO}} i\epsilon_{xy}. \quad (4.36)$$

An important parameter indicating the usefulness of a material for applications based on a magneto-optical Kerr effect (such as magneto-optical recording or magneto-optical visualization of electrical currents and magnetic fields) is the respective Figure-Of-Merit (F.O.M.), which is defined as a product of the reflectivity and the polarization Kerr rotation angle:

$$FOM = R\theta_k. \quad (4.37)$$

As mentioned above, only the normal incidence polar Kerr effect is considered here, with light incident from air or vacuum, so the reflectivity then can be estimated to

$$R \approx \left| \frac{\sqrt{\epsilon_0^{(eff)}} - 1}{\sqrt{\epsilon_0^{(eff)}} + 1} \right|. \quad (4.38)$$

These formulas were applied to the case of the composite material consisting of Au nanodiscs embedded in YIG (effective dielectric permittivity is given by Eq. (4.30)), and to the composite material consisting of Au nanospheres embedded into a YIG (effective dielectric permittivity is given by Eq. (4.32)). The results of the calculations are presented in Fig. 4.25 (nanodiscs) and in Fig. 4.26 (nanospheres). In both these figures the spectral dependences of the reflectivity (Figs. 4.25a and 4.26a), of the Kerr polarization rotation (Figs. 4.25b and 4.26b), and of the F.O.M. (Figs. 4.25c and 4.26c) are presented for different values of the τ -parameter. One can see that a significant enhancement of both the Kerr rotation and the F.O.M. is predicted in such composites for the near IR close to percolation. Similarly to the Faraday effect evaluated previously, the spectral band where the maximal enhancement is theoretically predicted is red-shifting as the metal concentration approaches percolation conditions ($\tau \rightarrow 0$). However, unlike the average local electromagnetic field enhancement, and similarly to the Faraday enhancement studied earlier, the maximal enhancement factor saturates at some vicinity of percolation.

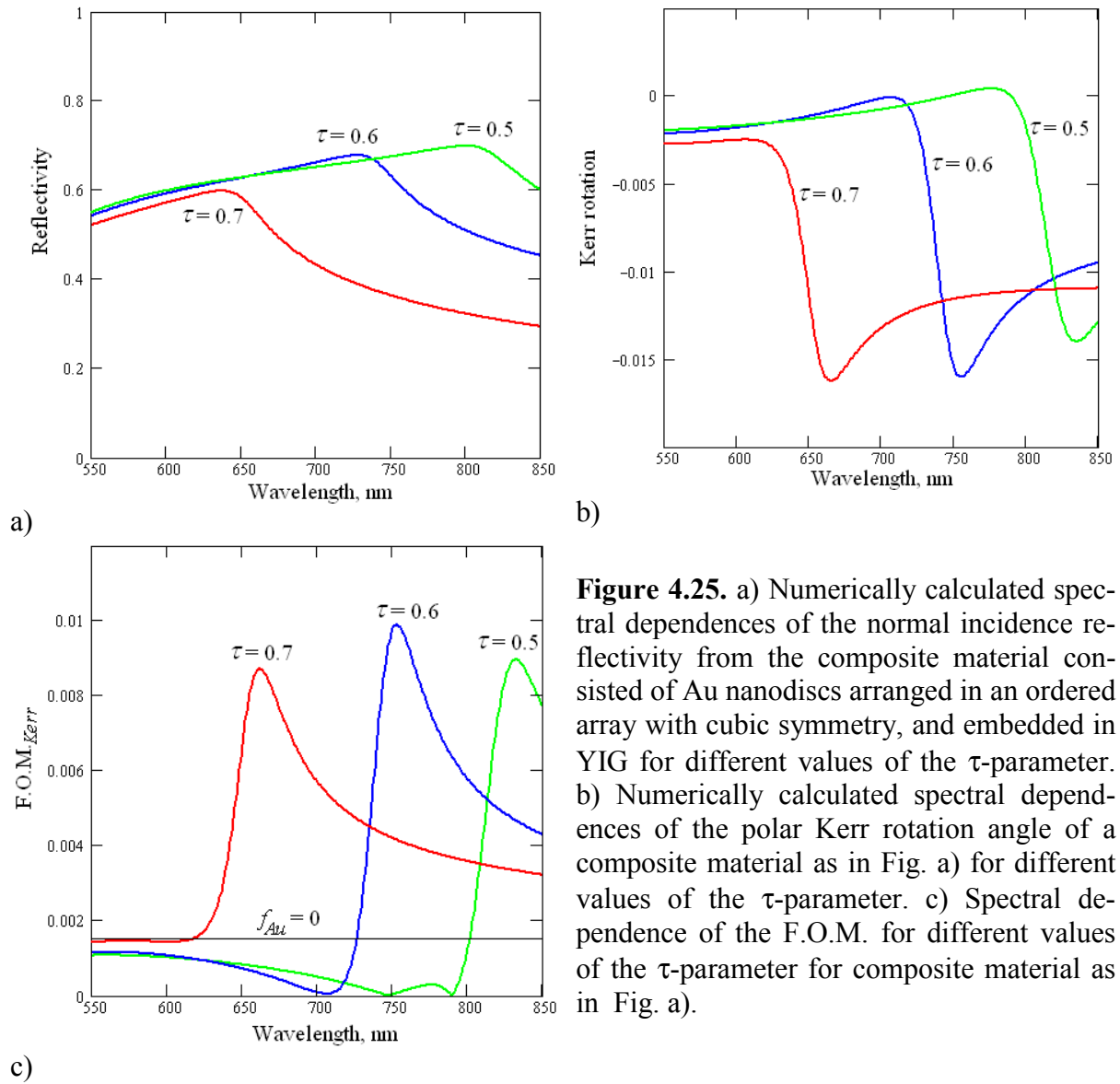


Figure 4.25. a) Numerically calculated spectral dependences of the normal incidence reflectivity from the composite material consisted of Au nanodiscs arranged in an ordered array with cubic symmetry, and embedded in YIG for different values of the τ -parameter. b) Numerically calculated spectral dependences of the polar Kerr rotation angle of a composite material as in Fig. a) for different values of the τ -parameter. c) Spectral dependence of the F.O.M. for different values of the τ -parameter for composite material as in Fig. a).

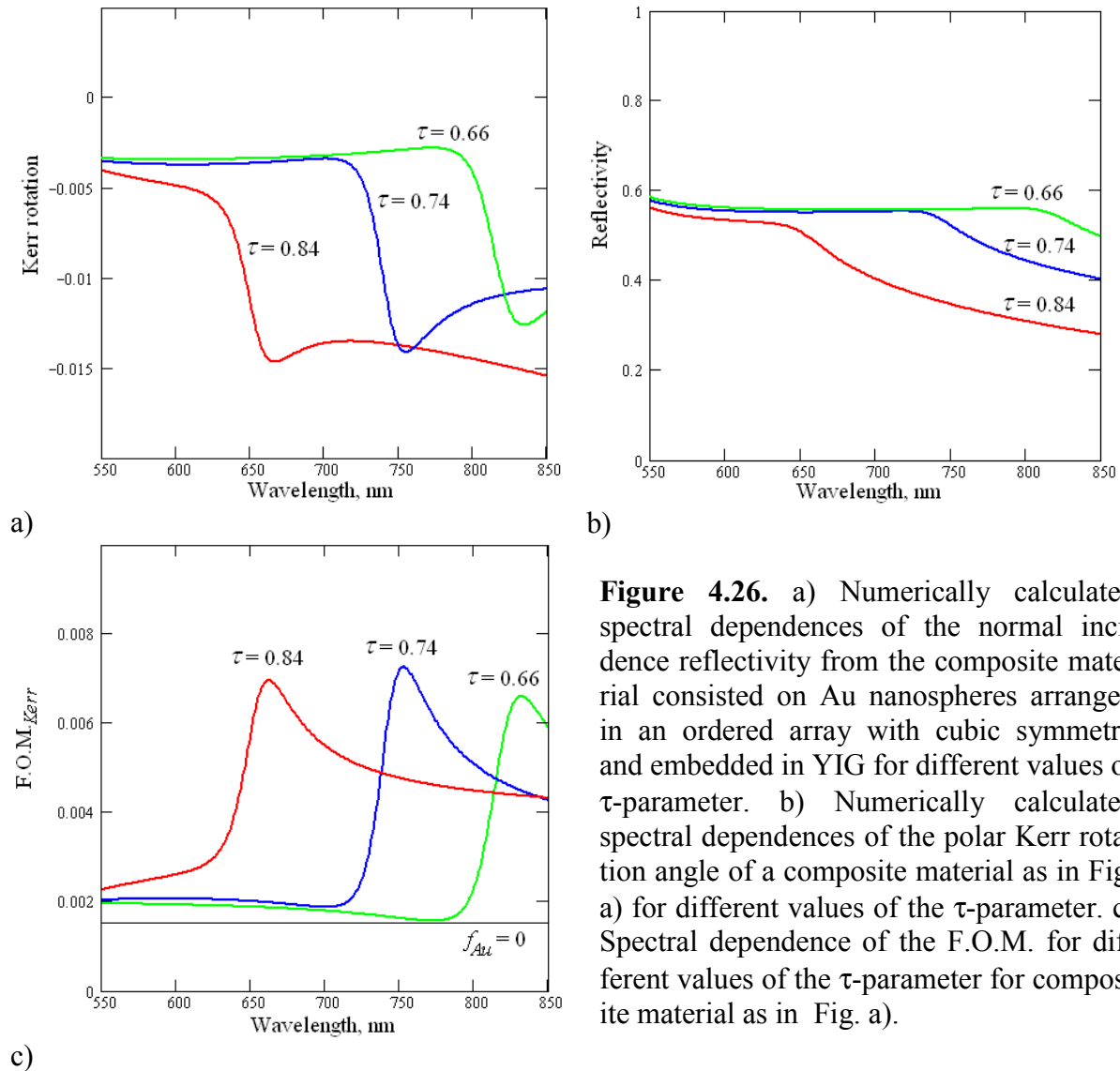


Figure 4.26. a) Numerically calculated spectral dependences of the normal incidence reflectivity from the composite material consisted on Au nanospheres arranged in an ordered array with cubic symmetry and embedded in YIG for different values of τ -parameter. b) Numerically calculated spectral dependences of the polar Kerr rotation angle of a composite material as in Fig. a) for different values of the τ -parameter. c) Spectral dependence of the F.O.M. for different values of the τ -parameter for composite material as in Fig. a).

4.19. Application of Scaling Theory to the Estimation of Magneto-Optical Effects in Metal-Dielectric Nanocomposites.

Let's consider now the case of a random composite material made of noble metal nanoparticles embedded into a magneto-optically active dielectric material, such as YIG, very near the metal percolation conditions.

Unlike the case of ordered nanoparticle arrays considered above, the dielectric and optical properties of random metal-dielectric nanocomposites near the percolation threshold cannot be analytically derived (moreover, these properties strongly depend on the distribution of the nanoparticles), so the scaling approach (see [8] and references therein) was developed.

In such an approach (valid only for $\tau \ll 1$ and $W \gg 1$), the following estimate of the effective dielectric constant of the composite material was found to be reasonably accurate:

$$\frac{\varepsilon^{(eff)}}{\varepsilon_m} = |f_m - p_c|^t S \left(\frac{\varepsilon_d / \varepsilon_m}{|f_m - p_c|^{t+s}} \right) \quad (4.39)$$

Where $S(y)$ is a scaling function of complex variable y , which has the following asymptotic forms:

$$S(y) = \begin{cases} A + By + \dots & |y| \ll 1 \quad f_m > p_c \\ B'y + \dots & |y| \ll 1 \quad f_m < p_c \\ A'' y^{t/(t+s)} & |y| \gg 1 \quad \forall f_m \end{cases} \quad (4.40)$$

In this expression s and t are so-called percolation critical exponents, which define the so-called fractal dimensionality and for three-dimensional composite $t \approx 2.0$ and $s \approx 0.7$ [169, 170]. From (4.40) under the assumption that $W \gg 1$ (near IR and longer wavelengths for gold) it follows:

$$\varepsilon^{(eff)} \approx \begin{cases} A'' \varepsilon_m^{s/(t+s)} \varepsilon_d^{t/(t+s)} & \left| \frac{\varepsilon_d}{\varepsilon_m} \right| \gg |f_m - p_c|^{t+s} \\ B' \varepsilon_d |f_m - p_c|^{-s} & \left| \frac{\varepsilon_d}{\varepsilon_m} \right| \ll |f_m - p_c|^{t+s} \quad f_m < p_c \\ B \varepsilon_d |f_m - p_c|^{-s} & \left| \frac{\varepsilon_d}{\varepsilon_m} \right| \ll |f_m - p_c|^{t+s} \quad f_m > p_c \end{cases} \quad (4.41)$$

By applying Eq. (4.21) to Eq. (4.41), one can estimate the Faraday coefficient in such a metal-dielectric composite to

$$\theta_F \approx \begin{cases} \frac{\pi}{\lambda} \sqrt{A''} \frac{t}{t+s} \cdot \frac{\operatorname{Re}(\varepsilon_m^{s/2(t+s)})}{\varepsilon_d^{(t+2s)/2(t+s)}} \varepsilon_{xy} & \left| \frac{\varepsilon_d}{\varepsilon_m} \right| \gg |f_m - p_c|^{t+s} \\ \frac{\pi}{\lambda} \sqrt{B'} \frac{\varepsilon_{xy}}{\sqrt{|f_m - p_c|^s}} & \left| \frac{\varepsilon_d}{\varepsilon_m} \right| \ll |f_m - p_c|^{t+s} \quad f_m < p_c \\ \frac{\pi}{\lambda} \sqrt{B} \frac{\varepsilon_{xy}}{\sqrt{|f_m - p_c|^s}} & \left| \frac{\varepsilon_d}{\varepsilon_m} \right| \ll |f_m - p_c|^{t+s} \quad f_m > p_c \end{cases} \quad (4.42)$$

The limit $\left| \frac{\varepsilon_d}{\varepsilon_m} \right| \gg |f_m - p_c|^{t+s}$ corresponds to the near IR spectral range and a situation extremely close to percolation-threshold conditions. In this case a divergence of the dielectric function and of the Faraday coefficient is not expected for the metal concentration approaching percolation (as follows from Eqs. (4.41) and (4.42)). The enhancement of the Faraday rotation in such a composite is proportional to $\operatorname{Re}(\varepsilon_m^{s/2(t+s)})$, i.e. in the near IR (where the real

part of metal dielectric constant is approximately $\text{Re}(\epsilon_m) \approx 1 - \frac{\lambda^2}{\lambda_p^2}$, the Faraday rotation can be estimated as

$$\frac{\pi}{\lambda} \sqrt{A''} \frac{t}{t+s} \cdot \frac{\epsilon_{xy}}{\epsilon_d^{(t+2s)/2(t+s)}} \left(1 - \frac{\lambda^2}{\lambda_p^2}\right)^{s/2(t+s)}. \quad (4.43)$$

Further, if we limit ourselves to the case of $\frac{\lambda^2}{\lambda_p^2} \gg 1$ (which is the case for Au and Ag in near IR), and assume that $\sqrt{A''} \frac{t}{t+s} \approx 1$, the enhancement of the Faraday effect G_F compared to the pure magneto-optical dielectric material with no metal inclusions will be

$$G_F \approx \frac{1}{\epsilon_d^{s/2(t+s)}} \cdot \frac{\lambda^{2s/2(t+s)}}{\lambda_p^{2s/2(t+s)}}. \quad (4.44)$$

As mentioned above, for a three-dimensional composite, $t \approx 2.0$ and $s \approx 0.7$ obtains; we have

$$G_F \sim \lambda^{0.26}. \quad (4.45)$$

At similar conditions the field enhancement $\bar{G} = \left\langle \left| \frac{\bar{E}}{\bar{E}_0} \right|^2 \right\rangle$ can be estimated to [171]

$$\bar{G}^{3D} \sim C \frac{|\epsilon_m|}{\text{Im}(|\epsilon_m|)} \cdot \left(\frac{|\epsilon_m|}{\epsilon_d} \right)^{t+s}, \quad (4.46)$$

where C can be approximated as a constant and v is another critical exponent, approximately equal for 3D composites to 0.89. At $\frac{\lambda^2}{\lambda_p^2} \gg 1$, Eq. (4.46) predicts \bar{G}^{3D} to be independent of the wavelength. For two-dimensional composites near the percolation threshold it is predicted (see [172]) that the field enhancement factor \bar{G}^{2D} is wavelength dependent and can be estimated to

$$\bar{G}^{2D} \sim C' \frac{|\epsilon_m|^{3/2}}{\epsilon_d \text{Im}(|\epsilon_m|)} \sim \lambda^{0.5}. \quad (4.47)$$

This means that G_F and $\sqrt{\bar{G}^{2D}}$ have similar spectral dependences at $\left| \frac{\epsilon_d}{\epsilon_m} \right| \gg |f_m - p_c|^{t+s}$ (near IR and very close to the percolation threshold).

The case of $\left| \frac{\epsilon_d}{\epsilon_m} \right| \ll |f_m - p_c|^{t+s}$ in Eq. (4.42) corresponds to the mid and far infrared spectral region and some (although small) distance in the parameter space from the percolation of the composite. In this case the developed model here predicts the divergence of the Faraday rotation as the metal concentration approaches the percolation threshold, and the value of the Faraday rotation is predicted to be independent of the metal dielectric constants (i.e., on the wavelength). This case is qualitatively similar to the theoretical estimation of \bar{G}^{3D} , where also no dispersion is predicted.

In the case of magneto-optically active metals embedded in non-magneto-optically active dielectrics we can estimate the Faraday coefficient by applying the Eq. (4.21) to (44.1) to

$$\theta_F \approx \begin{cases} \frac{\pi}{\lambda} \sqrt{A''} \frac{s}{t+s} \cdot \frac{\epsilon_d^{t/2(t+s)}}{\text{Re}\left(\epsilon_m^{(2t+s)/2(t+s)}\right)} \epsilon_{xy} & \left| \frac{\epsilon_d}{\epsilon_m} \right| \gg |f_m - p_c|^{t+s} \\ 0 & \left| \frac{\epsilon_d}{\epsilon_m} \right| \ll |f_m - p_c|^{t+s} \end{cases} \quad (4.48)$$

Since $\frac{\epsilon_d^{t/2(t+s)}}{\text{Re}\left(\epsilon_m^{(2t+s)/2(t+s)}\right)} \ll 1$ for all metals in the visible and IR range, Eq. (4.48) predicts the degradation of the magneto-optical activity near the percolation threshold for such a nanocomposite material.

4.20. Discussion of the Magneto-Optical Effects in Metal Dielectric Nanocomposites

From all the cases considered above it is apparent that a substantial electromagnetic enhancement of the magneto-optical effects is expected in metal-dielectric nanocomposites. The particular value of the enhancement factor and the optimal metal concentration needed to obtain the maximal enhancement, strongly depend on the wavelength. The highest possible enhancement factors (x50 and possibly above) are expected in the near IR wavelength range at near-metal-percolation conditions.

The theory presented here predicts that the enhancement of the magneto-optical activity in metal-dielectric composites is proportional to the enhancement of the electromagnetic field in the magneto-optical material at metal concentrations sufficiently far from the percolation threshold. Near the percolation threshold, at least according to the formalism used, the correlation of the magneto-optical enhancement and the electromagnetic enhancement is not that straightforward. It is my opinion that this is caused by the non-reciprocity of the Faraday effect.

While the enhancement of magneto-optical effects is much less pronounced in such composites compared to the enhancements of nonlinear optical effects, the value of achievable enhancement factors (x50 and above in some cases) may be useful for a number of applications. Such an enhancement allows to grow much thinner magneto-optical films in order to produce the specified optical effects. Another prospect that is opened by the strong enhancement

of the magneto-optical rotation is the possibility of making certain components out of materials that are cheaper and/or easier to manufacture. For example, magneto-optical imaging at present requires Bi:YIG films with tight specifications and an unreliable supply. According to the theoretical results of this paper, a similar performance might be obtained in a composite material made of a mixture of gold and cobalt nanoparticles in, for example, a dielectric matrix. Another possibility is to use very thin YIG films with significantly relaxed specifications (which might be synthesized by a number of techniques) and to enhance the polarization rotation by depositing and/or mixing such films with Au or Ag nanoparticles. Other applications of such materials in optical isolators can be also expected.

4.21. MO Core-Shell Nanoparticle Composites

The last part of this chapter is devoted to the theoretical investigations of the magneto-optical properties of nanocomposites consisting of core-shell type nanoparticles. Core-shell types of plasmon nanoparticles (also known as “nanoonions” or “nanomatrushkas”) are gaining significant attention nowadays because of the significant technological advances in nanoparticle fabrication. Such a construction of nanoparticles provides researchers an additional freedom in tailoring the optical properties of nanoparticles to the design goals. While for isolated metal nanoparticles the spectral position of the plasmon resonance (absorption peak) is nearly fixed for each type of metal², the spectral position of the plasmon resonance can be tailored in a wide range (see [127] for a recent review) for core-shell nanoparticles

Various bimetallic core-shell nanoparticles have been experimentally realized and studied [173-175], as well as metal-dielectric core-shell nanoparticles [176, 177]. Most efforts in the development of core-shell nanoparticles so far were focussed on linear optical effects. However, it was recently theoretically shown that nonlinear optical effects (such as SHG- second harmonic generation) can also be considerably enhanced in core-shell nanoparticle with a metal core and weakly nonlinear shell materials [122]. Such an enhancement was predicted to occur due to the strong enhancement of the electromagnetic field in a shell of such a nanoparticle. On the other hand, as was shown previously in this chapter (see Eq. 4.28 and related discussion), magneto-optical effects are to some extent proportional to the local electromagnetic field and should be enhanced in core-shell nanoparticles as well.

Magneto-optical effects of core-shell nanoparticles have already been studied within some limits. In [178] the effective dielectric permittivity tensor of a composite material consisting of a Co core and a cobalt oxide shell was derived based on a MG theory, and the magneto-optical Kerr effect was evaluated for such composites. The enhancement of the magneto-optical Kerr effect around the plasmon resonances in nanoparticles with a Na core (treated as magneto-optically active metal) surrounded by a lossless isotropic dielectric shell was recently theoretically predicted in [163]; again based on MG theory. It is my objective to develop the EMA-type of theory for treatment of core-shell nanoparticles (since it is more accurate and self-consistent than MG) and to study the Faraday effect in more practical material systems, where the enhancement of magneto-optical effects is expected to be optimal.

The isolated coated sphere is optically identical to the sphere of the same radius with dielectric permittivity [179]

² The plasmon frequency shows considerable size dependence even in the assumption that the metal nanoparticle is much smaller than the wavelength of light, see the discussion related to Eq. 4.1

$$\epsilon_{CS}^{eff} = \frac{2\epsilon_S + \epsilon_C + 2Q^3(\epsilon_C - \epsilon_S)}{2\epsilon_S + \epsilon_C - Q^3(\epsilon_C - \epsilon_S)} \epsilon_S, \quad (4.49)$$

where $Q = R_C/R$; R is the outer radius of a shell, R_C is the radius of the core, ϵ_S is the dielectric constant of the shell material, and ϵ_C is the dielectric constant of the core material.

This means that one can use Equations 4.19-4.25 with a substitution of Eq. (4.49) to the corresponding spots. With such a formalism we can now proceed to the evaluation of different practical cases.

4.21.1. Magneto-Optical Properties of the Composite Material Consisting of YIG Core/Au Shell Nanoparticles Embedded into Isotropic Dielectric Material

The first case that I will examine is a nanocomposite material consisting of nanoparticles having a YIG core and an Au shell, as schematically shown in Fig. 4.27. As mentioned previously in this chapter, YIG is material that is transparent in the visible and near IR range and possesses unique magneto-optical properties, while the Au is second best choice (after Ag) for the highest quality plasmon resonance at these wavelengths. Numerically calculated spectral dependences of the loss coefficient in such a composite for different Q- factors and 1 % filling fraction (of core-shell nanoparticles embedded in glass) are presented in Fig. 4.28. As one can see at low values of Q-factor (corresponding to small YIG core in a large Au shell) the plasmon absorption peak is close in the position to the plasmon peak of the composite made of pure Au nanoparticles. As the Q- factor increases (corresponding to the increase of the YIG content in core-shell structure) the plasmon absorption band experience the red shift. This is due to the fact that the plasmon mode is getting more localized in a YIG layer than in glass. Quite interestingly, the strength of the plasmon absorption band increases with the increase of the value of Q factor up to roughly the value of 0.8 (corresponding to volume filling fraction of YIG in nanoparticle of ~50 %), where it reaches the maximum.

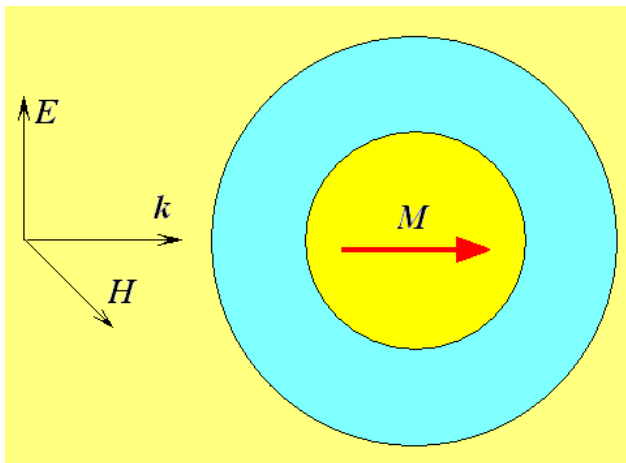


Figure 4.27. Schematic drawing of the YIG core/Au shell nanoparticle showing the orientation of the magnetization vector and the electromagnetic wave vector as considered here.

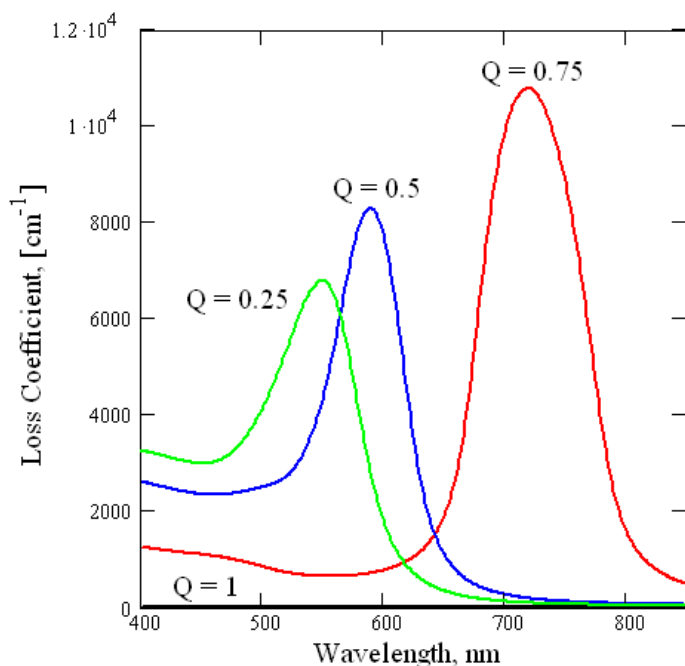


Figure 4.28. Numerically calculated spectral dependences of loss coefficients for a composite material consisted of “YIG”-core/Au shell nanoparticles with 1 % filling fraction embedded in glass for different values of the Q -parameter.

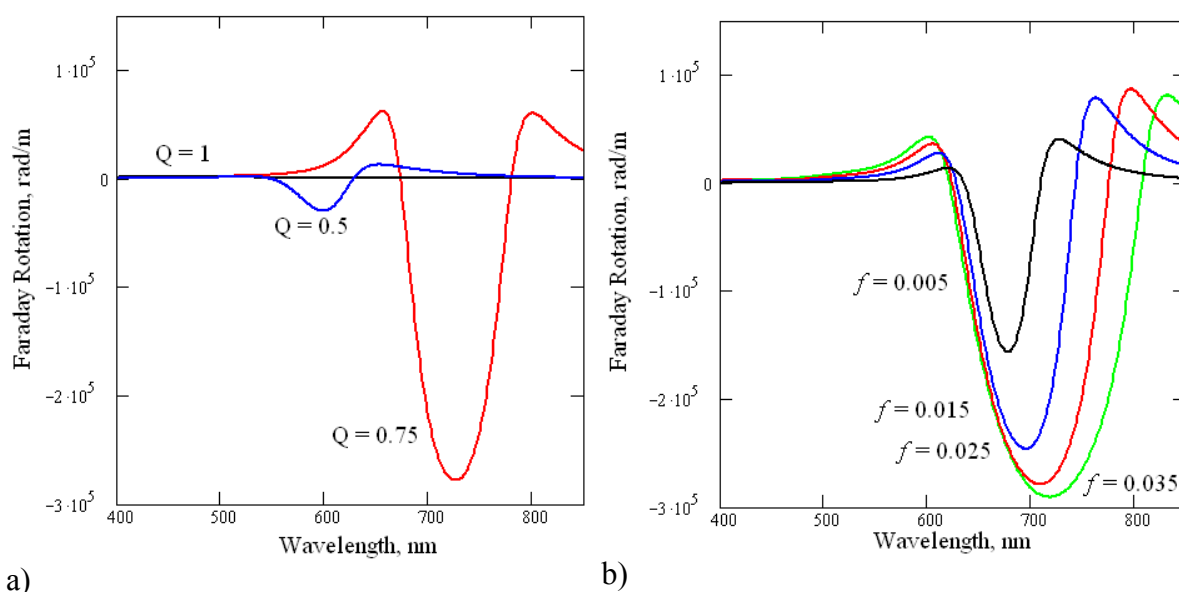


Figure 4.29. a) Numerically calculated spectral dependences of the Faraday rotation for a composite material consisting of “YIG”-core/Au shell nanoparticles with 1 % filling fraction embedded in glass for different values of Q -parameter; b) numerically calculated spectral dependences of the Faraday rotation of the composite material from above with $Q = 0.7$ embedded in glass for different filling fractions of core-shell particles.

The calculated spectral dependences of the Faraday rotation in such a nanocomposite material are given in Fig. 4.29. Fig. 4.29a) shows the effect of varying the Q -factor of nanoparticles for a fixed filling fraction of the nanoparticles in a nanocomposite, while Fig. 29b) illustrates the influence of the filling fraction of the nanoparticles at a fixed Q -factor. As expected from Eq. 4.28, the enhancement of the Faraday rotation in such a composite is following the increase in strength of the absorption in a plasmon peak, as illustrated in Fig. 4.28 at least for a low concentration limit. If we compare the values of the Faraday rotation for the {YIG

core/Au shell nanoparticles embedded in glass} nanocomposite with those of the {Au nanoparticles embedded in YIG} nanocomposite (shown in Fig. 4.14c), we find that even at a 1 % filling fraction of core-shell nanoparticles (and thus at a less than 1 % YIG filling fraction in a nanocomposite) the Faraday effect is predicted to be of the same order of magnitude as that of pure YIG. In other words, the prediction here is that such a core-shell nanocomposite enhances by more than two orders of magnitude the value of the magneto-optical rotation per fraction of magneto-optical! Such an enhancement can have significant practical applications since it is simpler to synthesize YIG reproducibly in the form of nanoparticles through chemical reactions, then to grow good-quality epitaxial thin films of YIG materials.

4.21.2. Magneto-Optical Properties of a Composite Material Consisting of YIG Shell/Au Core Nanoparticles Embedded into an Isotropic Dielectric Material

The next core-shell nanocomposite that will be analyzed is an Au-core/YIG-shell nanoparticle dispensed in glass, as schematically shown in Fig. 4.30. The calculated spectral dependences of the Faraday rotation in such a nanocomposite material are given in Fig. 4.31. Fig. 4.31a) shows the effect of varying the Q-factor of the nanoparticles at a fixed filling fraction of the nanoparticles in a nanocomposite, while Fig. 31b illustrate the influence of the filling fraction of the nanoparticles at a fixed Q- factor. Compared to the case of YIG-core/Au-shell nanoparticles considered above, the Q-factor in such a composite has a far smaller influence on the spectral position of the plasmon band. The plasmon band experiences a relatively weak blue-shift with the increase of the Q-factor (corresponding in this case to the increase of the Au content in a nanoparticle). At a fixed filling fraction of nanoparticles the enhancement of the Faraday effect also grows with the increase of the Q factor up to a value of ~ 0.9 , corresponding to a 70 % metal filling fraction.

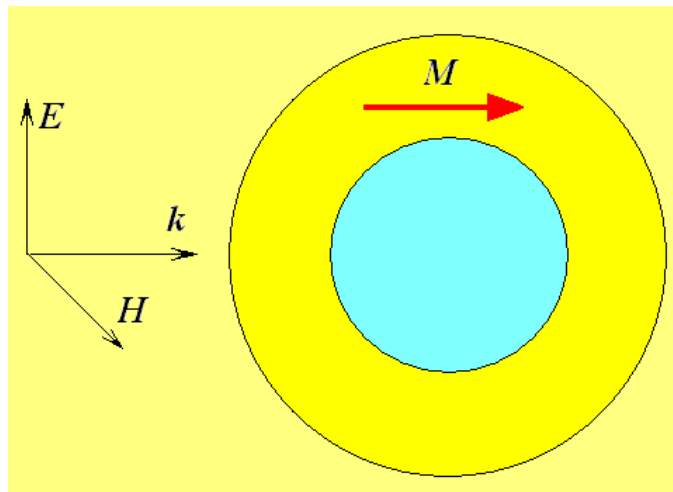


Figure 4.30. Schematic drawing of the YIG shell/Au core nanoparticle embedded into e.g. glass, showing the orientation of the magnetization vector and the electromagnetic wave vector as considered here.

In order to illustrate the enhancement effect of the Faraday rotation per fixed filling fraction of YIG in a nanocomposite, Fig. 4.32 shows the calculated spectral dependences of the Faraday rotation for different values of the Q-factor. One can see that the maximum enhancement factor occurs at $Q = 0.9$. However, by comparing Figs. 4.31 and 4.29, we can conclude that the YIG-core/Au-shell nanoparticle composite is preferential from the viewpoint of the polarization rotation.

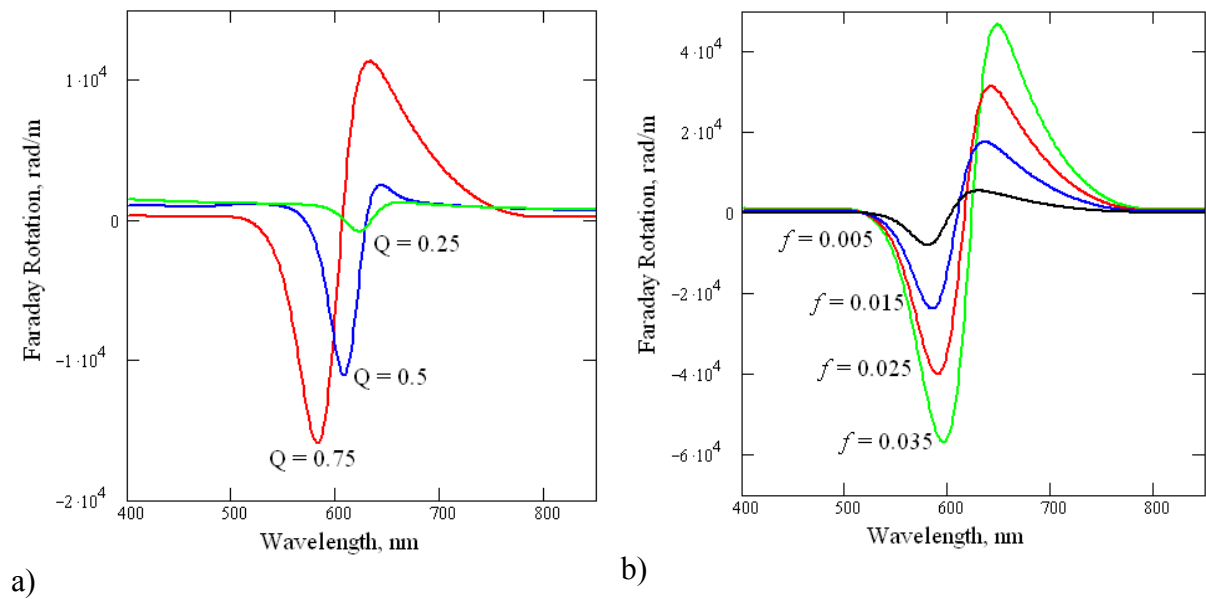


Figure 4.31. a) Numerically calculated spectral dependence of the Faraday rotation of a composite material consisting of Au-core/"YIG" shell nanoparticles with a 1 % filling fraction embedded in glass for different values of Q -parameter; b) numerically calculated spectral dependences of the Faraday rotation of composite material from above for $Q = 0.75$ and various filling fraction.

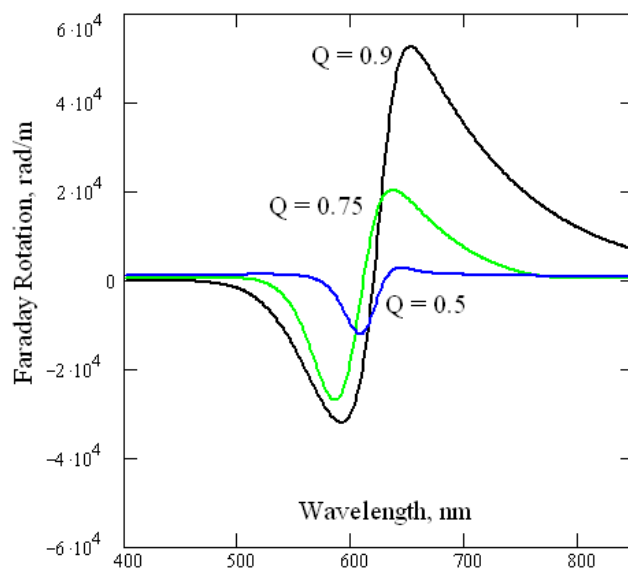


Figure 4.32. Numerically calculated spectral dependences of Faraday rotation of the composite material consisted of Au-core/"YIG" shell nanoparticles with 1 % YIG filling fraction embedded in glass for different values of Q -parameter.

4.21.3. Magneto-Optical Properties of the Composite Material Consisting of Ni Shell/Au Core Nanoparticles Embedded into Isotropic Dielectric Material

In addition to metal-dielectric core-shell nanoparticles I will analyze the magneto-optical rotation in nanocomposite materials made of bimetallic core-shell nanoparticles with one of the metal being magneto-optically active (such as Ni, Co or Fe) and the other optimized for plasmon excitation (such as Au). In this section we will analyze the case of nanoparticles made of an Au core and a Ni shell, as schematically shown in Fig. 4.33.

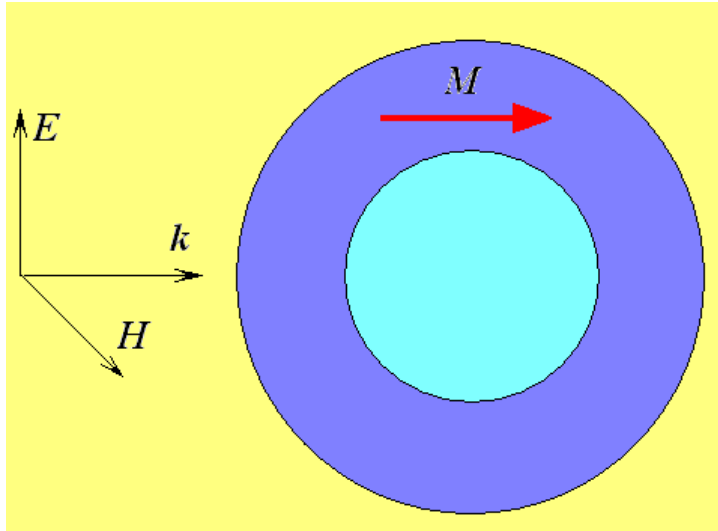


Figure 4.33. Schematic drawing of the Ni shell/Au core nanoparticle showing the orientation of the magnetization vector and the electromagnetic wave vector as considered here.

The calculated spectral dependences of the Faraday rotation in such a nanocomposite material are given in Fig. 4.34. Fig. 4.34a) shows the effect of varying the Q-factor of the nanoparticles at a fixed filling fraction of the nanoparticles in a nanocomposite, while Fig. 34b) illustrate the influence of the filling fraction of the nanoparticles at a fixed Q- factor. Unlike the case of metal-dielectric core-shell nanoparticles considered above, such a material shows only marginal enhancement of the Faraday rotation in a narrow spectral band due to the Au shell if compared to the case of the pure Ni nanoparticles ($Q = 0$). The reason for this is that the energy of the plasmon mode in a nanoparticle is mainly localized in the dielectric material surrounding the nanoparticle and in the Ni shell, while the localization of the plasmon mode in a gold core is small. Because of this the improvement in the quality of the resonance due to the Au core is insignificant. In other words, two effects counterbalance each other: the higher the Au filling fraction in a nanoparticles, the higher is the enhancement of the electromagnetic field and the lower is the fraction of the magneto-optical metal causing the significant Faraday effect. On the other hand, the higher the fraction of the magneto-optical metal in a nanoparticle, the lower is the electromagnetic field enhancement, since all magneto-optically active metals have a fairly low ratio of real to imaginary parts of the dielectric constant at visible and near IR wavelengths, meaning poor quality plasmon resonances.

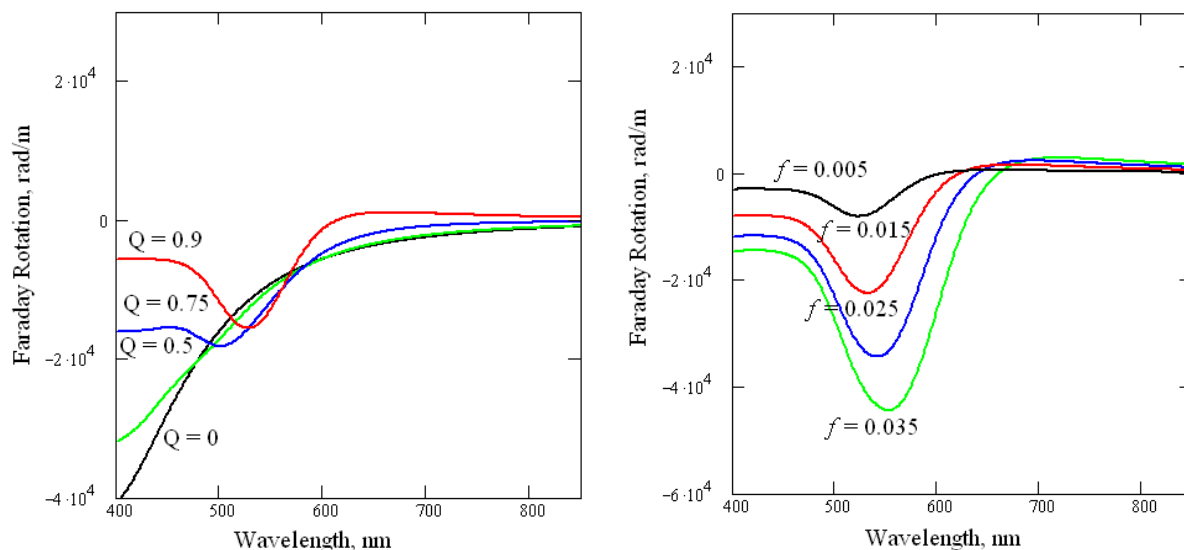


Figure 4.34. a) Numerically calculated spectral dependences of the Faraday rotation for a composite material consisting of Au-core/Ni shell nanoparticles with 1 % total metal filling fraction embedded in glass for different values of Q -parameter; b) numerically calculated spectral dependences of the Faraday rotation of the above composite material with $Q = 0.9$ for different filling fractions of core-shell particles.

In order to illustrate the effect of the enhancement of the value of the Faraday rotation per fixed filling fraction of magneto-optically active metal in a nanocomposite, Fig. 4.35 shows the calculated spectral dependences of the Faraday rotation for different values of the Q -factor. One can see that the maximal enhancement factor occurs at $Q = 0.9$ (corresponding to a 50 % volume filling fraction of Au in a nanoparticle). By comparing these results with that of the YIG/Au core shell structure (see Fig. 4.32), we can see again that the enhancement value of the Faraday rotation per fixed filling fraction of magneto-optically active metal in Ni core/Au shell nanoparticles is much less spectacular.

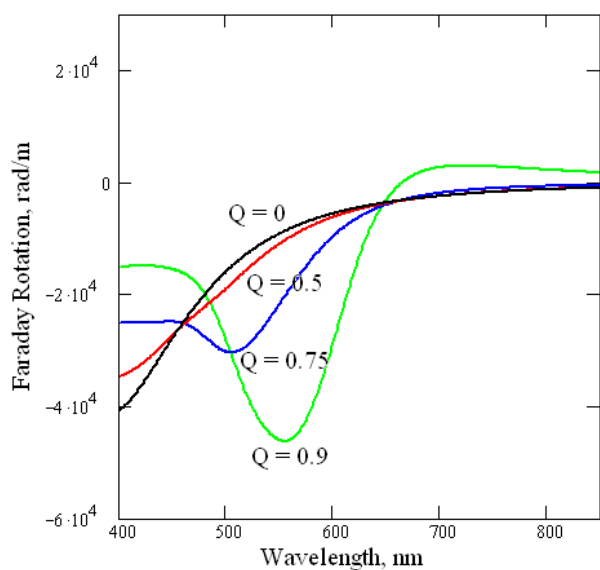


Figure 4.35. Numerically calculated spectral dependences of the Faraday rotation for a composite material consisting of Au-core/Ni shell nanoparticles with 1 % MO-metal filling fraction embedded in glass for different values of the Q -parameter.

4.21.4. Magneto-Optical Properties of a Composite Material Consisting of Au Shell/Ni Core Nanoparticles Embedded into an Isotropic Dielectric Material

The last bimetallic core-shell nanoparticle composite that we will analyze is the case of nanoparticles made of Au shell and Ni core, as schematically shown in Fig. 4.36.

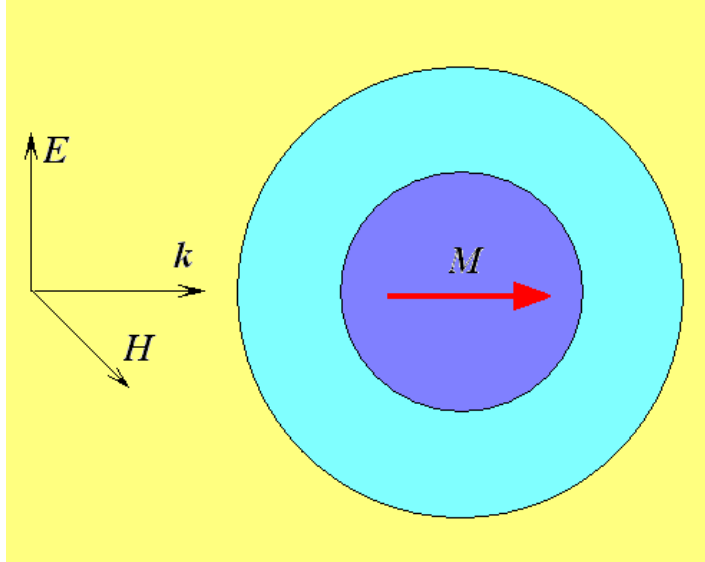


Figure 4.36. Schematic drawing of the Ni core/Au shell nanoparticle showing the orientation of the magnetization vector and the electromagnetic wave vector, considered here.

The calculated spectral dependences of the Faraday rotation in such a nanocomposite material are given in Fig. 4.37. Fig. 4.37a shows the effect of varying the Q-factor in nanoparticles at fixed filling fraction of the nanoparticles in a nanocomposite, while Fig. 37b illustrate the influence of the filling fraction of the nanoparticles at a fixed Q-factor. For such a material the calculations predict only a marginal enhancement of the Faraday rotation compared to the case of pure Ni nanoparticles ($Q = 1$) over a limited spectral band with a maximum enhancement achievable at $Q \sim 0.75$ (corresponding to $\sim 40\%$ volume fraction of Ni) - quite similar to the previously analyzed Au core/Ni shell composite system. The reason for this again can be found in the fact that the energy of the plasmon mode in a nanoparticle is mainly localized in the dielectric material surrounding the nanoparticle, so the presence of the Au shell effectively reduces the localization of the plasmon mode in a magneto-optically active metallic core. This effect effectively cancels the overall enhancement of the electromagnetic field of the plasmon.

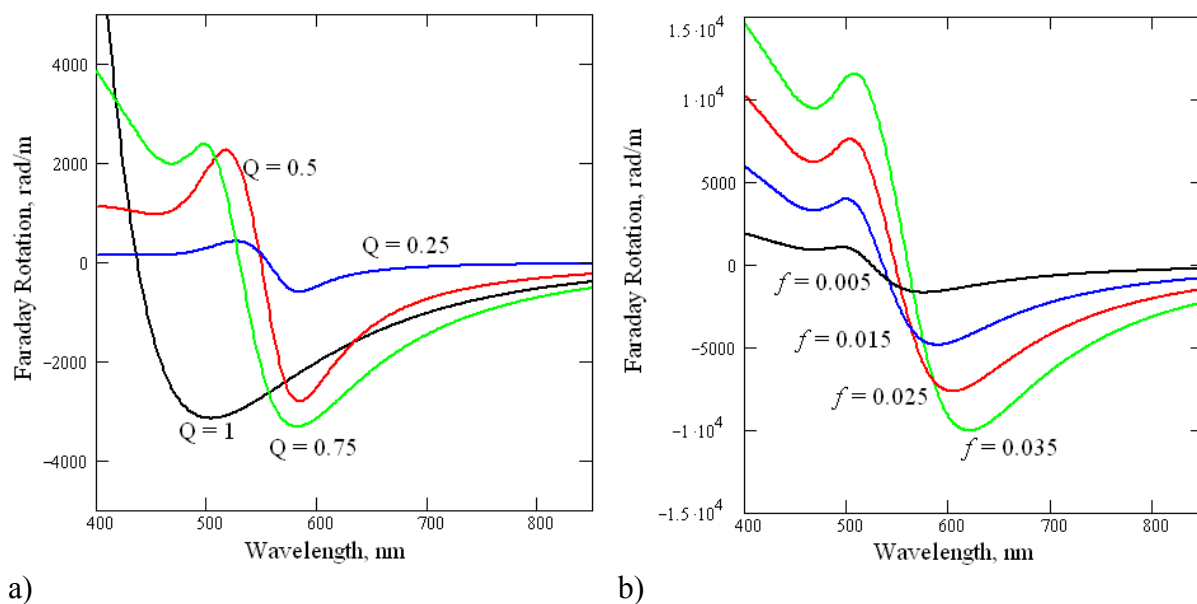


Figure 4.37. a) Numerically calculated spectral dependences of the Faraday rotation of a composite material consisting of Au-shell/Ni core nanoparticles with 1 % filling fraction embedded in glass for different values of Q -parameter; b) numerically calculated spectral dependences of the Faraday rotation for the above with $Q = 0.75$ for different filling fractions of core-shell particles.

4.22. Discussion of the Magneto-Optical Effects in Nanocomposite Materials Containing Core-Shell Nanoparticles

Based on the numerical calculations presented above, it can be concluded that composite materials consisting of core-shell nanoparticles embedded in a lossless dielectric material hold significant promise for magneto-optical applications. Core-shell nanoparticles not only provide the opportunity to tailor the spectral position of the plasmon band, but also show significant increase in the value of the Faraday rotation due to the electromagnetic field enhancement in a core-shell structure (discussed in [122] in relation to the enhancement of the Second Harmonic Generation in core-shell nanoparticles). In particular, it was theoretically predicted that a composite material made from gold-coated YIG nanoparticles dispersed in glass with less than 1 % YIG filling fraction can exhibit a Faraday effect comparable to a pure YIG thin film at certain wavelengths. If such a prediction will be experimentally confirmed, such a composite material could find significant applications, e.g. for magneto-optical memories, magneto-optical imaging.

Chapter V

Summary and Conclusions

5.1. Summary

A complete theory of light propagation through ordered thick macroporous silicon arrays was developed. It was shown that

- In the EUV-visible spectral range (from below 100 nm to roughly 700 - 800 nm) the light propagates through macroporous silicon by the leaky waveguide transmission channel, where leaky waveguide modes are confined in pores.
- In the near IR to mid IR spectral range (from roughly 700 - 800 nm to a wavelength roughly equal to 2 – 5 times of the pore array period) the light propagates through the waveguide transmission channel, where waveguide modes are confined mostly in the silicon islands between the pores.
- In that part of the mid IR range to the far IR range (from a wavelength roughly equal to 2 – 5 times of the pore array periods and up to the free carrier absorption edge of silicon) the light propagates through the macroporous silicon as through an effective medium with some effective optical properties.

An improved effective medium theory was developed for calculations of effective dielectric constants of porous semiconductors and applied to the explanation and identification of types of optical anisotropies in several porous semiconductor materials and composite materials made on the basis of porous silicon. The following items were accomplished:

- The optical anisotropy of electrochemically etched mesoporous Si on (110)-oriented substrate was explained, and the dependence of the optical birefringence of this material on various material parameters was obtained.
- The optical anisotropy of electrochemically etched porous InP and GaAs on (100) substrates with crystallographic pores was predicted to be of either uniaxial or biaxial type, depending on the pore structure. The triangular cross section of pores in porous InP and GaAs (100) substrates was predicted to play a major role in its anisotropic optical behavior.
- The optical anisotropy of materials composed of strongly polarizable metal ellipsoids aligned into several subsets (such as silver-filled mesoporous silicon etched on (110)-oriented substrate) was evaluated. An uniaxial behavior of such materials was predicted. At small metal filling fractions of the composite material dramatic enhancements of the optical anisotropy at some wavelengths was theoretically demonstrated. It was further predicted that the optical anisotropy of silver-filled mesoporous silicon etched on (110)-oriented substrates would have different signs (positive or negative) at different portions of the spectrum. In addition, it was theoretically demonstrated that such a material might exhibit “indefinite” (meaning different signs of the different elements of the effective dielectric permittivity tensor) dielectric properties at some wavelengths for intermediate filling fractions.

A specifically modified kind of effective medium theory was developed for the evaluation of the nonlinear optical properties of porous semiconductors in the small nonlinearity/small porosity limit. It was applied to the study of second harmonic generation (SHG) from a composite material consisting of mesoporous (110)-Si and pores filled with silver, e.g. by electroplating. The theory developed permitted a determination of the SHG tensor coefficients of such composites. It was shown that:

- The SHG of a composite material consisting of mesoporous (110)-Si with the pores filled with silver can be greatly enhanced in some wavelength ranges due to the local electromagnetic field enhancement around the surface plasmon resonance conditions of the metal-filled pores. Moreover, some peculiarities of the SHG generation efficiency were predicted, which are due to spectral peculiarities of the effective dielectric constant such a composite (originating from the morphology of the mesoporous (110)-Si). The optimum material parameters for an experimental observation of the theoretically predicted effects were identified.

Based on the theoretical formalism developed, it was shown that porous Silicon in various geometries and morphologies can be used for novel optical elements by combining theoretical insights with suitable porous structures and some pre- and post-processing of the Silicon. The following novel optical elements were designed, modeled and in most cases experimentally fabricated/optically tested:

- Environmentally stable optical components from mesoporous Silicon for far IR spectral range.
- Long wave pass filters for the mid and far IR spectral range.
- Macroporous Silicon UV Filters.
- Polarization components for the UV range.
- Retroreflection suppression plates.
- Omnidirectional IR and visible wavelengths filters.

A number of fabrication processes have been developed and/or adapted for the fabrication of these components. Experiments in most cases fully confirmed the feasibility and the unique performance characteristics of these optical components. Some of these components (such as long wave pass filters) are already successfully commercialized and are used by the international scientific research community.

A modified effective medium approximation was developed that accounts for higher order interactions between metal nanoparticles in metal-dielectric composite materials,. The mathematical formalism was developed and applied to actual experimental data. By comparison of experimental results and theoretical predictions it was shown that:

- The approximation presented provides a much better fit to experimental results than the classical EMA - even at low metal filling fractions.
- It was demonstrated that the theory developed expands the applicability range of EMA up to ~20 % metal filling fractions at very little additional computational expenses.
- It was shown that the theory developed permits to extract additional information from the optical characterization of the composite material, such as the distribution of the

particle distance in a composite (in addition to the correct identification of the concentration of the metal particles).

The magneto-optical effects in metal-dielectric nanocomposite materials have been analyzed in detail. The theoretical formalism was developed and applied to the analysis of such materials at low, medium, and near-percolation metal concentrations. The predicted magneto-optical enhancement factors were compared with electromagnetic field enhancement factors. Several practical realizations of such composite materials were considered, and some possible applications were discussed. In particular, the following was shown:

- A substantial electromagnetic enhancement of the magneto-optical effects is expected in metal-dielectric nanocomposites.
- The enhancement of the magneto-optical activity in metal-dielectric composites is proportional to the enhancement of the electromagnetic field in the magneto-optical material at metal concentrations sufficiently far from the percolation threshold.
- Near the percolation threshold, the correlation of the magneto-optical enhancement and the electromagnetic enhancement is not that straightforward.
- The particular value of the enhancement factor and the optimum metal concentration needed to get the maximal enhancement strongly depends on the wavelength.
- The highest possible enhancement factors (x50 and possibly above) are expected in the near IR wavelength range at near-metal-percolation conditions.
- Composite materials consisting of core-shell nanoparticles embedded in a lossless dielectric material hold significant promise for magneto-optical applications. Core-shell nanoparticles not only provide the opportunity to tailor the spectral position of the plasmon band, but also show significant increase in the value of the Faraday rotation due to the electromagnetic field enhancement in a core-shell structure. Particularly, it was theoretically predicted that a composite material made of gold-coated YIG nanoparticles dispersed in glass with less than 1 % YIG filling fraction can exhibit comparable Faraday effect to the pure YIG thin films at certain wavelengths.

5.2. Outlook and Future Research

While the material presented in this thesis provides a good background for the understanding of how porous semiconductors can be modified to serve as a base material for different optical components, there is still a lot of work that needs to be done in the immediate future:

- The fabrication of mesoporous silicon far IR filters needs to be made reproducible enough to allow a commercially viable product. In addition, application-based designs of particular filter structures adapted for particular user's requirements have to be developed.
- A similar situation obtains with macroporous Silicon UV Filters, where still a number of processes need to be optimized or fine tuned, and more application-specific designs need to be developed.
- Even more process optimization is needed for polarization components for the UV range. Large progress in the optimization of the electrochemical etching is required to prove the theoretically predicted advantages of such optical components.
- It is still not experimentally proven that omnidirectional IR and visible wavelengths filters are feasible. Optically functional structures have still to be made and tested,

which will require substantial optimization of the electrochemical etching/pore coating/filling processes.

- It is yet to be experimentally identified whether porous semiconductor other than silicon could be used for the optical components.

While I believe that with the material provided in this thesis, the theoretical background and the understanding of optical anisotropies of porous semiconductor materials are sufficiently established, there is certainly a lot of interesting work that can be done in the future in this regard:

- The electrochemical etching of III-V compound semiconductors on (100) substrates need to be sufficiently optimized to experimentally verify the achievability of the biaxial anisotropy in such porous materials. Further, it needs to be identified whether the fabrication process could be sufficiently optimized to produce well-controlled biaxial anisotropy as is needed for a number of optical applications. Only in such a case such materials can be successfully commercialized.
- The technique of metal-filling the pores needs to be developed, and the theoretical predictions of strong anisotropy and indefinite optical properties need to be experimentally verified. It is still to be shown whether such properties could find the use in optics, and whether it could be the base of viable commercial products.
- It is yet to be experimentally proven whether the theoretically predicted enhancement of the nonlinear optical effects in metal-filled porous semiconductor composites is correct.
- The nonlinear optic effective medium theory can be (and probably should be) further expanded to medium metal concentrations (somewhat similar to the expansion of the linear optic EMA presented in Chapter IV) and then can be applied to the case of porous GaP, where there is still no acceptable theoretical explanation of the experimentally observed significant enhancement of the SHG.

The prospects of the future research in magneto-optical phenomena in metal-dielectric composites are even more exciting:

- The structures with the highest theoretically predicted enhancements of the magneto-optical effects should be experimentally realized and tested. It is especially interesting to evaluate such structures near the percolation conditions, where no experimental data is available yet.
- The magneto-optical phenomena theoretically considered in this thesis should not only be investigated in the far field, but also in the near field. Near field investigations (such as with specifically modified Scanning Near Field Optical Microscope (SNOM)) may reveal the local distribution of the light polarization in such structures. It is especially interesting to examine the near-percolation structures, since in such a case enormous local electromagnetic fields are expected. Such an investigation may provide the understanding why the theory presented here predicts significant deviations between the electromagnetic enhancement and the magneto-optical enhancement in metal-dielectric composites.
- The nonlinear magneto-optical effects can be theoretically investigated in metal-dielectric composites as well. If following the analogy to linear optics, such composites might provide much more significant enhancements of nonlinear magneto-optic effects than that of linear magneto-optical effects investigated in this thesis.

- Engineering of magneto-optical materials can be attempted with the combination of DDA and EMA as presented in this thesis. The key will be to theoretically identify what kind of unit cell structure such materials should have, and what would be the performance limits of such materials. The difference to the engineering of magneto-optical properties via photonic crystals (already analyzed in a substantial number of publications) is in the size of the unit cell and the dimensions of the “building blocks”. Here I propose to investigate the subwavelength structures.
- It would be very interesting to evaluate the possible applicability of magneto-optically-active materials in nanostructures exhibiting left handedness (i.e. negative refraction) at certain wavelengths. It is known that negative refraction occurs if the real parts of the effective magnetic susceptibility and the dielectric permeability have negative signs simultaneously. The magneto-optical activity of a composite may provide a coupling between different modes in such structure and interesting (possibly) unique optical effects may take place at such conditions.
- At last, but not the least, it needs yet to be shown whether the fabrication of metal-dielectric magneto-optical composites can be optimized sufficiently to permit some commercial applications.

Appendix A

Publications of V. Kochergin with Relevance to the Thesis

A.1 Scientific Journals and Proceedings

1. V.E. Kochergin, A.A. Beloglazov, M.V. Valeiko, P.I. Nikitin, “*Phase properties of a surface-plasmon resonance from the viewpoint of sensor applications*”, *Quantum Electronics*, **28** (5), pp. 444-448 (1998)
2. V.E. Kochergin, M.V. Valeiko, A.A. Beloglazov, T.I. Ksenevich, P.I. Nikitin, “*Visualization of the angular dependence of the reflected-radiation phase under conditions of a surface-plasmon resonance and its sensor applications*”, *Quantum Electronics*, **28** (9), pp. 835-839 (1998).
3. A.V. Kabashin, V.E. Kochergin, P.I. Nikitin, “*Surface plasmon resonance bio- and chemical sensors with phase-polarization contrast*”, *Sensors and Actuators B-CHEM*, **54** (1-2), pp. 51-56 (1999).
4. V.E. Kochergin, A.Y. Toporov, M.V. Valeiko, “*Polariton enhancement of the Faraday magneto-optic effect*”, *JETP Letters*, **68** (5), pp. 400-403 (1998).
5. P.I. Nikitin, A.A. Beloglazov, V.E. Kochergin, M.V. Valeiko, T.I. Ksenevich, “*Surface plasmon resonance interferometry for biological and chemical sensing*”, *Sensors and Actuators B-CHEM*, **54** (1-2), pp. 43-50 (1999).
6. A.V. Kabashin, V.E. Kochergin, A.A. Beloglazov, P.I. Nikitin, “*Phase-polarization contrast for surface plasmon resonance biosensors*”, *Biosensors and Bioelectronics*, **13** (12), pp. 1263-1269 (1998).
7. V. Kochergin, I. Avrutsky, Y. Zhao, “*High sensitivity waveguide grating sensor, based on radiative losses*”, *Biosensors and Bioelectronics*, **15** (5-6), pp. 283-289 (2000).
8. I. Avrutsky, Y. Zhao, V. Kochergin, “*Plasmon assisted resonant tunneling of light (PARTL) through periodically corrugated thin metal film*”, *Optics Letters*, **25** (9), pp. 595-597 (2000).
9. I. Avrutsky, V. Kochergin, Y. Zhao, “*Optical demultiplexing in a planar waveguide with colloidal crystal*”, *IEEE Photonics Technology Letters*, **12** (12), pp. 1647-1649 (2000).
10. V. Kochergin, E.V. Kochergin, “*Optical tunneling through fiber Bragg grating with gain*”, *Optical Communications*, **211** (1-6), pp. 121-128 (2002).
11. I. Avrutsky, V. Kochergin, “*Optical filtering by leaky guided modes in macroporous silicon*”, *Appl. Phys. Lett.*, **82** (21), pp. 3590-3592 (2003).

12. V. Kochergin, M. Christophersen, H. Föll, “*Effective Medium Approach for Calculations of Optical Anisotropy in Porous Materials*”, Appl. Phys. B, **79** (6), pp. 731-739 (2004).
13. V. Kochergin, M. Christophersen, H. Föll, “*Adjustable optical anisotropy in porous GaAs*”, Appl. Phys. Lett., **86**, 042108 (2005).
14. V. Kochergin, M. Christophersen, H. Föll, “*Surface Plasmon Enhancement of an Optical Anisotropy in Porous Silicon/metal Composite*”, Appl. Phys. B., **80** (1), pp. 81-87 (2005).
15. V. Kochergin and H. Föll, “*Novel optical elements made from porous silicon*”, **Review Paper** accepted for publication, Materials Science and Engineering R (2006).
16. V. Kochergin and H. Föll, “*Commercial applications of porous Si: optical filters and components*”, accepted for publication, Physica Status Solidi (c) (2006).
17. P.I. Nikitin, V.E. Kochergin A.A. Beloglazov, M.V. Valeiko, T.I. Ksenevich, “*Surface plasmon resonance interferometry for high-sensitive and wide-range sensing*”, Proceedings of EUROSENSORS XII, Southampton, UK (1998).
18. A.A. Beloglazov, A.V. Kabashin, V.E. Kochergin, M.V. Valeiko, P.I. Nikitin, “*Interferometry using surface plasmon resonance*”, Proceedings of the Xth conference on Sensors and Transducers for measurement and control, Gurzuf, Ukraine, V. **1**, p. 89-91 (1998) (in Russian).
19. P.I. Nikitin, A.A. Beloglazov, A.V. Kabashin, M.V. Valeiko, V.E. Kochergin, “*Surface plasmon resonance interferometry for sensor applications*”, Proceedings of Europt(r)ode IV, 4th European Conference on Optical Chemical Sensors and Biosensors, Muenster, Germany, p. 145-146 (1998).
20. A.V. Kabashin, V.E. Kochergin, P.I. Nikitin, “*Phase-polarization contrast for surface plasmon resonance sensor systems*”, Proceedings of Europt(r)ode IV, 4th European Conference on Optical Chemical Sensors and Biosensors, Muenster, Germany, p. 177-178 (1998).
21. A.V. Kabashin, V.E. Kochergin, P.I. Nikitin, “*Phase-polarization contrast for surface plasmon resonance biosensors*”, Proceedings of **Biosensors’98**, 2-5 June, 1998, Berlin.
22. V. Kochergin, P.R. Swinehart “*Improved magneto-optical imaging films employing surface plasmon resonance*”, Proceedings of “Magneto-Optical Imaging”, Eds. T.H.Johansen and D.V.Shantsev, Kluwer Academic Publishers, NATO Science Series, Vol. **142**, pp. 337-344 (2003).
23. I. Avrutsky, V. Kochergin, Y. Zhao, “*Optical bio-sensors based on diffraction efficiency of waveguide gratings.*” OSA-99/ILS-XV, paper TuXX44, Santa Clara, CA, September 26-30, 1999.

24. I. Avrutsky, Y. Zhao, V. Kochergin, “*Surface plasmon assisted tunneling of light through thin metal film.*” OSA-2000/ILS-XVI, paper ThQ5, Providence, Rhode Island, October 22-26, 2000.
25. I. Avrutsky, V. Kochergin, Y. Zhao, “*Optical demultiplexing using colloidal crystal waveguides.*” OSA-2000/ILS-XVI, paper WW6, Providence, Rhode Island, October 22-26, 2000.
26. I. Avrutsky, V. Kochergin, P. Swinehart, “*Optical filtering by leaky waveguides*”, Proceedings of 2003 Frontiers in Optics/Laser Science XIX Conference, paper ThFF6, 2003 Frontiers in Optics/Laser Science XIX, Tucson, AR, October 5 - 9, 2003.
27. V. Kochergin, M. Christophersen, P.R. Swinehart, “*Macroporous Silicon-based polarization components*”, Proc. SPIE Vol. **5515**, Nanoengineering: Fabrication, Properties, Optics, and Devices; Elizabeth A. Dobisz, Louay A. Eldada; Eds., pp. 132-141 (2004).
28. V. Kochergin, M. Christophersen, P.R. Swinehart, “*Macroporous Silicon UV filters for space and terrestrial environments*”, Proc. SPIE Vol. **5554**, pp. 223-234, Photonics for Space Environments IX; Edward W. Taylor; Ed., (2004).
29. M. Christophersen, V. Kochergin, P.R. Swinehart, “*Macroporous Silicon filters for mid-to-far IR range*”, Proc. SPIE Vol. **5524**, pp. 158-168, Novel Optical Systems Design and Optimization VII; Jose M. Sasian, R. John Koshel, Paul K. Manhart, Richard C. Juergens; Eds. (2004).
30. V. Kochergin, H. Föll, “*Effective Medium Approach For Calculation of Linear and Nonlinear Properties of Porous Semiconductor Composites*”, Proc. MRS Spring Annual Meeting, San Francisco, USA, (2005).
31. V. Kochergin, O. Sneh, M. Sanghavi, P.R. Swinehart, “*Macroporous silicon deep UV filters*”, Proc. ESTC-05 Conference, June 2005, Baltimore, Maryland, USA.
32. V. Kochergin, M. Sanghavi, P.R. Swinehart, “*Porous silicon filters for low-temperature far IR applications*”, Proc. SPIE Vol. **5883**, pp. 184-191, *Infrared Spaceborne Remote Sensing 2005*; Marija Strojnik; Ed.
33. W. R. McGovern, V. Kochergin, M. R. Sanghavi, P. R. Swinehart, “*Porous silicon optical filters for far-IR and low-temperature applications*”, will be published in Proc. Great Lakes Photonics Symposium 12-16 June 2006.

A.2 Books

1. “*Omnidirectional Optical Filters*” Vladimir Kochergin, Kluwer Academic Publishers, Boston, ISBN 1-4020-7386-0 (2003).

A.3 Patents

A.3.1 Issued Patents

1. V. Kochergin and P. Swinehart, US Patent **6,549,687** “*System and method for measuring physical, chemical and biological stimuli using vertical cavity surface emitting lasers with integrated tuner*”, issued April 15, 2003.
2. V. Kochergin and P. Swinehart, US Patent **6,819,812** “*System and method for measuring physical, chemical and biological stimuli using vertical cavity surface emitting lasers with integrated tuner*”, issued Nov 16, 2004.
3. V. Kochergin and P. Swinehart, US Patent **6,836,578** “*System and method for measuring physical stimuli using vertical cavity surface emitting lasers with integrated tuner*”, issued Dec. 28, 2004.
4. V. Kochergin, US Patent **6,934,068** “*Magnetic field and electrical current visualization system*”, issued Aug 23, 2005.
5. V. Kochergin and P. Swinehart, US Patent **7,031,566** “*Spectral filter for green and shorter wavelengths*”, issued Apr. 18, 2006.
6. V. Kochergin and P. Swinehart, US Patent **7,045,052** “*Method of manufacturing a spectral filter for green and longer wavelengths*”, issued May 16, 2006.

A.3.2 Patents Pending

7. V. Kochergin and P. Swinehart, US Patent Application **20030133657** “*Magneto-optical sensing employing phase-shifted transmission Bragg gratings*”, filed Dec. 21, 2002.
8. V. Kochergin and P. Swinehart, US Patent Application **20040045932** “*Method of manufacturing a spectral filter for green and shorter wavelengths*”, filed June 4, 2003.
9. V. Kochergin and P. Swinehart, US Patent Application **20050276536** “*Spectral filter for green and longer wavelengths*”, filed Oct. 15, 2003.
10. V. Kochergin, US Patent Application **20040239936** “*Surface corrugation enhanced Magneto-Optical Indicator film*”, filed Jan 26, 2004.
11. V. Kochergin, US Patent Application **20050058414** “*Porous retroreflection suppression plates, optical isolators and method of fabricating same*”, filed Aug. 23, 2004.

12. V. Kochergin, M. Christophersen, US Patent Application **20050199511** “*Semiconductor electrochemical etching processes employing closed-loop control*”, filed Jan. 15, 2005.
13. V. Kochergin, M. Christophersen, P.R. Swinehart US Patent Application **20060027459** “*Mesoporous silicon infrared filters and methods of making same*”, filed May 28, 2005.
14. V. Kochergin, US Patent Application **20050221128** “*Negative refractive index and opto-magnetic materials and method of fabrication same*”, filed Dec. 18, 2004.
15. V. Kochergin, US Patent Application “*Optical fiber diagnostic system using vertical; cavity surface emitting lasers with integrated tuning means*”, filed Nov. 21, 2004.
16. V. Kochergin, P.R. Swinehart, M. Maklad US Patent Application **20060103380** “*Magneto-optical resonant waveguide sensors*”, filed Nov. 15, 2005.
17. V. Kochergin, M. Sanghavi, W. McGovern US Patent Application “*Long wave pass infrared filter based on porous semiconductor material and the method of manufacturing the same*”, filed May. 16, 2006.
18. V. Kochergin, P.R. Swinehart, International Patent Application PCT/US03/32925) “*Spectral filter for green and shorter wavelengths and the method of manufacturing the same*”, filed Nov. 2003.

A.4 Conference Oral Contributions

1. A.A. Beloglazov, A.V. Kabashin, V.E. Kochergin, M.V. Valeiko, P.I. Nikitin, “*Interferometry using surface plasmon resonance*”, Xth conference on Sensors and Transducers for measurement and control, Gurzuf, Ukraine, May 1998.
2. P.I. Nikitin, V.E. Kochergin A.A. Beloglazov, M.V. Valeiko, T.I. Ksenevich, “*Surface plasmon resonance interferometry for high-sensitive and wide-range sensing*”, EUROSENSORS XII, Sept. 1998, Southampton, UK.
3. P.I. Nikitin, A.A. Beloglazov, A.V. Kabashin, M.V. Valeiko, V.E. Kochergin “*Surface plasmon resonance interferometry for sensor applications*”, Europt(r)ode IV, 4th European Conference on Optical Chemical Sensors and Biosensors, Muenster, Germany, March 29-April 1, 1998.
4. P.I. Nikitin, A.A. Beloglazov, V.E. Kochergin “*Surface plasmon resonance combined with surface-enhanced Raman scattering for chemical and biosensing*”, BIOS 98, San Jose, CA, USA, 21-29 January 1998.
5. V. Kochergin, P.R. Swinehart “*Improved magneto-optical imaging films employing surface plasmon resonance*”, NATO Advanced Research Workshop Magneto-Optical Imaging, 28-30 August 2003, Øystese, Norway.

6. I. Avrutsky, V. Kochergin, Y. Zhao, “*Optical bio-sensors based on diffraction efficiency of waveguide gratings.*” OSA-99/ILS-XV, Santa Clara, CA, USA, September 26-30, 1999.
7. I. Avrutsky, Y. Zhao, V. Kochergin, “*Surface plasmon assisted tunneling of light through thin metal film.*” OSA-2000/ILS-XVI, Providence, Rhode Island, USA, October 22-26, 2000.
8. I. Avrutsky, V. Kochergin, Y. Zhao, “*Optical demultiplexing using colloidal crystal waveguides.*” OSA-2000/ILS-XVI, Providence, Rhode Island, USA, October 22-26, 2000.
9. I. Avrutsky, V. Kochergin, P. Swinehart, “*Optical filtering by leaky waveguides*”, 2003 Frontiers in Optics/Laser Science XIX Conference, Tucson, AR, USA, October 5 - 9, 2003.
10. V. Kochergin, M. Christophersen, P.R. Swinehart, “*Macroporous Silicon-based polarization components*”, SPIE 49th Annual Meeting, Denver, CO, USA Aug 2004.
11. V. Kochergin, M. Christophersen, P.R. Swinehart, “*Macroporous Silicon UV filters for space and terrestrial environments*”, SPIE 49th Annual Meeting, Denver, CO, USA Aug 2004.
12. M. Christophersen, V. Kochergin, P.R. Swinehart, “*Macroporous Silicon filters for mid-to-far IR range*”, SPIE 49th Annual Meeting, Denver, CO, USA Aug 2004.
13. V. Kochergin, O. Sneh, M. Sanghavi, P.R. Swinehart, “*Macroporous silicon deep UV filters*”, ESTC-05 Conference, June 2005, Baltimore, MD, USA.
14. V. Kochergin, M. Sanghavi, P.R. Swinehart, “*Porous silicon filters for low-temperature far IR applications*”, SPIE 50th Annual Meeting (Optics and Photonics), San Diego, CA, USA, Aug. 2005.
15. **Invited talk:** V. Kochergin and H. Föll, “*Commercial applications of porous Si: optical filters and components*”, Int. Conference of Porous Semiconductors- Science and technology, March 2006, Barcelona, Spain.
16. W. R. McGovern, V. Kochergin, M. R. Sanghavi, P. R. Swinehart, “*Porous silicon optical filters for far-IR and low-temperature applications*”, Great Lakes Photonics Symposium 12-16 June 2006, Dayton, OH, USA.

A.5 Conference Posters

1. T.I. Ksenevich, V.E. Kochergin, P.I. Nikitin “*SPR interferometer for pesticide detection*”, Chemical, Biochemical and Environmental Fiber Sensors X, 1998.
2. V.E. Kochergin, M.V. Valeiko, A.A. Beloglazov, P.I. Nikitin “*Surface plasmon resonance interferometer for high sensitivity and wide range sensing*”, XVI International Conference On Lasers and Nonlinear Optics, July, 1998, Moscow, Russia.

3. A.V. Kabashin, V.E. Kochergin and P.I. Nikitin, "*Phase-polarization contrast for surface plasmon resonance sensor systems*", Europt(r)ode IV, 4th European Conference on Optical Chemical Sensors and Biosensors, Muenster, Germany, March 29-April 1, 1998.
4. A. Kabashin, A. Kochergin, P. Nikitin, "*Phase-polarization contrast for surface plasmon resonance biosensors*", Biosensors'98, 2-5 June, 1998, Berlin.
5. V. Kochergin, H. Föll, "*Effective Medium Approach For Calculation of Linear and Nonlinear Properties of Porous Semiconductor Composites*", MRS Spring Annual Meeting, San Francisco, USA, March 2005.

Bibliography:

- [1] M. Kerker, *J. Colloid Interface Sci.*, 105:297 (1985).
- [2] M. Faraday, *Philos. Trans. Royal Soc. London* **1857**, 147, 135.
- [3] Rouard P., *Contes Rendus de l'Academie de Science*, **195**, p. 896, 1932.
- [4] Bauer, G., *Ann. Phys.*, **19**, p. 434, 1934.
- [5] Strong J., *J. Opt. Soc. Am.*, **26**, p. 73, 1936.
- [6] Joannopoulos J.D., Meade R.D., Winn J.N., *Photonics Crystals: Molding the Flow of Light*, Princeton University Press, 1995.
- [7] Eds. K. Busch, S. Lölkes, R.B. Wehrspohn, and H. Föll, in *Photonic Crystals: Advances in Design, Fabrication, and Characterization*, Wiley-VCH Verlag GmbH & Co. KGaA, Weinheim (2004).
- [8] V.M. Shalaev, *Physics Reports* **272** (1996), 61-137.
- [9] A.N. Grigorenko *et al.*, *Nature* **438**, 335 (2006).
- [10] E. Ozbay, *Science* **311**, 189 (2006).
- [11] H. Föll, S. Langa, J. Carstensen, M. Christophersen, I.M. Tiginyanu, "Review: Pores in III-V Semiconductors", *Adv. Materials*, **15**, 183 (2003).
- [12] L.T. Canham, "Silicon quantum wire array fabrication by electrochemical and chemical dissolution of wafers", *Appl. Phys. Lett.* **57**, 1046 (1990).
- [13] V. Lehmann and U. Gösele, "Porous silicon: a quantum wire effect", *Appl. Phys. Lett.* **58**, 856 (1991).
- [14] D.A.G. Bruggemann, "Berechnung verschiedener physikalischer Konstanten von heterogenen Substanzen", *Ann. Phys.* **24**, 636 (1935).
- [15] H. Föll, M. Christophersen, J. Carstensen, and G. Hasse, "Formation and application of porous Si", *Mat. Sci. Eng. R* **39(4)**, 93 (2002).
- [16] M.J. Sailor, *Sensor application of porous silicon*, in: L.T. Canham (Ed.), *Properties of Porous Silicon*, IEE-Books, London (1997).
- [17] H. Föll, S. Langa, J. Carstensen, I.M. Tiginyanu, M. Christophersen, and K. Dichtel, "Pore Etching in Compound Semiconductors for the Production of Photonic Crystals", in *MRS Proceedings Spring Meeting: Materials and Devices for Optoelectronics and Microphotonics*, eds. R.B. Wehrspohn, S. Noda, C. Soukoulis, and R. März, L6.4 (2002).

- [18] J. Diener, N. Künzner, D. Kovalev, E. Gross, V.Y. Timoshenko, G. Polisski, and F. Koch, "Dichroic Bragg reflectors based on birefringent porous silicon", *Appl. Phys. Lett.* **78**, 3887 (2001).
- [19] D. Kovalev, G. Polisski, J. Diener, H. Heckler, N. Künzner, V.Yu. Timoshenko, and F. Koch, "Strong in-plane birefringence of spatially nanostructured silicon" *Appl. Phys. Lett.* **78**, 916 (2001).
- [20] J. Diener, N. Künzner, D. Kovalev, E. Gross, and F. Koch, "Dichroic behavior of multilayer structures based on anisotropically nanostructured silicon", *J. Appl. Phys.* **91**, 6704 (2002).
- [21] J. Diener, N. Künzner, E. Gross, D. Kovalev, and M. Fujii, "Planar silicon-based light polarizers", *Opt. Lett.* **29**, 195 (2004).
- [22] U. Grüning, V. Lehmann, S. Ottow, and K. Busch, "Macroporous silicon with a complete twodimensional band gap centered at 5 μm ", *Appl. Phys. Lett.* **68**, 747 (1996).
- [23] F. Müller, A. Birner, U. Gösele, V. Lehmann, S. Ottow, and H. Föll, "Structuring of macroporous silicon for applications as photonic crystals", *Journal of Porous Materials* **7**, 201 (2000).
- [24] M. Christophersen, J. Carstensen, A. Feuerhake, and H. Föll, "Crystal orientation and electrolyte dependence for macropore nucleation and stable growth on p-type Si", *Mater. Sci. Eng. B* **69-70**, 194 (2000).
- [25] S. Rönnebeck, S. Ottow, J. Carstensen, and H. Föll, "Crystal orientation dependence of macropore formation in n-Si with backside-illumination in HF-electrolyte", *Journal of Porous Materials* **7**, 353 (2000).
- [26] R.B. Wehrspohn, J. Schilling, J. Choi, Y. Luo, S. Matthias, S. Schweizer, F. Müller, U. Gösele, S. Lölkes, S. Langa, J. Carstensen, and H. Föll, in *Photonic Crystals: Advances in Design, Fabrication, and Characterization*, eds. K. Busch, S. Lölkes, R. Wehrspohn, and H. Föll, Wiley-VCH, Weinheim (2004).
- [27] T.V. Dolgova, A.I. Maidykovski, M.G. Martemyanov, A.A. Fedyanin, O.A. Aktsipetrov, G. Marowsky, V.A. Yakovlev, G. Mattei, N. Ohta, and S. Nakabayashi, "Giant optical second-harmonic generation in single and coupled microcavities formed from one-dimensional photonic crystals", *J. Opt. Soc. Am. B* **19**, 2129 (2002).
- [28] I.M. Tiginyanu, I.V. Kravetsky, G. Marowsky, and H.L. Hartnagel, "Semiconductor sieves as nonlinear optical materials", *phys. stat. sol. (a)* **175**, R5 (1999).
- [29] I.M. Tiginyanu, I.V. Kravetsky, S. Langa, G. Marowsky, H.L. Hartnagel, and H. Föll, "Porous III-V Compounds as Nonlinear Optical Materials", *phys. stat. sol. (a)* **197(1/2)** (2003).
- [30] V. Lehmann, R. Stengl, H. Reisinger, R. Detemple, and W. Theiss, "Optical shortpass filters based on macroporous silicon", *Appl. Phys. Lett.* **78**, 589 (2001).

- [31] S. Cruz, A. Hönig-d'Orville, and J. Müller, "Fabrication and optimization of porous silicon substrates for diffusion membrane application", *J. Electrochem. Soc.* **152(6)**, C418 (2005).
- [32] S. Langa, I.M. Tiginyanu, J. Carstensen, M. Christophersen, and H. Föll, "Self-organized growth of single crystals of nanopores", *Appl. Phys. Lett.* **82(2)**, 278 (2003).
- [33] S. Langa, M. Christophersen, J. Carstensen, I.M. Tiginyanu, and H. Föll, "Electrochemical pore etching in Ge", *Phys. Stat. Sol. a* **195**, R4 (2003).
- [34] ET&TE Etch and Technology GmbH, "", <http://www.et-te.com>.
- [35] S.W. Leonard, H.M. van Driel, K. Busch, S. John, A. Birner, A.P. Li, F. Müller, U. Gösele, and V. Lehmann, "Tunable two-dimensional photonic crystals using liquid-crystal infiltration" *Appl. Phys. Lett.* **75**, 3063 (1999).
- [36] S.W. Leonard, "Complete three-dimensional band gap in macroporous silicon photonic crystals", *Appl. Phys. Lett.* **81**, 2917 (2002).
- [37] H. Looyenga, *Physica* **31**, 401 (1965).
- [38] J.C.M. Garnett, "Colours in metal glasses and in metallic films", *Philos. Trans. Roy. Soc. London* **203**, 385 (1904).
- [39] Q.H. Wu, L. De Silva, M. Arnold, I.J. Hodgkinson, and E. Takeuchi, "All-silicon polarizing filters for near-infrared wavelengths", *J. Appl. Phys.* **95**, 402 (2004).
- [40] G. Vincent, "Optical properties of porous silicon superlattices", *Appl. Phys. Lett.* **64(18)**, 2367 (1994).
- [41] M.G. Berger, C. Dieker, M. Thoenissen, L. Vescan, H. Lueth, H. Muender, W. Theiss, M. Wernke, P. Grosse, P., "Porosity superlattices: A new class of Si heterostructures", *J. Phys. D.* **27**, 1333 (1994).
- [42] S. Frohnhoff, M.G. Berger, "Porous silicon superlattices", *Adv. Mat.* **6**, 963 (1994)
- [43] M. Krueger, M.G. Berger, M. Marso, W. Reetz, T. Eickhoff, R. Loo, L. Vescan, M. Thönissen, H. Lüth, R. Arens-Fischer, S. Hilbrich and W. Theiss, "Color-sensitive Si-photodiode using porous silicon interference filters", *Jpn. J. Appl. Phys.* **36**, L24 (1997).
- [44] J.M. Lauerhaas, G.M. Credo, J.L. Heinrich, and M.J. Sailor, "Reversible Luminescence Quenching of Porous Si by Solvents", *J. Am. Chem. Soc.* **114**, 1911 (1992).
- [45] M.J. Sailor, G. Credo, J. Heinrich, and J.M. Lauerhaas, "Method for Detection of Chemicals by Reversible Quenching of Silicon Photoluminescence", *U.S. Patent* **5,338,415** (1994).
- [46] V.S.-Y. Lin, K. Motesharei, K.S. Dancil, M.J. Sailor, and M.R. Ghadiri, "A Porous Silicon Based Optical Interferometric Biosensor", *Science* **278**, 840 (1997).

- [47] F. Cunin, T.A. Schmedake, J.R. Link, Y.Y. Li, J. Koh, S.N. Bhatia, and M.J. Sailor, "Biomolecular screening with encoded porous-silicon photonic crystals", *Nat.Mat.* **1**, 39 (2002).
- [48] Y.Y. Li, F. Cunin, J.R. Link, T. Gao, R.E. Betts, S.H. Reiver, V. Chin, S.N. Bhatia, M.J. Sailor., "Polymer Replicas of Photonic Porous Silicon for Sensing and Drug Delivery Applications", *Science* **299**, 2045 (2003).
- [49] L. Pavesi, *Riv. Nuovo Cimento* **20**, 1 (1997).
- [50] S. Setzu, P. Ferrand, R. Romestain, "Optical properties of multilayered porous silicon", *Materials Science and Engineering* **B69-70**, 34 (2000).
- [51] G. Lerondel, P. Reexe, A. Bruyant, and M. Gal, *Mat. Res. Soc. Symp. Proc.* **797**, 15 (2004).
- [52] L.T. Canham, A.G. Cullis, C. Pickering, O.D. Dosser, T.I. Cox, and T.P. Lynch, "Luminescent anodized silicon aerocrystal networks prepared by supercritical drying", *Nature* **368**, 133 (1994).
- [53] M. Krüger, S. Hilbrich, M. Thönissen, D. Scheyen, W. Theiß and H. Lüth "Suppression of ageing effects in porous silicon interference filters", *Optics Communications* **146**, 309 (1998).
- [54] M.G. Berger, R. Arens-Fischer, St. Frohnhoff, C. Dieker, K. Winz, H. Muender, H. Lueth, M. Arntzen, W. Theiss, W., "Formation and properties of porous Si superlattices", *Mat. Res. Symp. Proc.* **358**, 327 (1995).
- [55] H. Sugiyama and O. Nittono, "Microstructure and lattice disortion of anodized porous silicon layers", *J. Crystal Growth* **103**, 156 (1990).
- [56] G. Bomchil et al., *Microelectronic Eng.* **8**, 293 (1988).
- [57] V.Y. Timoshenko, Th. Dittrich, V. Lysenko, M.G. Lisachenko, F. Koch, F., "Free charge carriers in mesoporous silicon", *Phys. Rev. B* **V 64**, 085314 (2001).
- [58] J.M. Buriak, "Organometallic Chemistry on Silicon and Germanium Surfaces", *Chemical Reviews* **102 (5)**, p. 1271 (2002).
- [59] Buriak, J. M.; Allen, M. J. "Photoluminescence of Porous Silicon Surfaces Stabilized Through Lewis Acid Mediated Hydrosilylation" *J. Lumin.* **1999**, *80*, 29-35.
- [60] Buriak, J. M.; Stewart, M. P.; Allen, M. J. "Hydrosilylation Reactions on Porous Silicon Surfaces" *Mater. Res. Soc. Symp. Proc.* **1998**, *536*, 173-178.
- [61] Canham, L. T.; Reeves, C. L.; Newey, J. P.; Houlton, M. R.; Cox, T. I.; Buriak, J. M., Stewart, M. P. "Derivatized Mesoporous Silicon With Dramatically Improved Stability in Simulated Human Blood Plasma" *Advanced Materials*, **1999**, *11*, 1505-1509.

- [62] Robins, E. G.; Stewart, M. P.; Buriak, J. M. "Anodic and Cathodic Electrografting of Alkynes on Porous Silicon", *J. Chem. Soc., Chem. Commun.* **1999**, 2479-2480.
- [63] Lees, I.N., H. Lin, C.A. Canaria, C. Gurtner, M.J. Sailor, and G.M. Miskelly, Chemical Stability of Porous Silicon Surfaces Electrochemically Modified with Functional Alkyl Species. *Langmuir*, 2003. **19**: p. 9812-9817.
- [64] assigned to N. Sato, "Semiconductor Substrate and method for producing the same", *U.S. Patent 6,593,211* (2003).
- [65] assigned to N. Sato, "Method and apparatus for etching a semiconductor article and method of preparing a semiconductor article by using the same", *U.S. Patent 6,413,874* (2002).
- [66] G. Müller and R. Brendel, "Simulated annealing of porous silicon", *phys. stat. sol. (a)* **182**, 313 (2000).
- [67] G. Müller, N. Nerding, N. Ott, H.P. Strunk, and R. Brendel, "Sintering of porous silicon", *phys. stat. sol. (a)* **197(1)**, 83 (2003).
- [68] R Corban, H. Bousack, H.G. Bohn "Protective coatings for interference filters made of porous silicon", *phys. stat. sol. (a)* **197(2)**, 370 (2003).
- [69] A.M. Hynes, H. Ashraf, J.K. Bhardwaj, J. Hopkins, I. Johnston, and J.N. Shepherd, "Recent advances in silicon etching for MEMS using the ASETM process", *Sensors and Actuators* **74**, 13 (1999).
- [70] U. Gösele and Q.-Y. Tong, "Semiconductor wafer bonding", *Annual Review of Materials Science* **28**, 215 (1998).
- [71] H.A. Macleod, *Thin Film Optical Filters, 3rd Ed.*, Institute of Physics Publishing (2001).
- [72] K.R. Armstrong and F.J. Low, "Far-infrared-filters utilizing small particle scattering and antireflection coatings", *Appl. Optics* **13(2)**, 425 (1974).
- [73] J. Schilling, A. Birner, F. Mueller, R.B. Wehrspohn, R. Hillebrand, U. Goesele, K. Busch, S. John, S.W. Leonard, and H.M. van Driel, "Optical characterisation of 2D macroporous silicon photonic crystals with bandgaps around 3.5 and 1.3 μm ", *Opt. Mater.* **17**, 7 (2001).
- [74] J. Schilling, F. Müller, S. Matthias, R.B. Wehrspohn, U. Gösele, and K. Busch, "3D photonic crystals made out of macroporous silicon by modulation of pore diameter", *Appl. Phys. Lett.* **78**, 1180 (2001).
- [75] V. Lehmann, "Porous silicon matrix for chemical synthesis and chromatography", *Phys. Stat. Sol.* **202**, 1365 (2005).
- [76] Keilmann F., *Int. J. of Infrared and Millimeter Waves* **2**, p. 259, 1981.
- [77] Timusk T., Richards P.L., *Appl. Optics* **20**, p.1355, 1981.

- [78] Huggard P. G., Meyringer M., Schilz A., Goller K., Prettl W., "Far-infrared bandpass-filters from perforated metal screens," *Appl. Optics* **33**, p. 39, 1994.
- [79] E. D. Palik, *Handbook of Optical Constants of Solids*, Academic Press, 1988.
- [80] M. J. Adams, *An Introduction to Optical Waveguides*, Wiley, 1981.
- [81] A. Yariv, P. Yeh, *Optical Waves in Crystals*, Wiley, 1984.
- [82] J. A. Harrington, *Fiber and Integrated Optics*, **19**, 211 (2000).
- [83] M. Ritala and M. Leskela, in: *H.S. Nalwa, (Ed.), Handbook of Thin Film Materials, Vol. 1, Chapter 2, p. 103*, Academic Press, San Diego (1997).
- [84] S.M. George, A.W. Ott, and J.W. Klaus, "Surface chemistry for atomic layer growth", *J. Phys. Chem.* **100**, 13121 (1996).
- [85] O. Sneh, R.B. Clark-Phelps, A.R. Londergan, J.L. Winkler, and T.E. Seidel, "Thin film atomic layer deposition equipment for semiconductor processing", *Thin Solid Films* **402(1-2)**, 248, 2002.
- [86] V. Lehmann and S. Rönnebeck, "MEMS Techniques Applied to the Fabrication of Anti-Scatter Grids for X-Ray Imaging", in *Technical Digest of the 14th IEEE International Conference on Micro Electro Mechanical Systems*, 84, Interlaken (2001).
- [87] S. Ottow, V. Lehmann, and H. Föll, "Processing of three-dimensional microstructures using macroporous n-type silicon", *J. Electrochem. Soc.* **143**, 153 (1996).
- [88] G. Barillaro, A. Nannini, M. Piotto, "Electrochemical etching in HF solution for silicon micromachining", *Sensors and Actuators A* **102**, 195 (2002).
- [89] T.M. Geppert, S.L. Schweizer, J. Schilling, C. Jamois, R.B. Wehrspohn, A. v.Rhein, D. Pergande, S.L. Schweizer, R.B. Wehrspohn, R. Glatthaar, P. Hahn, A. Feisst, and A. Lambrecht, "Photonic crystal gas sensors", in *Proc.of the SPIE 5511*, 61 (2004).
- [90] L.A. Coleman, "Infrared Sensors: The Eyes of the Digital Battlefield", *Military and Aerospace Electronics*, 29 (1994).
- [91] N. George and D.J. Schertler, "Optical system for diffusing light", *U.S. Patent* **6,259,561** (2001).
- [92] J.W. Klaus, S.J. Ferro, and S.M. George, "Atomic Layer Deposition of Tungsten Nitride Films Using Sequential Surface Reactions", *J. Electrochem. Soc.* **147**, 1175 (2000).
- [93] M. Hejjo Al Rifai, M. Christophersen, S. Ottow, J. Carstensen, and H. Föll, "Potential, temperature and doping dependence for macropore formation on n-Si with backside illumination", *J. of Porous Materials* **7(1/2/3)**, 33 (2000).
- [94] V. Pellegrini, A. Tredicucci, C. Mazzoleni, L. Pavesi: *Phys. Rev. B* **52**, 14328 (1995).

- [95] J. Zettner, M. Thoenissen, Th. Hierl, R. Brendel, M. Schulz: *Progress in Photovoltaics: Research and Applications* **6**, 423 (1999).
- [96] A.D. Yaghjian: *Proc. IEEE*, **68**, 248 (1980).
- [97] M. Maldovan, M.R. Bockstaller, E.L. Thomas, W.C. Carter: *Appl. Phys. B* **76**, 877 (2003).
- [98] A. Shivola, I.V. Lindell: *J. Electromagnetic Waves Applic.* **3**, 37 (1989).
- [99] A.G. Cullis, L.T. Canham, P.D.J. Calcott: *J. Appl. Phys.* **82**, 909 (1997).
- [100] V. Lehmann, R. Stengl, A. Luigart: *Materials science and engineering B*, **69-70**, 11(2000).
- [101] C. Faivre, D. Bellet, *J. Appl. Cryst.* **32**, 1134 (1999).
- [102] L.D. Landau, E.M. Lifshits: *Electrodynamics of Continuous Media*, 2nd ed. (Butterworth-Heinenann, Oxford, 1984).
- [103] S. Langa, I. M. Tiginyanu, J. Carstensen, M. Christophersen, H. Föll: *J. Electrochem. Soc. Lett.* **3**, 514 (2000).
- [104] H. Föll, J. Carstensen, S. Langa, M. Christophersen, I. M. Tiginyanu: *Phys. Stat. Sol. A* **197**, 61 (2003).
- [105] B. H. Erne, D. Vanmaekelbergh, J.J. Kelly: *J. Electrochem. Soc.* **143**, 305 (1996).
- [106] S. Langa, J. Carstensen, M. Christophersen, H. Föll, and I.M. Tiginyanu, *Appl. Phys. Lett.*, **78**, 1074 (2001).
- [107] P. Schmuki, and L. E. Erickson, *Appl. Phys. Lett.*, **73**, 2600 (1998).
- [108] P. Schmuki, D. J. Lockwood, H. J. Labbe, and J. W. Fraser, *Appl. Phys. Lett.*, **69**, 1620 (1996).
- [109] H. Föll, S. Langa, J. Carstensen, S. Lölkes, M. Christophersen, and I. M. Tiginyanu, *III-Vs Review*, **16**, 42 (2003).
- [110] G. Sauer, G. Brehm, S. Schneider, K. Nielsch, R.B. Wehrspohn, J. Choi, H. Hofmeister, and U. Gösele, *J. Appl. Phys.* **91** 3243 (2002).
- [111] S. Matthias, J. Schilling, K. Nielsch, F. Müller, R.B. Wehrspohn and U. Gösele: *Adv. Mater.* **14** 1618 (2002)
- [112] H. Kuwata, H. Tamaru, K. Esumi, K. Miyaho: *Appl. Phys. Lett.* **83**, 4625 (2003).
- [113] M. Moskovits: *Reviews of Modern Physics* **57**, 783 (1985).
- [114] *Properties of Porous Silicon* Edited by Leigh Canham, (IEE Publishing, June 1998).

- [115] D.R. Smith, D. Schurig: *Phys. Rev. Lett.*, **90**, 77405 (2003)
- [116] Lo K.Y., Lue J.T.: *IEEE Photonics Technology Letters* 5 (6), p. 651 (1993).
- [117] Gusev D.G., Soboleva I.V., Martemyanov M.G., Dolgova T.V., Fedyanin A.A., Aktsipetrov O.A.: *Phys. Rev. B* 68 (23): Art. 233303 (2003).
- [118] Falasconi M., Andreani L.C., Malvezzi A.M., Patrini M., Mulloni V., Pavesi L.: *Surface Science* 481 (1-3), p. 105-112 (2001).
- [119] Monecke J., Bezrukova J., Cordts W., Richardson G.: *Phys. Stat. Solidi B* 241 (3), p R8-R10 (2004).
- [120] O. Levy, D. Stroud: *Phys. Rev. B* 56 (13), 8035 (1997).
- [121] X.C. Zeng, D.G. Bergman, P.M. Hui, and D. Stroud: *Phys Rev. B* 38, 10970 (1988).
- [122] P.M. Hui, C.Xu, and D. Stroud: *Phys. Rev. B* 69, 014203 (2004).
- [123] D. Stroud: *Superlattices and Microstructures*, 23 (3/4), 567 (1998).
- [124] A. D. McFarland and R. P. Van Duyne, *Nano Lett.* **3**, 1057 (2003).
- [125] K. Kneipp *et al.*, *Phys. Rev. Letters* **78**, 1667 (1997).
- [126] P. M. Hui and D. Stroud, *Appl. Phys. Lett.* **50**, 950 (1987).
- [127] L.M. Liz-Marzan, *Langmuir* **22**, 32-41 (2006).
- [128] G. Mie, *Ann. Phys.* 25:329 (1908).
- [129] W.A. Curtin *et al.*, *Phys. Rev. Lett.* V54 N10, p 1071, 1985.
- [130] D. Stroud, D.J. Bergman, *Phys. Rev. B*, V25, N3, 2061 (1982).
- [131] X. Zhang, D. Stroud, *Phys. Rev. B.*, V48, N9, 6658 (1993).
- [132] R.S. Koss, D. Stroud, *Phys. Rev. B*, V35, N17, 9004 (1987).
- [133] D.J. Bergman, *Physics Reports* 43 (1978).
- [134] R. Fuchs and F. Claro, *Phys. Rev. B*, 39 (6), p. 3875, 1989.
- [135] P.M. Hui, D. Stroud, *Phys. Rev. B*, V33, N4, 2163 (1986).
- [136] P.M. Hui, D. Stroud, *Phys. Rev. B*, V49, N17, 11729 (1994).
- [137] V.A. Markel *et al.*, *Phys. Rev. B*, V53, N5, 2425 (1996).
- [138] V.A. Markel *et al.*, *Phys. Rev. B*, V70, 054202 (2004).

- [139] R.G. Barrera et al., *Phys Rev. B* 39(14), 9998 (1989).
- [140] R.G. Barrera et al., *J. Chem. Phys.* 96(2), 1574 (1992).
- [141] L.G. Grechko et al., *Appl. Phys. Lett.*, 76 (14), 1854 (2000).
- [142] U. Schürmann, W.A. Hartung, H. Takele, V. Zaporojtchenko, and F. Faupel *Nanotechnology* 16, 1078 (2005).
- [143] K. Behnke, T. Strunskus, V. Zaporojtchenko, and F. Faupel, in: *Proc. 3rd Int. Conf. MicroMat 2000*, B Michel, T. Winkler, M. Werner, H. Fecht (Eds.), 2000, 1052.
- [144] V. Zaporojtchenko, K. Behnke, T. Strunskus, F. Faupel, *Surface Science* 454-456 (2000), 412-416.
- [145] V. Zaporojtchenko, J. Zekonyte, A. Biswas, F. Faupel, *Surface Science* 532-535 (2003), pp. 300-305.
- [146] P. B. Johnson and R. W. Christy, *Phys. Rev. B* 6, 4370 (1972).
- [147] S. Berthier, *J. Phys. I. France* 4 (1994), 303-318.
- [148] P. Norlander, et al., *Nano Lett.*, 4(5), pp. 899-903, 2004.
- [149] E. Prodan, et al., *Science*, 302, 419 (2003).
- [150] E. Prodan and P. Norlander, *J. of Chem. Phys.*, 120 (11), 5444 (2004).
- [151] J.M.Gerardy and M.Ausloos, *Phys. Rev. B*, 22, 4950 (1980).
- [152] J.M.Gerardy and M.Ausloos, *Phys. Rev. B* 25, 4204 (1982).
- [153] J.M.Gerardy and M.Ausloos, *Phys. Rev. B* 27, 6446 (1983).
- [154] B.U. Felderhof and R.B. Jones, *Phys. Rev. B* 39 (9), 1989, p.5669-5677.
- [155] Faraday M., *Philos. Transd. R. Soc. London*, XIX, 1, 1846.
- [156] Voigt, W., *Ann. Phys. (Leipzig)*, 4, 197, 1901.
- [157] Voigt, W., *Kgl. Ges. Wiss. Nachr., Math.-Phys. Kl.*, 1898, 355.
- [158] Bonod, N., et al., *Journal of the Optical Society of America B*, Vol. 21 (4), pp. 791-797, (2004).
- [159] Hermann, C. et al., *Phys. Rev. B*, Vol. 64 (23), pp. 2354221-23542211, (2001).
- [160] Safarov, V.I. et al., *Phys. Rev. Lett.*, Vol. 73 (26), pp. 3584-3587, (1994).
- [161] Kochergin V.E. et al, *JETP Letters*, 68 (5), Sept. 1998, p.400.

- [162] P.H. Lissberger and P.W. Saunders, *Thin Solid Films* **34**, 323 (1976).
- [163] M. Abe and T. Suwa, *Phys. Rev. B*, **70**, p. 235103 (2004).
- [164] M. Abe and M. Gomi, *Jpn. J. Appl. Phys.* **23**, 1580 (1984).
- [165] C.-Y. You et al., *Phys. Rev. B* **55** (9), 5953 (1997).
- [166] Genov D.A., et al., *Nano Lett.*, Vol. 4 (1), pp.153-158, (2004).
- [167] R.M.A. Azzam, N.M. Bashara “*Ellipsometry and polarized light*”, North Holland, Amsterdam (1977), p.37.
- [168] C.-Y. You and S.-C. Shin, *Appl. Pys. Lett.* **69** (9), pp. 1315-1317 (1996).
- [169] D.J. Bergman, D. Stroud, *Solid State Phys.* **46** (1992), p. 14.
- [170] D. Stauffer, A. Aharony, *An introduction to Percolation Theory*, 2nd Edition, Taylor and Francis, London, 1994.
- [171] M. Gadenne et al., *Europhys. Lett.* **53** (3), pp. 364-370 (2001).
- [172] V.A. Podolskiy et al., in *Photonic Crystals and Light Localization in the 21st Century*, pp. 567-575, Edited by C.M. Soukulis, Kluwer Academic Publishers, Netherlands.
- [173] R.H. Morriss and L.F. Collins, *J. Chem. Phys.* **41**,3357 (1964).
- [174] P. Mulvaney, *Langmuir* **12**, 778 (1996).
- [175] L.M. Liz-Marzan and A.P. Philipse, *J. Phys. Chem.* **99**, 15120 (1995).
- [176] F. Caruso et al., *Adv. Mater.* **13**, 1090 (2001).
- [177] V. Salgueirino-Maceira et al., *J. Phys. Chem. B* **107**, 10990 (2003).
- [178] R. Carey et al., *IEEE Trans. Magn.* **33**, 3256 (1997).
- [179] A.L. Adeb and M. Kerker, *J. Appl. Phys.* **22**, 1242 (1951).

Curriculum Vitae

Name: Vladimir Kochergin
Address: 640 Brook Run Dr., Westerville OH 43081
Born: Aug. 27, 1975, Donetsk, Ukraine
Matrimonial status: Married
Citizenship: Russian
Parents: Evgeniy Kochergin and Elena Kochergin

School education:

1982-1983 5th elementary school of Slavyansk, Ukraine
 1983-1984 57th elementary school of Donetsk, Ukraine
 1984-1985 54th elementary school of Donetsk, Ukraine
 1985-1988 54th middle school of Donetsk, Ukraine
 1988-1992 17th high school of Donetsk, Ukraine
 June 1992 Graduation from 17th high school, Ukraine, with silver medal.

University Education:

1992-1993 (2 semesters) Studied at the Department of Aerodynamics and Flight Technique, Moscow Institute of Physics and Technology (MIPT), Moscow, Russia
 1993-1996 (6 semesters) studied at the Department of Physic and Energetic Problems, MIPT, Moscow, Russia

Master Course: Optics

June 1996 Received a Bachelor Degree for Applied Physics and Mathematics from MIPT, Moscow, Russia.
 1996-1998 (4 semesters) studied at the Department of Physic and Energetic Problems, MIPT, Moscow, Russia

Master Course: Laser Physics

June 1998 Received a Master Degree for Applied Physics and Mathematics from MIPT, Moscow, Russia.
 1998-1999 (1 semester) Studied on a PhD program, MIPT, Moscow, Russia
 Courses Taken:
 Foreign Language (English), Patent Law, Philosophy.
 2000-2001 (2 semesters) Studied on a PhD program at ECE Department, Wayne State University, Detroit, MI
 Master Course: Photonics.
 2003-2006 External PhD program at „Technische Fakultät der Christian-Albrechts-Universität zu Kiel“.

Academia Experience:

1995- 1999 Research assistant at the Low Temperature Laser Plasma Laboratory, General Physics Institute (GPI), Russian Academy of Science, Moscow, Russia

1999- 2000 research associate at ECE Department, Wayne State University, Detroit, MI

Industry experience:

2000-2006 Engineer II, Engineer III, Engineer IV, Lake Shore Cryotronics, Inc., Westerville, OH, US

(Vladimir Yevgenyevich Kochergin)

List of Abbreviations

ALD – Atomic Layer Deposition.

Bi:YIG – Bismuth-doped Yttrium Iron Garnet.

BSI - Back Side Illumination.

CVD – Chemical Vapor Deposition.

EMA- Effective Medium Theory.

FSI - Front Side Illumination.

FTIR – Fourier Transform Spectrometer.

GaAs - Gallium Arsenide.

GaP - Gallium Phosphide.

Ge - Germanium.

IBAD - Ion Beam Assisted Deposition.

ICP RIE – Inductively Coupled Plasma Reactive Ion Etching.

InP - Indium Phosphide.

IR – Infrared.

LWIR – long wavelength IR.

LPCVD – Low Pressure Chemical Vapor Deposition.

MEMS - Microelectromechanical Systems.

MG – Maxwell Garnet approximation.

MO – magneto-optics.

MPSi – Macroporous Silicon.

PC - Photonic Crystals.

PBG – Photonic Bandgap.

PECVD – Plasma Enhanced Chemical Vapor Deposition.

RIE – Reactive Ion Etching.

SHG – Second Harmonic Generation

Si - Silicon.

SPR – Surface Plasmon Resonance.

SP – Surface Plasmon.

TE – Transverse Electric.

TEM – Transmission Electron Microscope.

TM – Transverse Magnetic.

SEM - Scanning Electron Microscope.

UV – Ultra-violet.

WDM - Wavelength Division Multiplexing.

YIG – Yttrium Iron Garnet.

Acknowledgements

First of all, I would like to thank Prof. Dr. Föll for the opportunity to defend this dissertation. Second, I would like to thank my wife Elena, my kids Anna and Eugene and my parents back in Ukraine for supporting me all the time.

The material of this dissertation was prepared with the great assistance of dozens of colleagues. I would like to thank the Lake Shore Cryotronics, Inc. management team, Mr. Michael Swartz particularly, for the financial support of my research. I would like to thank Dr. Philip R. Swinehart and Prof. Dr. Föll for the discussions, directions, suggestions and encouragement during my research. I am also grateful to Professors Yang Zhao and Ivan Avrutsky, who introduced me to this field of research. I would like to thank Dr. William McGovern, Mahavir Sanghavi and Dr. Marc Christophersen for their help with sample processing and characterization. I would like to thank Mr. Robert R. Toomey, Mr. Russell Goose, Mr. Ralph F. Orban and Mr. Jeff Hardman for the assistance in sample processing and equipment installation/maintenance. I would like to thank Dr. Saman Dharmatilleke for the help in electroplating. I am grateful to Dr. Kimberly D. Pollard for the useful discussions of the chemistry of silicon anodic etching and Mr. Christopher McGee for the help with electrochemical system development and for the help with the drawings. I would like to thank Professor Ivan Avrutsky for the help in optical evaluations of the some macroporous filters and Dr. Begg for the help with SEM investigation of some samples. I would like further to thank Dr. Ofer Sneh (Sundew Technologies) and Dr. Chris Keller (MEMS Precision Instruments) for the help with ALD and LPCVD deposition. I would like to thank Dr. Volker Lehmann for macroporous silicon membrane samples. Further, I would like to thank Dr. Zaporajtchenko and Prof. Dr. Franz Faupel for the scientific guidance in the area of nanocomposite materials. I would like to thank Dr. Carstensen for the help with electrochemical etching equipment and for the preparation of the certain samples.

At last but not the least I would like to thank NASA JPL SBIR Office (Dr. Michael Ressler), NASA LRC SBIR Office (Dr. Dave Johnson and Dr. Cook), NASA GSFC SBIR Office (Dr. Scott Owens), MDA SBIR Office (Mr. Alex Gilmore) and NSF SBIR Office (Dr. Winslow Sergeant) for the generous financial support of my research.

EIDESSTATTLICHE ERKLÄRUNG

Ich erkläre hiermit, dass ich keine anderen als die von mir angegebenen Quellen und Hilfsmittel zur Erstellung meiner Dissertation verwendet habe. Den benutzten Werken wörtlich oder inhaltlich entnommene Stellen sind als solche gekennzeichnet.

(I herewith declare that for this thesis I have not used sources and aids other than those cited. Parts taken literally or as content from the references given have been properly indicated.)

Vladimir Kochergin
November 2006